LATERALLY SEPARATED MUONS FROM COSMIC RAY AIR SHOWERS MEASURED WITH THE ICECUBE NEUTRINO OBSERVATORY

DISSERTATION

zur Erlangung des Doktorgrades
Doctor rerum naturalium (Dr. rer. nat.)

Der Fachgruppe Physik vorgelegt von

DENNIS SOLDIN

Juni 2017

BERGISCHE
UNIVERSITÄT
WUPPERTAL

Bergische Universität Wuppertal
Fakultät für Mathematik und Naturwissenschaften
(Astroteilchenphysik)

Die Dissertation kann wie folgt zitiert werden:

urn:nbn:de:hbz:468-20180910-115302-5
[http://nbn-resolving.de/urn/resolver.pl?urn=urn%3Anbn%3Ade%3Ahbz%3A468-20180910-115302-5]

GUTACHTER:

Prof. Dr. Klaus Helbing
Prof. Dr. Hermann Kolanoski

ABSTRACT

Cosmic rays enter the Earth's atmosphere with energies up to 10^{20} eV, producing extended air showers, which contain up to billions of secondary particles that can be detected on the ground. Inside these showers, hadrons with large transverse momentum may be produced, which subsequently decay into muons, also carrying large transverse momentum. These muons separate from the shower core while traveling to the ground, producing lateral separations from the core up to several hundred meters. Together with the dense muon core bundle, they produce distinctive double-track signatures in the IceCube Neutrino Observatory. The corresponding lateral separation distributions are a measure of the underlying transverse momentum of hadrons, and therefore yield important information on hadron production during the air shower development.

In this work, the lateral separation of atmospheric muons, between 135 m and approximately 450 m, is measured using three years of IceCube data, taken between May 2012 and May 2015. A dedicated Monte Carlo for the simulation of laterally separated muons from air showers is presented. This is used to develop selection criteria in order to isolate the events of interest from IceCube data. In addition, a specific double-track reconstruction is introduced, which enables a precise measurement of the lateral separation and arrival direction of muons. Using existing energy estimation methods, which are optimized for the reconstruction of this class of events, the first primary energy dependent analysis of the lateral separation distribution of muons far from the shower core is performed.

After applying all selection criteria, 80951 events are left with an effective lifetime of 960 days. The resulting lateral separation distributions are studied with emphasis on the angular arrival directions and the transverse momentum of muons, which is estimated based on Monte Carlo simulations. In addition, the sensitivity of laterally separated muons on the mass composition of cosmic ray nuclei and the seasonal variations of the resulting muon fluxes over three years are studied.

Finally, the prospects for a search of double-track signatures, produced by exotic particles in cosmic ray air showers, which are predicted by theories beyond the standard model, are discussed. It is shown that, considering recent constraints on existing theoretical models, such as supersymmetry, the expected fluxes are below 10^{-3} events per year. Hence, it is concluded that the observation of exotic double-tracks from air showers, using existing neutrino telescopes, is not feasible.

CONTENTS

1 INTRODUCTION

"In order to change the world,
you have to get your head together first."
– James M. Hendrix *

Over 100 years ago, cosmic rays were first discovered by Hess (1912) and confirmed by Kohlhörster (1913) on balloon flights, where an increase of the ionization rate of air with altitude was observed [1, 2]. This effect was explained by radiation and was also observed on a balloon flight during a near-total eclipse of the Sun. Thus, Hess concluded that this increase was caused by radiation entering the atmosphere from outer Space. From studies on the effect of the Earth's magnetic field on this radiation in the 1930's, it was identified as being highly dominated by charged (massive) particles [3]. From these observations the term cosmic rays was coined, forming a new field of research, called astroparticle physics.

Over the last 80 years, this field of research has developed remarkably and knowledge of cosmic rays has improved significantly ever since. Today it is known that cosmic rays are highly dominated by ionized nuclei, about 90% protons, roughly 9% alpha particles, and the remainder are heavier nuclei [4]. These particles enter the atmosphere with energies up to about 10^{20} eV, producing a cascade of secondary particles, which form an extensive air shower that can be detected on the ground. However, many fundamental properties are still unknown and several major questions of the nature of cosmic rays are still open:

- What are the sources of cosmic rays and how are they accelerated?
- What is the origin of the spectral shape of primary energies?
- Is the cosmic ray flux isotropic?
- What is the mass composition of high-energy cosmic rays?

In order to answer these questions, the propagation of cosmic rays through Space, as well as the underlying physics of extensive air showers in the atmosphere need to be understood in detail.

Inside atmospheric particle showers, hadrons with large transverse momentum can be produced, which subsequently decay into muons. The muons separate from the shower core while traveling through the atmosphere, producing large lateral separations of up to several hundred meters from the shower core at the ground. These muons, together with a centered muon bundle, form

* As quoted by T. Brown, in *"Jimi Hendrix: The Final Days"* (1997).

distinctive double-track signatures, which can be observed in large neutrino telescopes. Laterally separated muons are typically produced early during shower development and therefore they yield important information on the shower development, as well as on the transverse momentum of hadrons, produced in high-energy cosmic ray interactions. Thereby, they can be used to test hadronic models and predictions from perturbative quantum chromodynamics. Since the lateral separation distributions of muons is highly related to the transverse momentum of their parent particles, they can be used to estimate the underlying transverse momentum distributions of hadrons, produced in high-energy collisions of heavy nuclei. This enables comparison to accelerator data and thereby laterally separated muons provide a direct connection between astroparticle and high-energy particle physics.

In addition, the underlying transverse momentum distributions depend on the energy per nucleon of the incident nucleus, and therefore on the mass of the primary cosmic ray. Hence, laterally separated muons can be used to draw conclusions on the elementary mass composition of cosmic rays. This represents a complementary approach to existing composition measurements, which are typically performed using large surface array detectors and mostly depend on various model assumptions.

In this work, a measurement of the lateral separation distribution of muons far from the shower core is presented, using three years of data from the *IceCube Neutrino Observatory* (IceCube), taken between May 2012 and May 2015. IceCube is a cubic-kilometer neutrino telescope, located in Antarctica at the geographic South Pole. Based on Monte Carlo simulations, the resulting distributions are used to determine the underlying transverse momentum distributioins of hadrons, which are compared to recent experimental accelerator data. The lateral separation distributions are also used to derive the mean logarithmic mass number of cosmic rays. Finally, the seasonal variations of lateral separated muons are measured, which can be used to study atmospheric effects on the corresponding muon fluxes.

In addition, it was previously proposed in literature [5, 6], that similar double-track signatures may be produced by exotic particles, which are predicted by several theories beyond the standard model and are potentially produced in hadronic cosmic ray interactions. Therefore, the feasibility for the direct detection of exotic particles in large neutrino telescopes is discussed in relation to various supersymmetric benchmark models. The prospects for other models beyond the standard model, such as higher-dimensional Kaluza-Klein theories, are also investigated as possible scenarios which could also produce double-track signatures in large neutrino telescopes, such as IceCube.

An introduction to the physics of cosmic rays is given in Chapter 2, with special emphasis on the production of extensive air showers in the Earth's atmosphere and the subsequent generation of laterally separated muons. The propagation of relativistic particles through dense matter is discussed in Chapter 3, which represents the general detection principle for many air shower experiments, including large neutrino telescopes. The IceCube experiment is

described in Chapter 4, where the detector design, as well as various physics applications, are discussed in detail. The Monte Carlo simulations of extensive air showers, used in this work, are presented in Chapter 5. Among common simulation packages, a dedicated approach to produce simulations of laterally separated muon events in IceCube is introduced, which enables detailed studies of the experimental data. The data selection is described in Chapter 6, including dedicated double-track reconstructions, as well as an estimator for the underlying transverse momentum. A primary energy estimator is also presented, which leads to energy-dependent studies of the resulting distributions of laterally separated muons. The results of this analysis are presented in Chapter 7, with a detailed discussion on the resulting lateral separation distributions, as well as the corresponding angular arrival directions of laterally separated muon events in IceCube. These distributions are used in order to derive the mean mass composition of the cosmic ray flux. In addition, the resulting transverse momentum distributions are shown and the corresponding seasonal variations of atmospheric muons are presented. In Chapter 8 the search for exotic particles in neutrino telescopes is discussed and the expected fluxes in IceCube are calculated, assuming various SUSY benchmark models, proposed in literature. Finally, a summary, subsequent discussions, and an outlook are given in Chapter 9.

2 COSMIC RAY AIR SHOWERS

"Astronomy? Impossible to understand
and madness to investigate."
– Sophocles *

The term *cosmic ray* refers to a particle that enters the Earth's atmosphere from outer space. These particles have a rate of approximately 1000 per square meter per second. Most of them have relativistic energies, i.e. energies somewhat larger than their rest masses, following a spectrum approximated by an inverse power law, with the highest energies reaching up to about 10^{20} eV. These particles are highly dominated by ionized nuclei, with about 90% being protons, roughly 9% alpha particles, and the rest being heavier nuclei [4]. When interacting with atomic nuclei within the atmosphere they can initiate cascades of secondary particles that form an *extensive air shower* (EAS) which can be detected on the ground.

In the following the basic concept of cosmic rays will be introduced (Section 2.1), covering the primary energy spectrum and the mass composition among other aspects. The development of extended air showers in the atmosphere is described in Section 2.2 with particular emphasis on the production of leptons in Section 2.3. An overview of various detection methods and recent experimental results will be shown in Section 3.2, including measurements from balloon and satellite experiments, as well as recent data from ground-based observatories.The physics of muons with large transverse momentum, which can be produced within high-energy air showers, will be discussed in Section 2.4.

2.1 COSMIC RAYS

The energy spectrum of cosmic rays can be measured directly using balloon or space-based experiments, and indirectly using ground-based observatories (see Section 3.2 for details). Thus, the spectrum of cosmic rays is well known over many orders of magnitude in energy. The knowledge of the elementary mass composition on the other hand, especially at the highest energies, is fairly uncertain. Furthermore cosmic ray sources and details on possible accelerating mechanisms are also largely unknown. However, in the following possible scenarios for cosmic ray sources, including potential accelerating mechanisms, and their resulting particle spectra will be discussed.

* As quoted by R. Cohen, in *"Chasing the Sun"* (2011).

2.1.1 THE SOURCES OF COSMIC RAYS

The lowest energy cosmic rays entering the Earth's atmosphere ($\leqslant 100\,\mathrm{MeV}$) are mainly produced in the Sun and are characterized by large temporal fluctuations associated with violent solar events [4, 7]. However, it was already noticed by Hess and others that the bulk of cosmic rays are uncorrelated with the solar activity [1–3]. Hence, the main origin of cosmic ray particles lies presumably outside the solar system.

It was suggested in the 1930's that cosmic rays are potentially produced in *supernovae* (SNs) [8], when a star has exhausted its hydrogen and helium supply and collapses under its own gravity. The remnant of a supernova is often a cold, dense *neutron star* with strong magnetic fields (*magnetar*). Due to an increasing rotation rate during the core collapse the resulting neutron star can rotate up to several hundred times per second (*pulsar*) [9]. Consequently, in the following decades the Crab Nebula [10] and magnetic variable stars [11] were suggested as potential sources of cosmic rays. Today supernova remnants (SNRs) are widely discussed as favorable candidates for accelerating cosmic rays up to energies of about $\sim 1\,\mathrm{PeV}$ [12–14] (see also Section 2.1.2). Although the sources of cosmic rays are still widely unknown, the dominant contribution is expected to originate from within our galaxy.

However, cosmic rays with energies of several hundred PeV have been observed (see for example Refs. [15–18]). For the highest energy cosmic rays, the gyroradii associated with typical galactic field strengths are larger than our galaxy (see also Section 2.1.2). Therefore their sources are assumed to be of extra-galactic origin. This results in a large variety of further possible source candidates, such as active galactic nuclei (AGNs) [19], magnetars [20], or gamma-ray bursts (GRBs) associated with the merger of compact objects, such as neutron stars or massive black holes [21, 22].

The production of cosmic rays at the highest energies is thought to be highly related to the emission of high-energy neutrinos, for example in the *fireball model* for GRBs [21, 23], or from particle acceleration in AGNs [24, 25]. IceCube has recently observed a flux of astrophysical neutrinos with energies up to the $\sim$ PeV region [26–29]. Future studies of astrophysical neutrinos at the highest energies will further improve knowledge of the acceleration mechanisms of particles in the Universe. Due to their unique role as astrophysical messengers, this will contribute to the constraint of potential source scenarios for cosmic rays at the highest energies.

2.1.2 ACCELERATION MECHANISMS

Standard stars, such as the Sun, can provide acceleration mechanisms for particles up to the GeV range. This acceleration is associated with time-dependent magnetic fields, which appear as sunspots for example, and can have magnetic field strengths up to ~ 1000 Gauss. The magnetic fields are produced by turbulent plasma through the *cyclotron mechanism* (see for example Refs. [7, 9]). In

addition, sunspots frequently appear in pairs with opposite magnetic polarity. As the sunspots approach each other they generate electrical fields of $\sim 10\,\mathrm{V/m}$. However, in the presence of these fields charged particles can be only accelerated up to energies of $\leqslant 100\,\mathrm{GeV}$.

The acceleration of cosmic rays to higher energies can be explained in the context of *Fermi acceleration* [30], based on interactions with dense shock fronts or interstellar magnetic clouds (see for example Ref. [7]).

The ejected envelope of a supernova, for example, forms a shock front traveling through the interstellar medium with velocity u_1. Assuming gas recedes behind this front with velocity u_2, it can be shown that the relative energy gain of a particle colliding with the shock front, with a velocity $v \simeq c$, is given by [9]

$$\frac{\Delta E}{E} \simeq \frac{4}{3} \cdot \frac{u_1 - u_2}{v} \,. \tag{2.1}$$

If the particle gets trapped between two shock fronts it can be reflected at the inner shock front. Thereby it gains the energy fraction

$$\frac{\Delta E}{E} \simeq 2 \cdot \frac{\Delta v}{v} \,. \tag{2.2}$$

Both mechanisms of shock acceleration are linear in the relative velocity and referred to as *first order Fermi acceleration*. It is possible to explain resulting particle energies of maximal $\sim 1\,\mathrm{PeV}$ using this mechanism within realistic scenarios [25, 31].

The acceleration of charged particles due to interactions with magnetic clouds is described by *second order Fermi acceleration*. Thereby, a cosmic ray particle with velocity v, interacting with a magnetic cloud of velocity u, on average gains the relative energy fraction

$$\frac{\Delta E}{E} \simeq 2 \cdot \frac{u^2}{v^2} \,. \tag{2.3}$$

The energy gain caused by this mechanism is quadratic in the velocity of the cloud. Hence, the energy gain per collision is rather small and acceleration via this mechanism requires a long time.

Cosmic ray energies of above $\sim 1\,\mathrm{PeV}$ can not be explained in terms of acceleration associated with the mechanisms described above. The *gyroradius* of a charged particle in a magnetic field B is given by

$$r_L = \frac{R}{cB} \,, \tag{2.4}$$

with the *magnetic rigidity*

$$R = \frac{pc}{Ze} \,, \tag{2.5}$$

where p is the total momentum of a particle with electrical charge Ze. In order to accelerate a proton, for example, to an energy $E \simeq pc$, the radius r of the accelerator must be larger than

$$r_L > \frac{E}{cB} \tag{2.6}$$

$$\Rightarrow E_{max} < r_L \cdot cB \,. \tag{2.7}$$

Taking inefficiencies in the acceleration process into account, for typical values of R and B generated during supernova shocks, the maximum energy must be less than $E_{max} \leqslant 1\,\text{PeV}$ [31]. Consequently there is a characteristic *rigidity cutoff*, R_c, where an acceleration process reaches its limit [32], and the maximum energy is given by the relation

$$E_{max} = Ze \cdot R_c \ . \tag{2.8}$$

Therefore, the mechanism of cosmic ray particle acceleration up to energies well above 1 PeV is yet unknown. To reach these large energies, particles have to be accelerated over large distances r, or there must be stronger magnetic fields present. Since at the highest energies the gyroradii of cosmic ray particles are associated with typical galactic fields that are larger than our galaxy, there must be additional acceleration mechanisms present.

Under realistic conditions, rotating magnetized neutron stars (pulsars), for example, can generate magnetic fields of up to $\sim 10^{12}$ Gauss. Since the rotation axis of pulsars does not necessary match the direction of the magnetic field, this can lead to strong electric field strengths of about 10^{15} V/m [9]. Although the details of this mechanism are largely unknown, this would imply a proton gaining ~ 1 PeV per meter travelled, which potentially results in very high cosmic ray energies [7, 20].

Further possible acceleration mechanisms are associated with extremely energetic astrophysical events, such as binary mergers of neutron stars or black holes, and gamma-ray bursts [19]. These are beyond the scope of this work and a comprehensive overview of various acceleration scenarios can be found for example in Refs [7, 9, 25, 31, 33].

2.1.3 COSMIC RAY SPECTRUM

While the sources of cosmic rays and details on their acceleration mechanism are largely unknown, the energy spectrum can be measured experimentally and is fairly well known. Figure 2.1 shows the cosmic ray spectrum measured by various experiments over several orders of magnitude [34]. The primary spectrum of all nuclei can be parametrized by multiple inverse (broken) power laws of the form [4]

$$\frac{d\Phi}{dE_0} = \frac{dN}{dt\,dA\,d\Omega\,dE_0} \propto E_0^{-\gamma} \ , \tag{2.9}$$

where E_0 is the energy of the primary nucleus. In order to account for different structures observed in the particle spectrum, in a first approximation this flux can be parametrized as

$$\frac{d\Phi}{dE_0} \simeq 1.8 \cdot E_0^{-\gamma} \, \frac{\text{nucleons}}{\text{cm}^2\,\text{s}\,\text{sr}\,\text{GeV/A}} \ , \tag{2.10}$$

where the spectral index γ changes from 2.7 to 3.0 at $E_{knee} \simeq 4\,\text{PeV}$, the so-called *knee*, and to $\gamma \simeq 3.2$ at around 0.6 EeV (*second knee*) [35, 36]. At the *ankle*, around

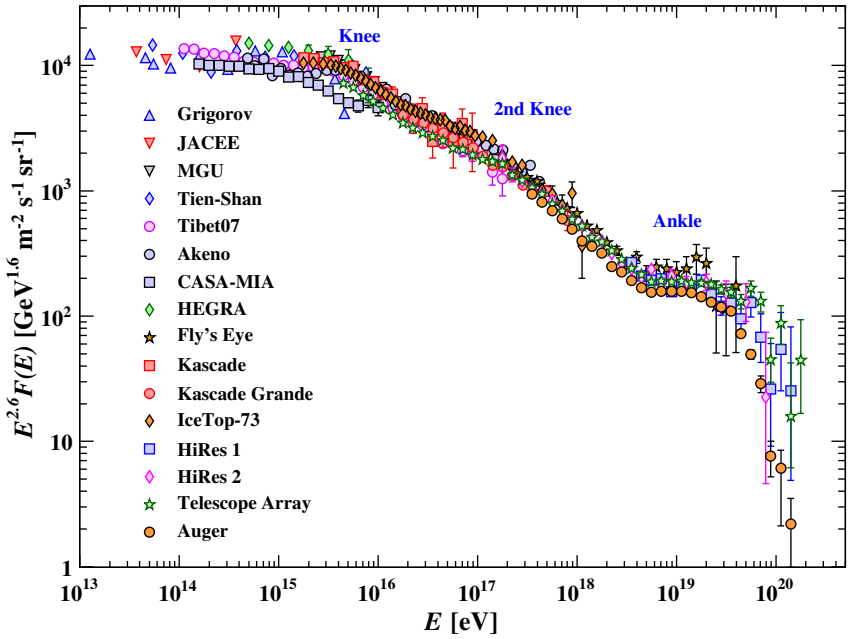

Figure 2.1: All particle primary spectrum of cosmic rays using data from various experiments. Figure taken from Ref. [34].

$E_{ankle} \simeq 4\,\text{EeV}$, the spectral index changes back to $\gamma \simeq 2.7$ [15, 18]. The origin of these structures is not yet fully understood. It is common to interpret them in terms of various particle *populations*, produced by different cosmic ray sources [12, 13, 32, 37–39]. The associated energy spectra may be characteristic of certain acceleration mechanisms and can therefore explain the observed features. More sophisticated flux models, assuming different populations and taking several primary nuclei into account, are discussed in Section 2.1.4.

The spectrum of cosmic ray primary particles reaches over roughly 20 orders of magnitude in energy, up to a predicted upper limit of around $E_{GZK} \simeq 6 \cdot 10^{19}$ eV, the *GZK suppression* (after Greisen, Zatsepin, and Kuzmin (GZK)) [40, 41]. This suppression is expected to be caused by interactions of the cosmic rays with photons of the Cosmic Microwave Background (CMB), producing a short-lived delta resonance that decays into protons or neutrons, and positive and neutral pions via

$$\gamma_{CBM} + p \to \Delta^+ \to \begin{cases} p + \pi^0 \\ n + \pi^+ \end{cases} \tag{2.11}$$

This theoretical motivated cutoff is not confirmed experimentally yet, and there is some tension with earlier results reported by the AGASA Collaboration [42]. However, recent data from the HiRes Collaboration [15], and results from

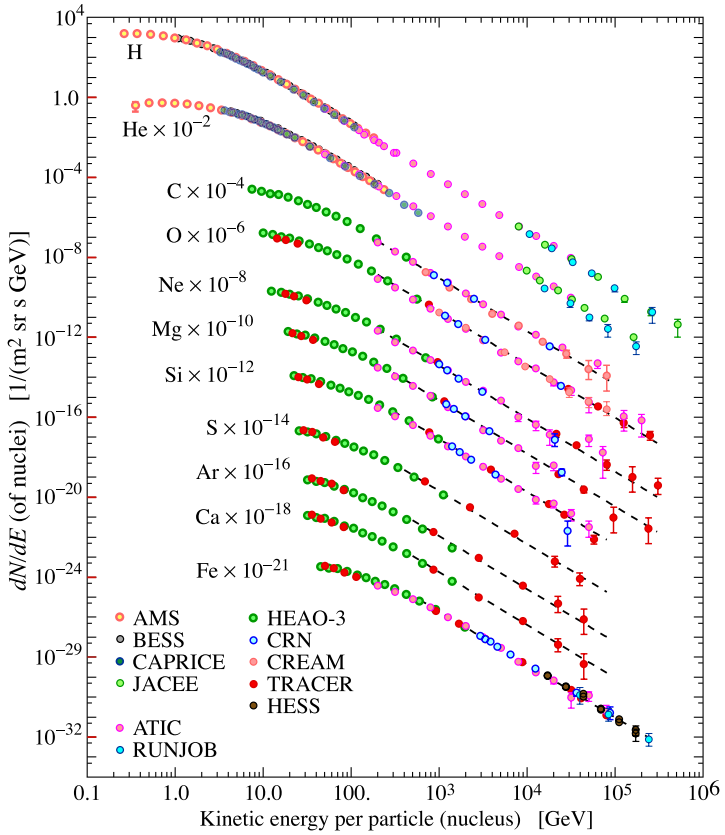

Figure 2.2: Cosmic ray spectra for several chemical elements using data from various experiments. Figure taken from Ref. [34].

the Pierre Auger Observatory [18], shown in Figure 2.1, do suggest a suppression of cosmic rays above $\sim 4 \cdot 10^{19}$ eV.

2.1.4 MASS COMPOSITION

Due to the steep energy spectrum of cosmic rays, the average chemical composition of cosmic rays is highly dominated by particles in the low energy regime, i.e. in the GeV range. Here, the mass composition is experimentally well known from direct measurements (see Section 3.2). The resulting energy spectra, taken by various experiments, are shown in Figure 2.2 [34].

However, due to the very low particle fluxes in the high-energy range (above a few TeV), the description of the elemental composition of high-energy cosmic rays relies on indirect measurements (see also Section 3.2), which are experimentally more challenging. The interpretation of data in terms of the primary mass composition usually strongly relies on (hadronic) model assumptions, which in turn cause large systematic uncertainties on the measurement, as discussed for example in Ref. [43]. Hence, today's knowledge of the mass composition of cosmic rays at high energies is largely uncertain.

Theoretically, the elemental composition of cosmic ray nuclei can be described assuming multiple populations of cosmic rays originating from different potential sources. This is done in order to describe the spectral features of the cosmic ray flux (knee, second knee, ankle), shown in Figure 2.1. The composition is typically described using the five different elemental groups: p, He, CNO, Mg − Si, and Fe, as discussed in Refs. [37, 38]. The cosmic ray spectrum can be divided into three populations of cosmic rays. The first population is associated with the acceleration of particles by the shock fronts of supernova remnants, as explained in Section 2.1.2, where the knee is associated with a cutoff of this population [12, 13]. The second population is expected to be a higher-energetic galactic component with unknown origin. The final population at the highest energies (around the ankle) originates from potential extra-galactic sources [37].

These spectral features are expected to depend on the magnetic rigidity cutoff [25, 31, 32], as defined in Equation (2.8). If each of the populations j contains the elemental groups i, then the all particle spectrum can be parametrized by [38]

$$\Phi_i(E_0) \equiv \frac{dN_i}{d\ln(E_0)} = \sum_j a_{i,j} \cdot E_0^{-\gamma_{i,j}} \cdot \exp\left(-\frac{E_0}{Z_i R_{c,j}}\right) . \tag{2.12}$$

A fit to recent experimental data using this model was performed in Ref. [38]. Assuming that all three populations contain all of the 5 elemental groups, the resulting parametrization is referred to as the H3A parametrization. The resulting elemental abundances, using the H3A model, are shown in Figure 2.3, where they are compared to experimental data (for further details see Ref. [38]). The so-called H4A parametrization assumes the highest-energetic (extra-galactic) population being protons only. A third parametrization, using the same approach but with qualitatively different parameters [39], is referred to as GST parametrization. In particular, it uses different characteristic rigidity cutoffs to fit recent experimental data, resulting in harder energy spectra, especially for the first, lowest-energetic population. The corresponding parameters for the cosmic ray primary flux models used in this work can be found in Appendix A.1.

2.2 EXTENSIVE AIR SHOWERS

Cosmic rays enter the Earth's atmosphere with initial energies up to 10^{20} eV, where they interact with air nuclei, producing cascades containing billions of secondary particles. While propagating through the atmosphere these cascades of secondary particles form an extensive air shower that can be detected with large surface or large-volume detectors on the ground, of which neutrino detectors are a key example (see Section 3.2). In general, these particle cascades can be divided into two classes, described in the following.

Electromagnetic Cascades

Pure electromagnetic cascades are produced by gamma radiation, electrons, or positrons that undergo elastic scattering processes with air nuclei in the

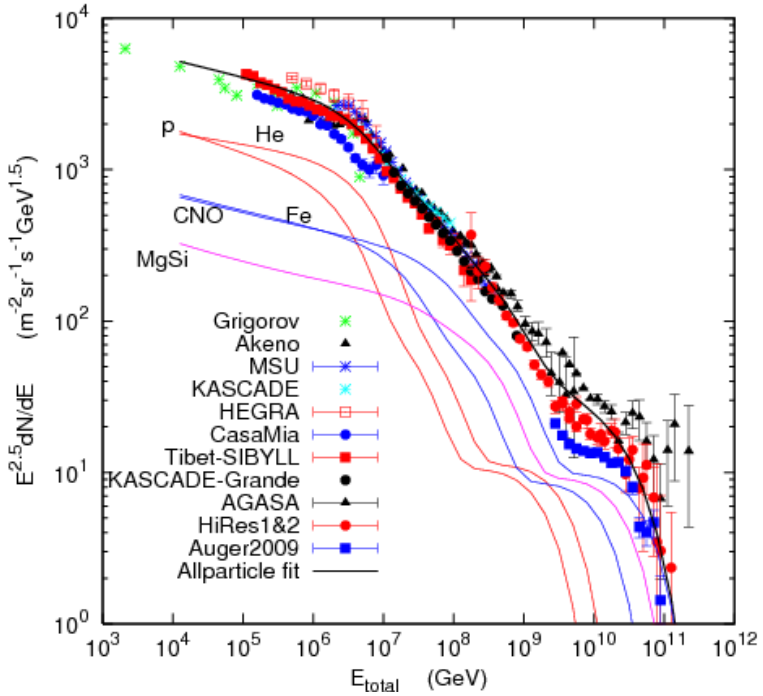

Figure 2.3: All particle spectrum using data from various experiments. Solid lines show the H3A primary flux parametrization, as described in the text. Figure taken from Ref. [38].

atmosphere. A high-energy photon entering the atmosphere will most likely produce an electron-positron pair, as shown in Figure 2.4 (a). Following the so-called *Heitler model* [44, 45], these pairs, as well as primary electrons or positrons entering the atmosphere, produce gamma radiation due to bremsstrahlung, which in turn produces another e^+e^- pair. These processes continue until the energy drops to a level where collisional energy losses start dominating (see Section 3.1) and the shower development rapidly stops. These cascades form the *electromagnetic component* of extensive air showers.

Hadronic Cascades

Hadronic cascades are produced by nuclei entering the atmosphere with high energies and interacting hadronically with an air nucleus. In deep-inelastic scattering processes many secondary hadrons are produced, predominantly light mesons, such as pions and kaons, but also short-lived vector mesons or heavier hadrons and nuclei. These hadrons can either decay or re-interact in the atmosphere, producing another generation of hadrons, as shown in Figure 2.4 (b). This procedure continues until the hadrons decay (mainly into muons and neutrinos) or reach the ground. As described in Section 2.3, this *hadronic component* produces the muons during the air shower development, and therefore represents the main focus of this work.

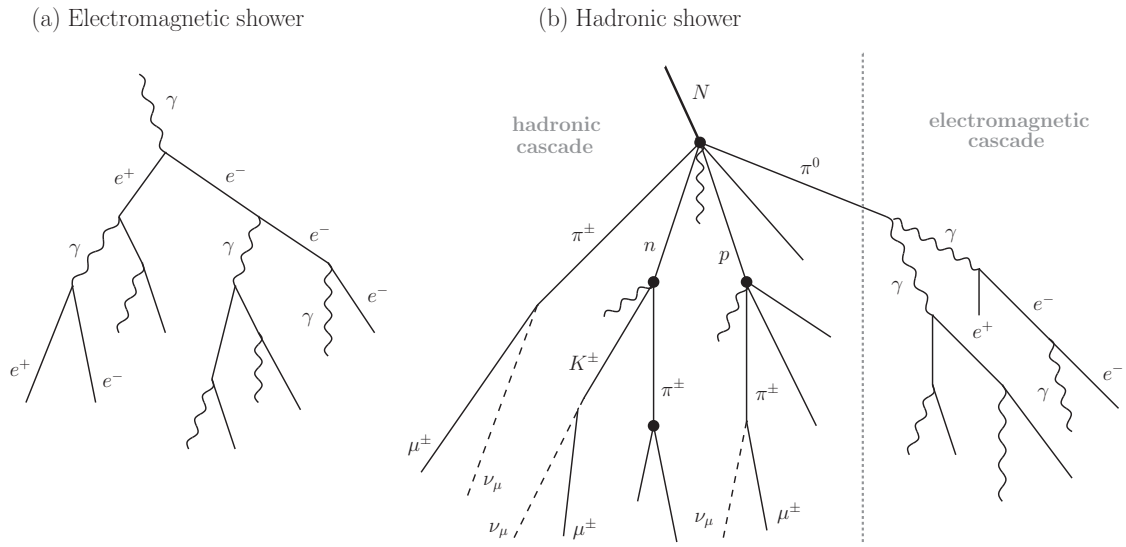

Figure 2.4: Schematic concept of air shower development. (a) Pure electromagnetic shower initiated by a gamma photon. (b) Hadronic shower from primary Nucleus N, including a large hadronic cascade and an electromagnetic sub-shower (see text for details). Black solid circles indicate hadronic interactions with air nuclei.

Neutral pions produced in these hadronic cascades predominantly decay into two photons, producing electromagnetic sub-showers as described above, contributing to the electromagnetic component. This process is also shown in Figure 2.4 (b).

2.2.1 ATMOSPHERE

The development of extensive air showers depends significantly on the Earth's atmosphere, which provides the target nuclei for all particle interactions. The atmospheric density profile can be described by a simple *isothermal model*, where the density at altitude H is given by

$$\rho(H) = \rho_0 \cdot e^{-H/h_0} \tag{2.13}$$

with the *scale height* $h_0 = 6.4\,\mathrm{km}$ and $X_0 = \rho_0 h_0 = 1300\,\mathrm{g/cm^2}$. To a good approximation, the atmospheric chemical composition is independent of the altitude up to about $\sim 100\,\mathrm{km}$ [46] and the average mass number of air is roughly given by $\langle A \rangle = 14.5$.

The atmospheric *slant depth* X is defined as the integral over the density profile along the path dl of the initial particle with an arriving (zenith) angle θ [46]

$$X(L,\theta) = \int_L^\infty \rho(H(l,\theta))\,dl = X_0 \cdot e^{-H(L,\theta)/h_0}\,, \tag{2.14}$$

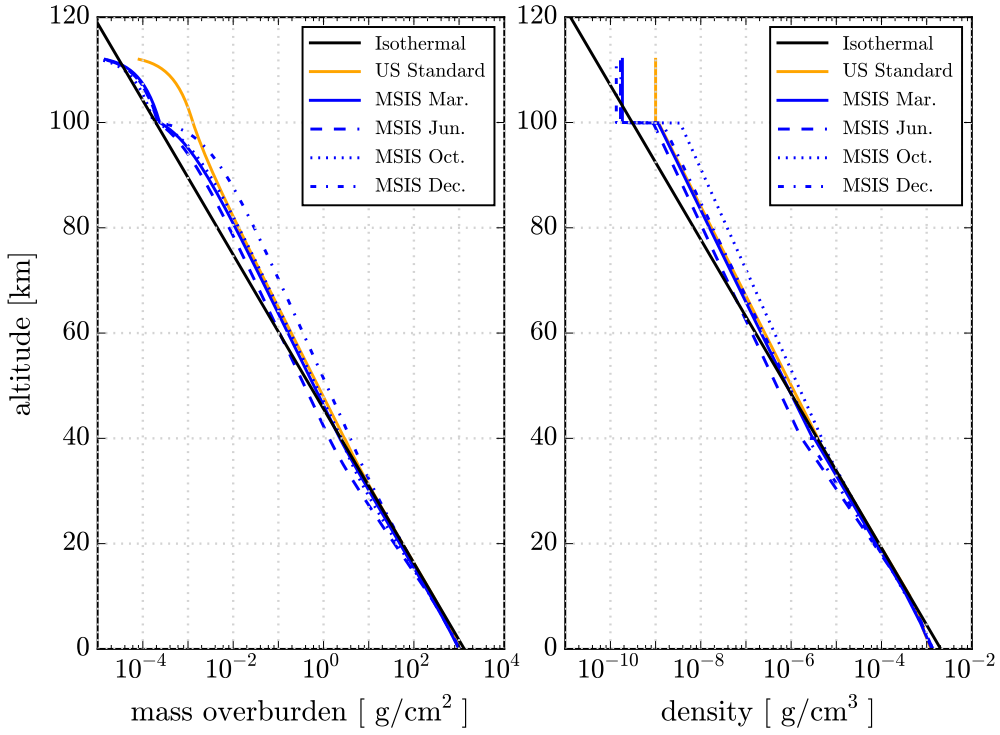

Figure 2.5: The atmospheric density profile for the simple isothermal model in Equation (2.13), and using the MSIS parametrizations [47], as well as the standard middle European and US standard atmosphere parametrizations, all taken from [48]. The dashed black lines indicate the section scaled up, shown on the right hand side (linear scale). The blue band shows the maximum seasonal fluctuations (Dec.-Jun.) for the MSIS model.

where the distance L to the ground is related to the atmospheric height by

$$\begin{aligned} H(L,\theta) &= \sqrt{R_\odot^2 + 2LR_\odot\cos(\theta) + L^2} - R_\odot \\ &\simeq L\cdot\cos(\theta) + \frac{L^2}{2R_\odot}\cdot\sin^2(\theta) \end{aligned} \tag{2.15}$$

with the Earth's radius $R_\odot = 6371\,\text{km}$ [34]. For directions not too far from vertical, i.e. $\theta \leqslant 60°$, the curvature of the earth can be neglected [4, 46], and Equation (2.15) is approximated by

$$H(L,\theta) \simeq L\cdot\cos(\theta), \tag{2.16}$$

and thus

$$\rho(X,\theta) \simeq \frac{X\cdot\cos(\theta)}{h_0}\,. \tag{2.17}$$

The *mass overburden* is defined as vertical profile $T(H) \equiv X(H,\theta = 0°)$.

Figure 2.5 shows the atmospheric mass overburden for the isothermal model as a function of atmospheric altitude. Also shown, for comparison, are the

MSIS-90-E models for the South Pole atmosphere, and the middle European and US standard atmospheric profiles [47, 48]. These models use a 5-layer parametrization, given in Appendix A.2, and are used in common air shower simulation software packages, such as CORSIKA [48] (see also Section 5.1).

2.2.2 CASCADE EQUATIONS

Whether a particle decays or interacts with an air molecule in the atmosphere depends on the particle's *decay length* and *interaction length* respectively. The decay length (in g/cm^2) for a hadron h at speed v depends on its *mean lifetime* τ_h, and the density profile (Equation (2.13)) of the atmosphere and is given by [4]

$$\lambda_{dec,h}(E_h, H) = c\beta\gamma\tau_h\rho(H) \,, \tag{2.18}$$

where c is the speed of light. γ is the Lorentz factor and $\beta = v/c$. The interaction length (in g/cm^2) of a hadron h is given by [46]

$$\lambda_{int,h}(E_h, H, \theta) = \frac{\rho(H)}{\sum_A \sigma_{hA}(E_h) \cdot n_A(H)} \,, \tag{2.19}$$

where $n_A(H)$ is the number density of nuclei with atomic number A at height H. σ_{hA} is the inclusive inelastic cross-section for collisions of the hadron with a nucleus of mass number A. Assuming a constant mass composition of the atmosphere and using the average mass number of $\langle A \rangle = 14.5$, Equation (2.19) can be approximated by

$$\lambda_{int,h}(E_h) \simeq \frac{\langle A \rangle}{\sigma_{h-air}(E_h) \cdot N_0} \,, \tag{2.20}$$

with $N_0 = 6.022 \cdot 10^{23}\, g^{-1}$ [49].

The propagation of particles through the atmosphere can be described by the *cascade equations* [4]. These equations depend on the properties of the atmosphere and they take the interactions of all types of hadrons that are produced into account. Since many hadrons are involved in the shower development, usually a set of coupled differential equations needs to be solved. In matrix notation they are given by

$$\frac{d\Phi_h(E,X)}{dX} = -\left(\frac{1}{\lambda_{int,h}} + \frac{1}{\lambda_{dec,h}}\right) \cdot \Phi_h(E,X) + \\ + \sum_h \int \frac{F_{hj}(E_h, E_j)}{E_h} \frac{\Phi_j(E_j)}{\lambda_{int,j}} dE_j \,, \tag{2.21}$$

where $\lambda_{dec,h}$ und $\lambda_{int,h}$ are given in Equation (2.18) and Equation (2.19) and the atmospheric slant depth X is given in Equation (2.14). These equations basically consist of three terms: the first two terms describe re-interactions and decays of particles in the atmosphere, while the last (regeneration) term describes

the production of new particles within the shower development. The function $F_{hj}(E_h, E_j)$ is the dimensionless inclusive cross-section for an initial particle h to produce an outgoing particle of type j:

$$F_{hj}(E_h, E_j) \equiv E_j \cdot \frac{dN_j(E_j, E_h)}{dE_j} \tag{2.22}$$

Here, dN_j is the average number of particles of type j in the energy interval dE_j produced per collision by an incident particle h [4].

Since there are up to billions of particles produced during shower development, in practice these equations need to be solved numerically using detailed Monte Carlo (MC) simulations. Commonly used software packages for the treatment of the shower development in the atmosphere are, for example, CORSIKA (see also Section 5.1) [48] or MCEq [50].

2.3 ATMOSPHERIC LEPTONS

The number of leptons produced during the shower development can in principle be derived from the cascade equations (Equation (2.21)). Whether a hadron interacts in the atmosphere or decays, producing a lepton, depends on the ratio of the first two terms in these equations, i.e. on the decay and interaction lengths, given in Equation (2.18) and Equation (2.19). The *critical energy* ϵ_h of a hadron h, which corresponds to the condition where the decay length is equal to the scale height h_0, is given by [49]

$$\epsilon_h \equiv \frac{h_0 \cdot m_h}{c \cdot \tau_h} \,, \tag{2.23}$$

where m_h is the mass and τ_h the mean lifetime of the decaying hadron, and h_0 is given in Equation (2.13). The critical energies for for pions and kaons, for example, are given by $\epsilon_\pi = 115\,\text{GeV}$ and $\epsilon_K = 850\,\text{GeV}$. Below these critical energies, pions and kaons will most likely decay within the atmosphere, producing the dominant contribution to the lepton flux from cosmic ray air showers, the *conventional* flux. These mesons predominantly decay into leptons, where the relevant decay channels and corresponding *branching fractions* [34] are given by

$$\begin{aligned}
\pi^\pm &\to \mu^\pm + \nu_\mu(\bar{\nu}_\mu) && (\sim 100\%)\\
K^\pm &\to \mu^\pm + \nu_\mu(\bar{\nu}_\mu) && (\sim 63.5\%)\\
K^0_L &\to \pi^\pm + \mu^\mp + \nu_\mu(\bar{\nu}_\mu) && (\sim 27.0\%)\\
K^0_L &\to \pi^\pm + e^\mp + \nu_e(\bar{\nu}_e) && (\sim 38.7\%)
\end{aligned}$$

As described in Section 2.2, electrons produce electromagnetic sub-showers containing gamma photons and electrons. Additionally, decays of neutral pions produced in hadronic interactions via

$$\pi^0 \to 2\gamma \qquad (\sim 100\%)$$

also initiate sub-showers due to pair-production and bremsstrahlung processes, where electrons and positrons are produced.

However, at high energies $E_h > \epsilon_h$, the decay of pions and kaons is suppressed, since they re-interact within the atmosphere rather than decaying into leptons. The relative contribution from heavier hadrons increases with increasing energy, because the critical energies of hadrons scale with the mass. Although these hadrons typically have very small branching fractions into leptons, they are expected to dominate the lepton fluxes at very high energies. Having decay lengths of below 1 cm at typical energies, these hadrons decay immediately and this contribution is therefore called *prompt* lepton flux. This contribution is dominated by decays from charmed hadrons, such as $D^{\pm}$ and D^0, and from the short-lived (unflavored) vector mesons η, η', and ω [34, 50], via

$$\begin{aligned} D^{\pm} &\to \mu^{\pm} + X && (\sim 17.6\%) \\ D^0 &\to \mu^{\pm} + X && (\sim 6.7\%) \\ \eta &\to \mu^+ + \mu^- + \gamma && (\sim 3.1 \cdot 10^{-4}) \\ \eta' &\to \mu^+ + \mu^- + \gamma && (\sim 1.1 \cdot 10^{-4}) \\ \omega &\to \mu^+ + \mu^- + \pi^0 && (\sim 1.3 \cdot 10^{-4}) \end{aligned}$$

The D mesons have many different decay modes, therefore they are combined and denoted with X. The individual decay modes can be found in [34]. The critical energy of prompt hadrons is approximately given by $\epsilon_{\text{prompt}} \simeq 5 \cdot 10^7$ GeV [49].

In principle, the coupled cascade equations (Equation (2.21)) need to be solved for a detailed description of the lepton fluxes on the ground. Recent calculations, based on numerical solutions of the cascade equations, with an explicit treatment of all relevant particles involved in the shower development, can be found in [50]. Figure 2.6 shows the expected energy spectra of vertical atmospheric muons on the ground from different hadronic components, calculated with the MCEq software package [50]. These calculations are based on Sibyll 2.3 [51] and use a South Pole atmospheric profile (Jun.). They favor a transition energy of roughly $E_{\mu,c} \simeq 700$ TeV where the prompt component becomes the dominant contribution.

In a good approximation, the total atmospheric muon spectrum can be parametrized, assuming a simple isothermal model, and using the critical energies defined in Equation (2.23), by [4, 38]

$$\begin{aligned} \frac{d\Phi_\mu}{dE_\mu} \simeq \frac{0.14 \cdot E_\mu^{-2.7}}{\text{cm}^2\,\text{s}\,\text{sr}\,\text{GeV}^{-3.7}} \cdot \Bigg[& \left(1 + \frac{1.1 \cdot E_\mu \cos(\theta)}{\epsilon_\pi}\right)^{-1} + \\ & + 0.054 \cdot \left(1 + \frac{1.1 \cdot E_\mu \cos(\theta)}{\epsilon_K}\right)^{-1} \\ & + 9.1 \cdot 10^{-6} \cdot \left(1 + \frac{1.0 \cdot E_\mu \cos(\theta)}{\epsilon_{\text{prompt}}}\right)^{-1} \Bigg] \,. \end{aligned} \tag{2.24}$$

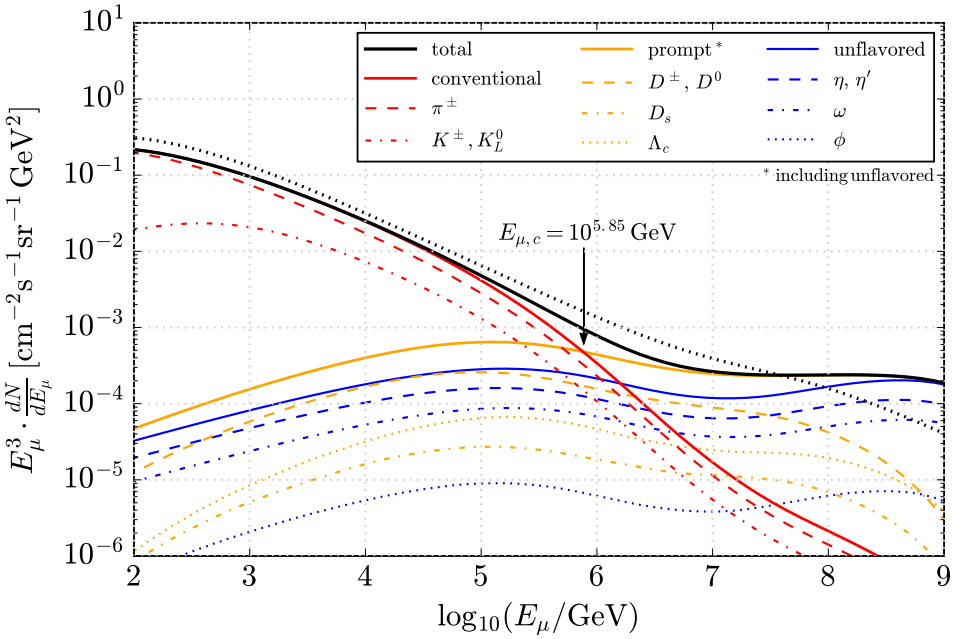

Figure 2.6: The vertical atmospheric muon flux from different components calculated using MCEq [50] with Sibyll 2.3 [51] as hadronic model for the South Pole atmosphere (Jun.). Also shown is the (total) vertical muon flux from the parametrization in Equation (2.24), as black dotted line.

The vertical ($\theta = 0$) muon flux using this parametrization is also shown in Figure 2.6, as black dotted line.

Most of the muons produced during air shower development are highly relativistic with velocities of about $\beta \sim 1$ and can reach the ground before decaying due to time dilatation effects. However, at low energies, muons produced in the air shower can decay into electrons and a neutrino-pairs via

$$\mu \to e^{\pm} + \nu_e(\bar{\nu}_e) + \bar{\nu}_\mu(\nu_\mu) \; . \qquad (\sim 100\%)$$

For the energies considered in this work ($E_\mu \sim 1$ TeV), muon decays are negligible, since the path length of these muons is in the order of $\sim 10^7$ km.

Experimentally, the atmospheric muon spectrum has been measured up to a few PeV, for example using data taken by IceCube in its 79-string configuration [52]. The total muon flux, including the contribution from a prompt component, is consistent with the spectra shown in Equation (2.24) [50] and other theoretical predictions [46, 49, 53]. In addition, studies on atmospheric muons in IceCube are on-going, using improved analysis techniques, new unfolding methods, and further years of data [54].

2.4 LATERALLY SEPARATED MUONS

While the bulk of muons produced during the shower development forms a rather dense core, the *muon bundle*, muons can also be produced with large *transverse momentum* p_T. These muons then separate from the shower core while traveling to the ground, resulting in separations up to several hundred meters from the bundle core. These isolated muons are henceforth referred to as *laterally separated muons* (LS Muons).

Generally, the transverse momentum of any particle, produced from an interaction with initial particle momentum in z-direction, using cartesian coordinates (x, y, z), is defined as:

$$p_T \equiv \sqrt{p_x^2 + p_y^2} \, . \tag{2.25}$$

The corresponding *longitudinal momentum* is defined as $p_z \equiv p_{\parallel}$. The *transverse energy* of the particle is then given by

$$E_T = E \cdot \sin(\phi_T) = \sqrt{p_T^2 c^2 + m^2 c^4} \, . \tag{2.26}$$

For the highly relativistic particles considered in this work, $mc \ll p$, and the small-angle approximations

$$c \cdot p \simeq E \quad , \quad \frac{p_T}{p} = \sin(\phi_T) \simeq \phi_T \tag{2.27}$$

are used. The *transverse angle* is then approximately given by

$$\phi_T \simeq \frac{c \cdot p_T}{E} \, . \tag{2.28}$$

At low energies, the transverse momentum distributions of particles can be described in the context of the so-called *statistical-bootstrap model* (SBM) [55, 56]. This model is motivated from methods used in statistical mechanics which are applied in order to describe particle physics phenomena. The SBM was invented in the early 1970's, however in modern physics particle interactions in the low-energy regime are more commonly described in the context of *lattice quantum chromodynamics* (LQCD) [57]. The SBM uses well-known methods from thermodynamics, and due to historical reasons, the following discussion will be based on the SBM for simplicity. A LQCD-inspired discussion would yield analogous phenomenological results. For a general introduction in LQCD, see for example Refs. [57, 58].

The SBM assumes hadron states being compounds of various constituents, confined within a potential box, where the individual constituents are treated as non-interacting [56]. The individual constituents are assumed to be hadrons themselves. Hence, each hadron is a bound state of other hadrons which are held together by forces carried by further hadrons. The types of all possible hadrons, including all possible resonances and bound states, form a *hadronic mass spectrum*. Using this *bootstrap* approach, the total energy density of the

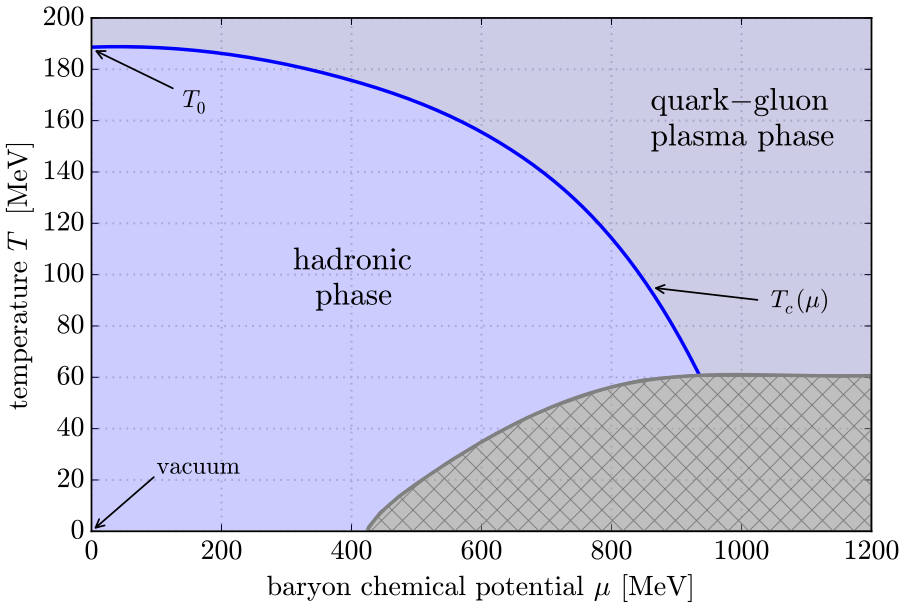

Figure 2.7: Phase transition from the hadronic to the quark-gluon plasma phase as originally described within the bootstrap model in Ref. [55]. The blue curve represents the critical temperature $T_c(\mu)$, as described in the text and with the model parameters given in Ref. [55]. In the shaded gray region the SBM becomes unreliable.

system can be derived, based in the *grand canonical formalism*, as shown in Ref. [56]. When calculating the corresponding mass spectrum, singularities occur at a *critical temperature* $T_c(\mu)$, where μ is a *baryon chemical potential* [55]. This divergent behaviour is interpreted as *phase transition* which defines a *hadronic phase* and a *quark-gluon plasma* (QGP) phase in the T-μ-plane, as shown in Figure 2.7. The corresponding limiting temperature $T_0 \equiv T_c(\mu = 0)$ defines the *boiling point* at which hadronic matter is no longer stable and subsequently converts into *quark matter* before entering the QGP phase. T_0 is the most fundamental constant within the SBM and referred to as *Hagedorn temperature*. It varies from roughly $\sim 140\,\mathrm{MeV}$ (SBM) to above $\sim 200\,\mathrm{MeV}$ (LQCD), depending on the method used to derive its value [59]. It is close to the mass of the lightest hadrons (π/K), which are the most abundant hadrons produced in particle interactions, and de-confined first by thermal fluctuations.

In addition, the bootstrap model allows calculations of the transverse momentum distributions of hadrons. The *momentum spectrum* in the SBM is generally given by [60]

$$f(\vec{p}, m, T)\,d^3p = \kappa \cdot \exp\left(-\frac{\sqrt{p^2c^2 + m^2c^4}}{T}\right) d^3p\,, \tag{2.29}$$

where m is the mass of a particle with momentum $\vec{p}$ at temperature T. κ is a constant. Thereby, the momentum spectrum $f(\vec{p}, m, T)$ represents the mean number of particles with mass m and momentum $\vec{p}$. As shown in Ref. [60],

using $d^2p = 2\pi p_T \, dp_T \, dp_\parallel$ and integrating over the longitudinal component $p_\parallel$, the transverse momentum distribution is given by

$$\frac{dN(p_T, m, T)}{2\pi p_T \, dp_T} = \kappa \cdot \sqrt{p_T^2 c^2 + m^2 c^4} \cdot \cdot \sum_{\beta=1}^{\infty} (\pm 1)^{\beta+1} \cdot K\left(\beta \cdot \frac{\sqrt{p_T^2 c^2 + m^2 c^4}}{T}\right), \tag{2.30}$$

with $+$ for bosons, $-$ for fermions, and a constant β. The function $K(x)$ has an exponential form and is given in Ref. [60]. Equation (2.30) assumes thermal equilibrium, which is a valid approximation for low transverse momenta of about $p_T \leqslant 1\,\mathrm{GeV}/c$ [55]. Neglecting Fermi and Bose statistics for the energies (temperatures) considered in this work ($p_T \gg m$), Equation (2.30) can be approximated by

$$\frac{dN}{2\pi p_T \, dp_T} \simeq \alpha \cdot \exp\left(\beta \cdot \frac{p_T}{T}\right), \tag{2.31}$$

with constants α and β. Thus, the p_T distributions in the context of SBM follow an exponential behaviour, which is in good agreement with measurements at low transverse momentum $p_T \leqslant 1.5\,\mathrm{GeV}/c$ [55, 61]. Moreover, recent theoretical calculations in the context of the more sophisticated lattice QCD [62, 63] are (at least) in quantitative agreement with various predictions from the SBM [59]. Further details on the transverse momentum distribution in the context of the SBM, as well as related comprehensive discussions, can be found in Refs. [56, 59, 60].

However, the SBM predictions are generally only valid for temperatures $T < T_c$ and in order to account for large momentum transfer in high-energy hadronic interactions, additional effects need to be taken into account. It is known from various accelerator measurements, that the high-p_T tails of hadron transverse momentum distributions closely follow a power law [61, 64–69]. This behaviour can be described in the context of *perturbative quantum chromodynamics* (PQCD), which is based on the *parton model*, where a hadron is formed by many point-like constituents (see for example Refs. [58, 70–74]). These so-called *partons* (gluons or quarks), which move almost collinear, share the total momentum of the hadron. According to the *renormalization group equations* the strong coupling constant α_s decreases logarithmically as

$$\alpha_s(p^2) \simeq \frac{1}{b_0 \cdot \ln(p^2/\Lambda_{QCD})}, \tag{2.32}$$

where p is the particle's momentum and b_0 is a constant, given in Refs. [75, 76]. The QCD scale $\Lambda_{QCD} \simeq 220\,\mathrm{MeV}$ is the value at which the renormalization scale μ diverges and it forms an *infrared cutoff* of the (effective) theory. The strong coupling decreases logarithmically with increasing momentum, which is a unique feature of QCD, known as *asymptotic freedom* [75, 76]. This allows calculations of hadronic interactions, described by Feynman diagrams, in the

context of *perturbation theory*, treating the individual partons as free particles. In order to derive finite solutions in the context of PQCD, the underlying scattering process needs to be sufficiently hard. This is typically associated with high transverse momenta approximately above $p_T \geqslant 2\,\mathrm{GeV/c}$ (*hard-scattering*), which is referred to as high p_T throughout this work. Only these hard-scattering processes can be described using perturbation theory. For a comprehensive introduction to perturbative QCD, see for example Ref. [58].

Based on PQCD calculations, it can be shown that the transverse momentum distributions of hadrons follow a power law of the form

$$\frac{dN}{2\pi p_T\, dp_T} \propto p_T^{\beta} \cdot f(x_T)\,, \tag{2.33}$$

where the spectral index β depends on the underlying collision energy [70, 71]. The *parton distribution functions* $f(x_T)$ account for the probability density of a parton being produced with a transverse momentum fraction x_T.

Hard-scattering processes are associated with a large four-momentum transfer $Q^2 \gg \Lambda_{QCD}$ between the interacting partons, and the production of high transverse momenta. In hard-scattering processes the high-p_T hadrons are usually not produced as isolated particles, but within clusters of collimated particles, referred to as high-p_T *jets*. In the leading order of α_s it can be shown that high-p_T hadrons are produced in jet pairs with hadrons, having nearly opposite, *back-to-back*, directions (*di-jets*). Moreover, collisions of multiple partons can produce *multi-jets* with high p_T, which can also be described using PQCD [77, 78].

The transverse momentum of hadrons in the soft, low-energy regime can be described using the SBM or LQCD and the resulting distributions are expected to follow an exponential distribution. In contrast, in the hard regime ($p_T \geqslant 2\,\mathrm{GeV/c}$) PQCD calculations predict power law behaviour. As mentioned before, these expectations are in agreement with recent experimental data.

Hence, throughout this work the transverse momentum distributions of particles are described by the *Hagedorn function* [55] of the form

$$\frac{dN}{2\pi p_T\, dp_T} = \alpha \cdot \left(1 + \frac{p_T}{p_0}\right)^{\beta}\,. \tag{2.34}$$

The *normalization* α, the *spectral index* β, and the *transition parameter* p_0 are free parameters. This functional form is an empirical formula which accounts for the low and the high-p_T regime of hadrons. It is essentially the same as the *Tsallis function* [79, 80], which is often referred to in literature, where the transition parameter is associated with the temperature as $p_0 \to \beta \cdot T_0$. The Hagedorn function follows an exponential distribution for low $p_T < p_0$ and behaves like a power law towards high $p_T > p_0$,

$$\left(1 + \frac{p_T}{p_0}\right)^{\beta} \longrightarrow \begin{cases} \exp(\beta \cdot p_T/p_0) & , \quad \text{for } p_T \to 0\,, \\ (p_T/p_0)^{\beta} & , \quad \text{for } p_T \to \infty\,, \end{cases} \tag{2.35}$$

as expected from SBM and PQCD predictions. Subsequently the transition parameter p_0 is highly related to the critical temperature $T_c(\mu = 0) \equiv T_0$

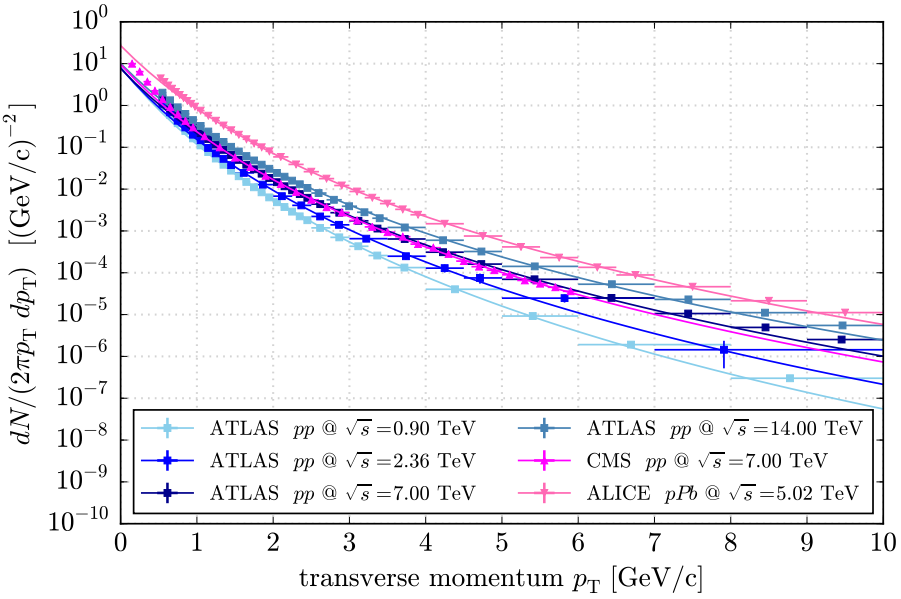

Figure 2.8: Transverse momentum distributions of charged hadrons measured by various LHC experiments in proton-proton (proton-lead) collisions at different energies. Solid lines show the corresponding Hagedorn fits of the form Equation (2.34) with $p_0 = 2\,\mathrm{GeV/c}$. The data is taken from [66–69].

and therefore to the phase transition from the hadronic to a QGP phase. As shown in Ref. [55], this function is not unique and similar resulting curves can be obtained from very different sets of parameters α, β, and p_0. Thus, in order to compare different distributions, the transition parameter will be mostly set to a fixed value of $p_0 = 2\,\mathrm{GeV/c}$ throughout this work, according to experimental data at energies similar to those considered in this work. Figure 2.8 shows the transverse momentum distribution of charged hadrons measured by various experiments at the LHC [66–69], fit with a Hagedorn function from Equation (2.34), with $p_0 = 2\,\mathrm{GeV/c}$ and α, β being free parameters. The function describes experimental data rather well, especially in the relevant region for this work, for $2\,\mathrm{GeV/c} \leqslant p_T \leqslant 6\,\mathrm{GeV/c}$.

Within Monte Carlo (MC) simulations, discussed in detail in Chapter 5, hadronic interactions can be described by various hadronic models. These usually have a dedicated treatment for soft and hard interactions which varies between different models. Figure 2.9 shows the transverse momentum distribution of several hadrons obtained from simulated proton collisions at 1 PeV with nitrogen nuclei at rest. The corresponding Hagedorn fits, using $p_0 = 2\,\mathrm{GeV/c}$, are shown as lines. These simulations are generated using the software package CRMC [81] as an interface to the EPOS-LHC hadronic model [82], as described in Section 5.4.

The transverse momentum distributions yield information about the transition from soft to hard interactions. Thus, they play an important role in model building processes and allow unique tests of hadronic models (see for example

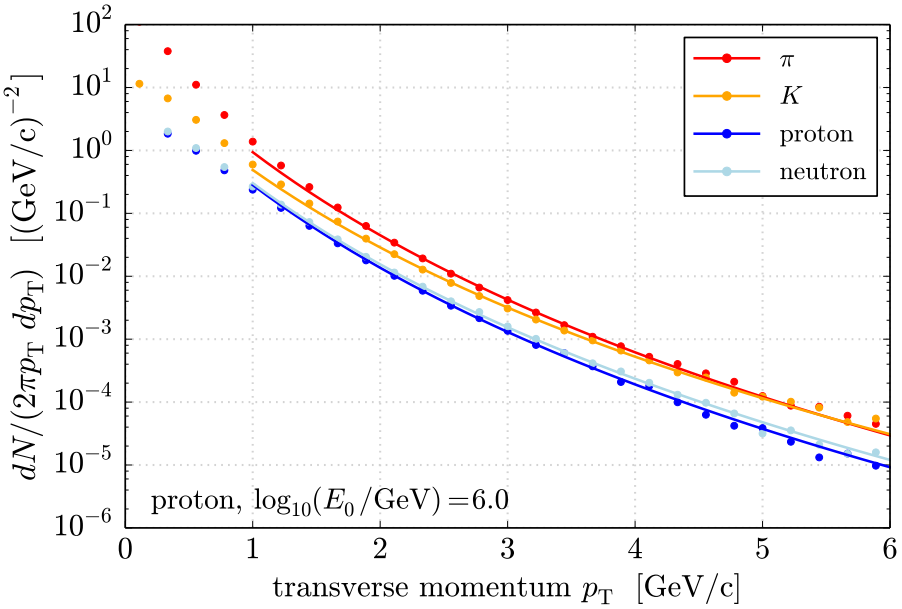

Figure 2.9: Transverse momentum distribution of various hadrons produced in proton-nitrogen collisions at 1 PeV in the proton's laboratory frame. These distributions are obtained from MC simulations using EPOS-LHC as hadronic model [82].

Ref. [82]). An overview of the most common hadronic models used in modern physics is given in Section 5.2.

In addition, it is known from heavy ion collisions at various accelerator experiments, as well as from calculations in the context of PQCD, that the p_T distributions of hadrons depend on the energy per nucleon of the colliding nuclei. Thus, the transverse momentum of hadrons produced in high-energy cosmic ray interactions depends on the atomic mass number of the initial nucleus and is therefore sensitive to the mass composition of cosmic rays. The composition sensitivity of high-p_T hadrons is discussed in detail in Section 5.4.3 and Section 7.5.

As previously described in Section 2.3, muons are produced by the decay of hadrons within a cosmic ray air shower, predominantly from pions and kaons. The resulting transverse momentum of muons closely follows the distributions of the underlying parent particles produced at height H. Muons with large transverse momentum, imparted to them by their parent particles, can thereby separate from the compact muon bundle. Assuming the parent particles being produced at height H and the zenith angle direction of the primary particle is given by θ. According to Equation (2.28) and using simple geometry (see also

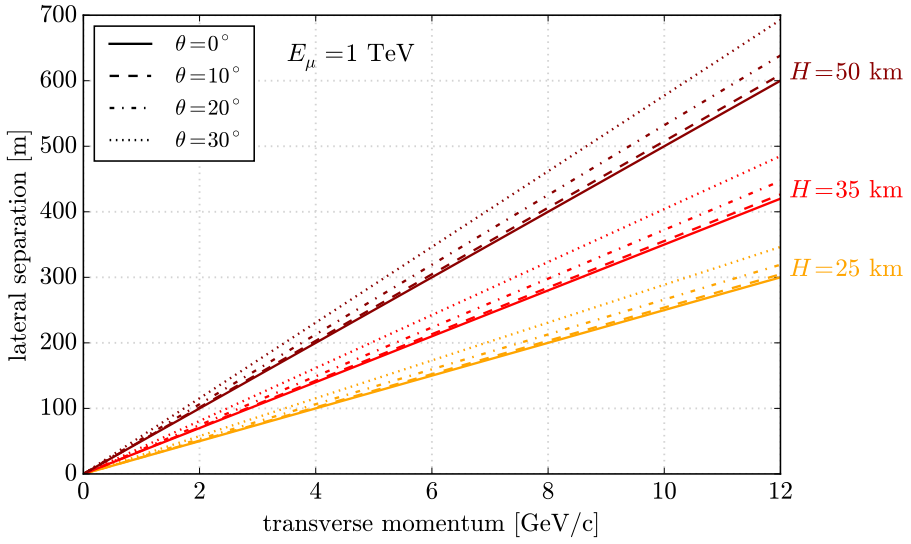

Figure 2.10: Lateral separation according to Equation (2.36) as a function of the transverse momentum for various heights of production and zenith angle directions.

Figure 2.11), the *lateral separation* d_T between the muon and the shower core at the surface (sea level) is given by

$$\begin{aligned} \phi_T = \frac{c \cdot p_T}{E} &\simeq \frac{d_T \cdot \cos(\theta)}{H} \\ \Rightarrow \quad d_T &\simeq \frac{c \cdot p_T \cdot H}{E \cdot \cos(\theta)} \,. \end{aligned} \tag{2.36}$$

The Earth's magnetic field strength at the South Pole is about 55 µT [48]. According to Equation (2.4), for typical muon energies above 500 GeV considered in this work, the resulting gyroradii are in the order of more than ~ 30000 km. Thus, geomagnetic effects on the lateral separation of these muons can be neglected. In addition, in Section 3.1.3 it is shown that multiple scattering within the atmosphere can also be neglected. Hence, LS MUONS are a direct probe of the transverse momentum of the underlying hadrons and therefore enable tests of PQCD predictions, as discussed above.

With typical muon energies within the TeV range recorded in ICECUBE, transverse momenta larger than 2 GeV/c can potentially produce muon lateral separations of several hundred meters when reaching the ground. The resulting lateral separation of a LS MUON according to Equation (2.36), with a typical energy of 1 TeV is shown in Figure 2.10 as a funtion of the transverse momentum, for several zenith angle directions θ and production heights H. Together with the muon bundle, these laterally separated muons generate distinct *double-track signatures* in large Cherenkov telescopes, such as ICECUBE (see Chapter 4), as schematically shown in Figure 2.11.

A previous measurement of the lateral separation distribution of isolated LS MUONS between 135 m and ~ 350 m has been performed using ICECUBE in

its 59-string configuration (IC59) and 335 days of data [83]. The experimental results are further discussed in Chapter 7. In addition, the MACRO experiment [84], located deep-underground at Grand Sasso, has measured the separation of muon pairs produced in air showers up to 70 m [85].

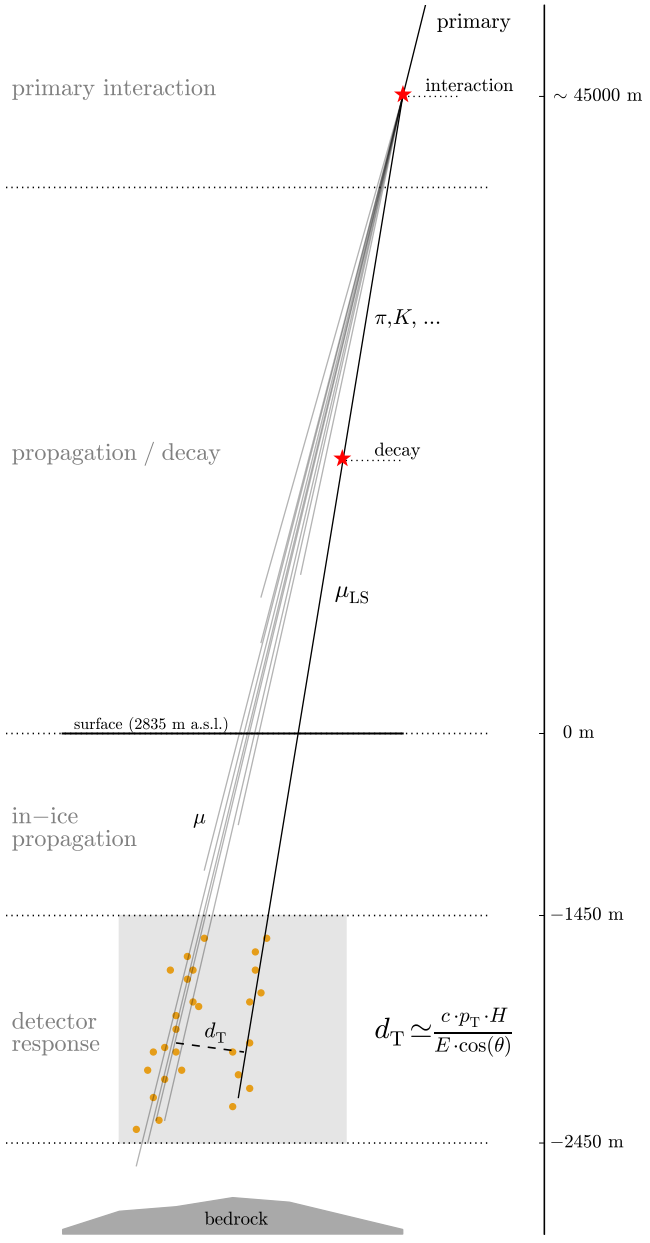

Figure 2.11: LS Muon production in IceCube.

3

DETECTION PRINCIPLES

"Isolated material particles are abstractions, their properties being definable and observable only through their interaction with other systems."

*– Niels H. D. Bohr**

The energy spectrum of cosmic rays follows a very steep power law, extending over almost 20 orders of magnitude. Using Equation (2.10) the expected cosmic ray rate is on the order of 1000 primary nuclei per square meter per second. In the range around 100 GeV, the rate is only about one particle per square meter per second. Going to even higher energies, the expected rate of cosmic ray primaries decreases rapidly to about one particle per square meter per year around the knee and to one particle per square kilometer per year at the ankle. Thus, for increasing particle energies, the detector sensitivity scales largely with its size and volume.

Although there exists a large variety of detector designs used for the measurement of cosmic rays, they generally rely on either direct or indirect measurements. In energy regions where the primary particle flux is sufficiently large, cosmic rays can be detected directly using instrumentation developed for balloon flights or space missions. These instruments have typical detector volumes on the order of below $1\,\mathrm{m}^3$. Examples for experiments performed during balloon flights are ATIC [86] and CREAM [87]. The PAMELA [88] and AMS [89–91] experiments are space-based, located on a satellite and the international space station (ISS) respectively.

Selected particle spectra from this type of measurements are shown in Figure 2.2 and a comprehensive review on space-based and ballon experiments can be found for example in Refs. [4, 9, 33, 92].

However, these experiments are very limited in size and capacity, and in order to detect cosmic rays at higher energies, above some TeV, very large ground-based observatories are needed. Since cosmic rays interact in the atmosphere, forming extensive air showers, as described in Section 2.2, experiments of this type rely on indirect measurements of the resulting shower constituents at the ground. Typical air shower experiments are based on large surface detector arrays or instrumented detector volumes in the deep water or ice. These detectors usually rely on the measurement of light, which is generated when secondary particles of the air shower pass the detector volume. Using detailed timing information and the light yield measured by these experiments, many conclusions on the shower development and the cosmic ray primary can be drawn. This enables for example studies on the energy spectrum of primary cosmic rays and their mass composition, as shown in Figure 2.1 and Figure 2.3.

* In *"Atomic Physics and the Description of Nature"* (1934).

In addition, there exist various other indirect detection techniques, such as air Cherenkov [93, 94] and fluorescence telescopes [95], or radio antenna arrays [96, 97]. These are not relevant for the detection of cosmic rays in the context of the IceCube experiment and are therefore beyond the scope of this work. For further reading see for example Ref. [33].

In the following, the basic principles of light emission from charged particles passing dense matter are described. This is done in Section 3.1 with emphasis on muons, which represent the main air shower constituent measured in deep underground detectors, such as IceCube. A general overview on surface detector arrays, using water Cherenkov tanks to measure the light of secondary particles, is given in Section 3.2. The detection principles of large-scale neutrino telescopes, such as IceCube, are discussed in Section 3.3.

3.1 MUON PROPAGATION IN MATTER

While energy losses of muons traveling through the atmosphere can mostly be neglected for the energies considered in this work, charged particles with relativistic velocities passing dense matter, such as water or ice, interact with the surrounding medium. Due to various scattering processes they lose energy, resulting in photon emission that can be detected, together with Cherenkov radiation, using optical sensors deployed within the medium.

The mean rate of the energy loss of muons with energy E, traveling the distance x through a medium, is described by the *stopping power* [98, 99]. It can be generally parametrized as

$$\left\langle -\frac{dE}{dx} \right\rangle = a(E) + b(E) \cdot E \,, \tag{3.1}$$

where the function $a(E)$ describes *collisional* energy losses and $b(E)$ describes all *radiative* losses, which scale with the energy. At intermediate energies (below $\sim$ 500 GeV) collisional losses in the form of ionization and excitation of the surrounding medium, dominate the energy losses of muons. However, for energies above $\sim$ 1 TeV, radiative losses are the dominating effect and need to be taken into account. Generally, the muon (critical) energy, at which radiative losses start to dominate, is defined as $E_{\mu,c} = a(E_{\mu,c})/b(E_{\mu,c})$. Relevant processes, causing photon emission and energy losses of muons while traversing dense matter, are described in the following.

3.1.1 IONIZATION

A muon traveling through matter undergoes inelastic collisions with electrons of atomic nuclei, which are described by the tree-level Feynman diagram shown in Figure 3.1. Thereby the surrounding medium is mainly ionized, but also excited. These collisional energy losses of a particle with energy E occur approximately

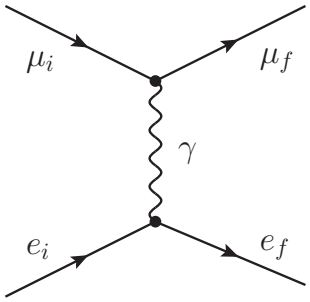

Figure 3.1: Feynman diagram of the ionization process induced by a muon μ scattering with an electron e.

continuously along the particle's track and can be described by *Bethe's formula* [100, 101]:

$$\left\langle -\frac{dE}{dx} \right\rangle = Kz^2 \frac{Z}{A} \frac{1}{\beta^2} \left[\frac{1}{2} \ln \left(\frac{2m_e c^2 \beta^2 \gamma^2 W_{max}}{I^2} \right) - \beta^2 - \frac{\delta(\beta\gamma)}{2} \right], \tag{3.2}$$

where m_e is the electron mass, z the charge number of the incident particle ($z = 1$ for muons). Z and A are the atomic and mass number of the surrounding medium respectively, I is the mean excitation energy, and $K = 4\pi N_A r_e m_e c^2$, where $r_e = e^2/4\pi\epsilon_0 m_e c^2$ is the classical electron radius. The maximum energy transferred to an electron in a single collision W_{max}, is given by

$$W_{max} = \frac{2m_e c^2 \beta^2 \gamma^2}{1 + 2\gamma m_e/m + (m_e/m)^2}, \tag{3.3}$$

with $m = m_\mu$ being the incident particle's mass. The δ term is a correction to the energy loss, due to density effects in the medium. With increasing particle energy its electrical field extends and the first term in Equation (3.2) increases with $\ln(\beta\gamma)$. In real media, this effect is limited because the medium is ionized, which limits the field extension (see for example Ref. [101]).

The mean energy loss of a muon in ice due to ionization using Bethe's formula is shown in Figure 3.2, in units of MeV g/cm^2. Although the stopping power increases slowly with the atomic number Z, using these units, it is approximately the same for most materials. Particles with energies minimizing the the stopping power are purely ionizing and are therefore referred to as *minimum ionizing particles* (MIPs).

3.1.2 RADIATIVE ENERGY LOSSES

While for energies below about ~ 500 GeV the energy loss due to ionization is the dominating effect, at higher energies around $E_{\mu,c} \sim 1$Tev, radiative energy losses become important. These processes usually have small cross sections and can produce hard spectra [101, 102]. Moreover, they are associated with large energy

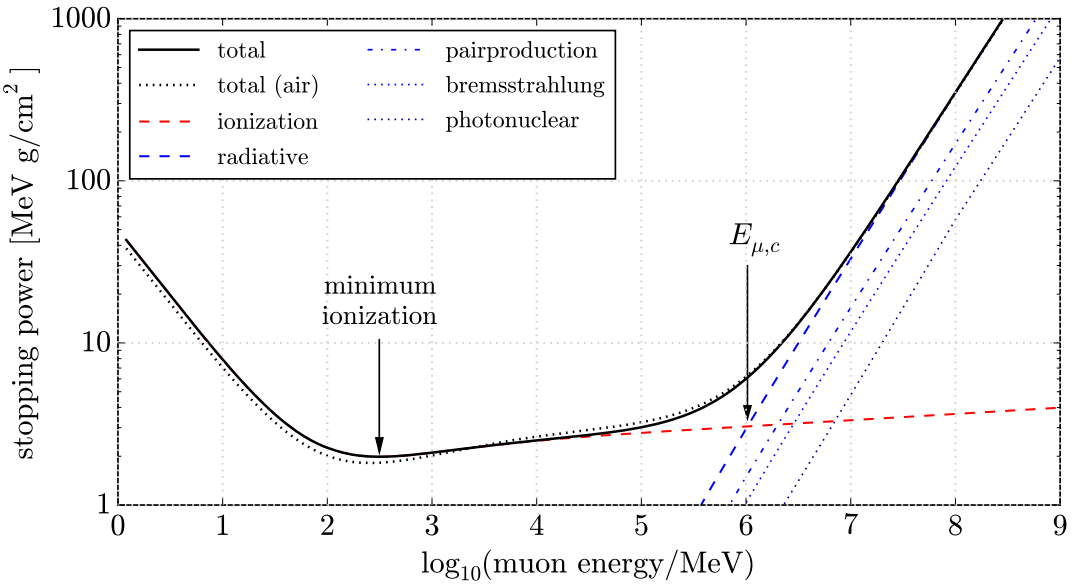

Figure 3.2: Muon stopping power in ice. The contributions from ionization (red), according to (3.1), and radiative losses (blue), taken from Ref. [34], are shown separately. For ionization the coefficients from Ref. [99] are used.

fluctuations and the production of electromagnetic and hadronic cascades, as described in Section 2.2. As a consequence, radiative energy losses are not continuously distributed along the particle's track. In contrast to ionization, these energy losses are also referred to as *catastrophic* energy losses. The relevant processes causing such radiative energy losses are described in the following.

Bremsstrahlung

Charged particles are decelerated in the presence of an electromagnetic field caused by another charged particle, for example an atomic nucleus, and will thereby emit *bremsstrahlung*. The cross-section of this process can be divided into an elastic component σ_{el} and two inelastic components $\Delta\sigma^{in}_{a,n}$ [100, 102],

$$\sigma_{brems} = \sigma_{el} + \Delta\sigma^{in}_{a} + \Delta\sigma^{in}_{n} \,. \tag{3.4}$$

The first term describes the elastic scattering of a charged particle on an atomic nucleus with mass number Z, which is given by the two (tree-level) Feynman diagrams shown in Figure 3.3. Elastic scattering is the dominant process contributing to the emission of bremsstrahlung. The other two terms represent the inelastic scattering of muons on the electrons of the atom ($\Delta\sigma^{in}_{a}$) and the effect of nucleus excitation ($\Delta\sigma^{in}_{n}$). The corresponding Feynman diagrams can be found in Section A.5 (Figure A.3). The resulting elastic bremsstrahlung cross-sections are given in Refs.[102–105] and the inelastic case is discussed in Refs. [105, 106]. They are usually expressed as a function of fractional energy loss v and roughly scale with v^{-1} [101, 107]. Bremsstrahlung represents the main contribution to

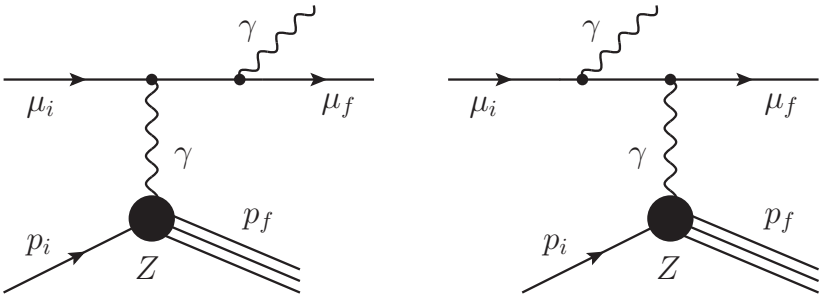

Figure 3.3: Feynman diagrams of the elastic interaction of a muon μ with a parton p of the atomic nucleus Z producing bremsstrahlung.

the hard radiative energy losses. It induces electromagnetic cascades, discontinuously distributed along the muon track. A comprehensive discussion of the cross-sections and the resulting stopping power, can be found for example in Refs. [101, 108]. The contribution from bremsstrahlung to the stopping power is shown in Figure 3.2.

Pair Production

High energy muons can produce electron-positron pairs in presence of the electromagnetic field of an atomic nucleus. On tree-level, this *pair production* process is described by the two Feynman diagrams, shown in Figure 3.4, in addition to two Feynman diagrams, where the muon interacts with a nucleus (shown in Section A.5). The electron-positron pair production cross-sections can be for example found in Refs. [108–110]. With ν being the fractional energy loss, they roughly scale with ν^{-2} to ν^{-3} [107]. Thus, they are somewhat softer than bremsstrahlung emission and can be treated as being approximately continuous [101].

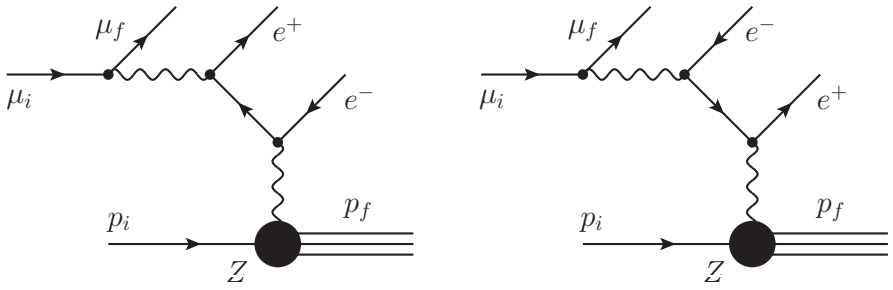

Figure 3.4: Feynman diagrams of electron-positron (e^-, e^+) pair production induced by a muon μ interacting with a parton p of an atomic nucleus Z.

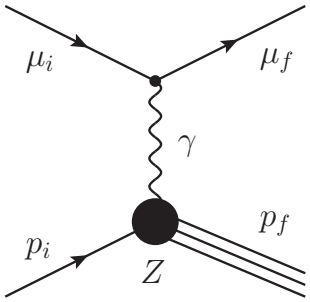

Figure 3.5: Feynman diagram of a photonuclear interaction between muon μ and a parton p of the atomic nucleus Z.

Another possible pair production process is the generation of a muon pair. The Feynman diagrams for these processes are the same as those shown in Figure 3.4, with the electron and positron substituted by muons. However, the cross-sections for the muon pair production is expected to be $\sim 2 \cdot 10^4$ times smaller compared to the electron case [108], and will therefore not be discussed further. The contribution from electron-positron pair production to the stopping power of a muon in ice can be found in Figure 3.2.

Photonuclear Interaction

Inelastic scattering of a high energy muon with an atomic nucleus within the surrounding medium, a so-called *photonuclear* interaction, causes an energy loss of the incident muon. This interaction is described by the Feynman diagram shown in Figure 3.5 (tree-level). The resulting cross section can be for example found in Refs. [108, 111, 112].

The corresponding stopping power caused by photonuclear interactions is shown in Figure 3.2 and represents the smallest contribution to the radiative losses. However, photonuclear interactions can cause hard energy losses and large deflections by producing electromagnetic and hadronic cascades along the particle track within a medium [101, 102]. Since this can have an impact on the reconstruction of energy losses and the muon track trajectory in IceCube, it needs to be taken into account and will be included in all simulations used in this work.

3.1.3 MULTIPLE SCATTERING

Charged particles traveling through dense matter suffer from repeated elastic Coulomb scattering on atomic nuclei, where each individual interaction is generally described by the Rutherford cross-section [113]. Assuming the atomic nuclei are much heavier than the incident particle's mass, the energy transfer during those interactions is negligible. However, these *multiple scattering* processes can

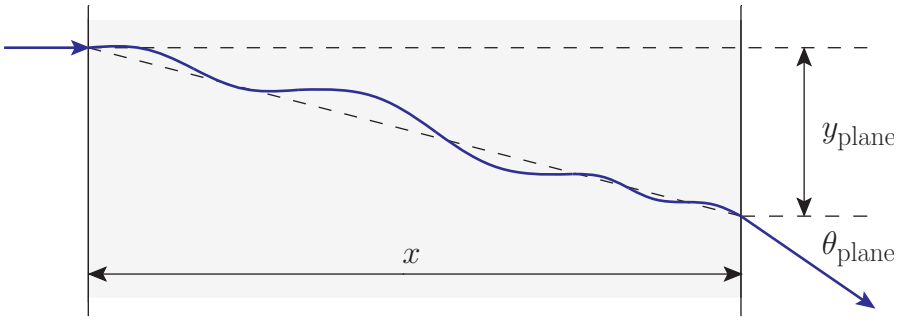

Figure 3.6: Schematic drawing (inspired by Ref. [34]) of multiple scattering processes within a dense medium and construction of the resulting particle deflection, as described in Molière scattering theory (see text).

cause significant angular deflections in matter and thus need to be considered for (charged) particles traversing large distances in a dense medium.

Multiple scattering can be described in the context of *Molière scattering* theory, as described in Refs. [114, 115]. The Coulomb scattering distributions can be estimated using the (small-angle) *Highland approximation* [116]. The angular distribution, after traveling a given distance x, is assumed to follow a Gaussian with its width approximated by $\sqrt{2}\theta_0$, given by

$$\theta_0 = \frac{13.6\,\text{MeV}}{c\beta p} \cdot Z \cdot \sqrt{\frac{x}{X_0}} \left[1 + 0.038 \cdot \ln\left(\frac{x}{X_0}\right)\right], \tag{3.5}$$

where p is the momentum and Z the charge of the particle. x/X_0 is the thickness of the traversed medium in radiation lengths. The radiation length X_0 can be obtained experimentally and parametrized as

$$X_0 = \frac{716.4 \cdot A\ \text{g}\,\text{cm}^{-2}}{Z(Z+1) \cdot \ln(287/\sqrt{Z})}, \tag{3.6}$$

with the mass number A. Equation (3.6) is in agreement with theoretical predictions to better than 2.5% for most elements [101, 117].

Subsequently, the angular distribution θ_{plane}, projected onto a two-dimensional plane, and the corresponding mean deflection $\langle y_{\text{plane}} \rangle$, as defined in Figure 3.6, are given by [101]

$$\theta_{\text{plane}} = \frac{1}{2\pi\theta_0} \cdot \exp\left(-\frac{\theta_{\text{plane}}^2}{2\theta_0^2}\right) d\theta_{\text{plane}}, \tag{3.7}$$

and

$$\langle y_{\text{plane}} \rangle = \frac{1}{\sqrt{3}} \theta_0 \cdot x. \tag{3.8}$$

The deflections are identical in all directions orthogonal to the direction of motion. Thus, the calculation of the spacial distributions is straight-forward and is discussed for example in Refs. [101, 108].

For numerical calculations, Equation (3.7) and Equation (3.8) can be expressed using independent Gaussian variables RD_1 and RD_2, with mean zero and variance one [101], by

$$\theta_{plane} = \theta_0 \cdot RD_1 \tag{3.9}$$

and

$$y_{plane} = \frac{1}{2}\theta_0 \cdot x \cdot RD_1 + \frac{1}{\sqrt{12}}\theta_0 \cdot x \cdot RD_2 \,. \tag{3.10}$$

With increasing deflection angles, this effect behaves more like Rutherford scattering [101], deviating from a simple Gaussian distribution. In addition, for a more precise treatment the finite size of the nucleus should be taken into account [118]. However, for small deflection angles, up to a few θ_0, the approach described above represents a very good approximation [108, 118].

Moreover, for $\sim$ TeV muons the momentum can be approximated by $p \simeq E$ (see Section 2.4). Since the mean deflection angle scales with the inverse of the momentum and with the thickness of the medium, as described in Equation (3.7), deflections in the atmosphere can be neglected. However, multiple scattering for muons propagating through ice is taken into account throughout this work, and implemented in any simulations, as described in Ref. [108] (see also Section 5.7).

3.1.4 CHERENKOV RADIATION

Charged particles passing through a dielectric medium polarize the surrounding atoms due to their electrical field. The subsequent return of the polarized atoms to the ground state causes the emission of photons in the medium [119–121]. In general, this radiation interferes destructively and at a distant point, the resultant field intensity is zero. However, if the particle travels faster than the phase velocity of light in this medium

$$v_{phase} = \frac{c}{n} \,, \tag{3.11}$$

where n is the index of refraction, the photons can interfere, such that at a distant point, a resulting field can be observed. This *Cherenkov radiation* [119] follows a fixed angle θ_C, the *Cherenkov angle*, and is emitted continuously along the particle's track. Depending on the velocity of the charged particle $v_{particle}$ and the phase velocity of light in the medium, the Cherenkov angle is given by

$$\cos(\theta_C) = \frac{v_{phase}}{v_{particle}} = \frac{1}{n\beta} \,, \tag{3.12}$$

where $\beta = v_{particle}/c$. Equation (3.12) is derived using the *Huygens-Fresnel principle* [122, 123], as illustrated in Figure 3.7 (see caption for details). The resulting Cherenkov angle defines a fixed cone, in which the wavefronts interfere constructively. Thus, Cherenkov light emission carries important directional information

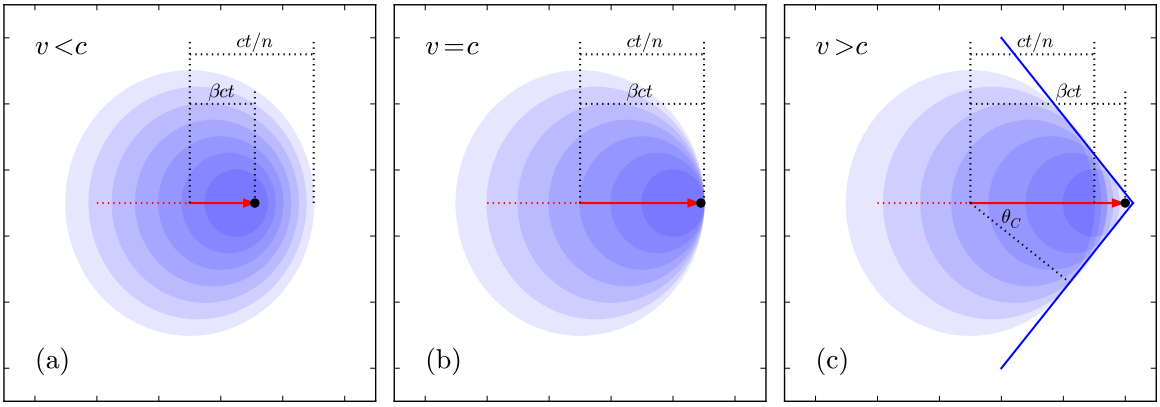

Figure 3.7: Huygens-Fresnel construction of the Cherenkov angle θ_C produced by light waves emitted along a particle track. For particle velocities $v < c$ (a), the wavefronts do not cross each other and can therefore not interfere constructively. For particle velocities at the (phase) velocity of light in the medium (b), and above (c), the wavefronts overlap and interfere, producing a light cone along the particle track. The light cone has a fixed Cherenkov angle θ_C, which is given by the particle's velocity and the refraction index of the surrounding medium (see text for details).

of the incident particle and has significant experimental consequences. It enables precise reconstructions of particle trajectories in a dense medium and provides the main detection principle for large-scale Cherenkov telescopes, such as IceCube (see Chapter 4).

In ice for example, the refraction index is $n = 1.32$ for a photon wavelength of 400 nm [124], which determines the *Cherenkov threshold*,

$$v_C \equiv v_{\text{phase}} \simeq 0.75c \, . \tag{3.13}$$

This results in a Cherenkov angle of roughly $\theta_C \simeq 41°$ for muons traveling through the ice at the speed of light.

The energy spectrum of photons produced along the charged particle track x is described by the *Frank-Tamm formula* [119, 120]

$$\frac{dE_\gamma}{dx\,d\omega} = \frac{\mu \cdot e^2}{4\pi} \cdot \omega \cdot \left(1 - \frac{1}{\beta^2 n^2}\right), \tag{3.14}$$

where ω is the angular frequency of the emitted Cherenkov photons, $\mu = \mu_0 \mu_r$ is the permeability of the surrounding medium, and e the elementary charge. The energy loss due to Cherenkov radiation in typical media, such as water or ice, is only on the order of several keV per cm. This corresponds to roughly $\sim 0.1\%$ of the energy loss by ionization, and can therefore be neglected for the energies considered in this work [121].

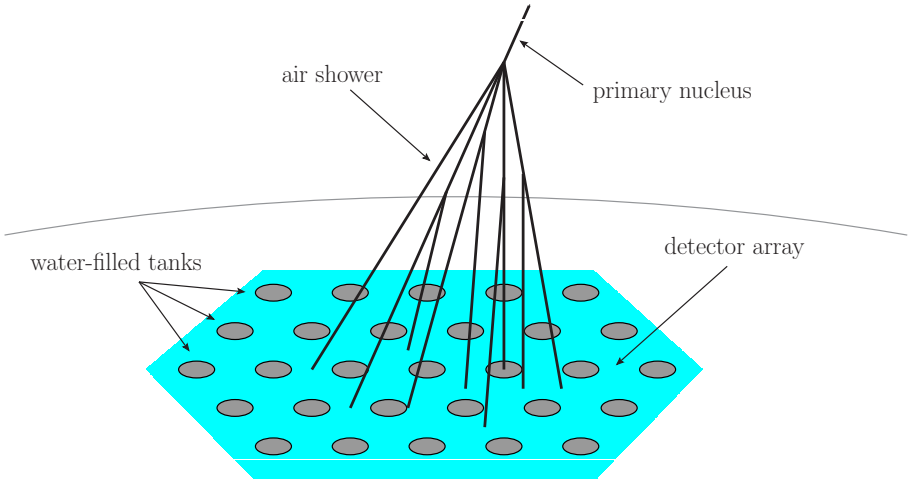

Figure 3.8: Detection principle of typical cosmic ray detectors based on large surface arrays, such as IceTop.

3.2 AIR SHOWER SURFACE ARRAYS

In order to measure cosmic ray air showers at the highest energies, the detector area needs to be sufficiently large. The energy sensitivity of these experiments, in principle, depends on the total area covered and the density of instrumentation. Therefore, experiments use an array of many detection units, which cover a large area. In contrast to scintillator arrays, such as the Telescope Array (TA) [16, 125], many surface detectors are based on water-filled tanks, equipped with light detection sensors. Whenever a high energy cosmic ray enters the atmosphere it initiates an air shower that produces millions of particles on the ground, as described in Section 2.2 and depicted in Figure 3.8. When a charged particle passes one of the water-filled tanks, it produces Cherenkov radiation, as explained in Section 3.1.4, which can be detected by optical sensors. Using the measured timing and light yield information from many detection units, the air shower can then be reconstructed and conclusions on the primary cosmic ray nucleus can be drawn.

Recent measurements of the primary cosmic ray spectrum from various experiments are shown in Figure 2.1. The KASCADE [35] and KASCADE-Grande [126] experiments, have measured primary cosmic ray energies from $\sim 1\,\mathrm{PeV}$ up to above $100\,\mathrm{PeV}$ [127, 128]. With detector areas of some $1000\,\mathrm{km}^2$, the Pierre Auger Observatory (Auger) [17, 129] and the Telescope Array (TA) project [16, 125] measure cosmic rays at the highest energies, up to more than $\sim 1\,\mathrm{EeV}$. Combining these and other measurements, the energy spectrum of cosmic rays is known over 20 orders of magnitude. Comprehensive overviews on various surface detector arrays, used in astroparticle physics, can be for example found in Refs. [3, 9, 33, 43, 130, 131].

IceCube's surface detector array IceTop [132] covers an area of roughly $1\,\mathrm{km}^2$ and measures cosmic ray air showers with energies from $\sim 1\,\mathrm{PeV}$, extending up

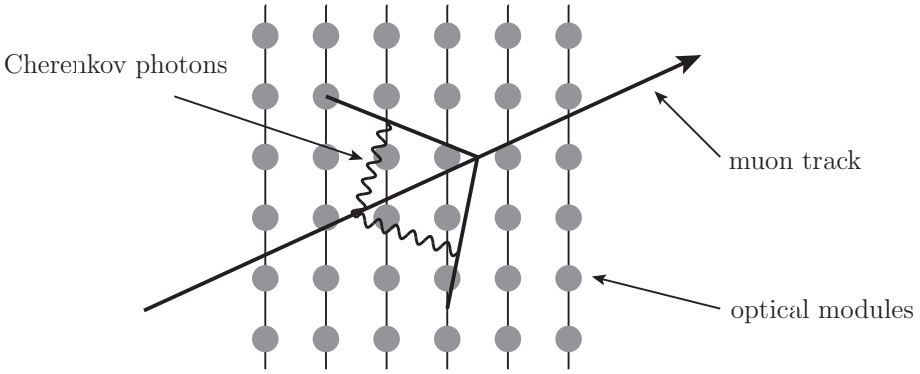

Figure 3.9: Principle of particle detection in large-volume Cherenkov telescopes, such as IceCube.

to above 100 PeV [133]. Its detector design and principle is described in detail in Section 4.2.

3.3 LARGE-VOLUME CHERENKOV TELESCOPES

In general, Cherenkov telescopes consist of multiple photon detection units deployed over a large detector volume, typically within deep water or ice. The main purpose of these Cherenkov detectors is the measurement of high energy neutrinos. When a neutrino interacts near-to or inside the instrumented volume, it produces relativistic secondary particles. These particles produce light inside the (transparent) detector volume through several emission processes, as described in Section 3.1. In water or ice, and for the particle energies considered here, the most important photon emission process is Cherenkov light production, which produces a light front along the particle track. This is detected by the optical sensors deployed in the surrounding medium, as indicated in Figure 3.9. Based on detailed timing and light yield information from multiple sensors, the initial particle track can be precisely reconstructed, and conclusions on the underlying physics can be drawn.

Since neutrino interactions occur very rarely due to their small interaction cross-section with matter, the detector volumes, which represent the interaction targets, need to be very large. In order to reduce the background rates, these detectors are buried deep underground, typically in water or ice, using the given physical advantages due to the optical transparency of the surrounding medium. Atmospheric muons with energies of more than several hundred GeV, produced in large numbers in cosmic ray air showers, can also reach these detectors. Hence, large-volume Cherenkov telescopes are also very good facilities to study atmospheric muons at the highest energies.

The detection concept was pioneered by the now decommissioned DUMAND [134] and AMANDA experiments [135, 136], located underwater near Hawaii and buried in the deep ice at the South Pole respectively. Today, the ANTARES

experiment is taking data in the Mediterranean sea [137, 138], which is also the planned site for the future KM3NeT detector [139]. The ANTARES detector is deployed at depths of about 2.5 km and has an instrumented volume of about $\sim 0.05\,\mathrm{km}^3$. In addition, the Baikal underwater neutrino telescope is located deep in the Siberian Lake Baikal, at depths of about 1.1 km [140]. This work uses data from the IceCube detector, buried in deep ice at the geographic South Pole. Its detector design and functionality are described in detail in Section 4.1.

Although one of the main purposes of IceCube are studies of neutrinos at the highest energies, the detector can address a large variety of measurements: Among the searches for high energetic astrophysical [26–29] and atmospheric [141, 142] neutrinos, these experiments also enable for example studies on neutrino-oscillation effects at low energies [143] and the search for sterile neutrinos [144]. There are many searches for effects related to theories beyond the standard model (BSM), such as neutrinos from WIMP annihilations in the Sun [145], inside the Earth [146], or in the galactic center [147]. Also searches for magnetic monopoles [148, 149], and the direct detection of exotic particle tracks [150, 151], are possible using large-volume Cherenkov telescopes (see also Chapter 8).

This work focuses on the measurement of atmospheric muons, produced in cosmic ray air showers and recorded by IceCube. Previous analyses have measured the spectrum of atmospheric muons [52, 54] and studies on the cosmic ray anisotropy and seasonal variation effects have been performed [152]. In this work the lateral separation distribution of atmospheric muons is measured and studied in detail, using recent data from the IceCube detector. A previous measurement of this kind has been performed in Ref. [83], using data taken with the partially completed detector in 2009.

4 THE ICECUBE NEUTRINO OBSERVATORY

"All science is either physics or stamp collecting."
*– Ernest Rutherford**

The *IceCube Neutrino Observatory* (IceCube) is a cubic-kilometer-scale neutrino telescope located in Antarctica at the geographic South Pole. It consists of many components, each individually designed for a particular science goal. The main part of the detector is an instrumented volume, deep in the Antarctic ice. *Digital optical modules* (DOMs), housing one *photomultiplier tube* (PMT) each, are used to detect Cherenkov light produced by high energy particles traversing the ice. The main purpose of the *IceCube in-ice array* (IC) is the detection of high energy neutrinos of astrophysical origin, with energies above ~ 100 GeV, in addition it is used to study many other phenomena, including high energy (above ~ TeV) atmospheric muons produced in cosmic ray air showers.

The in-ice detector also includes a denser instrumented sub-detector, called *DeepCore* (DC), that lowers the neutrino energy threshold to about 10 GeV. Located on the surface of the ice is the surface detector, called *IceTop* (IT), which measures cosmic ray air showers at the ground. All recorded data is transferred to the *IceCube laboratory* (ICL), which is located on the surface in the center of the IceTop array. The ICL houses the hardware for data acquisition (DAQ) and further processing. In the following, the detector design and the individual components of the IceCube experiment, as well as their functionality are described in detail.

4.1 THE ICECUBE IN-ICE ARRAY

The main detector component of IceCube is an instrumented volume in the deep ice, at depths between 1450 m and 2450 m [153]. It comprises of 86 cables, so-called *strings*, deployed in holes within the ice. These holes were hot-water drilled, following a hexagonal pattern, as shown in Figure 4.1. After refreezing of the water-filled holes, the strings are totally inaccessible and deployed permanently. Each string is equipped with 60 DOMs used for the light detection in the ice. The horizontal spacing between 78 of these strings is roughly 125 m, with the DOMs 60 m vertically apart from each other. The remaining 8 strings in the center of the detector volume form the denser instrumented sub-detector DeepCore [154], deployed in a triangular pattern. The spacing between the DC strings is roughly 72 m and the 50 DOMs on each string are deployed with a smaller vertical spacing of 7 m. The upper 10 DOMs on each DC string have

* As quoted by J. Birks in *"Rutherford at Manchester"* (1962).

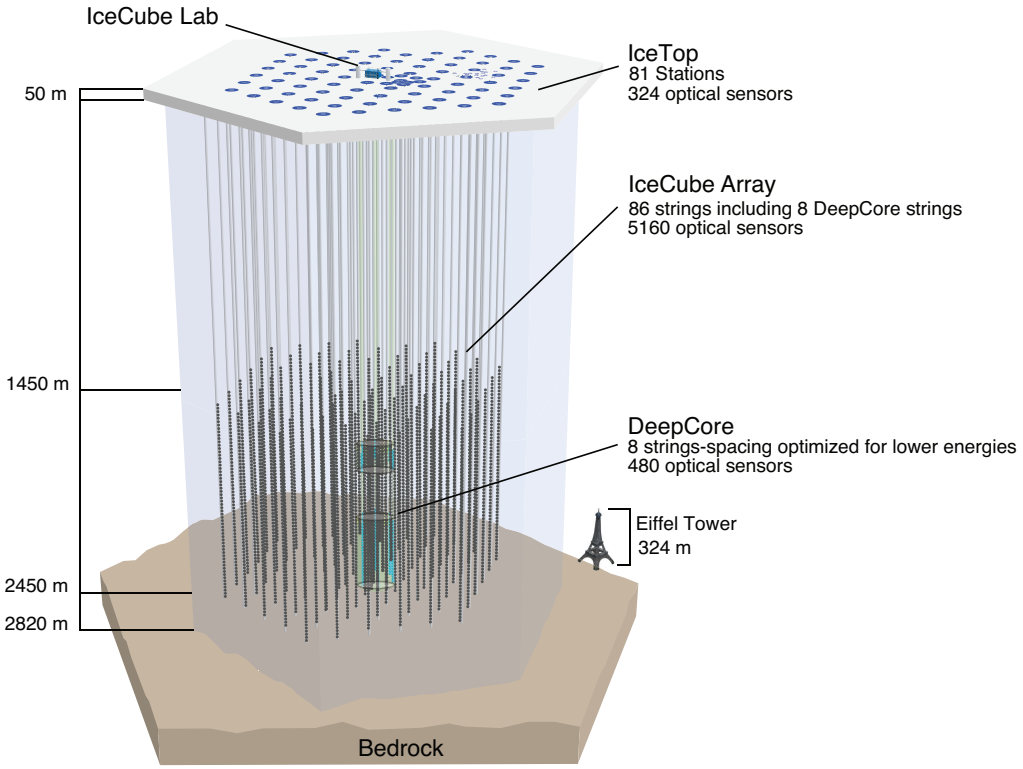

Figure 4.1: Schematic drawing of the IceCube detector with its surface component IceTop and the deep ice detector array, taken from Ref. [153]. Also shown is the denser instrumented detector component DeepCore (see text for details).

vertical distances of 10 m. DeepCore DOMs have a higher efficiency, in order to lower the detection threshold of the dense DeepCore volume to energies of 10 GeV.

4.1.1 ICE PROPERTIES

The ice at the geographic South Pole was formed over 100000 years by snowfall that produced nearly horizontal layers. The accumulated snow was compressed over the years, forming a compact glacier of clear ice today. Variations in the long term dust level of the atmosphere, as well as occasional volcanic eruptions, caused depth-dependent variations in the absorption and scattering lengths of photons in the ice [153]. Because the deep ice serves as a Cherenkov light radiator for IceCube, the description of the optical ice properties is crucial for the interpretation of recorded data.

Photons in the ice are mainly scattered on microscopic scattering centers, such as microscopic air bubbles or micron-sized dust grain, and is described by the *effective scattering length*, given by

$$\lambda_{\text{eff}}(\theta) = \frac{\lambda_s}{1 - \langle\cos(\theta)\rangle} , \tag{4.1}$$

where $\langle\cos(\theta)\rangle$ is the mean cosine of the scattering angle per single scatter [155]. λ_s is the scattering mean free path, which depends on the frequency of the photon. The *scattering coefficient* is then defined as

$$b_s = \frac{1}{\lambda_{\text{eff}}} . \tag{4.2}$$

The absorption of photons within a medium is described by the *absorption coefficient* (or absorptivity)

$$b_a = \frac{1}{\lambda_a} , \tag{4.3}$$

where λ_a is the absorption length, the distance at which the survival probability of photons drops to $1/e$ [155]. The absorption coefficient is related to the imaginary part of the refraction index n of a medium by

$$b_a = \frac{4\pi \cdot \text{Im}(n)}{\lambda} , \tag{4.4}$$

where λ is the wavelength of the photon.

These coefficients need to be determined experimentally, for example, by using artificial light sources deployed in the detector volume. In IceCube this is done using *light emitting diodes* (LEDs) which are deployed on the main board of the DOM (see Section 4.1.2). The photon arrival time distributions of the artificial signals are used to measure the scattering and absorption coefficients of the photons in ice [156]. Another method is based on so-called *dust logger* devices whcih are deployed in the holes together with IceCube [157]. These devices emit a thin beam of light and measure the reflected light in the ice. The refreezing process of the holes themselves also changes the ice properties close to the DOMs and therefore also needs to be considered.

For an accurate description and modeling of the ice, all of these measurements of optical properties are taken into account [155]. The resulting scattering and absorption coefficients are shown as a function of the photon wavelength and depth in the South Pole deep ice in Figure 4.2. The scattering of light closer to the surface, down to depths of roughly 1400 m, is strongly dominated by scattering on air bubbles. In the instrumented deep ice the air bubbles have been converted to air hydrates by the high pressure and the scattering is dominated by dust layer structures in the ice. At depths of around 2000 m the scattering and absorption coefficients are very large, caused by a prominent *dust layer*. This is associated with stadials during the last glacial period in the late Pleistocene, corresponding to an age of about 65000 years [158].

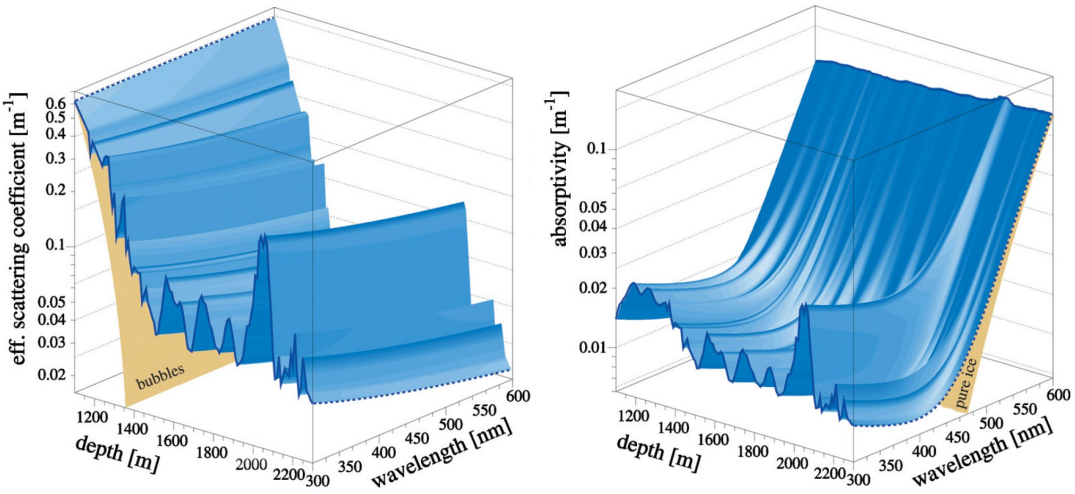

Figure 4.2: Scattering (left) and absorption (right) coefficients as a function of the photon wavelength and depth in the antarctic ice. Taken from Ref. [155].

4.1.2 DIGITAL OPTICAL MODULES

Each IceCube DOM consists of a 35 cm diameter pressure vessel of 13 mm thick borosilicate glass that is capable withstanding a pressure of approximately 70 MPa [153]. A schematic drawing of an IceCube DOM is shown in Figure 4.3. It houses a Hamamatsu R7081-02 PMT, which is sensitive to wavelengths of roughly $300 - 650$ nm with a 25 % peak quantum efficiency at 390 nm and a dark rate of about 500 Hz (at $-40°$C) [159]. DeepCore DOMs reach a peak quantum efficiency of approximately 33 %. The associated electronics and a data acquisition system are deployed on the DOM's main board [160]. The IceCube DOM additionally contains 12 light emitting diodes (LEDs) that can produce bright UV optical pulses for calibration purposes, deployed on the *flasher board*. They can be pulsed individually or in combinations at different output levels and pulse lengths. An additional low-amplitude LED is deployed on the main board, which is used for calibration purposes.

The photomultiplier is coupled to the vessel using an optical coupling gel and runs at typical high voltages of $1300 - 1500$ V with an amplification of $\sim 10^7$. The PMT electronics include a high voltage supply and a resistive divider with a total resistance of 130 MΩ. Additionally, it is surrounded by a mu-metal shielding, reducing the effect of the Earth's magnetic field by about a factor of 2. The vessel is filled with nitrogen at 0.5 atm pressure. While the photocathode of the PMT is grounded with respect to the DOM main board, the anodes are at high potential and their signals are coupled to DAQ electronics with a bifilar wound toroidal transformer with a frequency response from 8 kHz to above 100 MHz. For most of the DOMs, the decay time of a square wave signal is more than 15 µs. The first 1200 DOMs were built with a 1.5 µs time constant and can therefore show some droop [132, 153]. However, this is removed by a *droop correction*, applied during data analysis.

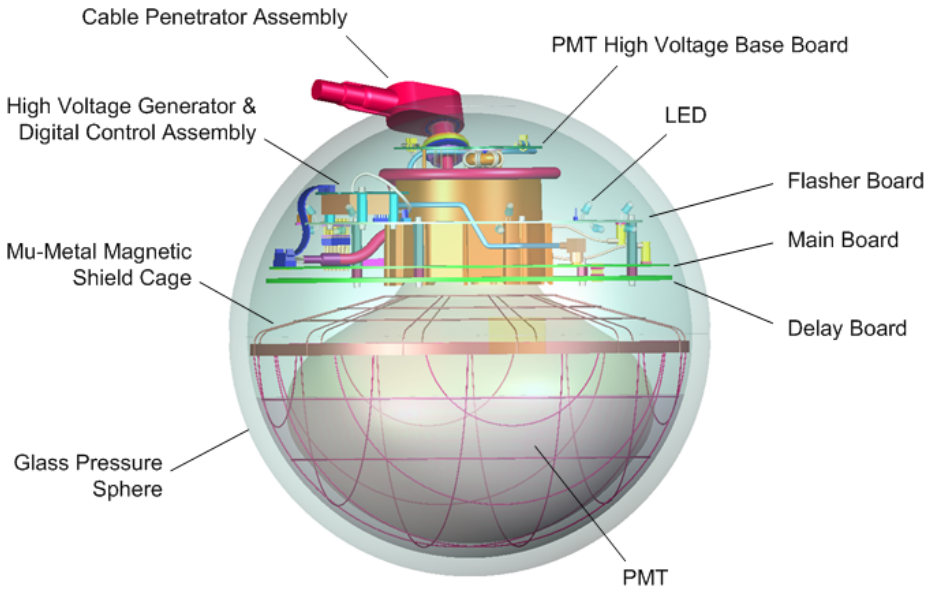

Figure 4.3: Schematic drawing of an IceCube DOM with its individual components, as described in the text. Taken from Ref. [161].

Figure 4.4 (left) shows the charge spectrum of a *single photoelectron* (SPE) produced with a low-amplitude LED [159]. The main peak to the right of the pedestal peak represents the actual SPE induced signal. Assuming a Gaussian distribution, the charge resolution is approximately 30 %. The low-charge excess at 0.3 times the SPE charge is caused by random noise [159, 162].

The arrival times of SPE pulses are shown in Figure 4.4 (right), where the first peak is produced from actual single photoelectrons. Assuming a Gaussian distribution, the time resolution is 2 ns, although about 4 % arrive more than 25 ns later. These late hits are expected to be caused by back-scattered electrons and are often referred to as *after-pulses* [159]. The PMT signal is split to the data acquisition system and to a 75 ns delay board, which provides enough time for a discriminator, before sending data to the surface.

4.1.3 DATA ACQUISITION

The PMT signals are recorded using two different fast waveform digitizers [160, 163], located on each DOM's main board: the *analog transient waveform digitizer* (ATWD) and a *fast analog to digital converter* (FADC). The digitization is triggered if the PMT pulse exceeds a voltage threshold corresponding to 0.25 *photoelectrons* (PE). The group of pulses collected by each DOM forms the total waveform and is referred to as a *hit*. A typical PMT waveform is schematically shown in Figure 4.5 (left).

The ATWD chip has three parallel inputs connected to the PMT (out of four inputs in total), with different gains with a ratio of 16: 2: 1/4, recording 128 analog samples for each input in a time window of 422 ns [160, 161]. Digitization

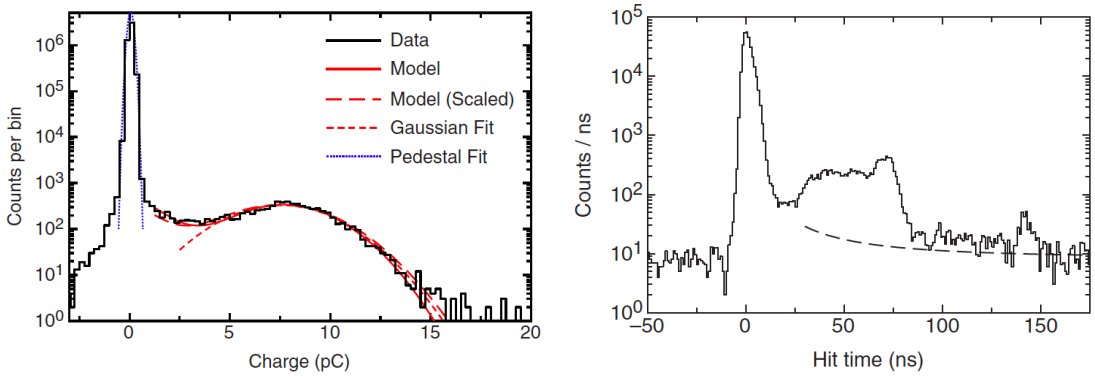

Figure 4.4: Typical SPE charge distribution (left) where the main SPE peak is described by a Gaussian. The arrival times of SPE hits (right) can also be described by a Gaussian, although ~ 4% of hits (also expected to be caused by back-scattered electrons) arrive with a delay of > 25 ns. Taken from Ref. [159].

starts with the highest gain channel and if a channel is saturated (above 768 counts per 3.3 ns), the next lowest gain is used, and so on. The digitization procedure takes 29 µs per waveform and, in order to reduce the dead time, each DOM contains two ATWD chips that operate alternating.

The FADC digitizer system uses a three-stage shaping amplifier and is continuously recording 256 samples, covering a time window of 6.4 µs [153]. It has a limited dynamic range and therefore overflows even for medium signals, but can provide useful information about late arriving photons. The waveform information from the three different ATWD input channels, as well as from the FADC are shown in Figure 4.5.

The waveform information is only saved and sent to the ICL on the surface when the *local coincidence* condition of neighboring DOMs is fulfilled. If two nearest-neighboring or next-to-nearest-neighboring DOMs record a single trigger within a 1 µs time window, the full waveform information is sent to the surface. This is referred to as *hard local coincidence* (HLC). Depending on the depth and the optical properties, the HLC hit rate is on the order of $3 - 15$ Hz per DOM.

In addition to the HLC hits, for an isolated hit, a *coarse charge stamp* is sent to the surface. This charge stamp contains the three highest FADC samples out of the first 16, and the time of these samples. These *soft local coincidence* (SLC) hits are sent to the surface with a rate of 350 Hz [153]. Although SLC hits are strongly dominated by noise hits, they can provide useful information for subsequent reconstructions, especially when applying additional software filter in further data processing steps.

For the data from single hits of each DOM, a 40 MHz system clock is used to assign a time stamp for each waveform with a corresponding resolution of 25 ns [153]. The system clock is digitized using the additional fourth ATWD channel. A DOM *launch* contains the time stamp, at least one ATWD waveform and the FADC waveform, as well as the local coincidence information. It is

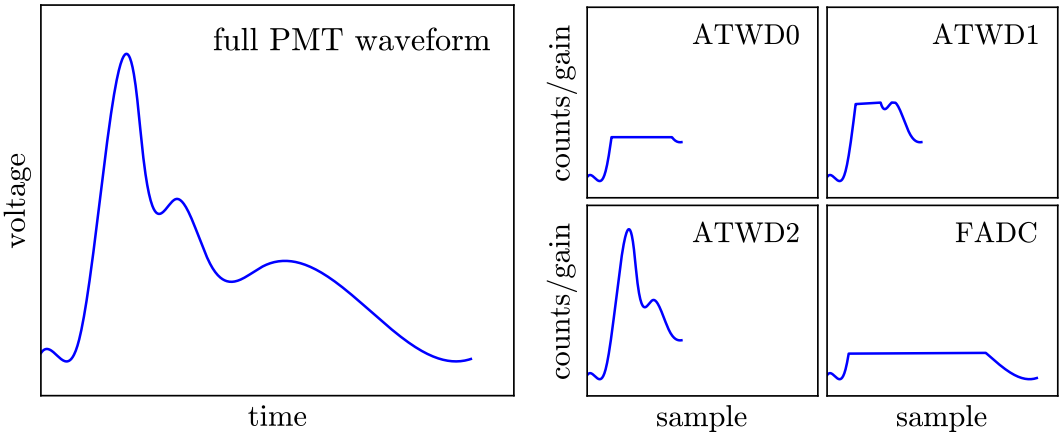

Figure 4.5: Schematic drawing of a typical PMT waveform (left) and the signal after digitization (right) for the ATWD highest-gain (0), medium-gain (1), and the lowest-gain (2) channel (see text). The signal from the FADC digitizer system is also shown.

transferred to the ICL by a cable, that contains 30 twisted pairs, such that each pair is connected to two DOMs in parallel.

The entire system is controlled by a *field programmable gate array* (FPGA) with an ARM CPU [160]. The FPGA controls the digitization and triggering, as well as buffers and compresses the data. It is re-programmable from the surface. The CPU initiates FPGA reconfiguration in real-time and handles higher-level computing tasks, such as calibration purposes for example.

4.1.4 DETECTOR CALIBRATION

The timing and charge information of each DOM launch transferred to the ICL is of particular importance for the interpretation of the recorded data. Thus, a precise calibration of the individual detector components is crucial for any subsequent analysis step, and a large variety of calibration techniques are used for the detector calibration in IceCube.

The main time calibration of the recorded pulses is a *reciprocal active pulsing calibration* (RapCal) [161, 164] that automatically performs timing calibrations every few seconds. Therefore, a timing signal is sent from the ICL to each DOM, which sends it back to the surface with a delay of a few microseconds. Thereby the transmission time is determined to less than 3 ns, although the transmission through the ~ 3.5 km cable widens the signal to ~ 1 µs [161].

Other timing calibrations measure the signal delay caused by the PMT and other electronics using the low-amplitude LED on the DOM main board (see Section 4.1.2). The LED's current is recorded by the ATWD, together with the PMT pulses, and the difference between them is used to determine the time delay caused by electronics. Charge calibrations are also performed using the on-board LED, flashed at low intensity. The measured PMT charge is accumulated by the

FADC and send to the surface, where an SPE peak is fit to it for calibration [153, 161]. Moreover, the LED is used to calibrate the gain of each individual ATWD channel [161].

The 12 LEDs installed on the flasher board are used for more sophisticated calibration purposes. Most important, as described in Section 4.1.1, the optical properties of the ice are determined. The LEDs are flashed individually or together, measuring the timing and the light transmission between the DOMs in the ice [155, 161]. Moreover, they are used to calibrate the position of the DOMs and to verify the system timing resolution [165].

In addition, two special calibration devices, used as *standard candles* in IceCube, are deployed on two strings, located in between two DOMs [153, 165]. They contain a 337 nm N_2 laser thats light beam is shaped to produce light approximately in the shape of a Cherenkov cone. Although the 337 nm light does not mimic the properties of Cherenkov light perfectly (see Section 3.1.4 and Section 4.1.1), it provides a reasonable approximation to cascades. Similar to the flasher LEDs, they can also be used to measure the charge amplitudes or the timing between the DOMs, and to perform geometry calibrations [165].

4.1.5 TRIGGERING AND DATA FILTERING

The data acquisition at the ICL on the surface is handled by the *DOMHub*, which is a computer that communicates with all of the DOMs. It contains 8 *DOR cards*, the *DOMHub Service Board* (DSB), and a *single board computer* (SBC), deployed on a PCI bus backplane [160]. A block diagram of the DOMHub is shown in Figure 4.6. Each DOR card receives signals from 8 DOMs, such that one DOMHub controls an entire detector string. The DOR cards also distribute ± 48 V DC power to the DOMs and monitor the power consumption as well as communication errors [153]. The DSB mainly distributes the system timing and reference signals to each of the DOR cards, where a GPS receiver provides a *master clock* signal, synchronized to UTC. The DOMHub hosts software that converts the time stamps from the DOMs into calibrated times using the system master clock. The calibrated data is combined into a single stream and monitored by a software trigger [166].

IceCube provides several DAQ triggers. The most important ones are the so-called *simple multiplicity triggers* (SMT). The SMT8 condition, for example, is satisfied, when 8 HLC hits are recorded within a 5 µs time window. Another commonly used trigger is the *string trigger* which selects time intervals when five out of seven neighboring DOMs recorded HLC hits within 1.5 µs [153].

In addition, there are more dedicated triggers, optimized for the search for exotic slow moving particles (*SLOP trigger*), or triggers that improve the sensitivity for low-energy and cascade-like events (*cylinder trigger*, *cluster trigger*), as well as triggers used for background estimation (*MinBias trigger*). There are also dedicated triggers for the sub-detectors DeepCore and IceTop. However, this analysis uses data that fulfills the standard SMT8 condition.

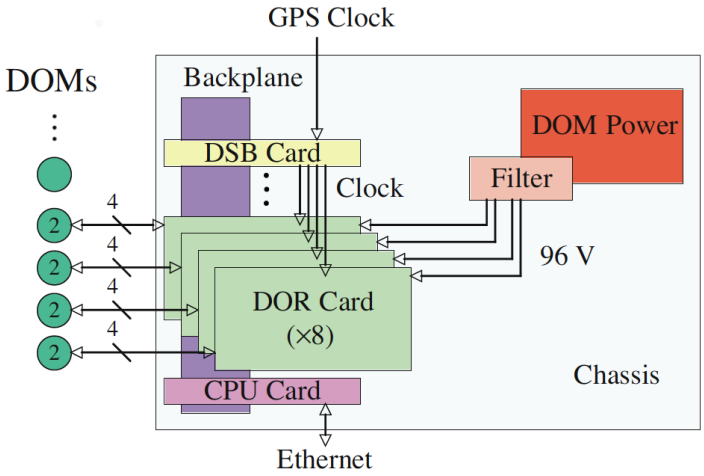

Figure 4.6: Block diagram of the DOMHub (see text for details). Taken from Ref. [160].

When one trigger condition is met, all data within a 10 µs trigger window is called an *event* and saved on tape. If multiple triggers occur, all of the (overlapping) data is saved as a single event. The total recorded event rate (including IceTop events, see Section 4.2 below) is roughly 2.5 kHz and selected events are immediately transmitted to the Northern Hemisphere via satellite with limited bandwidth. All triggered data is saved on tape at the ICL and sent during Austral summer to the North for further analyses.

The *on-line filtering system* uses simple selection algorithms, based on physics-based criteria and basic *first guess* reconstructions. It includes several filters that select particular events, such as upward-going muon-like events (*muon filter*), cascades (*cascade filter*) or starting events (*HESE filter*), and many more [153]. This analysis uses the *EHE filter*, that selects *(extremely) high-energy* (EHE) events in the in-ice volume. The details of this filter will be described in Section 6.1.

4.2 SURFACE DETECTOR ICETOP

The surface detector array IceTop [132] is located above the in-ice array at 2835 m altitude on the ice surface, corresponding to an atmospheric depth of approximately 680 g/cm^2. It consists of 162 Cherenkov tanks, filled with water, solidified due to ambient conditions, and equipped with two IceCube DOMs each (see Section 4.1.2). The tanks are arranged in pairs, separated from each other by about 10 m, forming a *station*. These 81 stations are deployed following the hexagonal pattern of the in-ice array with distances of roughly 125 m to each other. Analogous to DeepCore, at the center of IceTop, three stations are deployed at intermediate locations, forming a denser core of the array, the so-called *in-fill*. The IceTop array as well as the string locations in-ice, in IceCube coordinates, are shown in Figure 4.7.

Each tank is 1.8 m in diameter and is filled with 50 cm of water that is frozen in a controlled manner to avoid air bubbles produced in the freezing process

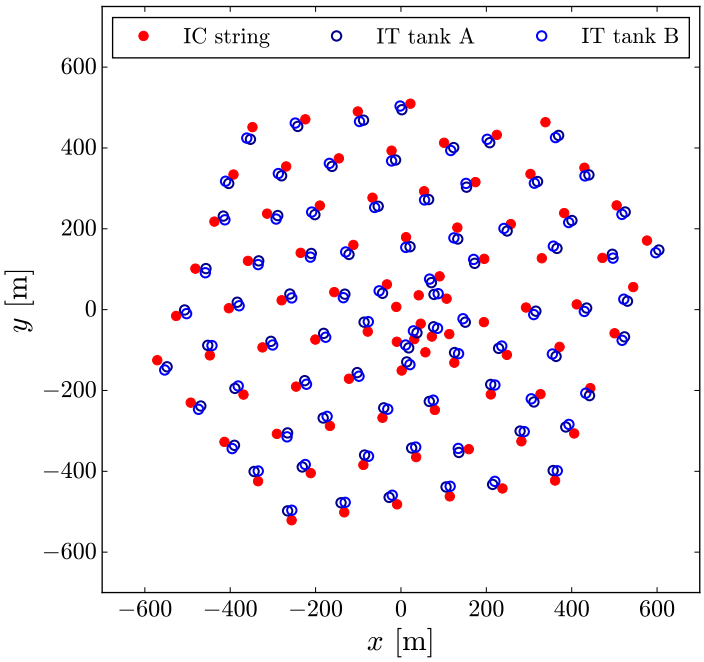

Figure 4.7: IceCube xy-coordinates of the in-ice strings (red) and IceTop tanks (blue).

[153]. In contrast to the in-ice DOMs, the two separated DOMs of each IceTop tank are operated at different gains: 10^5 (*low-gain*) and $5 \cdot 10^6$ (*high-gain*) to maximize the dynamic range. A schematic drawing of an IceTop tank is shown in Figure 4.8. Due to the large data rates of the surface array, each IceTop DOM is connected with its own twisted pair to the ICL and the IceTop DOMs use a different set of DOMHubs, with 32 DOMs per hub (8 stations) [160].

The trigger criteria for IceTop are based on the number of hit stations, where a station is hit if the high-gain DOM in one tank measures a signal in coincidence with the low-gain DOM of the other tank (HLC hit) [132]. Different trigger conditions then require, for example, 8 HLC hit stations (SMT8), or 3 hit stations (SMT3), lowering the energy threshold.

IceTop also uses dedicated on-line filtering. The most common filter is the *IceTopSTA3* filter, which requires three stations recording hits within a time window of 10 µs [132]. Using the IceTopSTA3 condition, IceTop has an primary energy threshold of 300 TeV. Other filters require five hit stations (*IceTopSTA5*), for example, or three hit stations within the in-fill (*IceTopInFillSTA3*).

The calibration of IceTop tanks is done in two steps. In a first step the PMTs and DOMs are calibrated using the same techniques, as used for in-ice calibrations, described in Section 4.1.4. In a second step, the tank signal charges are calibrated in units of *vertical equivalent muon* (VEM), which is the signal a vertical muon generates in the IceTop tank. This is done using natural atmospheric muons. All details about the IceTop tank calibration can be found in Ref. [132].

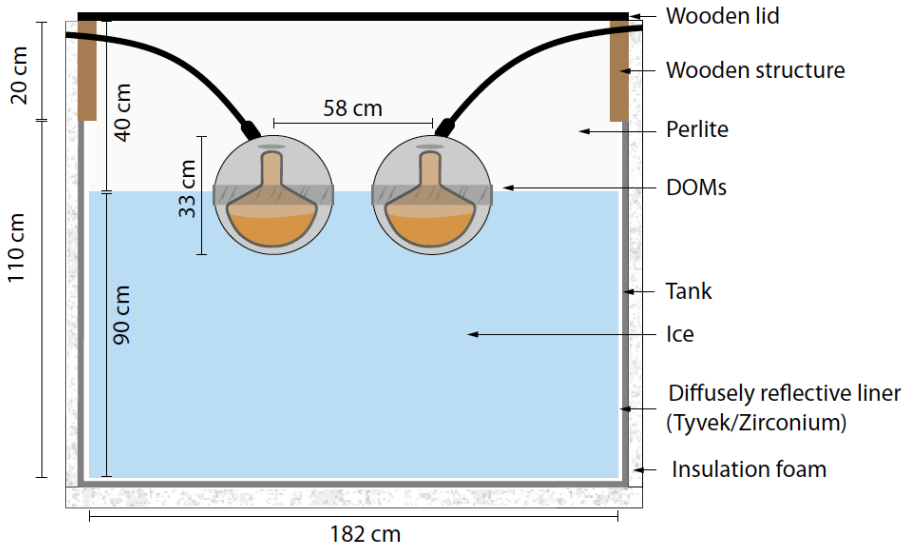

Figure 4.8: Cross-sectional schematic view of an IceTop tank. Taken from Ref. [132].

5 SIMULATION

"God does not care about our mathematical difficulties.
He integrates empirically."
– Albert Einstein *

In order to study physics models and to develop dedicated criteria for the selection of certain classes of events, computer simulations are an essential tool in modern physics. They usually rely on *Monte Carlo* (MC) methods, which are based on repeated random sampling to obtain numerical results for an underlying problem (see for example Ref. [167], for a general overview).

In the following, the simulations used throuhout this work to model the underlying physics and to develop criteria, used to select LS Muon events from IceCube data, are described. Section 5.1 gives an overview of the air shower simulation package CORSIKA [48], and the different hadronic interaction models described in Section 5.2. In Section 5.3 the treatment of different primary flux assumptions in the simulations is discussed. A dedicated method to simulate laterally separated muons in air showers events, which enables fast production of large simulated datasets and detailed studies on the underlying physics, is introduced in Section 5.4. An overview of the resulting distributions obtained from these air shower simulations, as well as a discussion of the differences of simulated datasets, is given in Section 5.5. The simulation of neutrino events in IceCube, forming a potentially (small) background contribution for this analysis, is described in Section 5.6. The subsequent simulation of the propagation of particles through the ice, as well as of the detector response and electronics, is described in Section 5.7.

5.1 CORSIKA

CORSIKA [48] is a software package used to perform the simulation of extensive air showers initiated by a primary cosmic ray particle. It includes a full simulation of the shower development by tracking the particles through the atmosphere until they decay or re-interact. It includes simulation of interactions and decays of nuclei, hadrons, leptons, and photons to energies of above 10^{20} GeV. CORSIKA accounts for ionization energy losses and multiple scattering in the atmosphere, using the gaussian approximation discussed in Section 3.1. In addition, it also includes deflections of charged particles due to the Earth's magnetic field.

For all showers with inclinations below 70°, CORSIKA assumes a flat model of the atmosphere, as introduced in Section 2.2.1. For events with higher incli-

* As quoted by L. Infeld, in *"Quest"* (1980).

nations, it instead used a detailed model which accounts for the curvature of the Earth. The MSIS-90-E models for the South Pole atmosphere are used for all CORSIKA simulations [47]. These models use a 5-layer parametrization, given in Appendix A.2, assuming four annual seasons. The resulting atmospheric profiles are shown in Figure 2.5, with the corresponding model parameters listed in Appendix A.2.

Whether an unstable particle re-interacts or decays within the atmosphere is determined based on the interaction and decay lengths, as described in Section 2.2.2. Since interactions at the highest energies, occurring during shower development, are well beyond the energy range of current accelerator experiments, their description largely relies on extrapolations based on theoretical models. Hadronic interactions of nuclei and hadrons with molecules in the air can be simulated using several (external) hadronic models. These models simulate the strong interactions of particles and handle their fragmentation and regeneration. A short overview of the hadronic models used in this work is given in Section 5.2. The nuclear fragmentation of non-interacting nuclei, so-called *spectators*, is handled by the CORSIKA code directly.

All decays of unstable hadrons h, with decay lengths below $\beta\gamma c\tau_h \leqslant 1\,\mathrm{cm}$ (see Equation (2.18)), are simulated within the hadronic model used, any other decays are handled by the CORSIKA code. However, most commonly used interaction models, such as SIBYLL 2.1 [168], do not consider decay channels with branching fractions below 10^{-4}. Thus, the prompt contribution to the muon flux is not included in most of the commonly used hadronic models, and hence not included in the CORSIKA simulations used in this work.

After the full simulation of the shower development, CORSIKA returns the type, energy, location, direction and arrival times of all secondary particles generated in an air shower at a given observation level. For all simulations throughout this work, an observation level of $H_{obs} = 2835\,\mathrm{m}$ is used, according to the surface coordinates of ICECUBE (see Section 4.2). This analysis uses SIBYLL 2.1, as hadronic model for all CORSIKA simulations at high energies, while low energy interactions are described using the GHEISHA model [169].

Any further details on the physics modeling, as well as technical information of the CORSIKA simulation package, are beyond the scope of this work and can be found in Ref. [48]. The in-ice propagation, light production, and detector response is simulated using the standard ICECUBE software framework ICETRAY and is described in Section 5.7.

In order to handle signal events (in figures of this work denoted as *sig*) and background contributions (denoted as *bkg*) separately, the CORSIKA simulations used throughout this analysis are divided into sub-samples:

- **Showers with an LS Muon** (sig):
  This sub-sample contains all showers that have at least one muon with a lateral separation from the shower core at surface level of above $d_T \geqslant 100\,\mathrm{m}$. Only muons with surface energies above $E_\mu \geqslant 460\,\mathrm{GeV}$ are considered here, in order to ensure that the muons reach the ICECUBE detector and can be observed. This class of events represents the signal of this analysis.

- **Single showers without an LS Muon** (bkg):
  This sub-sample contains all showers without any laterally separated muons ($d_T < 100$ m) and $E_\mu \geqslant 460\,\text{GeV}$. These showers represent the bulk of air shower events and are considered as background in this analysis.

- **Multiple showers within the same time-window** (bkg):
  This sub-sample contains all events which have more than one air shower, or an air shower accompanied by a separate neutrino event, within the same trigger time-window. The occurance of two coincident events from similar directions can mimic double track signatures in IceCube. Hence, these events can form an irreducible background for this analysis and are therefore considered separately.

The total CORSIKA fluxes shown in this work, generally indicated by (orange) solid lines, are the sum of the sub-samples defined above and the (very small) contribution of atmospheric neutrino events:

$$\Phi^{\text{CORSIKA}}_{\text{total}} = \Phi^{\text{CORSIKA}}_{\text{LS}} + \Phi^{\text{CORSIKA}}_{\text{single}} + \Phi^{\text{CORSIKA}}_{\text{multiple}} + \Phi^{\text{NuGen}}_{\nu} \,. \tag{5.1}$$

The neutrino simulations are generated using NuGen, as described in Section 5.6.

As primary flux models, the 5-component models, introduced in Section 2.1.4, are used in simulations. Therefore, the CORSIKA simulations are produced using 5 different primary types, p, $^{4}_{2}$He, $^{14}_{7}$N, $^{27}_{13}$Al, $^{56}_{26}$Fe, with the ratios 10 : 5 : 3 : 2 : 1. Various primary flux assumptions are then included in CORSIKA simulations via event weighting, as described in Section 5.3.

5.2 HADRONIC INTERACTION MODELS

The hadronic interactions of nuclei with air molecules during air shower development are typically handled by external hadronic event generators within air shower simulations, such as CORSIKA. These event generators simulate every interaction of the particles involved in the shower development, as well as any subsequent fragmentation and regeneration processes. In addition, they can handle the decay of particles. After the full simulation of an interaction, these models return a complete list of final state particles, including information on the particle types, their kinematic distributions, and the underlying production processes. This list is then further processed by the underlying simulation code.

Figure 5.1 shows the mean final state particle content per collision, obtained from various hadronic models for (fixed target) proton-nitrogen collisions at $E_0 = 100\,\text{TeV}$, using the CRMC software package as an interface [81] (see Section 5.4 for further details). All particles generated in the collisions were kept stable. The final state particles obtained from corresponding iron-nitrogen collisions are shown as shaded bars for comparison. Analogously, Figure 5.2 shows the mean particle content of collisions at $E_0 = 100\,\text{TeV}$, where the decay of hadrons with lifetime τ_h and $\beta\gamma c\tau_h \leqslant 1\,\text{cm}$ is handled by the underlying

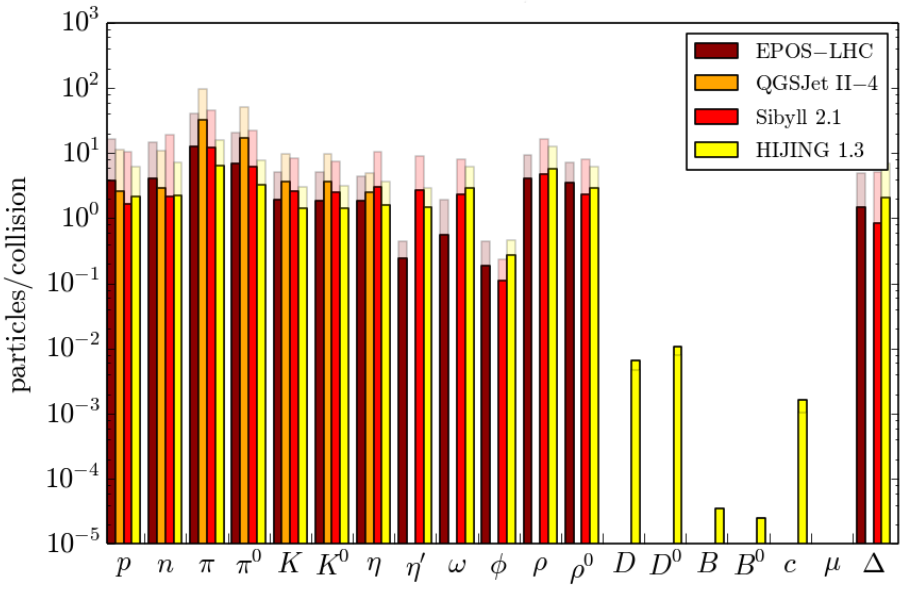

Figure 5.1: Particle content obtained from various hadronic models, produced in proton-nitrogen and iron-nitrogen (shaded) collisions at $E_0 = 100\,\text{TeV}$. All final state particles are kept stable (i.e. no subsequent decay).

hadronic model. This represents the default setting used in CORSIKA simulations throughout this work. In addition, the number of heavy nuclei, produced in proton-nitrogen and iron-nitrogen collisions at $E_0 = 100\,\text{TeV}$, is shown in Figure 5.3.

Figure 5.1 shows significant differences in the final state particle content obtained from different hadronic generators. This is due to the different modeling of hadronic interactions, which needs to be accounted for when interpreting simulated particle spectra. Thus, the general concepts and some basic differences between commonly used high energy hadronic models are briefly discussed in the following.

Sibyll 2.1

The hadronic event generator SIBYLL 2.1 [168] is specifically designed to simulate interactions during air shower development. It is based on the *minijet model*. Generally *particle jets* are hadronic clusters which carry a large transverse energy E_T and can therefore produce hadrons with large transverse momentum p_T (see also Section 2.4). Minijets are particle jets in a regime where E_T becomes smaller and can typically no longer be resolved in accelerator experiments [170]. However, the collisions can still be calculated using PQCD. It was observed that minijets can produce 80% of the transverse energy in central heavy ion collisions at LHC energies and therefore play an important role for the p_T modeling in SIBYLL [171].

For soft hadronic collisions particles fragment into a quark-diquark or quark-antiquark system, forming a color triplet or anti-triplet respectively. The components of opposite color of the interacting hadrons then form two *color strings* [172]. These strings are fragmented (*string fragmentation*) according to a (modified) *Lund algorithm*, assuming an energy independent number of strings, as described in Ref. [173]. In addition, strings produced in hard collisions, which potentially produce high-p_T hadrons, are included using the minijet model. Here the increasing inelastic cross-sections of hadrons are included by increasing the number of strings.

In hadron-nucleus collisions the number of interacting projectile nucleons are obtained from the number of soft strings. For nucleus-nucleus collisions a *semi-superposition* model is used and the number of interacting projectiles is determined from *Glauber theory* [174]. Spectator nucleons are fragmented according to a *thermal model*, as shown in Ref. [175]. In SIBYLL 2.1 only nucleons and anti-nucleons, charged pions, and all kaons are treated explicitly. All other particles are tracked but can only decay in the atmosphere. As shown in Figure 5.1, it does not include the treatment of heavy hadrons, such as D and B mesons. Since the prompt contribution of the atmospheric lepton fluxes is predominantly produced by the decay of these short-lived mesons, as described in Section 2.3, prompt lepton fluxes are not considered in the SIBYLL 2.1 hadronic model.

Since SIBYLL is particularly designed for the simulation of extensive air showers, it is characterized by a very good computational performance in comparison to other models. Hence, it is possible to produce large event statistics at rather small computational costs, and SIBYLL is therefore used as hadronic model for all CORSIKA simulations shown in this work. Further details and comprehensive documentation of the SIBYLL hadronic model can be found in Ref. [168].

QGSJet II-4

The QGSJET II-4 hadronic model [176, 177] is based on the QGS model [178], which uses the concept of *pomeron exchange* to describe hadronic interactions. Pomerons are trajectories in the context of *Gribov-Regge theory*, where collisions are described as multiple scattering processes with each individual scatter represented by pomeron exchanges [179, 180]. Each pomeron corresponds to microscopic parton cascades mediating the interactions between projectile and target hadrons. The pomerons form strings which are cut according to the *Abramovsky-Gribov-Kancheli rules* [181] to generate two strings each (*two-string model*). Similar to the procedure used in SIBYLL, the strings are fragmented using the Lund algorithm [172, 173], but with a deviating treatment of the initial string momenta. Hard interactions are then handled using a minijet model, similar to SIBYLL 2.1. A comprehensive overview on pomeron physics can be found for example in Ref. [182].

As shown in Figure 5.1, QGSJET has a very different treatment of unflavored mesons, compared to other models. It uses the so-called *duality picture*, where short-lived resonances ($\eta, \omega, \rho, \ldots$) are not treated explicitly, but their contributions are included in the spectra of stable ($\beta\gamma c\tau_h > 1\,\mathrm{cm}$) hadrons [183]. Hence,

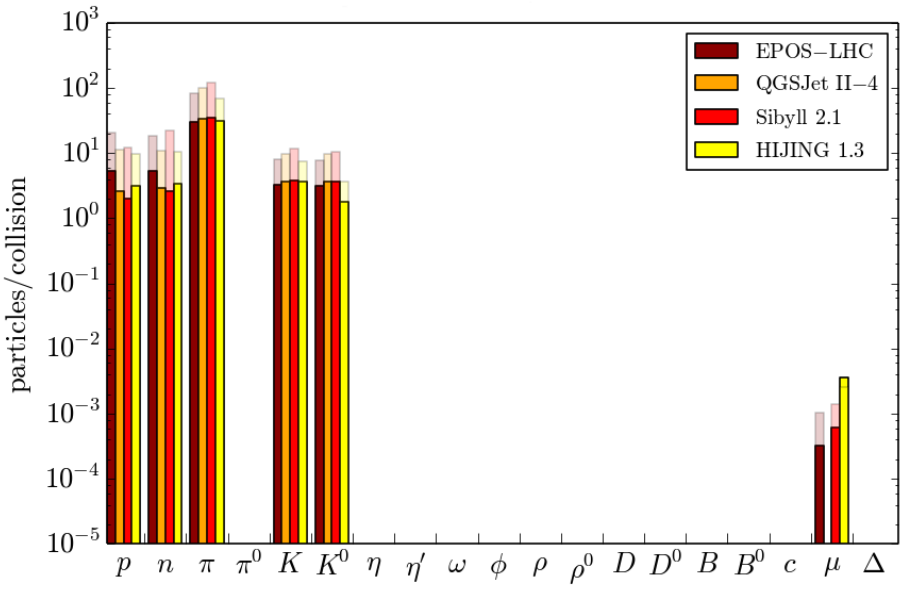

Figure 5.2: Particle content obtained from various hadronic models, produced in proton-nitrogen and iron-nitrogen (shaded) collisions at $E_0 = 100\,\text{TeV}$. The decay of unstable hadrons ($\beta\gamma c\tau_h \leqslant 1\,\text{cm}$) is handled within the underlying hadronic generator, corresponding to the CORSIKA default setting used in this work.

the spectra of stable hadrons, such as pions and kaons, contain both directly produced hadrons and those emerging from resonance decays. As previously discussed for the SIBYLL model, and as shown in Figure 5.1, QGSJET does not include an explicit treatment of hadrons containing heavy quarks, and therefore it does not consider the prompt contribution for subsequent lepton fluxes. Further details of the QGSJET model are beyond the scope of this work and can be found in Refs. [176, 177].

EPOS-LHC

The EPOS-LHC interaction model [82] is an update of the EPOS 1.99 model [184] with several modifications in order to describe experimental data from recent LHC measurements. It is generally based on *Gribov-Regge theory* [179, 180], as previously described for the QGSJET model. It was observed that at high energies (for example in the LHC energy regime) the hadronization can not be described by a simple two-string model, which neglects multiple scattering processes [185]. Therefore, a correction is introduced in EPOS-LHC, which is derived in the context of *color-reconnection*, as described in Refs. [185, 186].

In addition, EPOS-LHC includes fine-tuning in order to describe recent measurements from the LHC experiments. These changes are described in detail in Ref. [82], which account for various results from the TOTEM, ALICE, ATLAS, and CMS experiments at the LHC. Moreover, studies with special emphasis on the transverse momentum distributions have been performed in order to

optimize the p_T modeling in EPOS-LHC. It was shown that EPOS-LHC is in very good agreement with various transverse momentum measurements [82]. Hence, it is used as the default hadronic model for the dedicated simulation of LS MUON events in ICECUBE (LSMUONSIM) in order to describe hadronic interactions, as explained in Section 5.4.

However, as shown in Figure 5.1, EPOS-LHC does not account for the explicit treatment of charmed hadrons, such as D and B mesons. Thus, the prompt contribution to the lepton fluxes is not included in this model. Further details are beyond the scope of this work and a comprehensive description of the EPOS-LHC and previous models can be found in Refs. [82, 184].

HIJING 1.3

The hadronic event generator HIJING 1.3 [170] is based on the event generator PYTHIA 6, which simulates (hard) hadronic interactions using PQCD calculations [187]. Soft hadronic interactions are modeled by quark-diquark strings which are fragmented according to the Lund algorithm [172] and using the *dual-parton model* [188]. For hard interactions, HIJING uses a multi-minijet model which is based on PQCD calculations, as described for the PYTHIA model in Ref. [187]. The number of inelastic scatters are calculated using exact diffuse geometry, including several nuclear effects, such as nuclear shadowing and jet quenching [170]. As shown in Figure 5.1, HIJING represents the only model used in this analysis which includes a complete treatment of short-lived heavy hadrons, and therefore accounts for a prompt hadron flux.

A technical disadvantage of the Fortran HIJING 1.3 code is that it handles the center-of-mass energy internally with single precision real numbers. Hence, the maximum collision energy is limited due to floating point overflows and all HIJING simulations performed for this analysis are limited to initial energies at 10 PeV (fixed target). A detailed description of the model is beyond the scope of this work and can be found in Ref. [170].

Other models

Improved models have been recently published, including fine-tuning to describe recent accelerator data from LHC experiments and explicit treatment of charmed hadrons and prompt hadron fluxes. The DPMJET III model [189, 190] for example is based on the dual-parton model [188, 191], using Gribov-Regge theory to describe soft hadronic interactions and PQCD calculations for hard interactions. Additionally, it accounts for multiple jet production, higher-order pomeron graphs, and contains multiple scattering processes. DPMJET includes an explicit treatment of prompt hadron fluxes and further improvements, which are discussed in detail in Ref. [189].

The most recent release of the SIBYLL model (version 2.3) [51] is based on the previous SIBYLL 2.1 release which is described above. It includes improvements in order to describe recent experimental data from the LHC experiments and is able to handle prompt hadrons, such as D and B mesons. A detailed description

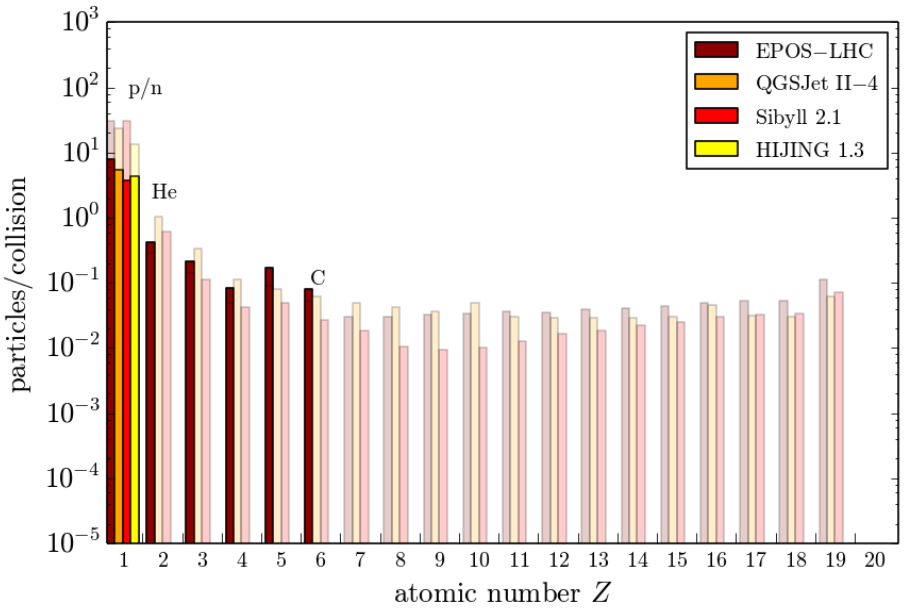

Figure 5.3: Number of atomic nuclei, with atomic numer Z, produced in proton-nitrogen and iron-nitrogen (shaded) collisions at $E_0 = 100\,\text{TeV}$, obtained from various hadronic models. All final state particles are kept stable.

of the model and its improvements compared to previous models can be found in Ref. [51].

The production of large simulated datasets requires a very large computational effort and datasets using these improved models were not available at the time of this analysis. However, these models can significantly improve the interpretation of experimental data and should therefore be considered in any future analyses of cosmic ray air showers.

5.3 PRIMARY WEIGHTING

The simulations used in this work are generated from an energy spectrum that does not necessarily reflect any realistic physics motivated model. This is done in order to enhance the statistics of high energy events by generating from a harder spectrum, because the physical fluxes follow very steep energy spectra (see Section 2.1.3). Thereby the computational effort is significantly reduced. However, simulated events need to be *re-weighted* to a realistic primary flux. This is done by applying the weights

$$\omega_0 = \frac{\text{expected spectrum}}{\text{generated spectrum}}, \tag{5.2}$$

to each simulated event. The generated spectrum is given by a simple power law

$$\frac{d\Phi}{dE_0} \propto E_0^{-\gamma} \tag{5.3}$$

with a fixed spectral index γ. For all CORSIKA simulations used in this work, a spectral index of $\gamma = 2.6$ ($\gamma = 2.65$ for protons) is used for the low energy region ($E_0 \leqslant 100\,\text{TeV}$) and $\gamma = 2.0$ in the high energy region ($E_0 > 100\,\text{TeV}$). All neutrino simulations (see Section 5.6) are generated from a spectral index of $\gamma = 2.0$.

For all air shower simulations, this analysis uses the 5-component H3A flux parametrization [38] as the (default) primary flux assumption (expected spectrum), which is described in Section 2.1.4. Studies on the systematic effects due to different flux assumptions, such as the H4A [38] and GST [39] models, are shown in Section 7.7. The simulations of atmospheric neutrinos are re-weighted to the Honda flux parametrization in Ref. [192], based on a H3A primary cosmic ray flux assumption, as explained in Section 5.6.

5.4 LS MUON SIMULATIONS

The simulation of cosmic ray air showers using commonly used software packages, such as CORSIKA, is computationally expensive. Due to limited computing resources, the statistics of CORSIKA datasets are constrained. The contributions of LS MUON events to the total air shower rate is significantly below 1%. In addition, the combined trigger and filter efficiency of this analysis is on the order of $10^{-5} - 10^{-6}$, as discussed in Section 6.9. Hence, even with existing CORSIKA datasets, consisting of several 10^{11} showers at surface level, the number of simulated air shower events that pass all selection criteria, described in Chapter 6, is on the order of only a few $\sim$ 1000 events. Drawing conclusions from these simulations would be challenging, especially when the final dataset is further divided into several sub-samples of different regions of interest, such as primary energy ranges, zenith angle regions, or primary particle types, etc. Moreover, during the simulation process in CORSIKA, detailed information about the air shower development is removed in order to reduce the storage size of the simulated datasets. The information about parent particles and their transverse momentum, for example, is lost.

Thus, in the following a dedicated method to produce high-statistics of Monte Carlo simulations of LS MUON events in ICECUBE, called LSMUONSIM, is presented. This method is based on existing CORSIKA simulations which are modified by adding one laterally separated muon to the muon bundle of the pre-simulated event. Since the existing datasets are already processed to detector level, this reduces the computational effort to produce LS MUON events significantly and improves the number of LS MUONS in existing simulations by a factor of roughly $100 - 1000$ (depending on the primary energy). Moreover, these simulations enable detailed studies of the production processes of LS MUONS,

on the underlying hadron distributions, various atmospheric effects, and many more.

5.4.1 GENERAL CONCEPT

The Monte Carlo simulation of LS MUON events using LSMUONSIM is based on existing CORSIKA air shower simulations, generated using SIBYLL as the hadronic model. In the deep ice these showers essentially consist of muon bundles in the detector, where the muon with the largest separation from the bundle core is replaced by an externally simulated laterally separated muon. The kinematics of this LS MUON are generated according to the primary interaction of the underlying CORSIKA shower, but constrained to the phase space relevant to the production of laterally separated muons.

In contrast to CORSIKA, hadronic interactions in the atmosphere are not simulated explicitly in LSMUONSIM by an external hadronic MC generator. Instead, the spectra of final state hadrons produced in hadronic interactions are obtained from probability distributions. These probability distributions are determined from simulated particle spectra obtained from a particular hadronic model. This is done with the software package CRMC [81], which serves as an interface to various hadronic interaction models, and is used to simulate particle collisions for several (fixed) collision energies.

Multiple CRMC simulations are (pre-)generated for various collision energies and using different initial particles which may be involved in the production of LS MUONS. Therefore, particle collisions are simulated at energies of $\log_{10}(E_0 \,/\mathrm{GeV}) = 3.0, 3.1, \ldots, 8.9, 9.0$. This is done assuming nitrogen ($^{14}_{7}\mathrm{N}$) as the target particle in order to reflect the mass composition of the Earth's atmosphere (see Section 2.2.1). Following the 5-component primary flux assumptions used in this analysis, the collisions are generated separately for p, $^{4}_{2}\mathrm{He}$, $^{14}_{7}\mathrm{N}$, $^{27}_{13}\mathrm{Al}$, $^{56}_{26}\mathrm{Fe}$ as the initial particles. In addition, hadron-nitrogen collisions are generated using neutrons, pions, and kaons as initial projectile, since their (secondary) interactions can potentially contribute to the production of LS MUONS. The production processes to generate LS MUONS, which are included in LSMUONSIM, are described in Section 5.4.2.

To enable studies on different hadronic interaction models, these collisions are generated based on various models. This work uses EPOS-LHC [82], QGSJET II-4 [176, 177], and SIBYLL 2.1 [168] as hadronic models in LSMUONSIM. As described in Section 5.2, these interaction models do not include an explicit treatment of heavy hadrons with prompt lepton production. Thus, the prompt component in LSMUONSIM is generated based on the HIJING 1.3 [170] model.

The resulting final state distributions from these simulations are then used as probability distributions in order to generate the kinematic variables of each hadron involved during the LS MUON production process. This is done using random sampling methods, as described in Section 5.4.3 and Section 5.4.4, with the input parameters based on tables derived from these distributions. By generating from a limited phase space, expected to be relevant for LS MUON production,

the shower is forced to produce a LS Muon. Hence, all hadrons involved in the LS Muon production are generated with energies above $E_{h,min} = 460\,\text{GeV}$ to ensure that resulting muons can reach the in-ice detector [52]. If the energy of any hadron drops below $E_{h,min}$, the shower is discarded from the LS Muon simulation. In order to enforce a large separation of the generated muon from the bundle core, the transverse momentum of hadrons is generated above $p_{T,min} = 1\,\text{GeV/c}$. A discussion on the phase space used for the simulation of LS Muons can be found in Section 5.5. Using this approach, the transverse momentum and energy of the LS Muon are generated. The *Pearson correlation coefficients* [193], defined in Appendix A.4, between energy and p_T of hadrons, are very closed to 0, as shown in Appendix B.5. Hence, the energy and transverse momentum of particles produced in a hadronic interaction are approximately uncorrelated, and are therefore generated independently from each other within LSMuonSim. The resulting lateral separation d_T is calculated based on Equation (2.36), according to the zenith angle and interaction height given by the underlying CORSIKA shower.

Many potential LS Muon production channels are included in LSMuonSim and are discussed in detail in Section 5.4.2. Each channel is simulated individually for each underlying CORSIKA shower. In order to produce a realistic LS Muon flux, the generation and decay probabilities of hadrons involved during the LS Muon production process are taken into account. This is done through physics modeling of the interactions and decay of each generated hadron. The resulting probabilities are incorporated in the simulations via event weighting, using the procedure described in Section 5.4.5.

The independently simulated laterally separated muon is finally combined with the underlying CORSIKA shower by replacing the muon with the largest separation from the underlying bundle core. This is done by removing all photoelectrons produced by the muon with the largest lateral separation generated within CORSIKA and merging the photons produced by the externally generated LS Muon and the remaining muon bundle.

5.4.2 PRODUCTION CHANNELS

As described in Section 2.3, muons generated in an air shower are predominantly produced from pion and kaon decays (conventional component). Consequently, this also represents the dominant process which produces laterally separated muons. Since the transverse momentum of a particle depends on the collision energy, high-p_T hadrons, and subsequently the resulting LS Muons, are mainly produced in the first few interactions during the shower development. All production processes included in LSMuonSim are indicated in Figure 5.4 and are described in the following.

During the simulation process, each relevant channel is generated explicitly for every single underlying CORSIKA air shower. The target particle in the atmosphere is approximated by nitrogen, $N_{air} = {}^{14}_{7}N$, in LSMuonSim because this is the most abundant element in the atmosphere. Since oxygen is the second

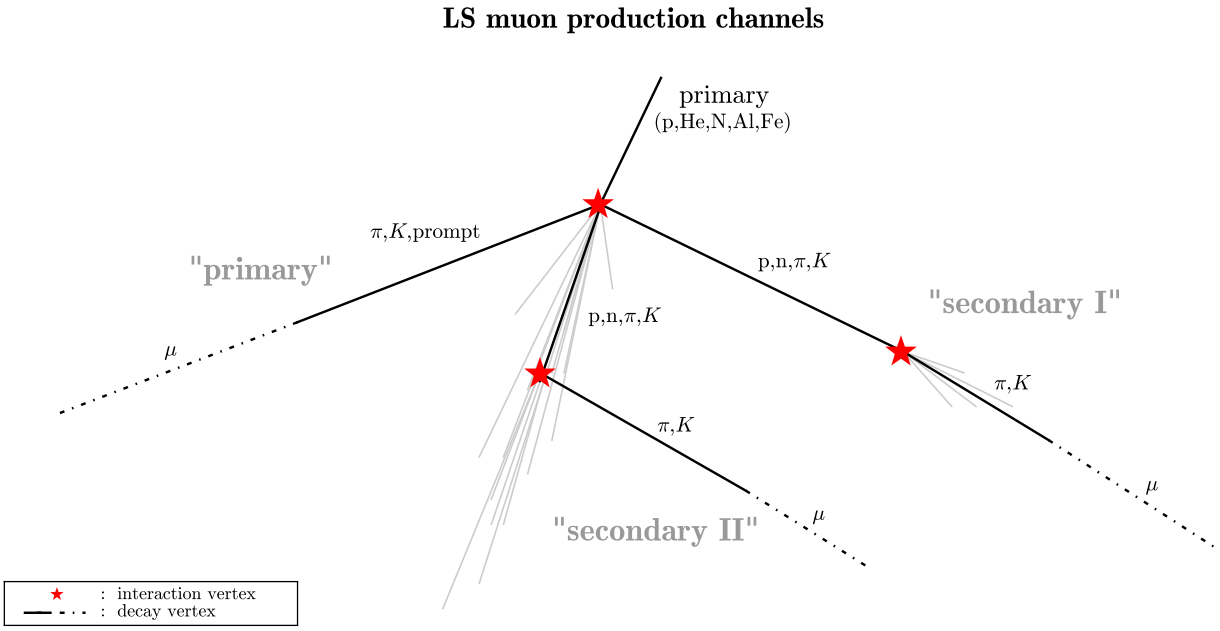

Figure 5.4: LS Muon production channels included in the LSMuonSim MC. The relevant production mechanisms are divided into three classes, denoted with *primary*, *secondary I*, and *secondary II*, as described in the text.

most abundant element and has a very similar mass number (see Section 2.2.1), air molecules are well approximated by nitrogen. The different channels shown in Figure 5.4, are divided into three classes. This results in a total of 20 sub-channels in total for the production of LS Muons and accounts for muons generated from all hadrons produced in the first and second interactions of the shower development. In the following the notation

$$
\begin{aligned}
N_{\text{nucl}} &\in \{p, {}^{4}_{2}\text{He}, {}^{14}_{7}\text{N}, {}^{27}_{13}\text{Al}, {}^{56}_{26}\text{Fe}\} \\
\pi &\in \{\pi^{+}, \pi^{0}, \text{and anti-particles}\} \\
K &\in \{K^{+}, K^{0}, \text{and anti-particles}\} \\
h &\in \{p, n, K, \pi\} \\
\text{prompt} &\in \{D^{+}, D^{0}, D_{s}^{+}, \Lambda_{c}^{+}, \Omega_{C}^{0}, B^{+}, B^{0}, B_{c}^{+}, \lambda_{c}^{0}, \text{and anti-particles}\}
\end{aligned}
$$

is used.

Primary

In the *primary* production channel a high-p_T hadron ($p_T \geqslant 1\,\text{GeV/c}$, $E_h \geqslant 460\,\text{GeV}$) is produced during the primary interaction. This hadron decays into a muon while traveling to the ground before re-interacting hadronically with molecules in the atmosphere. The particles imparting the transverse momentum to the muons are dominated by pions and kaons. In addition, the component from prompt (heavy) particle decays is also explicitly included in the simulations.

Hence, there are four production sub-channels which are simulated separately for each CORSIKA shower:

$$
\begin{aligned}
N_{nucl} + N_{air} &\xrightarrow{p_T \geqslant 1\,GeV/c} \pi^{\pm} + X \\
&\qquad \pi^{\pm} \rightarrow \mu^{\pm} + \nu_{\mu}(\bar{\nu}_{\mu}) \\
N_{nucl} + N_{air} &\xrightarrow{p_T \geqslant 1\,GeV/c} K^{\pm} + X \\
&\qquad K^{\pm} \rightarrow \mu^{\pm} + X \\
N_{nucl} + N_{air} &\xrightarrow{p_T \geqslant 1\,GeV/c} K^{\pm} + X \\
&\qquad K^{\pm} \rightarrow \pi^{\pm} + X \\
&\qquad\qquad \pi^{\pm} \rightarrow \mu^{\pm} + \nu_{\mu}(\bar{\nu}_{\mu}) \\
N_{nucl} + N_{air} &\xrightarrow{p_T \geqslant 1\,GeV/c} \text{prompt} + X \\
&\qquad \text{prompt} \rightarrow \mu^{\pm} + X
\end{aligned}
$$

Since the transverse momentum of the LS MUONS is imparted by hadrons produced in the primary interaction, these muons carry direct information of the first interaction of the shower development.

Secondary I

In the *secondary I* production channel the primary interaction produces high-p_T hadrons ($p_T \geqslant 1\,GeV/c$, $E_h \geqslant 460\,GeV$) that re-interact in the atmosphere before decaying. The secondary interaction produces further mesons (pions and kaons) that decay into muons. In a first order approximation, only the first re-interaction in the atmosphere is taken into account. This is done because the collisional energy of particles produced in secondary interactions is significantly lower. Hence, the production of high energy particles, that can possibly generate muons with energies sufficiently large ($E_{\mu,min} \sim 460\,GeV$) to reach the deep ice detector, is highly suppressed. Thus, further particle generations can be neglected and the relevant sub-channels are:

$$
\begin{aligned}
N_{nucl} + N_{air} &\xrightarrow{p_T \geqslant 1\,GeV/c} h + X \\
&\qquad h + N_{air} \rightarrow \pi^{\pm} + X \\
&\qquad\qquad \pi^{\pm} \rightarrow \mu^{\pm} + \nu_{\mu}(\bar{\nu}_{\mu}) \\
N_{nucl} + N_{air} &\xrightarrow{p_T \geqslant 1\,GeV/c} h + X \\
&\qquad h + N_{air} \rightarrow K^{\pm} + X \\
&\qquad\qquad K^{\pm} \rightarrow \mu^{\pm} + X
\end{aligned}
$$

This results in 8 sub-channels in total for the secondary I production. Assuming the pions and kaons generated in the second interaction will mainly be produced

in the forward region with large Feynman-x, in this channel the transverse momentum imparted to the LS MUONS is also produced in the primary interaction, as in the primary channel.

Secondary II

The *secondary II* production channel is identical to secondary I, but with high-p_T mesons ($p_T \geqslant 1\,\mathrm{GeV/c}$, $E_h \geqslant 460\,\mathrm{GeV}$) produced in the secondary interaction of hadrons within the atmosphere. These mesons decay into muons while traveling to the ground:

$$
\begin{aligned}
N_{\mathrm{nucl}} + N_{\mathrm{air}} &\to h + X \\
h + N_{\mathrm{air}} &\xrightarrow{p_T \geqslant 1\,\mathrm{GeV/c}} \pi^{\pm} + X \\
\pi^{\pm} &\to \mu^{\pm} + \nu_{\mu}(\bar{\nu}_{\mu}) \\
N_{\mathrm{nucl}} + N_{\mathrm{air}} &\to h + X \\
h + N_{\mathrm{air}} &\xrightarrow{p_T \geqslant 1\,\mathrm{GeV/c}} K^{\pm} + X \\
K^{\pm} &\to \mu^{\pm} + X
\end{aligned}
$$

The secondary II channel therefore includes 8 sub-channels, which are simulated individually for each shower.

Further Generations

As shown in Appendix A.3.2 based on MC simulations, the mean energy of hadrons produced in an interaction is approximately two orders of magnitude smaller than the initial collision energy. Moreover, the probability to produce hadrons with large transverse momentum decreases with decreasing collision energy, as shown in Section 5.4.5. Subsequently, the mean energy of LS MUONS produced from the decay of hadrons generated later during the shower development, with respect to the processes described above, is estimated to be typically below $\sim 100\,\mathrm{GeV}$. However, the threshold energy for a vertical muon to reach the deep ICECUBE detector is about 460 GeV. Hence, the contribution of LS MUONS from further re-interactions during the shower development is expected to be well below the percent-level and is neglected in the following in order to reduce computational efforts. For a detailed discussion, see Appendix A.3.2.

5.4.3 TRANSVERSE MOMENTUM DISTRIBUTIONS

The transverse momentum distributions of hadrons can be described by the Hagedorn function (Equation (2.34)), as introduced in Section 2.4. According to

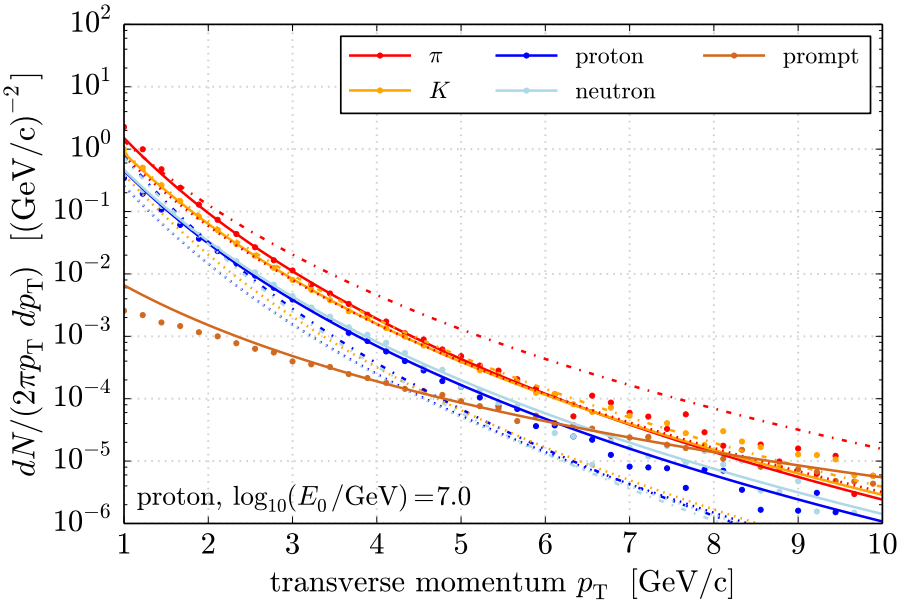

Figure 5.5: Transverse Momentum Distributions for proton collisions at 10 PeV obtained from EPOS-LHC as hadronic model, with the corresponding Hagedorn fits shown as solid lines. The resulting fits obtained from QGSJET II-4, and SIBYLL 2.1 are shown as dashed-dotted and dotted lines respectively. The prompt component is obtained from HIJING 1.3.

this distribution, the transverse momentum for high-p_T hadrons of is generated by LSMUONSIM, using the probability density function

$$\frac{dN}{dp_T} = 2\alpha\pi p_T \cdot \left(1 + \frac{p_T}{p_0}\right)^{\beta} . \tag{5.4}$$

This is done for each high-p_T hadron of the production channels discussed in Section 5.4.2 and with a fixed spectral index $\beta = -3$, $\alpha = 1$, and $p_0 = 2\,\mathrm{GeV}$. Based on the inverse of the *cumulative distribution function* (CDF) $\Phi(p_T)$ of Equation (5.4), as shown in Appendix A.3.3, the transverse momentum for each high-p_T hadron is then generated by

$$\begin{aligned} p_T(\Phi) &= \frac{-p_0 A - \sqrt{1 + p_0 A} - 1}{A} , \\ A &\equiv \frac{RD \cdot \Phi(p_{T,max})}{\pi p_0^3} - \frac{p_0 + 2p_{T,min}}{(p_0 + p_{T,min})^2} , \end{aligned} \tag{5.5}$$

where RD is a random number between 0 and 1. The corresponding CDF $\Phi(p_T)$ is given in Appendix A.3.3 (Equation (A.8)). The transverse momentum is generated only for the one hadron within the underlying production channel, which carries the high p_T. Any other hadrons produced are assumed to have large Feynman-x, and thus follow the forward direction of the initial particle. The transverse momentum is randomly generated between $p_{T,min} = 1\,\mathrm{GeV/c}$ and $p_{T,max} = 10\,\mathrm{GeV/c}$.

The spectral index for generation, $\beta = -3$, is used in order to enhance the statistics of high-p_T events. To account for realistic transverse momentum spectra of hadrons, the p_T distributions of all relevant hadrons (i.e. protons, neutrons, pions, kaons, and prompt) are obtained from CRMC simulations, as described in Section 5.4.1. These distributions are fit with the Hagedorn function (Equation (2.34)). By fixing the transition parameter p_0 to 2 GeV/c, corresponding to recent accelerator data (see Section 2.4), the fit depends only on the free parameters α (normalization) and β (spectral index). The transverse momentum distributions of hadrons produced in proton collisions at 10 PeV with a nitrogen nuclei at rest, obtained from various hadronic models, are shown in Figure 5.5. The corresponding Hagedorn fits are given by the lines.

The spectral index β is a measure of the steepness of the spectra and is shown in Figure 5.6 for several hadrons from simulated proton-nitrogen collisions as a (continuous) function of the initial energy E_0. These distributions are based on the EPOS-LHC model. Figure 5.7 shows the corresponding spectral indices from simulated iron-collisions collisions. As discussed in Section 2.4 and expected from PQCD, the spectral indices become larger with increasing collision energy and decreasing initial particle mass. Also shown are cubic spline interpolations (solid lines), obtained by using the python-based software package SciPy [194]. These spline interpolations are used to determine the expected p_T spectrum with a realistic spectral index $\beta(E_0)$, as a function of the collision energy E_0. Since the transverse momentum is generated using a fixed spectral index $\beta = -3$, the simulated spectrum needs to be re-weighted in order to account for a realistic p_T spectrum in simulations. This is done analogously to the primary weighting described in Section 5.3 by applying the weight

$$\begin{aligned} \omega_{p_T}(E_0, p_T) &= \frac{\text{expected } p_T \text{ spectrum}}{\text{generated } p_T \text{ spectrum}} \\ &= N_0 \cdot \left(1 + \frac{p_T}{p_0}\right)^{\beta(E_0)+3} \end{aligned} \tag{5.6}$$

to each LS Muon event, as explained in Section 5.4.5. The normalization factor N_0 is given in Appendix A.3.3 (Equation (A.11)). Spectral indices for all initial particles used in LSMuonSim can be found in Appendix B.1. There the spectral indices obtained from the QGSJet II-4 and Sibyll 2.1 models can also be found, which are used to study differences in the underlying hadronic models.

5.4.4 HADRON ENERGY SPECTRA

In contrast to the p_T generation, the energy is simulated for each hadron within each production channel (not only for the high-p_T hadron). This is done in order to derive the energy of the resulting LS Muon and to obtain a realistic LS Muon flux, as described in Section 5.4.5. The energy spectra of particles produced in the primary interaction, or in hadronic re-interactions in the atmosphere, are obtained from CRMC simulations, as discussed before. Therefore, the energy spectra of the relevant hadrons, generated at various collision energies and for

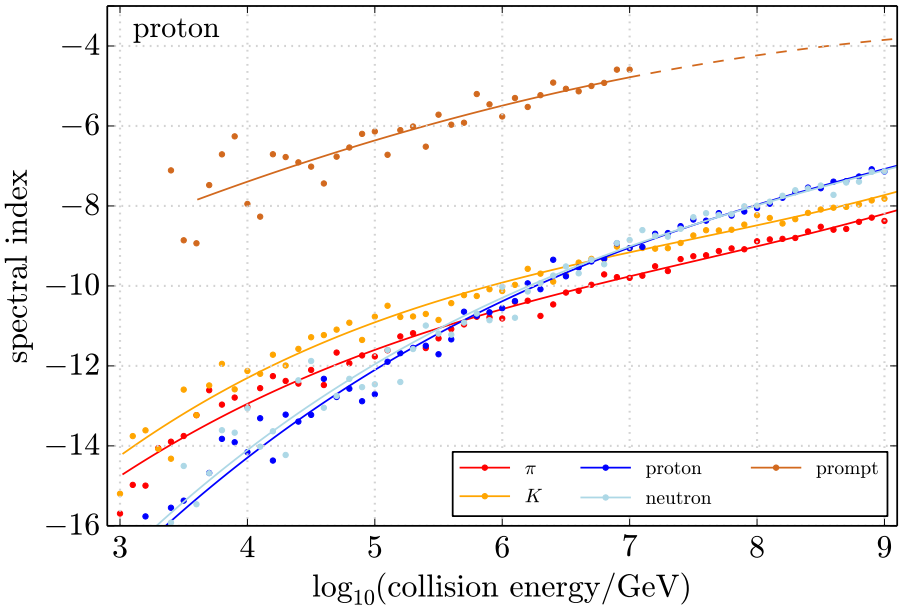

Figure 5.6: Spectral indices β from Equation (2.34) for different hadrons, obtained from proton-nitrogen collisions at various energies (EPOS-LHC). The prompt component is obtained from HIJING 1.3.

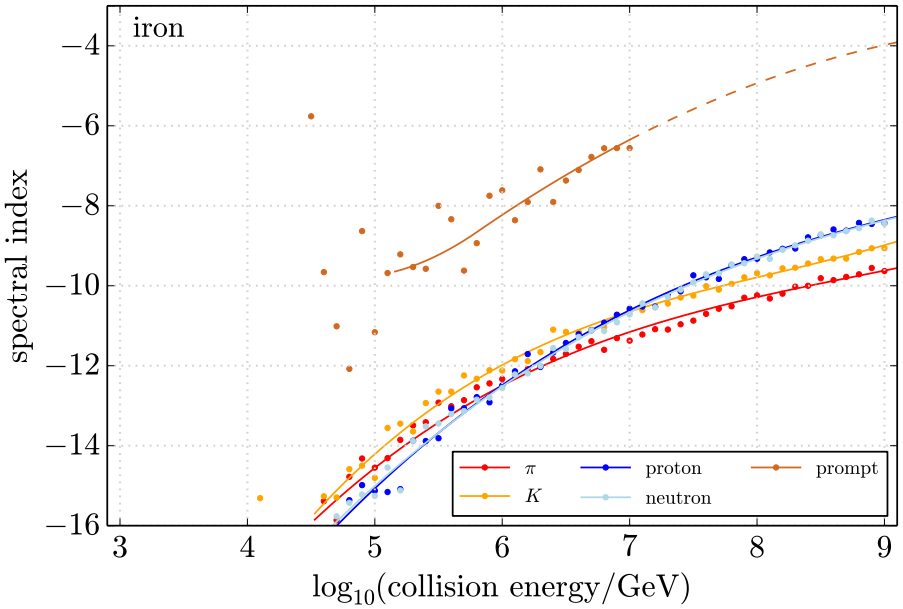

Figure 5.7: Spectral indices β from Equation (2.34) for different hadrons, obtained from iron-nitrogen collisions at various energies (EPOS-LHC). The prompt component is obtained from HIJING 1.3.

different initial particles, are fit using cubic spline interpolations from the SciPy package [194]. Figure 5.8 and Figure 5.9 show the energy spectra of hadrons, obtained from proton-nitrogen and iron-nitrogen collisions at 10 PeV. Solid lines show the spectra generated using EPOS-LHC, while the dashed and dotted lines indicate predictions from QGSJet II-4 and Sibyll 2.1 respectively. All energy distributions used in this work can be found in Appendix B.2.

From these interpolations the energies of all generated hadrons h are obtained for the underlying collision energy E_0. The hadron energy is generated above $E_{h,min} = 460\,\text{GeV}$ to ensure that the particles produced can potentially reach the in-ice detector [52]. Energy spectra are obtained only for discrete simulated collision energies $\log_{10}(E_{MC}/\text{GeV}) = 3.0, 3.1, \ldots, 8.9, 9.0$. Thus, the hadron energies are generated numerically from the binned spectra produced at energies E_{MC} closest to the desired collision energy E_0. This is done by deriving the inverted (discrete) CDF of the binned spectrum as described in Appendix A.3.1 and using it to generate the energy analogously to the transverse momentum.

For initial energies $\log_{10}(E_0/\text{GeV}) > 9.0$, the hadron energies are generated from the binned spectrum at the maximum energy $\log_{10}(E_{MC,max}/\text{GeV}) = 9.0$ and scaled with the scaling factor

$$s = \frac{E_0}{E_{MC,max}} \,. \tag{5.7}$$

To generate the energy spectra of particles produced from decays of hadrons h within LSMuonSim, the energy E_f of final state particles of type f is obtained using PYTHIA 8 simulations [195]. With an initial energy E_h of the decaying hadron, the energy fraction transferred to the resulting particle is given by

$$\begin{aligned} x(E_h) &= \frac{E_f}{E_h} \\ \Rightarrow E_f &= x(E_h) \cdot E_h \,. \end{aligned} \tag{5.8}$$

Figure 5.10 shows the energy fractions for the different decay channels included in the simulations. The resulting distributions are fit with cubic SciPy spline interpolations [194]. The energy fraction $x(E_h)$ of any particle produced from a hadron decay at E_h is generated from these interpolations. This is done analogously to the hadron energy generation by using numerical methods based on the inverted CDF (see Appendix A.3.1). The resulting particle energy E_f is then calculated according to Equation (5.8). As described in Section 3.1, additional energy losses of muons in the atmosphere are negligible for the energies considered here.

5.4.5 LS MUON FLUX CALCULATION

As described in Section 2.2.2, the muon flux on the ground depends on the interaction and decay probabilities of hadrons, as well as on the generation probabilities of particles being produced in re-interactions in the atmosphere. This needs to be considered in order to account for a realistic LS Muon flux on

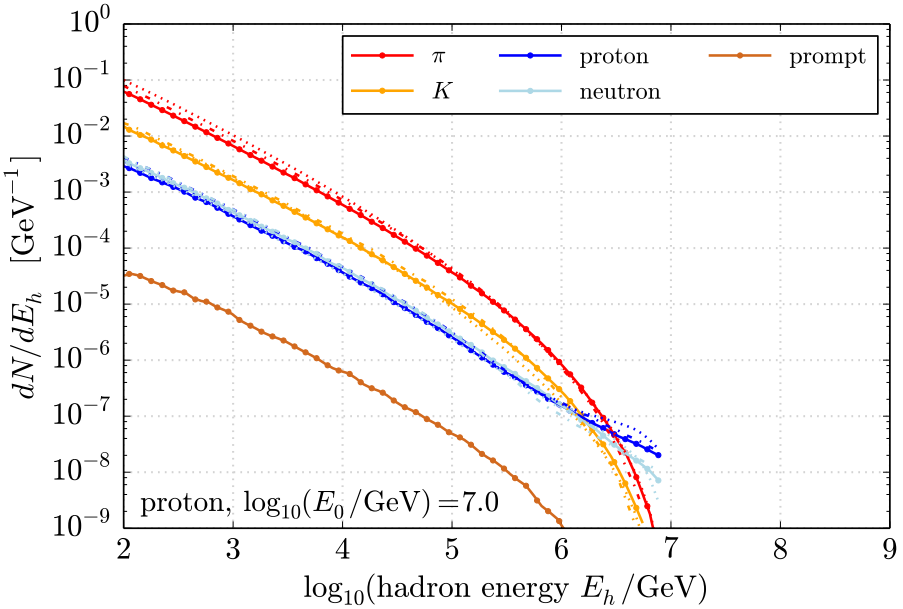

Figure 5.8: Simulated hadron energy spectra at 10 PeV assuming proton primaries. The spectra are obtained from EPOS-LHC (solid), QGSJET II-4 (dashed-dotted), and SIBYLL 2.1 (dotted) simulations. The prompt component is obtained from HIJING 1.3.

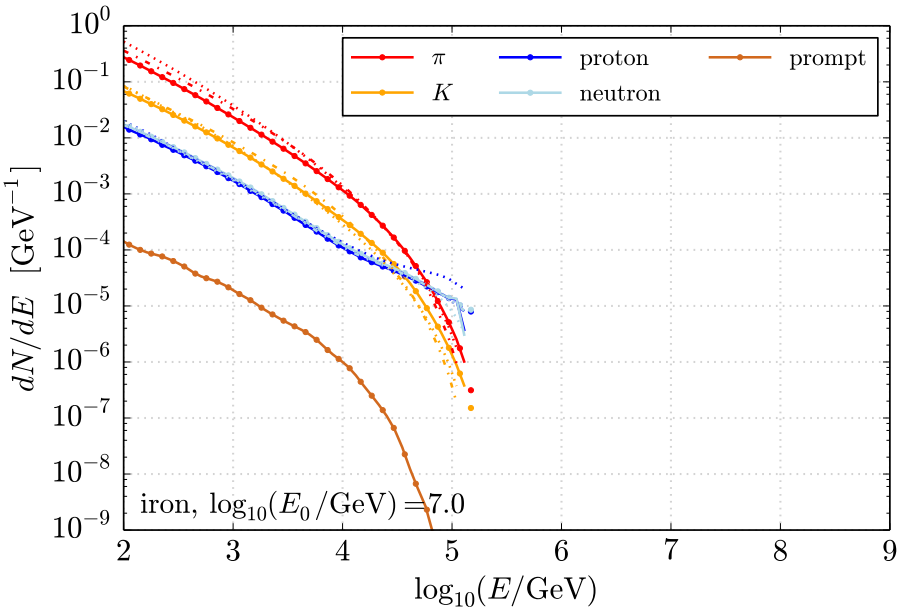

Figure 5.9: Simulated hadron energy spectra at 10 PeV assuming iron primaries. The spectra are obtained from EPOS-LHC (solid), QGSJET II-4 (dashed-dotted), and SIBYLL 2.1 (dotted) simulations. The prompt component is obtained from HIJING 1.3.

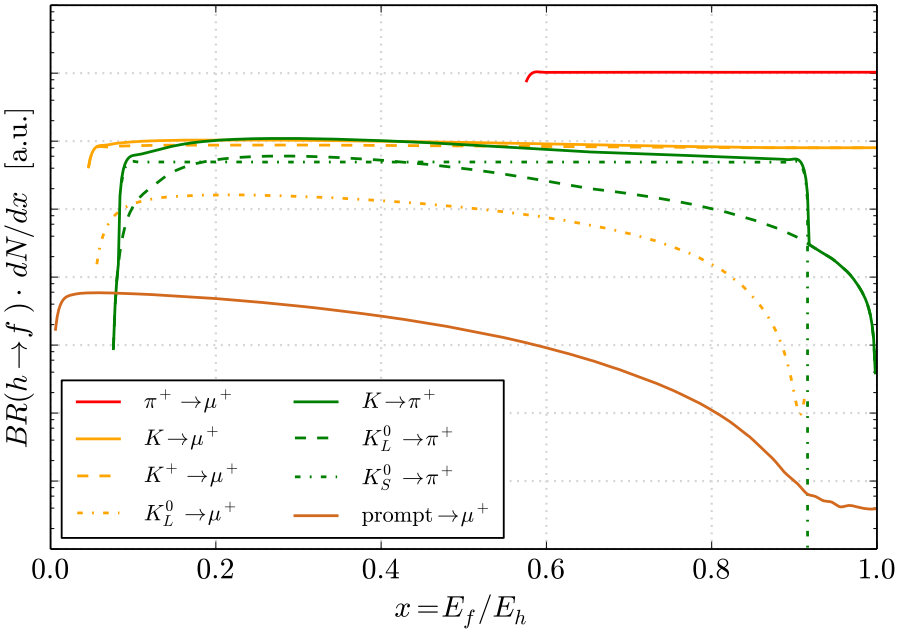

Figure 5.10: Energy fractions $x(E_h)$ of decay products f produced in the decay of a hadron with energy E_h for various relevant decay channels (see text for details). The energy fraction are obtained from PYTHIA MC simulations.

the surface. Therefore, the transverse momentum and energy distributions need to be normalized accordingly.

Particle Generation

The probability of hadrons being produced in the primary interaction and subsequent re-interactions in the atmosphere is obtained from hadronic models. The hadron *generation probability* is given by the number of collisions $N_{coll}(N_h \geqslant 1)$ producing at least one hadron h of a certain kind with energy $E_h \geqslant 460\,\text{GeV}$ per total number of simulated collisions at energy E_0:

$$\mathcal{P}_{gen,h} \equiv \mathcal{P}_{gen,h}(N_h \geqslant 1) = \frac{N_{coll}(N_h \geqslant 1)}{N_{coll}} \,, \tag{5.9}$$

where generation probabilities below 10^{-4} are neglected, i.e. $\mathcal{P}_{gen,h} \equiv 0$ for $\mathcal{P}_{gen,h} < 10^{-4}$. Consequently, the probability of producing at least one high-p_T hadron is given by the number of collisions $N_{coll}(N_h \geqslant 1, p_T \geqslant 1\,\text{GeV/c})$, producing at least one hadron with $p_T \geqslant 1\,\text{GeV/c}$ and $E_h \geqslant 460\,\text{GeV}$ per simulated collisions, denoted as $\mathcal{P}^*_{gen,h} \equiv \mathcal{P}_{gen,h}(N_h \geqslant 1, p_T \geqslant 1\,\text{GeV/c})$. The latter is shown for various hadrons in Figure 5.11 for proton-nitrogen collisions simulated with CRMC, using EPOS-LHC as hadronic model. Figure 5.12 shows the corresponding high-p_T generation probabilities obtained from simulated iron-nitrogen collisions. Also shown are spline interpolations which are used to obtain the generation probability of a hadron as a function of the initial energy

E_0. Predictions from other hadronic models used in this work can be found in Appendix B.3.

The generation probabilities are calculated separately for each interaction occurring within the underlying production channel, discussed in Section 5.4.2. They are included in LSMuonSim via an event weighting, accounting for a realistic flux estimate of LS Muons, as described further below.

Propagation and Decay

For unstable hadrons included in the production chain the decay into other particles needs to be taken into account. This is only done for pions, kaons, and the hadrons of the prompt component, defined in Section 5.4.2. All protons, neutrons, and heavier nuclei are kept stable during the simulation process, since their mean lifetime is well above the order of hundreds of seconds [34]. All muons are also considered to be stable, because for the minimum energies to reach the deep ice detector, $E_{\mu,\min} = 460\,\mathrm{GeV}$, their (decay) path length is at the order of $\sim 10^7$ km.

To simulate the decay of unstable hadrons h, produced at altitude H, only the decay term of the cascade equations (Equation (2.21)) needs to be taken into account. With the decay length defined in Equation (2.18) they reduce to

$$\frac{d\Phi_h(E,X)}{dX} = -\frac{\Phi_h(E,X)}{\lambda_{\mathrm{dec},h}} = -\frac{\Phi_h(E,X)}{c\beta\gamma\tau_h\rho(H)}\,. \tag{5.10}$$

The next decay vertex of the hadron is generated, similar to before, using the CDF, as described in Appendix A.3.4. Thereby the atmosphere is approximated using a simple isothermal model, as introduced in Section 2.2.1. The energy E_h of hadrons is simulated as described in Section 5.4.4. The resulting path length $L_{\mathrm{dec},h}$ of each hadron to the next decay vertex is then generated randomly by replacing Φ with a uniformly distributed number RD between 0 and 1:

$$L_{h,\mathrm{dec}}(E_h) = -c\beta\gamma\tau_h \cdot \ln(RD) \tag{5.11}$$

The same approach is used for any hadron produced at height H that re-interacts in the atmosphere at height H_h. Neglecting the decay and regeneration terms, the cascade Equation (2.21) reduces to

$$\frac{d\Phi_h(E,X)}{dX} = -\frac{\Phi_h(E,X)}{\lambda_{\mathrm{int},h}}\,. \tag{5.12}$$

Based on the CDF, as shown in Appendix A.3.4, the traveled path length $L_{\mathrm{int},h}$ of the hadron before interacting is then given by

$$\begin{aligned} L_{\mathrm{int},h}(E_h,\theta,H) &\equiv \frac{H-H_h}{\cos(\theta)} \\ &= \frac{H}{\cos(\theta)} + \frac{h_0}{\cos(\theta)} \cdot \ln\left(e^{-H/h_0} - \frac{\lambda_{\mathrm{int},h}\cdot\ln(RD)}{X_0}\right)\,, \end{aligned} \tag{5.13}$$

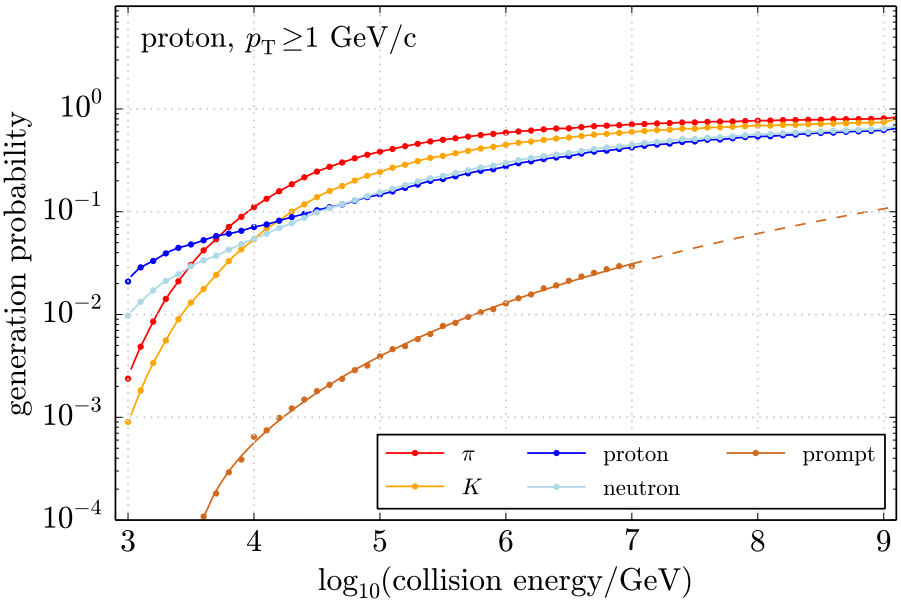

Figure 5.11: High-p_T hadron generation probabilities as a function of the energy of proton-nitrogen collisions, obtained from EPOS-LHC.

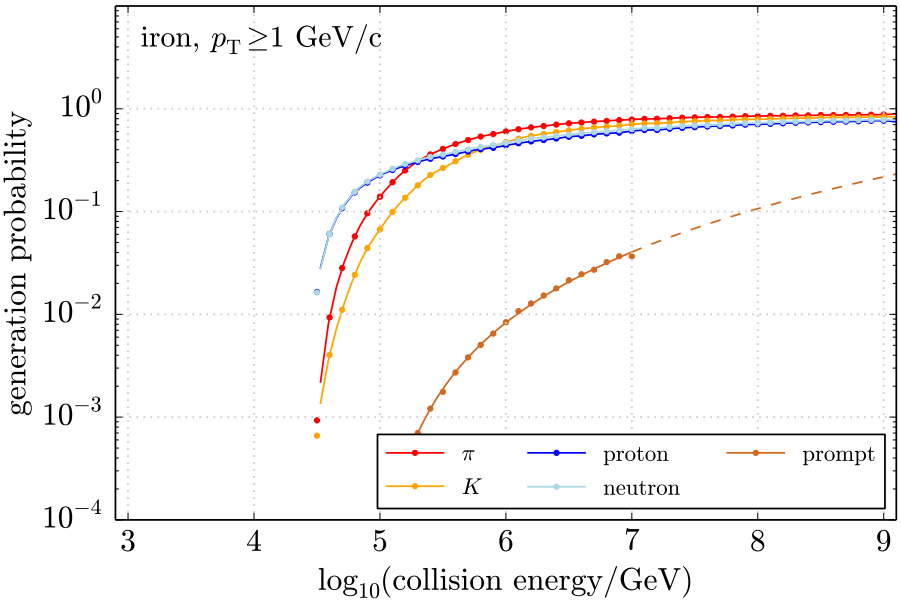

Figure 5.12: High-p_T hadron generation probabilities as a function of the energy of iron-nitrogen collisions, obtained from EPOS-LHC.

with $\lambda_{int,h}$ given in Equation (2.19) and RD is a random uniform number between 0 and 1. The cross-sections of hadrons used to calculate $\lambda_{int,h}$ are obtained from the underlying hadronic model and can be found in Appendix B.4. In order to avoid divergencies towards horizontal directions due to the $1/\cos(\theta)$ dependence, the approximation introduced in Ref. [196] is used:

$$\theta = 90^\circ \rightarrow \theta^* = 84.45^\circ \, . \tag{5.14}$$

The path lengths $L = H/\cos(\theta)$ for various interaction heights H are shown in Figure 5.13, for a flat atmosphere without any scaling (orange), including the θ-scaling from Equation (5.14) (red), and for a curved atmosphere, given by Equation (2.15) (blue). The height H_h at which a re-interaction occurs is calculated using Equation (5.13).

In order to estimate the resulting LS Muon flux, the decay and re-interaction probabilities of hadrons are calculated. This is done by deriving the interaction and decay path lengths $L_{int,h}$ and $L_{dec,h}$ for each decay and re-interaction process $N_{trial} = 10^4$ times. For each trial the resulting path lengths $L_{int,h}$ and $L_{dec,h}$ are compared to decide which of them occurs. The number of occurrences, in which the conditions

$$L_{dec,h} \leqslant L_{int,h} \quad \text{, for decay vertices} \tag{5.15}$$

$$L_{dec,h} > L_{int,h} \quad \text{, for interaction vertices} \tag{5.16}$$

are satisfied, is then counted. $N_{int/dec}$ is the number of occurrences and according to the *law of large numbers* [197], the corresponding decay or re-interaction probability of a hadron h is given by

$$\mathcal{P}_{int/dec,h} = \frac{N_{int/dec}}{N_{trial}} \, . \tag{5.17}$$

For all decays the branching fractions $BR(h \rightarrow X)$ of an hadron h, decaying into another hadron or muon, must be taken into account. This is done as shown below, with the branching fractions taken from the PDG [34].

Final Event Weighting

In order to esimate a realistic LS Muon flux, the total probability of each shower to produce at least one LS Muon is calculated. Therefore, all decay and re-interaction, as well as the hadron generation probabilities need to be considered. First the total probability to produce a LS Muon is determined for each production channel separately.

Generally, the probability $\mathcal{P}(N_A \geqslant 1)$ of an event A occurring at least once in k trials is given by [197]

$$\mathcal{P}(N_A \geqslant 1) = 1 - \mathcal{P}(\bar{A})^k = 1 - \big(1 - \mathcal{P}(A)\big)^k \, , \tag{5.18}$$

where $\mathcal{P}(A) = 1 - \mathcal{P}(\bar{A})$ is the probability of event A for a single trial and $\mathcal{P}(\bar{A})$ being its complementary probability. Using the *Poisson distribution* [198, 199]

$$Poi(k, \lambda) = \frac{\lambda^k e^{-k}}{k!} \, , \tag{5.19}$$

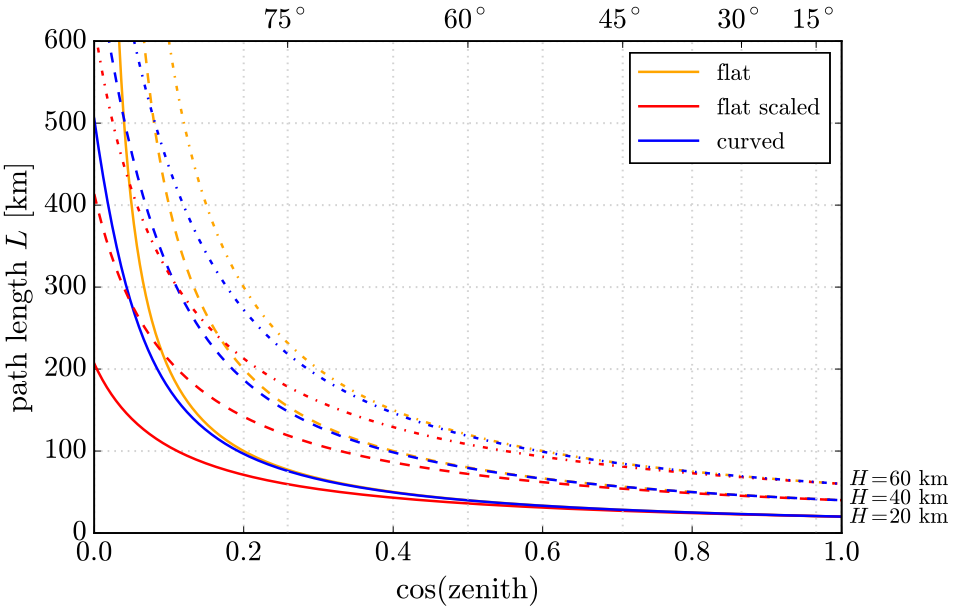

Figure 5.13: Path lengths according to different atmospheric models: simple flat atmosphere, where $L = H/\cos(\theta)$ (orange), flat atmosphere, assuming the θ-scaling from Equation (5.14) (red), used within LSMuonSim, curved atmospheric model according to Equation (2.15) (blue).

Equation (5.9) and Equation (5.18) can be re-written, as

$$\begin{aligned} \mathcal{P}_{\text{gen},h} &= 1 - \text{Poi}(0, \lambda_h) \\ \Rightarrow \lambda_h &= -\ln(1 - \mathcal{P}_{\text{gen},h}) \,, \end{aligned} \tag{5.20}$$

where λ_h is the corresponding *expectation value*, which represents the average number of generated hadrons h. In order to account for the p_T weighting, introduced in Section 5.4.3, the resulting expectation value of high-p_T hadrons h, produced in a collision with probability $\mathcal{P}^*_{\text{gen},h}$, is given by

$$\lambda^*_h = \omega_{p_T} \lambda_h \,, \tag{5.21}$$

with the event weight ω_{p_T} defined in Equation (5.6). For example for the primary LS Muon production channel, where pions are produced which decay into LS Muons, the (mean) number $\lambda^*_{\pi^\pm}$ of pions that potentially decay into a muon, each with probability $\mathcal{P}_{\text{dec},\pi^\pm} \cdot \text{BR}(\pi^\pm \to \mu^\pm + \bar{\nu}_\mu(\nu_\mu))$. Hence, according to Equation (5.18), the probability to produce at least one LS Muon from this particular channel is given by

$$\mathcal{P}_{\text{ch}}\left(N_{\mu_{\text{LS}}} \geqslant 1\right) = 1 - \left(1 - \mathcal{P}_{\text{dec},\pi^\pm} \cdot \text{BR}(\pi^\pm \to \mu^\pm + \bar{\nu}_\mu(\nu_\mu))\right)^{\lambda^*_{\pi^\pm}} . \tag{5.22}$$

Using the decay and re-interaction probabilities described above and taking the corresponding combinatorics into account, as shown for the pion case,

the probability to produce at least one LS Muon via each individual primary production channel is generally given by

$$\mathcal{P}_{ch}\left(N_{\mu_{LS}} \geqslant 1\right) = 1 - \left(1 - \mathcal{P}_{dec,h} \cdot BR(h \to \mu^{\pm} + X)\right)^{\lambda_h^*} , \tag{5.23}$$

where $h \in \{\pi^{\pm}, K, \text{prompt}\}$. For the production of LS Muons from pions, produced via kaon decays, the probability to produce at least one LS Muon is given by

$$\begin{aligned}\mathcal{P}_{ch}(N_{\mu_{LS}} \geqslant 1) = 1 - \Big(1 - \mathcal{P}_{dec,K} \cdot BR(K \to \pi^{\pm} + X) \cdot \\ \cdot \mathcal{P}_{dec,\pi^{\pm}} \cdot BR(\pi^{\pm} \to \mu^{\pm} + X)\Big)^{\lambda_K^*} ,\end{aligned} \tag{5.24}$$

These probabilities are calculated for each primary production channel separately.

Accounting for the combinatorics of two hadron generations, the probabilities to produce at least one LS Muon in the secondary I production channels is analogously calculated for each channel separately, using

$$\begin{aligned}\mathcal{P}_{ch}(N_{\mu_{LS}} \geqslant 1) = 1 - \Big(\left(1 - \mathcal{P}_{int,h_1}\right) + \mathcal{P}_{int,h_1} \cdot \\ \cdot \left(1 - \mathcal{P}_{dec,h_2} \cdot BR(h_2 \to \mu^{\pm} + X)\right)^{\lambda_{h_2}}\Big)^{\lambda_{h_1}^*} ,\end{aligned} \tag{5.25}$$

where $h_1 \in \{p, n, \pi, K\}$ and $h_2 \in \{\pi^{\pm}, K\}$. Finally, the probabilities to produce a LS Muon via secondary II production are given by

$$\begin{aligned}\mathcal{P}_{ch}(N_{\mu_{LS}} \geqslant 1) = 1 - \Big(\left(1 - \mathcal{P}_{int,h_1}\right) + \mathcal{P}_{int,h_1} \cdot \\ \cdot \left(1 - \mathcal{P}_{dec,h_2} \cdot BR(h_2 \to \mu^{\pm} + X)\right)^{\lambda_{h_2}^*}\Big)^{\lambda_{h_1}} .\end{aligned} \tag{5.26}$$

Following Equation (5.18) and accounting for all potential production channels, the total probability to produce at least one LS Muon from the underlying CORSIKA air shower is given by

$$\mathcal{P}_{tot}(N_{\mu_{LS}} \geqslant 1) = 1 - \prod_{ch}^{k} \left(1 - \mathcal{P}_{ch}(N_{\mu_{LS}} \geqslant 1)\right) , \tag{5.27}$$

where the product runs over all k channels with $\mathcal{P}_{ch}(N_{\mu_{LS}} \geqslant 1) > 0$. All LS Muons from each of these production channels are explicitly generated within LSMuonSim, therefore the underlying CORSIKA shower is re-used k times in order to produce one individual LS Muon for each of the k air showers.

Since the probabilities $\mathcal{P}_{ch}(N_{\mu_{LS}} \geqslant 1)$ do not exclude each other, each of the k generated events needs to be weighted accordingly to describe a realistic LS Muon flux. This is done by weighting each of the k showers to the corresponding fractional probability of each production channel using

$$\omega_{LS,ch} = \omega_0 \cdot \mathcal{P}_{tot}(N_{\mu_{LS}} \geqslant 1) \cdot \frac{\mathcal{P}_{ch}(N_{\mu_{LS}} \geqslant 1)}{\sum_{ch}^{k} \mathcal{P}_{ch}(N_{\mu_{LS}} \geqslant 1)} , \tag{5.28}$$

where ω_0 is the primary weight for the underlying CORSIKA shower, as introduced in Equation (5.2). By forcing every shower to produce a LS MUON and then re-using each shower for each individual channel, the statistics of LS MUON events from the underlying CORSIKA dataset are significantly enhanced.

These dedicated LS MUON events ($d_T \geqslant 100\,\text{m}$) are then combined with the background contributions from single ($d_T < 100\,\text{m}$) and multiple showers, obtained from CORSIKA, as well as atmospheric neutrino events generated using NUGEN. The total LSMUONSIM flux, generally shown as (red) solid lines throughout this work, is given analogously to Equation (5.1) by

$$\Phi_{\text{total}}^{\text{LSMuonSim}} = \Phi_{\text{LS}}^{\text{LSMuonSim}} + \Phi_{\text{single}}^{\text{CORSIKA}} + \Phi_{\text{multiple}}^{\text{CORSIKA}} + \Phi_{\nu}^{\text{NuGen}} \,, \tag{5.29}$$

where the neutrino simulations are obtained from the neutrino event generator NUGEN, as described in Section 5.6.

5.5 MONTE CARLO DISTRIBUTIONS

The simulated primary energy spectrum of all cosmic ray air showers at surface level is shown in Figure 5.14, obtained from CORSIKA (orange) and using LSMUONSIM (red). The primary flux assumption is based on the H3A [38] parametrization, as described in Section 2.1.4. Here, and in the following, the MC rate corresponds to the integrated event rate within a targeted cylinder volume of height 1200 m and with radius 600 m, as described in Section 5.7. The contributions from events containing a laterally separated muon with $d_T \geqslant 100\,\text{m}$ are shown separately (dashed, denoted as *sig*). As described in Section 5.1 and Section 5.4 the CORSIKA simulations are generated using SIBYLL 2.1 as hadronic model, while LSMUONSIM uses EPOS-LHC as default model to generate the LS MUON.

The contributions from different zenith angle regions are also shown (dash-dotted, dotted). While LSMUONSIM shows a strong suppression of LS MUON events towards low energies, the agreement between CORSIKA and LSMUONSIM predictions improves at intermediate zenith angle directions. In contrast, for very vertical events ($\theta < 30°$) CORSIKA shows a strong suppresion of LS MUON events compared to LSMUONSIM over all energies. This is related to the zenith angle distributions, shown in Figure 5.15, where the increase of the LS MUON rate towards horizontal directions significantly differs between CORSIKA and LSMUONSIM predictions. Similar effects can be observed for the interaction height of the corresponding showers, which is highly correlated to the zenith angle distribution.

Figure 5.16 shows the zenith angle distributions of LS MUON events ($d_T \geqslant 100\,\text{m}$), obtained from CORSIKA (left) and LSMUONSIM (right). The individual contributions from showers initiated at various atmospheric heights are shown separately as dashed lines. As expected from Equation (2.36), the simulated zenith angle distributions of LS MUONS depend on the altitude of the underlying primary interaction. Figure 5.17 shows the simulated altitudes of the primary interaction producing a LS MUON event, for different zenith angle regions. The

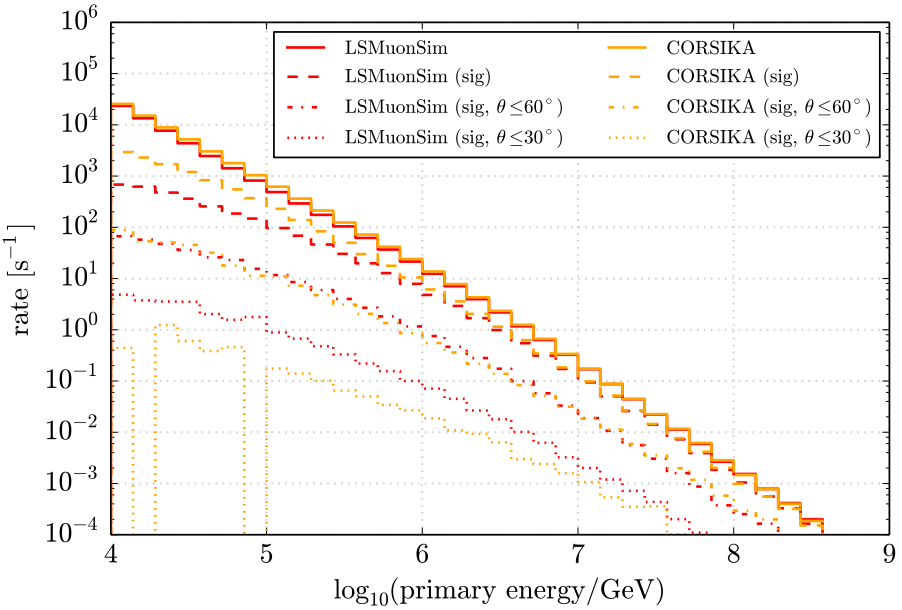

Figure 5.14: Simulated (true) primary energy spectrum at surface level, obtained from CORSIKA (SIBYLL 2.1) and LSMUONSIM (EPOS-LHC), assuming the H3A primary flux parametrization. The contributions from LS MUON events ($d_T \geqslant 100$ m) and from different zenith angle regions are also shown.

corresponding interaction height distributions of all simulated events (no constraint on lateral separation), as well as further distributions of the zenith angle direction of simulated air showers at surface level, can be found in Appendix C.2 and Appendix C.10. Although it is expected that LSMUONSIM underestimates the event rate for very horizontal events ($\theta > 60°$), the zenith angle differences compared to CORSIKA are not yet understood in detail.

The observation of significant zenith angle discrepancies between CORSIKA simulations and experimental data was previously observed for the analysis of laterally separated muons in ICECUBE in its 59-string configuration [83]. Moreover, analyses of high-energy atmospheric muons in ICECUBE reported similar effects [52, 54]. Although the discrepancies observed are smaller compared to laterally separated muons, these analyses have observed significant data/MC discrepancies related to the zenith angle distribution of atmospheric muon events in ICECUBE.

The subsequent propagation through the ice is highly zenith dependent and has significant effects on the distributions observed in the in-ice detector. Due to the large distances traveled through the ice close to horizontal directions, the muon rate is highly suppressed towards large zenith angles. In addition, this analysis uses a high-energy filtering (see Section 6.1), which predominantly selects events with primary energies above $\sim$ 100 TeV, where the agreement between simulations improves. Hence, the agreement between CORSIKA and LSMUONSIM improves significantly at detector level, although a disagreement

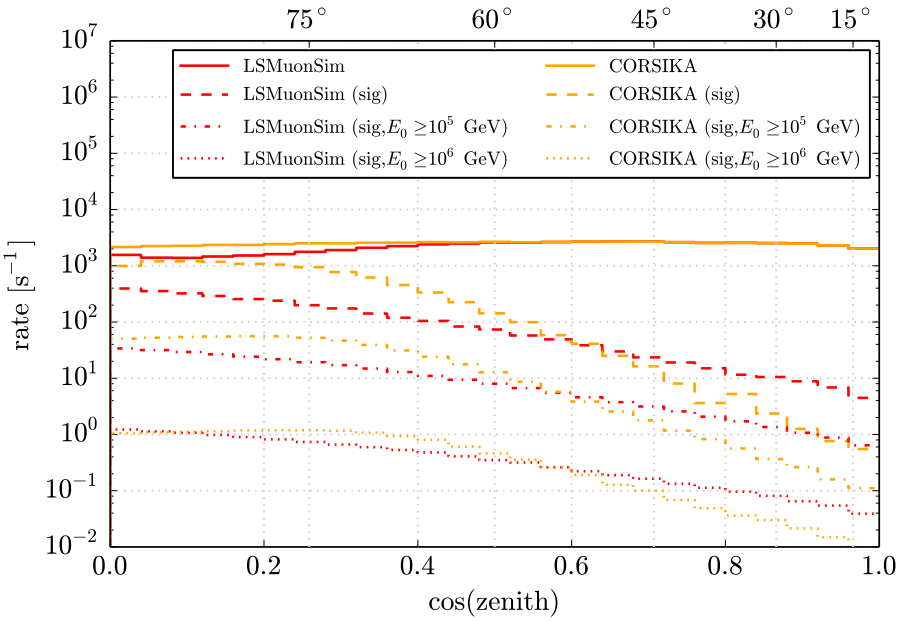

Figure 5.15: Simulated (true) zenith angle distribution at surface level, obtained from CORSIKA (SIBYLL 2.1) and LSMUONSIM (EPOS-LHC). The contributions from LS MUON events ($d_T \geqslant 100\,m$) and from different primary energies are also shown.

of MC is permanently present throughout this analysis. The zenith angle discrepancies are the main focus of discussions in Section 6.9 and Section 7.3.

The transverse momentum of simulated LS MUON events, obtained using LSMUONSIM, is shown in Figure 5.18 for different zenith angle regions. The mean transverse momentum $\langle p_T \rangle$ of these distributions increases with decreasing zenith angle. The more horizontal the initial direction of an air shower, the longer the time for the LS MUON to separate from the shower core. Thus, for horizontal showers a large p_T is necessary in order to produce a large separation from the core. In addition, $\langle p_T \rangle$ increases with increasing primary energy, as expected from PQCD. The potential contribution from events with lower transverse momenta ($p_T < 1\,GeV/c$) for LS MUON events in ICECUBE is part of the discussion in Section 7.4.

Figure 5.19 shows the individual contributions from each LS MUON production channel, described in Section 5.4.2. The dominating production channel is the primary production, contributing with approximately 93% to the total LS MUON flux predicted by LSMUONSIM. The secondary channels are rather suppressed and contribute roughly 5% (I) and 2% (II) to the total LS MUON flux. In addition, any further re-interaction further reduces the hadron energy. Hence, the production of laterally separated muons later during shower development is expected to be highly suppressed and is therefore not included in LSMUONSIM. Since the transverse momentum of the LS MUONS mainly originate from hadrons mainly produced in the first interaction, laterally separated muons are a direct probe of the primary cosmic ray interaction. The percentiles of LS MUONS origi-

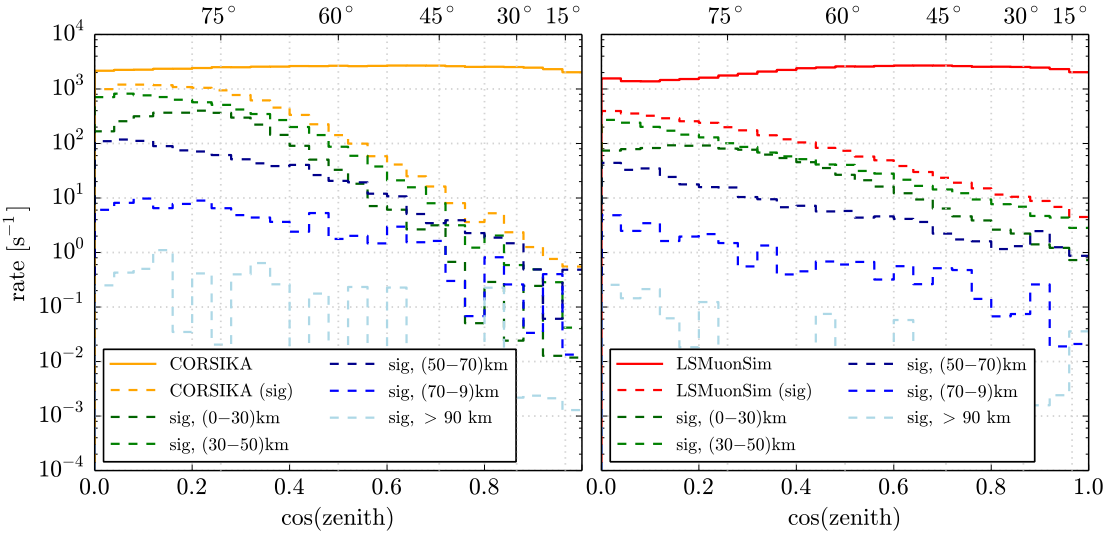

Figure 5.16: Simulated zenith angle distributions at surface level, obtained from CORSIKA (left) and LSMUONSIM (right). The dashed lines show the contribution of LS MUON events ($d_T \geqslant 100\,m$) for various primary interaction height regions.

nating from pion and kaon decays within LSMUONSIM are 96% and 4%, while the decay of prompt hadrons contributes with less than $6 \cdot 10^{-5}$ to the total LS MUON flux.

The lateral separation distributions of LS MUONS at surface level, obtained from CORSIKA and LSMUONSIM, are shown in Figure 5.20. As discussed above, LSMUONSIM predicts a smaller total rate of LS MUONS compared to CORSIKA. However, the agreement increases towards vertical directions, which is the dominating region for events measured in ICECUBE. Further MC distributions at surface level, such as LS MUON energy spectra and interaction height distributions, can be found in Appendix C. Studies on different hadronic models in the context of LSMUONSIM are discussed in detail in Section 7.7.

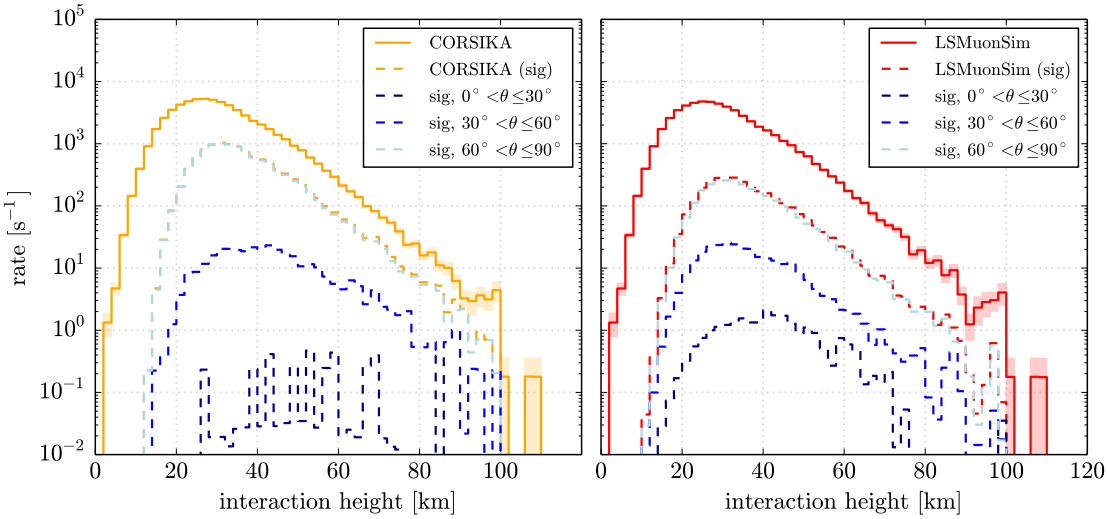

Figure 5.17: Simulated primary interaction height distributions at surface level, obtained from CORSIKA (left) and LSMUONSIM (right). The dashed lines show the contribution of LS MUON events ($d_T \geqslant 100\,m$) for various zenith angle regions.

5.6 NEUTRINO SIMULATIONS

Although the flux of atmospheric neutrinos is highly suppressed compared to the flux of cosmic ray air showers [29, 141], to estimate the small background contribution from neutrino events in this analysis, dedicated neutrino simulations are used. To simulate atmospheric neutrino events, the neutrino generator NUGEN is used, which is part of the ICETRAY software [200]. The physics implementation of this code is based on the ANIS neutrino generator [201]. It generates an equal number of neutrinos and anti-neutrinos and handles the propagation of the neutrino inside the Earth, as well as neutrino-nucleon interactions close to and inside the detector volume. NUGEN includes all three flavors of neutrinos (ν_e, ν_μ, ν_τ), which are generated with a ratio of $1:1:1$. In order to reduce the computational effort, NUGEN forces the neutrino to interact close to the detector volume. Hence, each event needs to be re-weighted in order to reflect a realistic neutrino flux. The probability for a neutrino to interact is calculated using the CTEQ5 neutrino-nucleon cross sections [202], and incorporated via event weighting, similar to the weighting procedures described in Section 5.3 and Section 5.4.5. In order to calculate the propagation of neutrinos inside the Earth, the *preliminary reference Earth model* (PREM) is used [203].

Analogous to the air shower simulations discussed above, neutrino events are generated from a harder energy spectrum (E^{-2}) to increase the event statistics at high energies. Thus, each event is re-weighted, as described in Section 5.3, where the atmospheric neutrino flux is parametrized using the Honda parametrization from Ref. [192], assuming a H3A primary cosmic ray flux [38]. Thereby, only the conventional ν_e/ν_μ flux is accounted for, while neutrinos originating from prompt hadron decay, as well as a potential ν_τ flux, are neglected. However, the

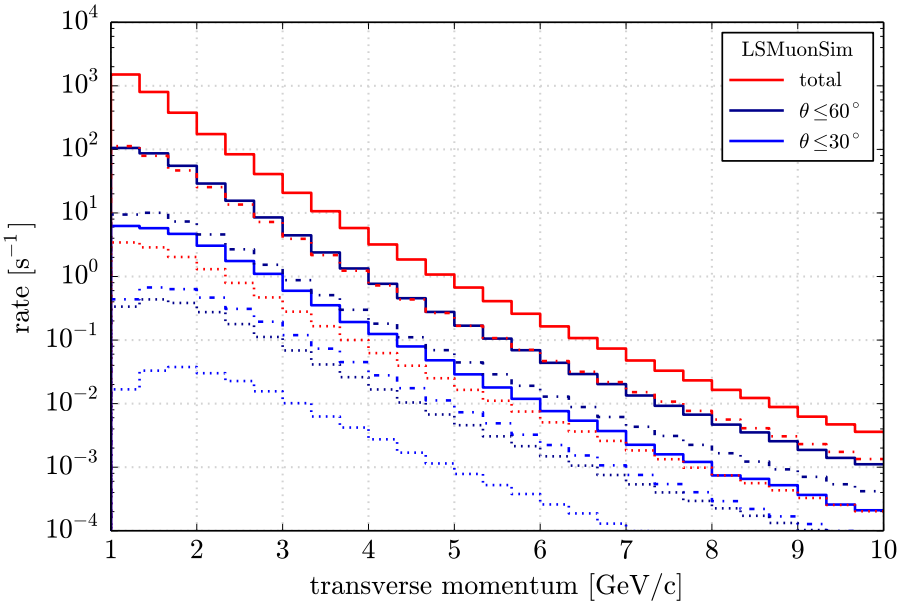

Figure 5.18: Simulated (true) transverse momentum distributions of LS MUONS at surface level, obtained from LSMUONSIM (EPOS-LHC), for different zenith angle regions. Additionally shown are the corresponding contributions from events with primary energies $E_0 \geqslant 1$ PeV (dashed-dotted) and $E_0 \geqslant 10$ PeV (dotted).

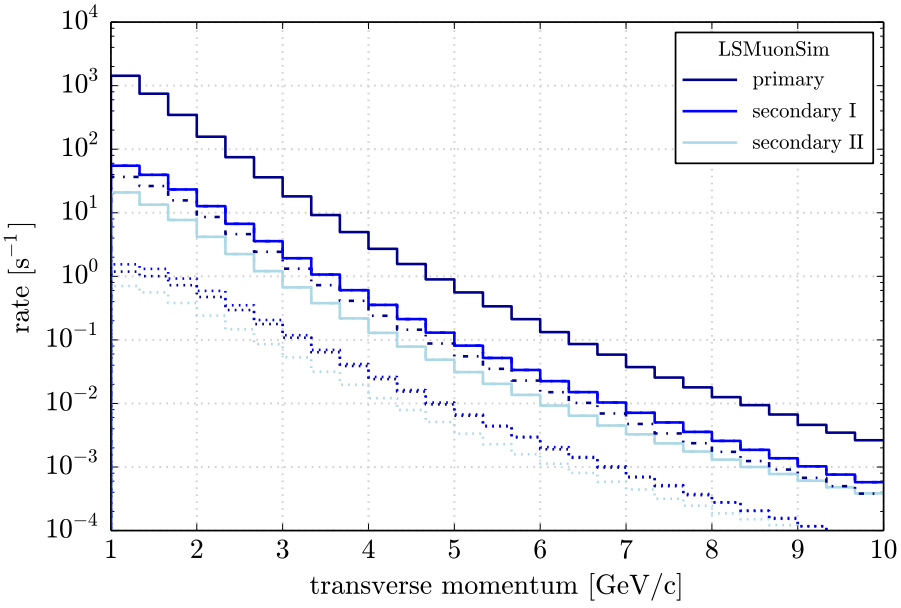

Figure 5.19: Individual contributions to the p_T distribution at surface level from the LS MUON production channels included in LSMUONSIM (EPOS-LHC), as described in Section 5.4.2. The corresponding contributions from events with primary energies $E_0 \geqslant 1$ PeV (dashed-dotted) and $E_0 \geqslant 10$ PeV (dotted) are shown separately.

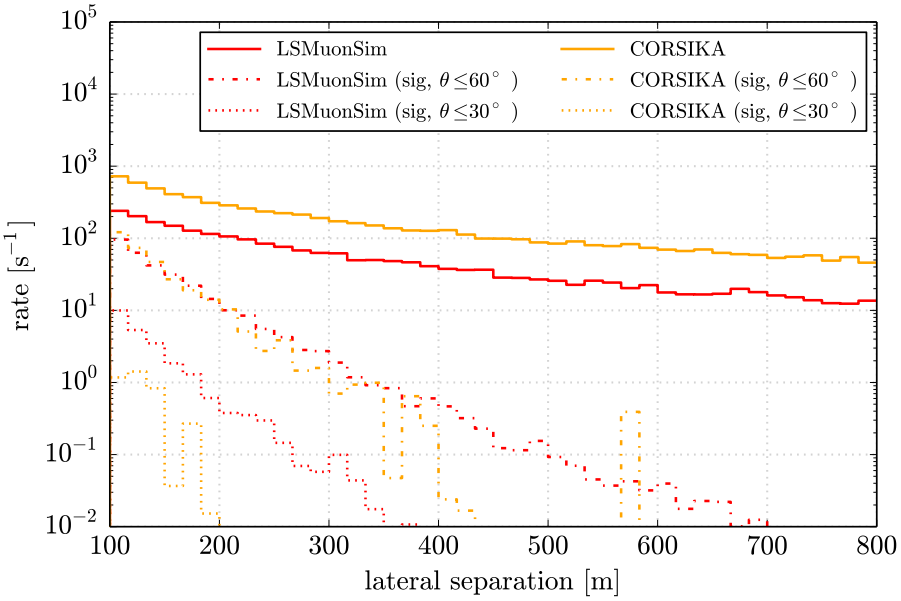

Figure 5.20: Simulated (true) lateral separation distribution at surface level. The total LS Muon fluxes (solid) obtained from CORSIKA and LSMuonSim, as well as the corresponding contributions from showers with zenith angle directions $\theta \leqslant 60^\circ$ (dashed-dotted) and $\theta \leqslant 30^\circ$ (dotted) are also shown.

prompt neutrino flux, and especially the flux of tau-neutrinos are both expected to be highly suppressed [50]. They are therefore not considered in this work.

The contribution from neutrino events is always included in the total CORSIKA and LSMuonSim distributions shown throughout this work, as defined in Equation (5.1) and Equation (5.29), even if not explicitly denoted. The contribution from neutrino events on higher analysis levels is highly suppressed (see Section 6.5), therefore the neutrino contribution will not be shown separately at higher analysis levels, although it is included in the total distributions shown.

5.7 IN-ICE PROPAGATION AND DETECTOR RESPONSE

In CORSIKA, and subsequently also in LSMuonSim, showers are generated with an axis which passes a fixed point on observation level. IceCube can be approximated with a cylindrical detector volume, therefore the target volume for the simulations is an upright cylinder centered on the IceCube in-ice detector volume, as indicated in Figure 5.21. In order to cover a volume extending the detector by a few 100 m, the target cylinder is chosen to have a height of $h = 1200\,\text{m}$ and radius $r = 600\,\text{m}$. All simulated showers are distributed uniformly in the *generation area* of the target volume, projected along the shower axis.

For the neutrino simulations generated with NuGen, the sampling area is a disk with radius $r = 600\,\text{m}$, perpendicular to the neutrino direction, and centered

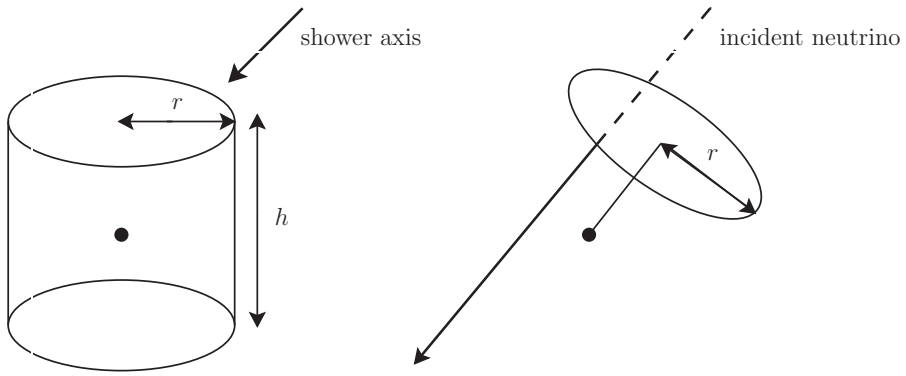

Figure 5.21: MC event generation areas as described in the text, for air shower (left) and neutrino simulations (right). The centered dot indicates the detector center.

on the detector volume. The neutrino events are then uniformly distributed over this generation area.

The propagation of particles through the ice is simulated using the PROPOSAL code [108], as integrated part of the IceTray software framework [200]. It handles all relevant energy losses of particles, as described in Section 3.1, and consideres deflections due to multiple scattering in the ice using a gaussian approximation (see Section 3.1.3). The Cherenkov light emission of charged particles, discussed in Section 3.1.4, and the subsequent photon propagation in the ice are simulated using the *photon propagation code* (PPC) [204], which handles the direct propagation of single photons. PPC includes the scattering and absorption of photons in the ice, based on the ice model discussed in Section 4.1.1.

In order to account for uncorrelated thermal noise in the detector, a constant Poissonian background (Equation (5.19)) of noise hits is added. In addition, a non-thermal noise component due to particle decays and scintillation/fluorecence in the surrounding medium and the detector components is simulated. Therefore, for each decay a second Poisson distribution is used to determine the number of generated non-thermal noise hits. The PMT response and the DOM readout electronics, as well as the subsequent triggering and filtering, are simulated using standard IceCube software implemented in IceTray, as described in Ref. [200]. Figure 5.22 shows the event display of a simulated LS Muon event in IceCube after simulating the in-ice propagation and detector response. Colored spheres represent hits in the detector and their size indicates the amount of observed light, with time-ordering from red to blue. The red lines indicate the simulated muon track and the true shower core direction.

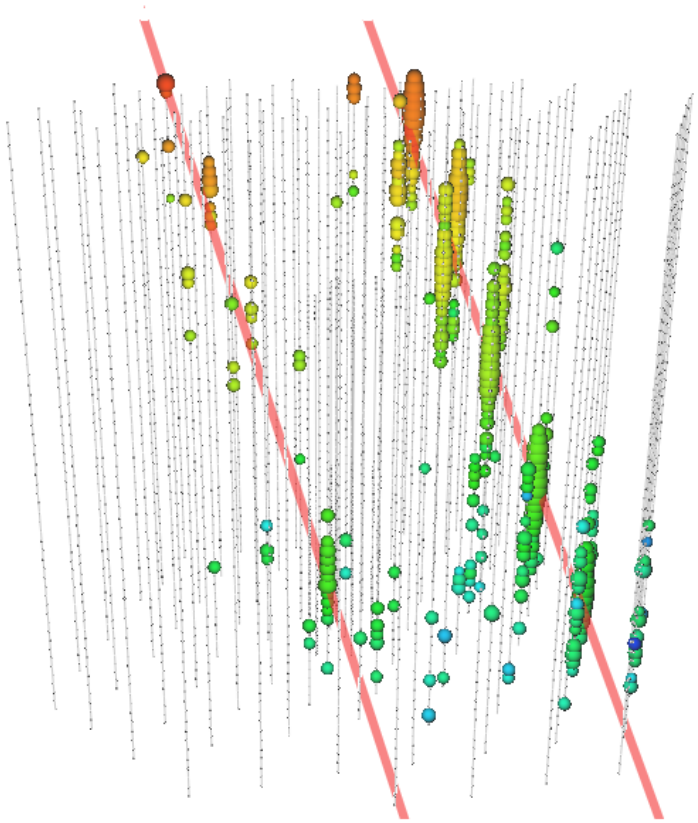

Figure 5.22: Simulated LS MUON event (LSMUONSIM) in ICECUBE after in-ice propagation and detector response (no noise hits included). The colored spheres represent the hits in the detector where their size indicates the amount of observed light with time-ordering from red to blue. Red lines indicate the true LS MUON track (left) and the true core direction of the muon bundle (right).

6 DATA SELECTION AND RECONSTRUCTIONS

"It is a capital mistake to theorize before one has data."

– Sherlock Holmes *

This analysis uses data taken by the IceCube Neutrino Observatory between May 2012 and May 2015. The data selection is performed as a *blind analysis*, where only 10% of the data, the *burnsample*, is used to develop the selection criteria described in the following. This is done in order to avoid biases during data selection. Therefore, Monte Carlo simulations are used to study the signal and background distributions separately and to develop criteria, selecting LS Muon events from IceCube data. The simulations and selection criteria are tested and verified against the burnsample. The latter is not included in the final *unblinded* data sample, which is presented in Chapter 7. The burnsample used in this analysis includes 102 days of data taken by IceCube during the given time period. The event reconstructions and subsequent selection criteria are based on the concepts used in the previous analysis of LS Muon events in IceCube in its 59-string configuration, as reported in Ref. [83].

After a basic pre-filtering of the data, which is described in Section 6.1 and Section 6.2, the general analysis concept is based on the unique double-track topology of LS Muon events in IceCube. Hence, the reconstruction of those tracks plays a crucial role for a precise measurement of the lateral separation of muons and their arrival direction. In Section 6.3 a dedicated method to reconstruct double-track events in IceCube is described, with a discussion on the resulting reconstruction accuracies given later in Section 6.6. The subsequent selection criteria to isolate LS Muon events in IceCube are introduced in Section 6.4, with the resulting event rates for all filter levels is discussed in Section 6.5. In Section 6.7 and Section 6.8 methods are described to estimate the underlying primary energy and the transverse momentum of LS Muons produced in air showers. This enables primary energy-dependent studies of the lateral separation of muons produced in air showers and an estimation of the underlying p_T distributions of their parent particles. Finally, the corresponding effective areas are derived in Section 6.9, which are neccessary to get an estimate of the resulting LS Muon distributions at surface level.

6.1 PRE-FILTERING

The trigger rate of IceCube's in-ice detector array is around 2.5 kHz. In order to reduce the event rate of the recorded data by selecting classes of events of

* In *"A Study in Scarlet"* by A. C. Doyle (1887).

interest and to enable further computing intensive reconstructions, pre-selection criteria are applied. Therefore, a general online-filter processing is performed, using common selection criteria, such as the number of recorded hits in a certain time window, or specific event characteristics derived using basic reconstructions [200]. Due to inhomogeneous charge distributions in the detector volume, all DeepCore hits are removed from events used in this analysis. This is done in order to avoid biases caused by the detector geometry in further event splitting algorithms (see Section 6.3).

In addition, a subsequent *hit cleaning* is applied to each event in order to reduce noise hits. The *seeded-RT cleaning* is used, where all HLC hits are kept. This cleaning algorithm also keeps SLC hits if they have an HLC hit within a radius $R = 150\,\text{m}$ and within a time interval ΔT_1, such that their pulses overlap within a time interval of $\Delta T_1 = 1000\,\text{ns}$. Afterwards, an additional *time-window cleaning* is applied where only hits within the time interval $\Delta T_2 = 6000\,\text{ns}$, containing the most hits, are kept. Finally, the *(extremely) high-energy filter* (EHE filter) is applied on the remaining hits, such that only events with more than 1000 photoelectrons (PE) are kept. The resulting event rate after pre-filtering is below 1 Hz, which enables the performance of more sophisticated subsequent reconstructions. The resulting data sample is the starting point for this analysis, in the following the filter level after pre-filtering is referred to as *level-0* (Lo).

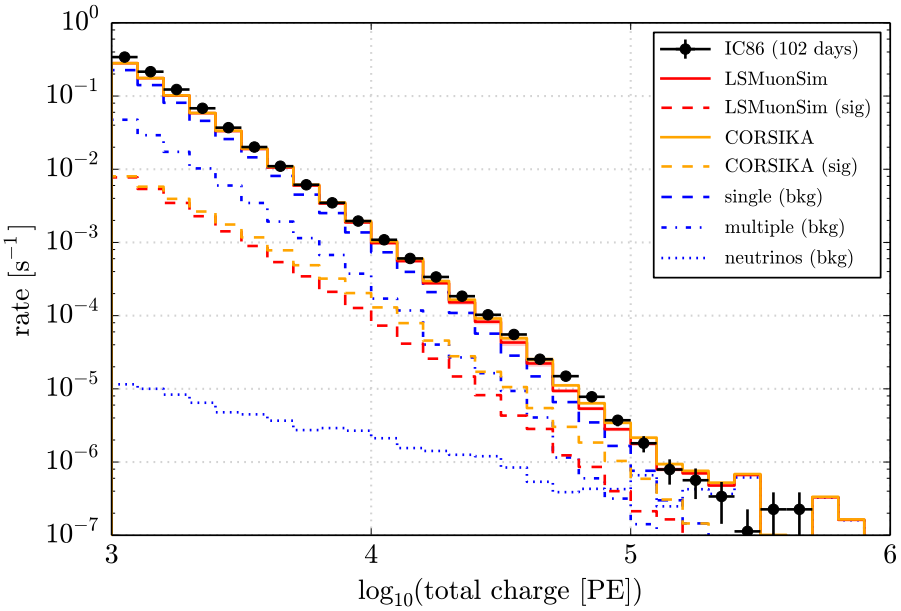

Figure 6.1: Total charge distribution in number of photoelectrons (PE) of burnsample events passing the pre-filtering criteria described in the text. MC distributions, obtained from CORSIKA (SIBYLL 2.1) and LSMUONSIM (EPOS-LHC), are also shown. The signal contributions and the individual background contributions, obtained from MC, are shown separately. Error bars represent the statistical uncertainties and are only shown for the total distributions (solid lines).

Figure 6.1 shows the charge distribution of burnsample events passing the pre-filtering criteria. The corresponding distributions of simulated events, obtained from CORSIKA (SIBYLL 2.1) and LSMUONSIM (EPOS-LHC), are also shown. The contributions from single showers without a muon with lateral separation above 100 m (*single*), and of showers containing at least one muon with a separation of more than 100 m from the shower core, are shown separately. The contribution from multiple air showers, recorded in the same time window (*multiple*), is also shown. In addition, the simulated distributions also include the minor contribution from neutrino events, obtained from NUGEN simulations. The total distributions (solid lines) represent the sum of these individual components, using the LS MUON flux predictions from CORSIKA and LSMUONSIM. The error bars (data) and bands (MC), shown in Figure 6.1 and throughout this work, represent the statistical uncertainties and are only shown for the total distributions (solid lines). The simulated charge distributions agree very well with the distributions obtained from experimental data. Further distributions of the total charge distributions at all filter levels of this work, can be found in Appendix C.3.

6.2 BASIC EVENT RECONSTRUCTIONS

After level-0 pre-filtering, basic track reconstructions are applied to all remaining events, which are then used as a starting point (*seed*) for further, more sophisticated reconstructions. Each event is reconstructed using a simple fit algorithm, based on two steps. First, a simple *line fit* is applied, assuming the photon arrival times at the DOMs are caused by Cherenkov photons emitted as plane waves, with velocity $\vec{v}$ along a 1-dimensional path in the detector [205]. The locations $\vec{x}_i$ of all hit DOMs at a time t_i are approximated by a line

$$\vec{x}_i \simeq \vec{x}_0 + \vec{v} \cdot (t_i - t_0) \tag{6.1}$$

and a χ^2-fit is applied by minimizing

$$\chi^2 \equiv \sum_{i=1}^{N_{hit}} \|\vec{x}_i - \vec{x}_0 - \vec{v} \cdot (t_i - t_0)\|^2 \,, \tag{6.2}$$

where N_{hit} is the number of hits, and $\vec{x}_0, \vec{v}, t_0$ are free parameters. χ^2 is minimized analytically.

This approach is further improved by applying a simple hit cleaning, similar to the seeded-RT cleaning discussed above: If there exists an HLC hit h_1 within a distance $R = 156\,m$ around another hit h_2, with h_1 recorded $\Delta T \geqslant 778\,ns$ earlier than h_2, then h_2 is considered as scattered hit and discarded from the fit [206]. In addition, the χ^2-fit in Equation (6.2) is replaced by a *Huber fit* [207], which is more robust against outliers due to scattered photons. Therefore, a so-called *Huber penalty function* is introduced, with its parameters based on simulated muon tracks, as described in Ref. [206]. This approach results in a

median angular accuracy of 4.2° for single muon tracks and is used throughout this work as initial seed reconstruction (*improved line fit*).

In a second step, the event is reconstructed using a more sophisticated *log-likelihood fit* (LLH), seeded with the improved line fit. Generally, the *likelihood* $\mathcal{L}$ for an underlying hypothesis with a probability density function $\mathcal{P}(x_i, a)$, is given by [205]

$$\mathcal{L}(x, a) = \prod_i \mathcal{P}(x_i, a) \,, \tag{6.3}$$

where $x_i \in \{x_1, \ldots, x_n\}$ are the experimentally measured values and $a = \{a_1, \ldots, a_k\}$ is a given set of parameters. The parameters a for an underlying probability density $\mathcal{P}$ can be estimated by finding the corresponding values that maximize the likelihood from Equation (6.3) for the measured values x_i (*maximum likelihood estimation*). When finding the maximum of the likelihood, the derivative needs to be calculated. Since this is often easier for the (negative) logarithm of the LLH function, in practice the negative *log-likelihood function*, $-\ln(\mathcal{L})$, is minimized (see for example Ref. [167]).

The likelihood fits used in this work are based on multi-photoelectron (MPE) arrival time information, with a corresponding MPE probability density function, taking the conical Cherenkov light emission into account. Thereby all photoelectrons recorded by a DOM are accounted for. This is done using a (analytical) *Pandel parametrization*, as described in Ref. [205]. In addition, the likelihood function is extended by including external information via *Bayes' Theorem* (*Bayesian likelihood*) [206, 208, 209]. In order to minimize $-\ln(\mathcal{L})$, a numerical *simplex algorithm* is used [167].

An example of the resulting first-guess particle track reconstruction is shown in Figure 6.3 (a), for a typical (simulated) LS MUON event. As a measure of the success of the fit, the *reduced* log-likelihood value (rlogl) is often used. It corresponds to the best obtained likelihood value, divided by the number of degrees of freedom. The resulting distribution of events passing level-0 is shown in Figure 6.2. In order to reduce the background contributions (blue lines), only events with a reduced log-likelihood of $6 \leqslant \text{rlogl} \leqslant 10$ are kept, in the following denoted as *level-1* (L1). Although there is no significant separation power, this selection removes clearly mis-reconstructed background events from the data sample without any additional computational effort. This improves the initial seeds for further reconstructions, as described in the following. Additional distributions of the reduced log likelihood of events at all filter levels can be found in Appendix C.6.

6.3 DOUBLE-TRACK RECONSTRUCTION

After performing the basic track reconstruction and subsequent level-1 filtering, a dedicated double-track reconstruction is applied to all remaining events. This reconstruction is based on hit splitting methods optimized for the underlying double-track event signature. It relies on a topological two-step hit splitting,

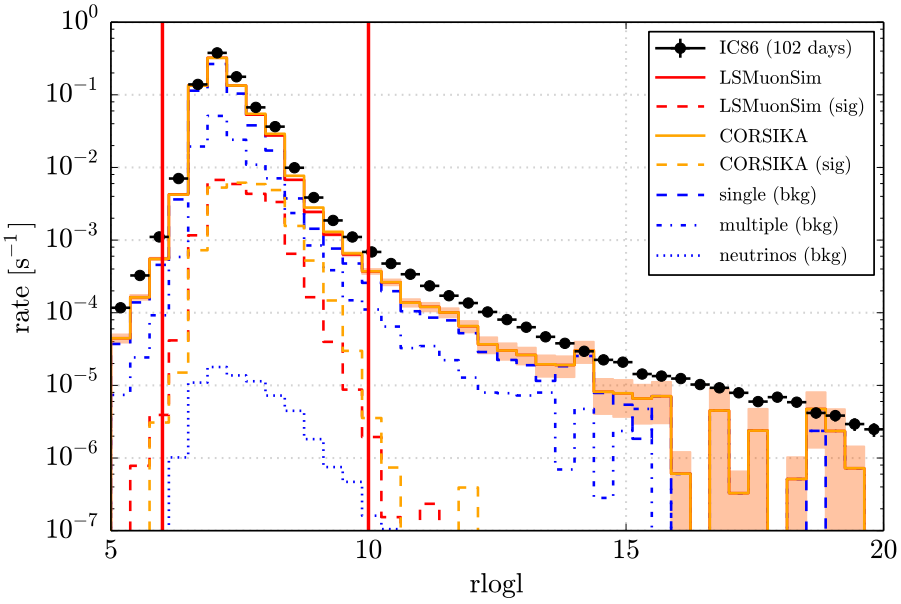

Figure 6.2: Reduced likelihood value, rlogl, of data and MC events passing the pre-filtering criteria (level-0). The contributions from signal events ($d_{T,true} \geqslant 100\,m$) and background contributions are shown separately. The vertical red lines indicate the level-1 selection criteria (see text for details). Statistical uncertainties are represented by the error bars/bands (total distributions only).

to separate the LS Muon hits from hits produced by the bulk of muons in the core bundle. Based on these split hit series, the LS Muon and the muon bundle can be reconstructed separately using maximum log-likelihood methods, as introduced above. In the following, the individual steps are described which are performed during the double-track reconstruction.

k-means Splitting

To decide which hits belong to the muon bundle and which belong to the LS Muon track, as a first step, a *k-means clustering* algorithm is applied, also referred to as *vector quantization* [210]. Generally the algorithm puts n data points into k clusters, which can be done in any D-dimensional space.

Each cluster is parametrized by a vector $\vec{m}_k$, which is called the *mean*. The k-means algorithm is initialized with randomized means $\vec{m}_k$. After the initialization step, it is an iterative algorithm, based on two steps:

- **Assignment step:**
  In the *assignment step*, each data points is assigned to the nearest mean.

This is done by expressing this assignment in terms of *responsibilities* $r_k^{(n)}$, such that

$$r_k^{(n)} = \begin{cases} 1 \text{ , if } \hat{k}^{(n)} = k \\ 0 \text{ , if } \hat{k}^{(n)} \neq k \text{ ,} \end{cases} \tag{6.4}$$

where $\hat{k}^{(n)}$ is the previous guess for the cluster $k^{(n)}$ to which the data point $\vec{x}^{(n)}$ belongs [210].

- **Update step:**
  During the *update step*, the means are adjusted in order to match the means $\vec{m}_k$ of the data points they are responsible for, where

$$\vec{m}_k = \frac{\sum_n r_k^{(n)} \vec{x}^{(n)}}{\sum_n r_k^{(n)}} \text{ .} \tag{6.5}$$

  This is basically done by minimizing the distances $d(\vec{m}_k, \vec{x}^{(n)}) = \|\vec{m}_k - \vec{x}^{(n)}\|$ (see Ref. [210] for details).

These steps are repeated until the assignments do not change anymore. The k-means algorithm always converges and can therefore be applied to a large variety of clustering problems.

In this analysis, it is applied to all events that pass the level-1 pre-filtering. This is done by projecting all hits onto a plane orthogonal to the first-guess track reconstruction. The k-means clustering is then applied in $D = 2$ dimensions for $k = 2$ expected cluster. This step is shown in Figure 6.3, where a typical simulated event, obtained from LSMuonSim, is shown in (a), with the first-guess track represented by the red line. The corresponding view from the perspective of the first-guess track direction is shown in (b). Figure 6.3 (c.1) and (c.2) show the split hit series after applying the k-means clustering algorithm from a side-view, as well as seen from the first guess direction (small panels).

Time Residual Splitting

Although the k-means clustering can separate hits from LS Muons with large separations from the bundle core very well (above a few 100 m), for most of the events the separation between the muon bundle and LS Muon is not necessarily obvious (see Figure 6.3). Hence, many times the hit series assigned to the LS Muon, obtained from the k-means clustering, still contains a large amount of hits originating from the muon bundle. In order to reduce the number of mis-assigned bundle hits from the LS Muon hit series, an additional *time residual splitting* is applied.

The *time residual* of a hit is given by the difference between the measured photon arrival time and the expected arrival time corresponding to straight-line propagation. In order to calculate the time residuals of hits, the hit series assigned to the muon bundle after k-means splitting is reconstructed with a

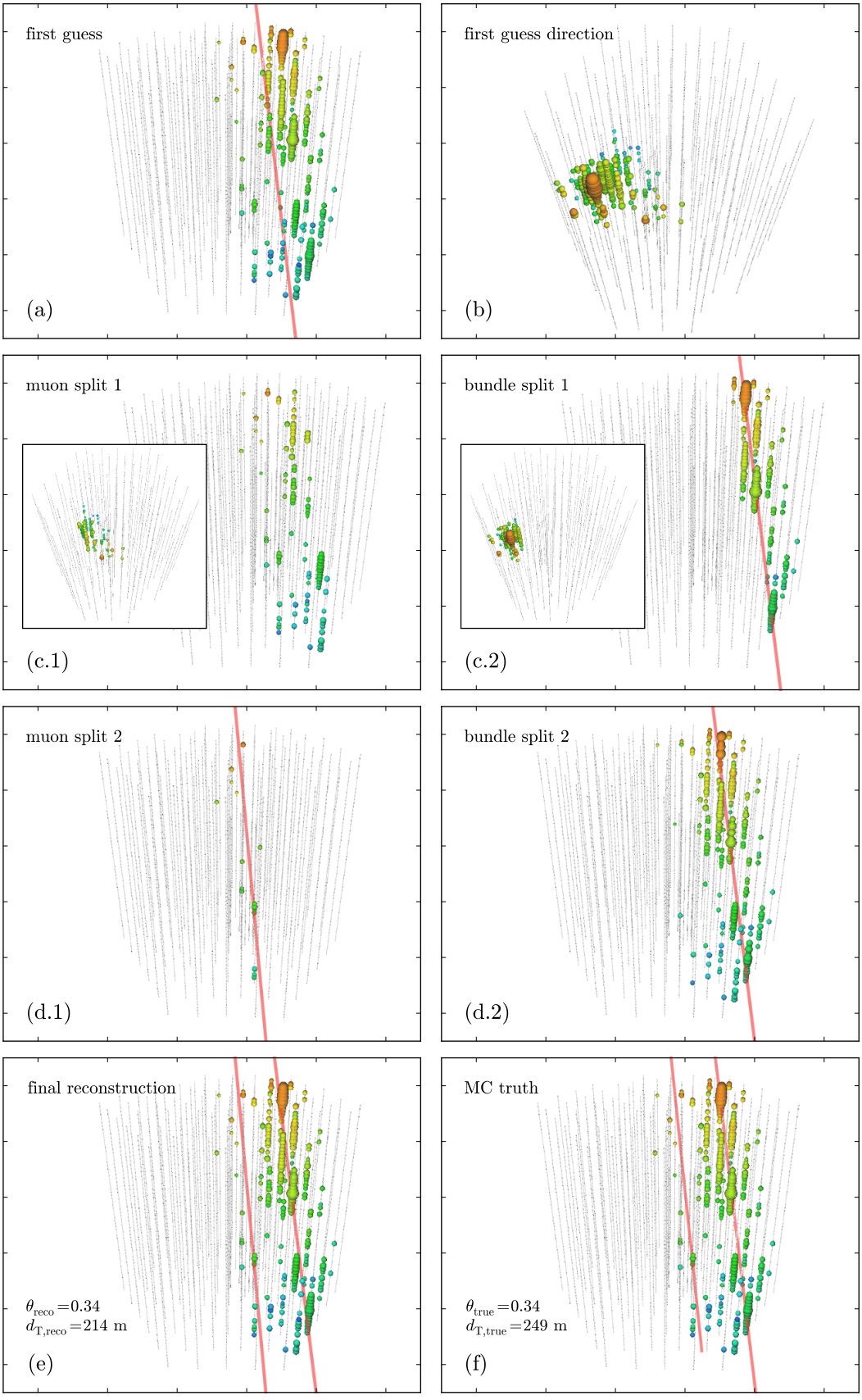

Figure 6.3: Simulated LS MUON event in ICECUBE, showing the different double-track reconstruction steps, as explained in the text. Colored spheres represent the hits in the detector where their size indicates the amount of observed light with time-ordering from red to blue.

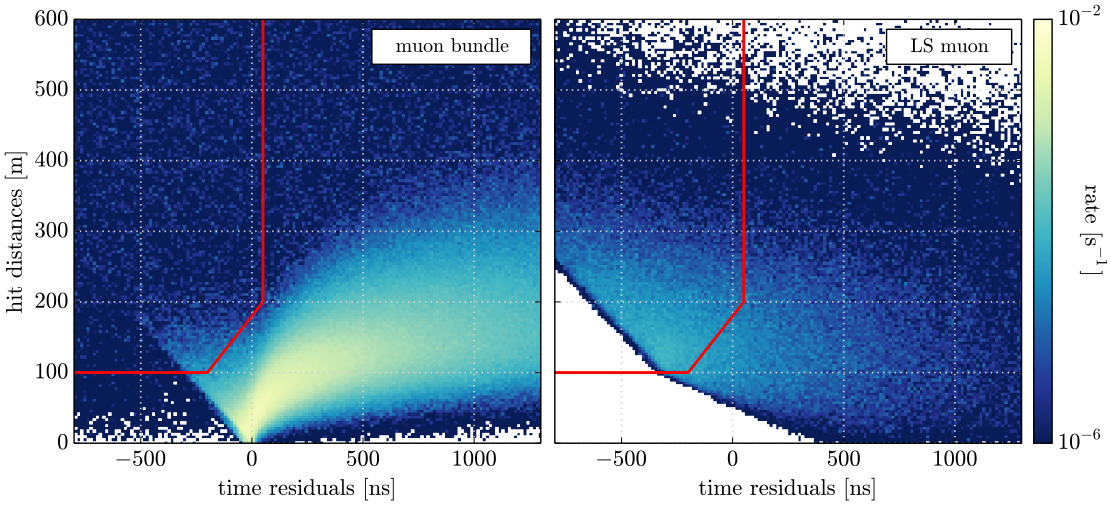

Figure 6.4: Time residuals versus distance of hits with respect to the true core position after k-means splitting. The selection applied is indicated as red lines, where hits in the upper left region are expected to belong to the LS Muon.

Pandel Bayesian likelihood fit, as described in Section 6.2. The time residual of each assigned hit is then calculated with respect to this reconstructed bundle track. The resulting track is shown in Figure 6.3 (c.2, red line). In addition, the perpendicular distance of each hit to the reconstructed track is calculated.

Figure 6.4 shows these hit distances as a function of the time residuals of hits with respect to the true shower core (assumed to follow the true primary direction), for simulated LS Muon events using LSMuonSim. Hits belonging to the muon bundle after k-means splitting are shown in the left panel, LS Muon hits are shown on the right-hand side. This hit assignment is based on the MC truth. The hit distributions with respect to the reconstructed bundle track are shown in Figure 6.5. In order to separate all hits produced by muons from the bundle core from the LS Muon assigned hits, the selection indicated by red lines in the figures is applied. Hits in the upper left area are considered as LS Muon hits, while other hits are assumed to originate from the bundle muons.

Final Double-Track Reconstruction

After successful hit splitting, the two individual hit series are reconstructed separately. Events with less than 8 hits assigned to the LS Muon are discarded in order to meet the double-track hypothesis requirement and to ensure that the LS Muon track can be reconstructed successfully. The two split hit series of the remaining events are then reconstructed, using a Pandel Bayesian LLH fit with an improved line fit as initial seed, as previously described. The resulting track reconstructions for the laterally separated muon and the muon bundle are shown in Figure 6.3 (d.1) and (d.2) respectively. Figure 6.3 (e) shows the total event with the resulting double-track reconstruction and the corresponding reconstructed zenith angle direction θ, and lateral separation d_T. The Monte Carlo truth of the

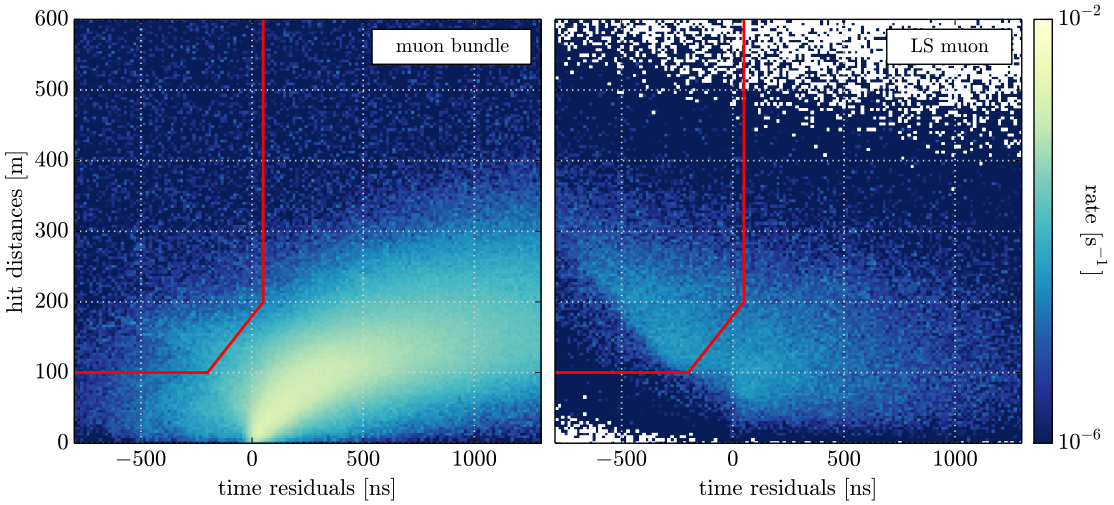

Figure 6.5: Time residuals versus distance of hits with respect to the reconstructed bundle track after k-means splitting. The selection applied is indicated as red lines, where hits in the upper left region are expected to belong to the LS MUON.

event is shown in Figure 6.3 (f) for comparison. The resulting accuracies for the double-track reconstruction are discussed in detail in Section 6.6.

Events are only kept, if all double-track reconstruction steps described above are performed successfully, including the requirement of the final LLH reconstructions to converge. Thereby roughly ~ 20% of LS MUON events are reconstructed successfully, while the background contribution is reduced by a factor of about 27 (see Section 6.5). This filter level is referred to as *level-2* in the following and all subsequent filters are performed on these double-track reconstructions.

6.4 EVENT SELECTION

After applying the double-track reconstruction (level-2), further selection criteria are applied in order to reduce background events, such as showers without an LS MUON and multiple showers detected within the same time window. In addition, mis-reconstructed events are removed from the data sample to ensure a high-quality final event sample. This enables precise measurement of the lateral separation and hence detailed studies on the resulting distributions. The event selection, which is described in the following, is based on the concepts used for the previous IC59 analysis, as presented in Ref. [83]. Thereby direct comparisons between previous results and this work can be made.

L3 – Opening Angle

In order to select the (nearly) parallel double-tracks from LS MUON events in ICECUBE, only events with opening angles between reconstructed LS MUON direction and bundle track below $\Delta\phi \leqslant 5^\circ$ are kept. The opening angles obtained

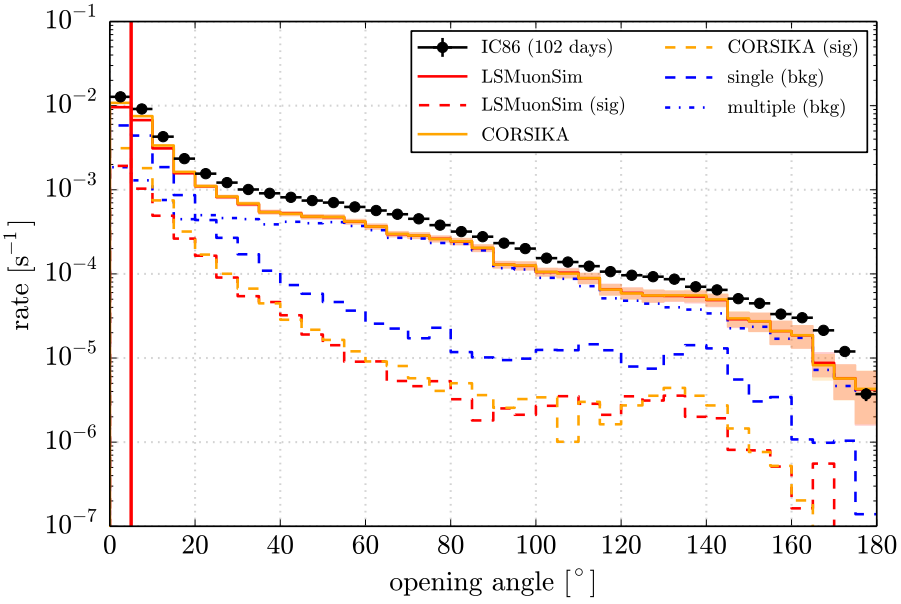

Figure 6.6: Opening angle distributions of reconstructed events passing level-2, obtained from experimental burnsample data and MC simulations. The contributions from signal ($d_{T,true} \geqslant 100\,m$) and background events are shown separately. The vertical red line indicates the level-3 selection criteria $\Delta\phi \leqslant 5°$ (see text for details).

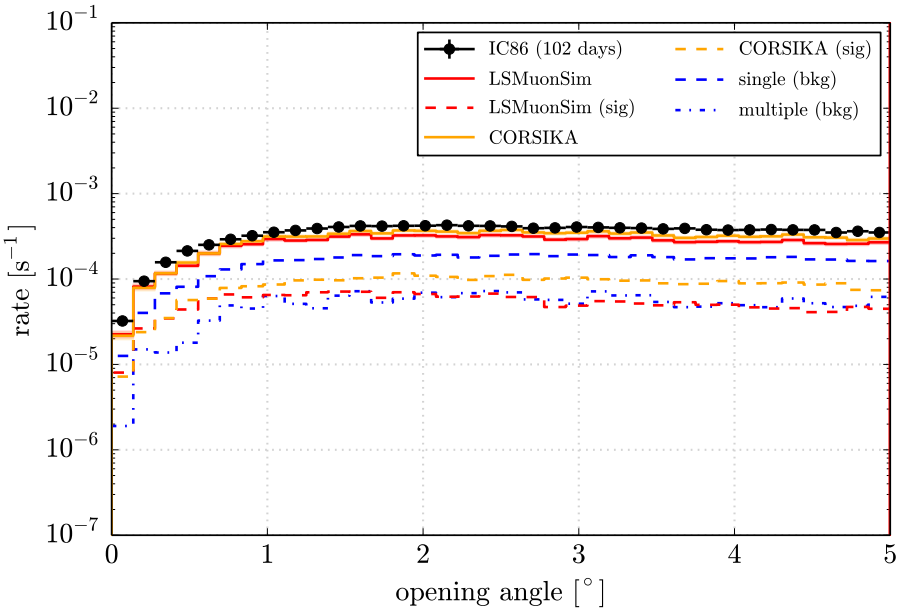

Figure 6.7: Zoomed in opening angle distribution of reconstructed events passing level-3, obtained from experimental burnsample data and MC simulations. The contributions from signal ($d_{T,true} \geqslant 100\,m$) and background events are shown separately.

from all reconstructed events (L2) are shown in Figure 6.6, where the cut applied is shown as vertical red line. While the MC distributions agree fairly well, they underestimate the burnsample event rate, especially towards large opening angles. Based on a comparison of the shapes of the distributions at large angles, this effect is likely caused by an underestimation of background events from multiple showers within the MC simulations. However, Figure 6.7 shows the distribution of the remaining events at *level-3* (L3), where the data/MC agreement improves. The background contributions from neutrino events is highly suppressed at this filter level and is henceforth not shown separately, although included in the total distributions. Additional distributions of the opening angles, for all filter levels, can be found in Appendix C.4.

Since the bundle track and the LS MUON are expected to be parallel ($\Delta\phi \simeq 0°$), these distributions also represent the accuracy of the opening angle reconstruction, and based on the LSMUONSIM simulations 68.3% of the remaining events (L3) are reconstructed with accuracy better than $\Delta\phi \leqslant 3.1°$. A comprehensive discussion on the accuracies of all reconstructions used in this work can be found in Section 6.6. Based on LSMUONSIM (CORSIKA) predictions, this selection keeps 45% (47%) of signal events ($d_{T,true} \geqslant 100\,m$) while reducing the background by a factor of 3.2.

L4 – Time Difference

The time difference, Δt, between reconstructed bundle track and the LS MUON track, when passing a plane through the center of the detector, perpendicular to the reconstructed bundle track, is shown in Figure 6.8. The LS MUON and the muon bundle are expected to arrive nearly simultaneously at the detector, hence events are selected with vanishing arrival time Δt. As shown in Section 6.6, the reconstruction accuracy of the arrival time of 68.3% of LS MUON events at level-3 is roughly $\Delta t \simeq 425\,ns$. Thus, and in order to enable a direct comparison to IC59 results [83], only events with a time difference of $\Delta t \leqslant 450\,ns$ are kept.

The corresponding distribution of surviving events is shown in Figure 6.9 and in the following this filter level is referred to as *level-4* (L4). The simulated distributions obtained from CORSIKA and LSMUONSIM show minor differences towards large time differences, above $\sim 200\,ns$. This is because LSMUONSIM does not account for the curvature of the air shower front and the LS MUON, which is added during the simulation process, is inserted with a time corresponding to the bundle arrival time. Hence, LSMUONSIM is expected to show smaller time differences between the bundle and LS MUON arrival times compared to the CORSIKA distributions, which account for the shower front curvature. However, this selection reduces the background contribution by a factor of 2 and keeps 70% (76%) of signal events, obtained from LSMUONSIM (CORSIKA). Additional distributions for all filter levels are shown in Appendix C.5.

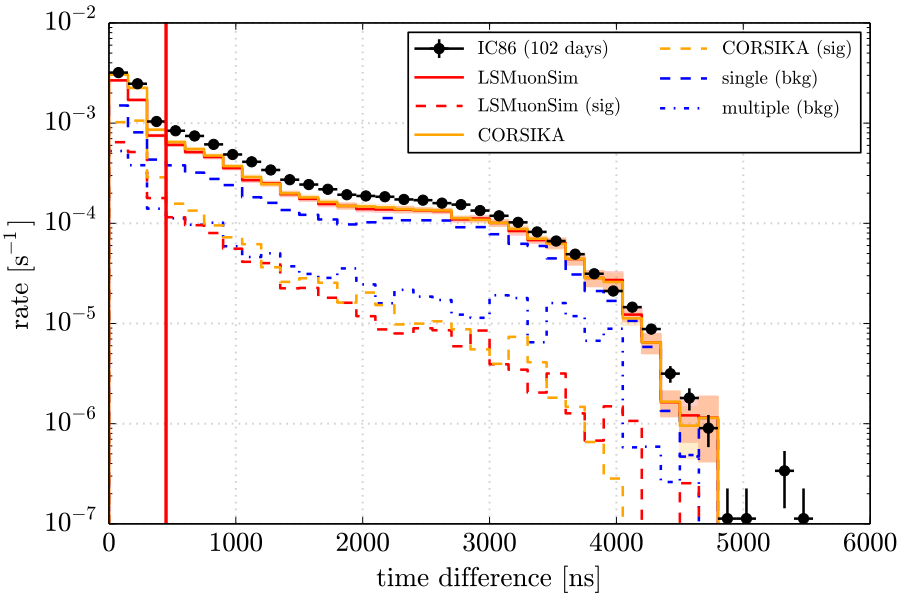

Figure 6.8: Time difference between reconstructed LS Muon and muon bundle track of all burnsample events passing level-3. The distributions obtained from CORSIKA (Sibyll 2.1) and LSMuonSim (EPOS-LHC) are also shown. The contributions from signal ($d_{T,true} \geqslant 100\,m$) and background are shown separately. The vertical red lines indicates the L3 selection criteria $\Delta t \leqslant 450\,ns$ (see text for details).

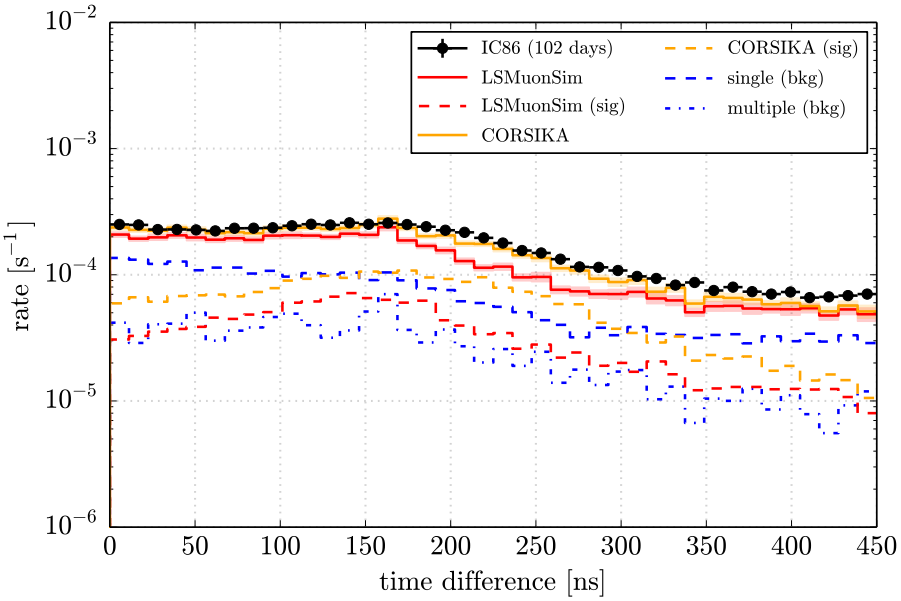

Figure 6.9: Zoomed in time difference between reconstructed LS Muon and muon bundle track of all burnsample events passing level-4. The distributions obtained from CORSIKA (Sibyll 2.1) and LSMuonSim (EPOS-LHC) are also shown. The contributions from signal ($d_{T,true} \geqslant 100\,m$) and background are shown separately.

L5 – Lateral Separation

The lateral separation d_T of the LS MUON is given by the perpendicular distance between the reconstructed bundle and LS MUON tracks, in the plane through the center of the detector. In order to select LS MUON events with large lateral separations, only events above $d_T \geqslant 135\,\text{m}$ are kept. This selection is referred to as *level-5* (L5). It is chosen to select separations larger than ICECUBE's horizontal string spacing of 125 m in order to avoid reconstruction biases due to the detector geometry. In addition, the double-track reconstruction accuracy of roughly $\sim 10\,\text{m}$ is accounted for in order to ensure a high-quality data sample at final filter level. The reconstruction accuracies at level-5 are discussed in detail in Section 6.6.

The lateral separation distribution of events at filter level-4 is shown in Figure 6.10, obtained from 102 days of burnsample data and taken from MC simulations. The final selection criteria is indicated by the vertical red line and the lower panel shows the corresponding data/MC ratio of the lateral separation distribution. After applying this selection criteria the expected event rate, obtained from 102 days of burnsample data, corresponds to 31122 ± 332 events per year. This final selection reduces the background contribution by a factor of ~ 26 and based on LSMUONSIM (CORSIKA) predictions, the signal-over-background ratio (S/B-ratio) at final filter level is roughly 3.9 (4.3). Additional distributions of the lateral separation for all analysis levels are shown in Appendix C.1.

6.5 EVENT RATES

The total event passing rates for the various filter levels, based on 102 days of burnsample data and obtained from MC simulations, are shown in Figure 6.11 (left axis). The individual MC contributions from signal and various background events are shown separately and the corresponding total event rates per year are additionally given in Table 6.1. The expected event rate at final filter level (L5), obtained from the 102 days of burnsample data, is 31122 ± 332 events per year. The expected total event rates, obtained from MC simulations, are 22151 ± 509 (LSMUONSIM) and 24157 ± 562 (CORSIKA) events per year, with an estimated signal-over-background ratio (S/B-ratio) of 3.9 and 4.3 respectively. The latter is also shown in Figure 6.11 for the different filter levels as dotted lines (right axis), obtained from LSMUONSIM (lightgrey) and CORSIKA (darkgrey) simulations. The S/B-ratio is further improved in later analysis steps, using a background subtraction based on a data-driven background estimate, as described in Section 7.2. Although there are differences between the data rate and MC predictions, as well as between the simulations themselves, they agree qualitatively.

The background contribution from neutrino events at final analysis level is negligible and the rate of mis-reconstructed single showers without LS MUON is also highly suppressed. However, a small contribution of multiple showers recorded within the same time window can mimic double-track events in

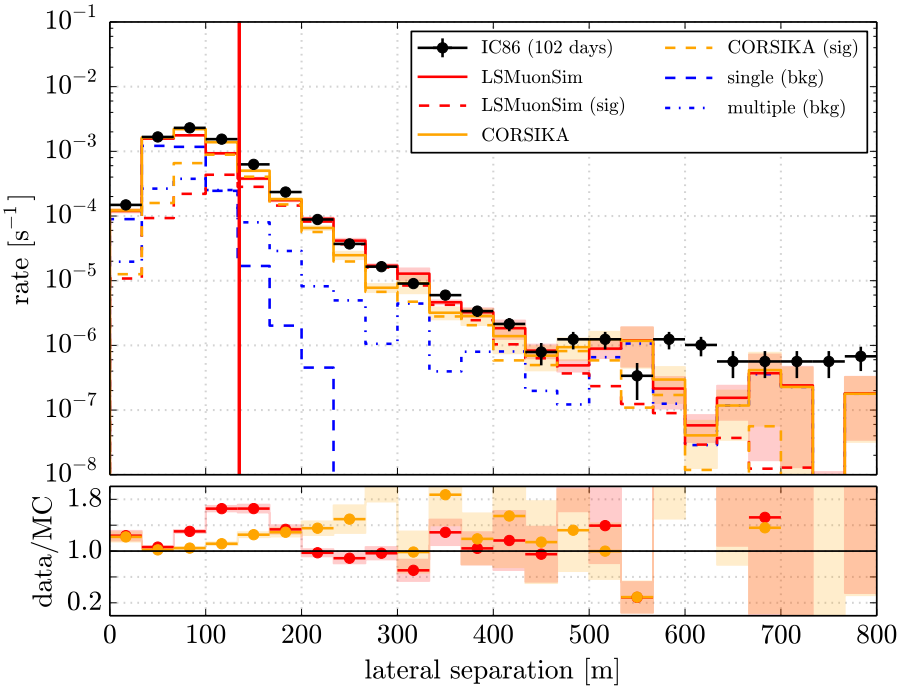

Figure 6.10: Lateral separation distribution of all events passing level-4, obtained from experimental burnsample data and MC simulations, where the contributions from signal ($d_{T,true} \geqslant 100\,m$) and background events are shown separately. The lower panel shows the corresponding data/MC-ratios.

IceCube and remains as an irreducible background at final event level. As described in Section 7.2, this background can be estimated from experimental data and is subtracted for further studies on the lateral separation distributions of LS Muons.

6.6 TRACK RECONSTRUCTION ACCURACY

The accuracies of reconstructions used in this work are derived, using the difference Δx_i between a reconstructed value $x_{reco,i}$ and the corresponding true value $x_{true,i}$, obtained from MC simulations:

$$\Delta x_i = x_{reco,i} - x_{true,i} \,. \tag{6.6}$$

The corresponding mean reconstruction accuracy Δx is then defined by the interval, containing $\pm 34.15\%$ of the events around $\Delta x = 0$. Thereby, asymmetric uncertainties are accounted for. In case of a gaussian distribution, centered at $\Delta x = 0$, this definition corresponds to the 68.3% (1σ) *confidence interval* [211, 212].

The resulting accuracies of the double-track reconstruction, described in Section 6.3, are shown in Figure 6.12. The left panel shows the difference between reconstructed and true lateral separation of LS Muon events, obtained from LSMuonSim at final filter level (L5). The resulting spatial accuracy of 68.3% ($\pm 34.15\%$) of the events is shown as shaded area in Figure 6.12, given

FILTER LEVEL		LSMUONSIM [10^3 events/yr]	CORSIKA [10^3 events/yr]	DATA [10^3 events/yr]
L0:	Pre-filtering	21860.6 ± 20.1	21949.9 ± 20.1	26142.6 ± 9.7
L1:	$6 \leqslant \text{rlogl} \leqslant 10$	21710.2 ± 19.9	21799.6 ± 19.9	25921.1 ± 9.6
L2:	Reconstruction	9051.7 ± 4.4	9784.9 ± 4.5	12657.2 ± 2.1
L3:	$\Delta\phi \leqslant 5°$	302.7 ± 2.1	340.5 ± 2.2	401.5 ± 1.2
L4:	$\Delta t \leqslant 450\,\text{ns}$	161.7 ± 1.6	194.2 ± 1.6	211.4 ± 0.9
L5:	$d_T \geqslant 135\,\text{m}$	22.2 ± 0.5	24.2 ± 0.6	31.1 ± 0.3

Table 6.1: Passing rates of events per year for the filter levels, as described in the text and shown in Figure 6.11. The total event rates obtained from CORSIKA simulations (SIBYLL 2.1) and LSMUONSIM (EPOS-LHC) are also given.

by $+16.1\,\text{m}$ and $-10.2\,\text{m}$. The corresponding distribution of the zenith angle directions are shown in the right panel, with resulting angular accuracies of $+0.5°$ and $-1.1°$. Additional distributions of the reconstructed lateral separation and zenith angle directions as function of the corresponding true value, obtained from simulations, are shown in Appendix C.11.

For the opening angle $\Delta\phi$ and time difference Δt of the reconstructed double-tracks, the corresponding (absolute) accuracies, $\Delta x \equiv |\Delta x|$, are derived assuming a symmetric 68.3% interval around $\Delta x = 0$. At final filter level they are given by $\Delta\phi = \pm 3.0°$ and $\Delta t = \pm 201\,\text{ns}$. All resulting accuracies of the double-track reconstruction, for the various analysis levels of this work, are shown in Table 6.2. The accuracies of the lateral separation are only shown for the last two filter levels, because they are not meaningful for lower filter levels due to the contribution of mis-reconstructed background events.

FILTER LEVEL		Δd_T [m]	$\Delta\theta$ [°]	$\Delta\phi$ [°]	Δt [ns]
L2:	Reconstruction	–	$+0.8/-1.6$	± 9.39	± 585
L3:	$\Delta\phi \leqslant 5°$	–	$+0.7/-1.4$	± 3.2	± 423
L4:	$\Delta t \leqslant 450\,\text{ns}$	$+467.0/-14.6$	$+0.6/-1.3$	± 3.1	± 205
L5:	$d_T \geqslant 135\,\text{m}$	$+16.1/-10.2$	$+0.5/-1.1$	± 3.0	± 201

Table 6.2: Reconstruction accuracies for 68.3% of the LS MUON events ($d_{T,\text{true}} \geqslant 100\,\text{m}$) at each filter level, obtained from LSMUONSIM. See text for details.

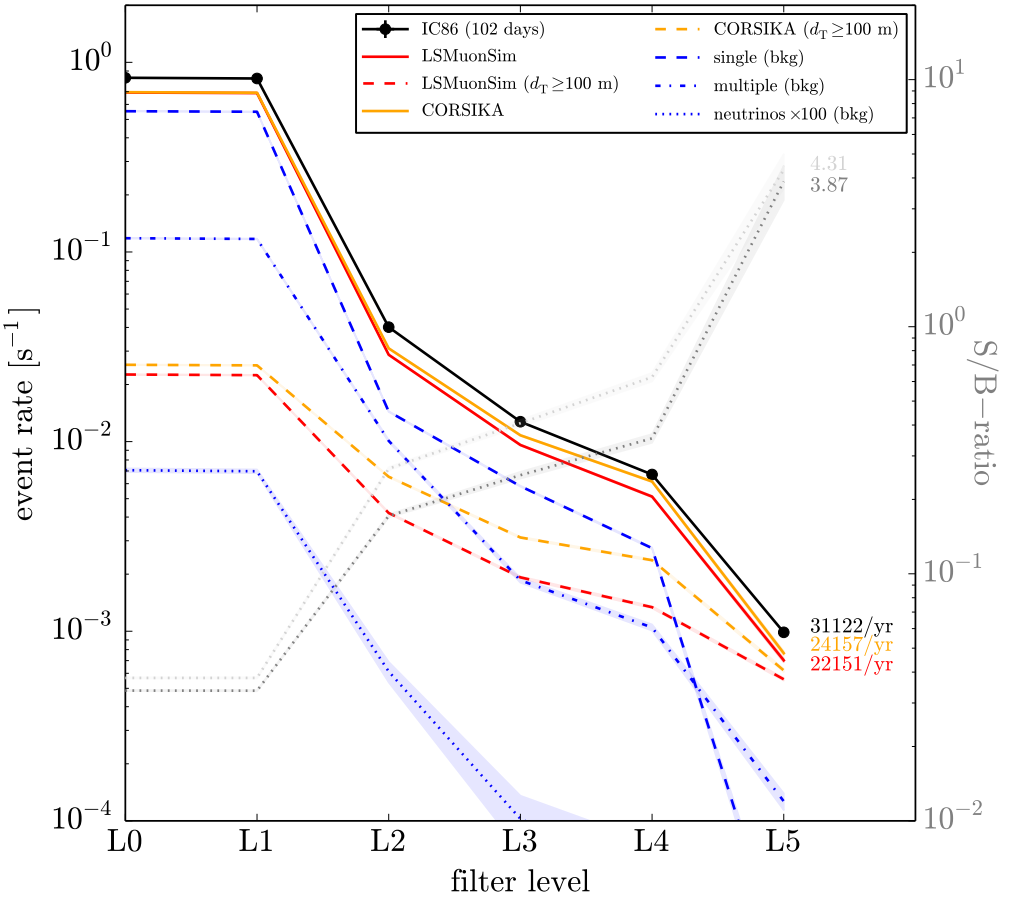

Figure 6.11: Event passing rates for filter levels (left axis), obtained from 102 days of burnsample data and MC simulations. The neutrino contribution is scaled with a factor of 100. Error bands represent the corresponding statistical uncertainties. The corresponding signal-over-background ratios are also shown, as grey dotted lines (right axis).

6.7 PRIMARY ENERGY ESTIMATOR

The primary energy estimation is based on the deposited energy of all muons along the reconstructed track in IceCube. Generally, the energy loss along a single muon track follows the stopping power, as defined in Equation (3.1). Using the logarithmic version of dE/dx, the energy $E = E_\mu$ of the initial muon is given by

$$f_1(E) \equiv \log_{10}(E) = \log_{10}\left(\frac{1}{b_1} \cdot \left[\frac{dE}{dx} - a_1\right]\right) . \tag{6.7}$$

Following Ref. [213], the energy losses along the muon track can be estimated using the *truncated mean method*, which divides the reconstructed track into several bins. The hits are binned according to their location by planes perpendicular to the track. The deposited energy dE/dx is then determined by finding the ratio of the observed photoelectrons and the expected PEs, obtained from MC

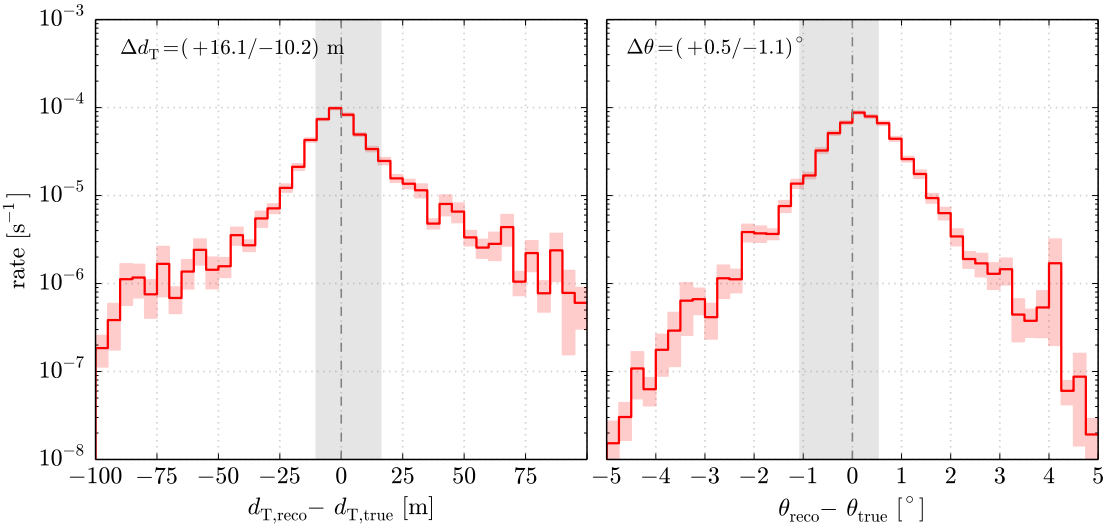

Figure 6.12: The differences of the true and reconstructed lateral separation (left panel) and zenith angle direction (right panel) of LS MUON events, obtained from LSMUONSIM. The shaded areas show the (asymmetric) intervals, containing 68.3% of the events, as described in the text.

FIT FUNCTION	a_i [cm^2/g]	b_i [cm^2/g]	c_i [cm^2/g]
$f_1(E)$	28447.8 ± 905.0	0.0431 ± 0.0002	–
$f_2(E)$	7.41 ± 0.14	-1.31 ± 0.05	0.2189 ± 0.0048

Table 6.3: Truncated energy estimator best fit parameters, as given in Equation (6.7) and Equation (6.8).

simulations. A fraction of the bins (40 %) with the highest ratios are discarded and the truncated dE/dx is calculated by summing the remaining photoelectrons and calculating the corresponding ratio of the total expected to observed PEs. Although designed for the energy estimation of single muons, this *truncated energy estimator* can also be reliably used to estimate the (mean) total energy losses of all muons combined in the core bundle, as described in the following.

Figure 6.13 shows the true primary energy $E_{0,true}$ of events at final filter level (L5), obtained from LSMUONSIM with an H3A flux assumption, as a function of the truncated shower energy. The truncated energy approximately accounts for the total deposited energy of all muons. The corresponding fit (solid line) represents a combined fit of Equation (6.7) and a second-order logarithmic polynomial [213]. This polynomial is used to fit the high-energy region for $dE/dx \geqslant 10^{5.82}$ GeV and given by

$$f_2(E) \equiv \log_{10}(E) = a_2 + b_2 \cdot \log_{10}\left(\frac{dE}{dx}\right) + c_2 \cdot \log_{10}^2\left(\frac{dE}{dx}\right) . \tag{6.8}$$

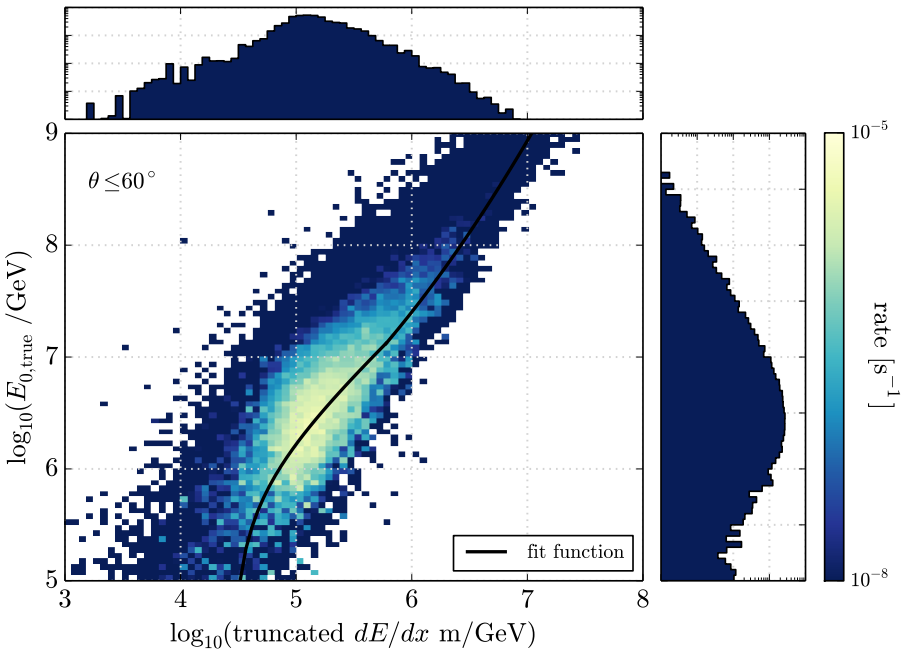

Figure 6.13: True total air shower energy as a function of the truncated deposited energy of final level events (L5) with $\theta \leqslant 60°$, obtained from LSMuonSim (EPOS-LHC, H3a). The truncated best fit function, as defined in Equation (6.9), is shown as solid line.

The resulting best fit parameters for the combined truncated energy fit function

$$f_{\text{truncated}}(E) = \begin{cases} f_1(E)\ , \text{ for } dE/dx < 10^{5.82}\,\text{GeV} \\ f_2(E)\ , \text{ for } dE/dx \geqslant 10^{5.82}\,\text{GeV} \end{cases} \tag{6.9}$$

are given in Table 6.3. As described in Chapter 7, for further studies only events from zenith angle directions $\theta \leqslant 60°$ are considered. Hence, the energy estimation is based on those simulated events at final filter level.

As shown in Figure 6.14, the resulting uncertainties of the primary energy estimate for the events considered are better than 0.3 in logarithmic energy. Other existing energy estimators, as described in Ref. [213], and dedicated methods based on the total charge measured in IceCube and the shower arrival direction, are not as accurate. The energy estimate is intended to divide the final dataset into a few energy bins in order to study energy-dependent effects on the lateral separation distribution of muons. This method is sufficiently precise in order to approximate the underlying shower energy for subsequent studies of this analysis. The reconstructed energy spectrum, as well as the final energy binning, are discussed in further detail in Section 7.1.

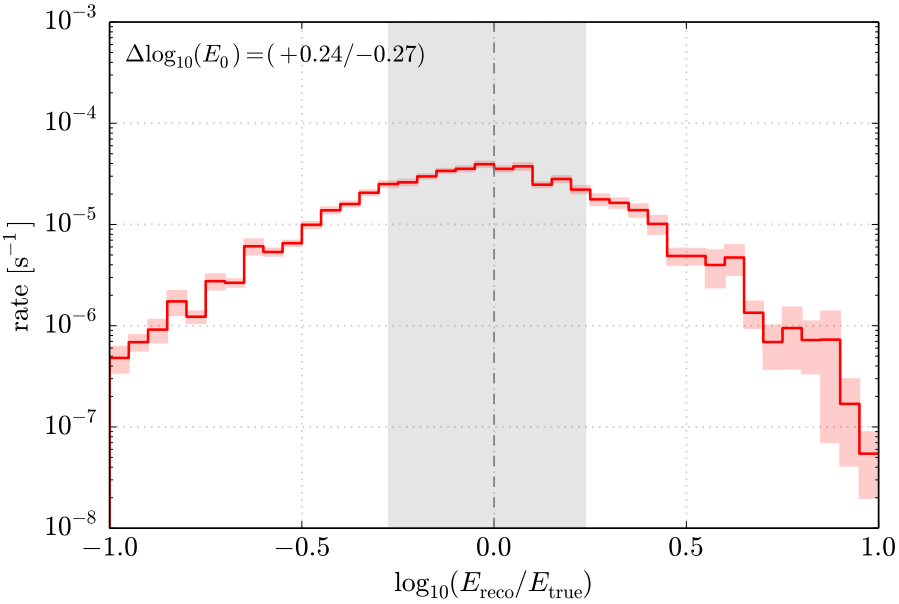

Figure 6.14: Reconstructed primary energy accuracy of final level events (L5) with zenith angle directions below $\theta_{\text{max}} = 60°$. The shaded area indicates the corresponding interval, containing 68.3% of the events.

6.8 TRANSVERSE MOMENTUM ESTIMATOR

The reconstructions of the transverse momentum of LS MUONS is based on Equation (2.36), with the p_T given by

$$p_T \simeq \frac{d_T \cdot E_\mu \cdot \cos(\theta)}{c \cdot H} \,. \tag{6.10}$$

The lateral separation and the zenith angle of each event at final level are obtained from the double-track reconstruction. However, the height of production of the muon's parent particle, as well as the muon energy are unknown. Standard energy estimation methods, such as the truncated method described in Ref. [213] and Section 6.7, depend crucially on the measured charge information. Due to the hit splittings and subsequent hit cleaning applied during this analysis, as described in Section 6.3, a reliable energy estimation of the LS MUON is not possible. Moreover, the interaction height information can not be reconstructed using the in-ice detector response alone. In principle the interaction height may be geometrically estimated, based on the opening angle and the lateral distance obtained from the double-track reconstruction described in Section 6.3. However, the reconstruction accuracies of $\Delta d_T = (+16.1/-10.2)\,\text{m}$ and $\Delta\phi = \pm 3.0°$ (see Section 6.6) result in uncertainties of the height estimate of roughly more than 10 km. Hence, the uncertainties are too large to draw reliable conclusions on the underlying height of production in the context of the p_T estimation.

Thus, the energies and interaction heights in Equation (6.10) are approximated by the mean LS MUON energy $E_\mu \simeq \langle E_\mu \rangle_i$ and height of the air shower production $H \simeq \langle H(\theta) \rangle$ of final level events obtained from MC simulations.

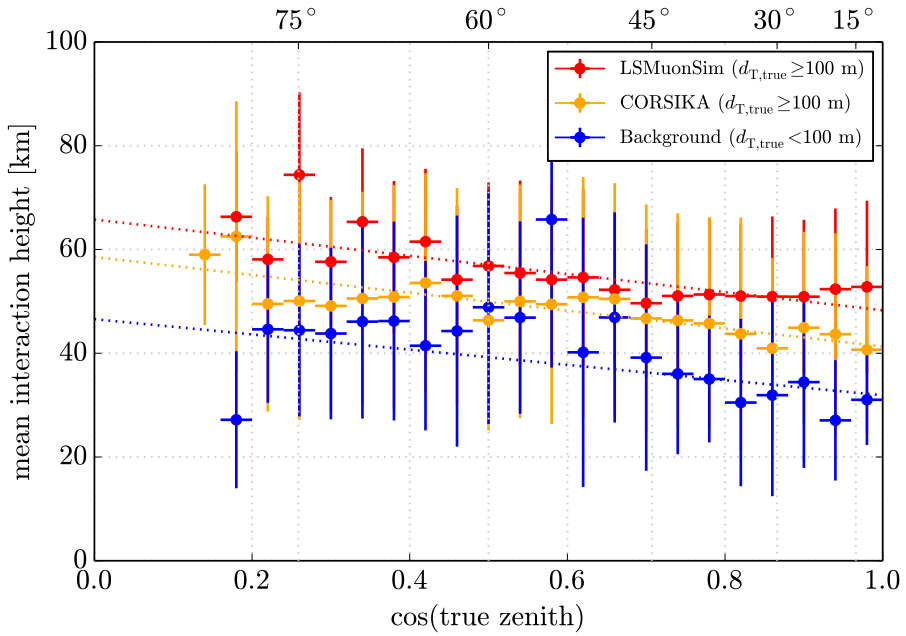

Figure 6.15: The mean first interaction height at final filter level (L5) as a function of the zenith angle direction from MC simulations. Signal (red/orange) and background contributions (blue) are shown separately. The dashed lines show the corresponding linear fits, as described in the text.

The mean energies are derived for each primary energy bin i separately, as described in Section 7.4. The corresponding mean interaction heights are derived, taking their zenith angle dependence into account. Figure 6.15 shows the mean first interaction height, obtained from CORSIKA and LSMuonSim, as a function of the zenith angle. The dashed lines represent linear fits of the form $\langle H(\theta) \rangle = \alpha \cdot \cos(\theta) + \beta$. Since the primary nucleus has more time to interact at higher altitudes towards horizontal directions, the mean altitude of the first interaction increases with increasing zenith angle. Although the heights obtained from CORSIKA and LSMuonSim agree within their large statistical uncertainties, the LS Muon events ($d_{T,true} \geqslant 100\,m$) obtained from CORSIKA show systematically lower altitudes with respect to the LSMuonSim predictions. These MC discrepancies, observed in the zenith angle distributions used in this work, are discussed in detail in Section 7.3. The fits of the mean heights are used for the transverse momentum estimation based on Equation (6.10) and the resulting p_T distributions at final filter level are discussed in Section 7.4.

For very large zenith angle directions the lateral separation is expected to be dominated by the large distance to the detector, rather than by a large transverse momentum of the muon. Hence, the calculation of the p_T of LS Muons is done only for events with zenith angle directions below $\theta_{max} = 60°$. A more comprehensive discussion on the zenith angle dependence of the p_T of LS Muons can be found in Section 7.4.

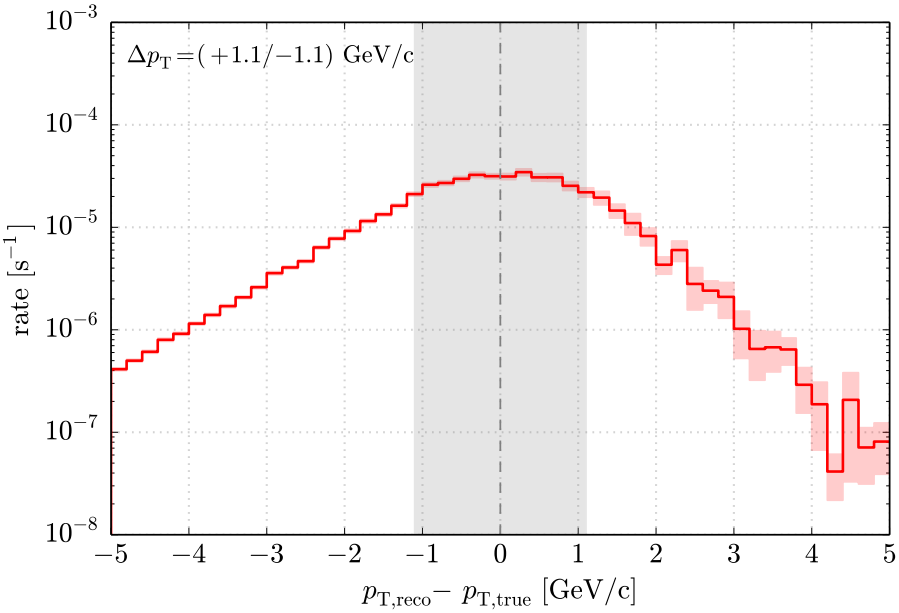

Figure 6.16: Reconstructed transverse momentum accuracy of final level events (L5) with zenith angle directions below $\theta_{max} = 60°$. The shaded area indicates the corresponding interval, containing 68.3% of the events.

In order to derive the uncertainties of the estimated transverse momentum of LS Muons, the 68.3% interval is used, as described for the double-track reconstruction in Section 6.6. The resulting accuracy of the transverse momentum estimate of LS Muon events, obtained from LSMuonSim, is shown in Figure 6.16. 68.3% of the events at final filter level are reconstructed with an accuracy Δp_T of better than $\pm 1.1\,\mathrm{GeV/c}$.

6.9 EFFECTIVE AREAS

The propagation of muons through the ice and subsequent detection efficiencies have significant effects on the LS Muon event rate measured in IceCube. Due to threshold effects, the detector efficiencies, and consequently the measured in-ice distributions highly depend on the underlying shower energy and arrival direction. These effects are discussed in Section 7.2 and Section 7.3 in more detail. In order to get an estimate of the lateral separation distribution of muons at the surface, the trigger and filter efficiencies of the underlying analysis need to be considered. This is done based on MC simulations, using the *effective area*, which is generally given by the formula

$$A_{eff} = A_{gen} \cdot \frac{N_{det}}{N_{gen}} \,. \tag{6.11}$$

A_{gen} is the area at which the simulated events were generated, N_{det} and N_{gen} are the number of detected (at final filter level) and generated MC events respectively.

Following the geometric definition in Section 5.7, the generation area, in units of $[m^2 sr]$, is given by [214]

$$A_{gen} = \pi \cdot \left[2\pi r^2 \cdot \left(\cos^2(\theta_{min}) + \cos^2(\theta_{max}) \right) + 2rl \cdot \left(\theta_{min} - \theta_{max} - \right. \right.$$
$$\left. \left. - \cos(\theta_{min}) \cdot \sqrt{1 - \cos^2(\theta_{min})} + \cos(\theta_{max}) \cdot \sqrt{1 - \cos^2(\theta_{max})} \right) \right] , \tag{6.12}$$

where the radius and the length of the targeted cylinder volume are $r = 600\,m$ and $l = 1200\,m$. The events are generated over the full sky, therefore the maximum and minimum generated zenith angles are given by $\theta_{min} = 0°$ and $\theta_{max} = 90°$.

The resulting effective areas, obtained from LSMuonSim, are shown in Figure 6.17 as a function of the lateral separation. To account for possible energy dependencies of the effective areas, they are derived for each energy bin separately, when estimating the corresponding distributions at surface level. Hence, the effective areas shown in Figure 6.17 represent the effective areas of LS Muon events for each energy bin. The final energy binning, used in this analysis, is discussed in Section 7.1. In addition, only events from zenith angles below 60° are considered, because the MC uncertainties are very large towards larger inclinations, as discussed in detail in Section 7.2. The resulting effective areas are interpolated with a log-linear function of the form $\log_{10}(A_{eff}) = \alpha \cdot d_T + \beta$, as shown in Figure 6.17 as solid lines. These interpolations are used in order to estimate the corresponding distributions at surface level. They decrease with increasing lateral separation of muons, because the probability of both tracks being contained within the detector volume decreases.

The effective areas as a function of the transverse momentum, obtained from LSMuonSim (EPOS-LHC), are shown in Figure 6.18. They are interpolated with a simple power law of the form $\log_{10}(A_{eff}) = \alpha \cdot p_T^{\beta}$, shown as solid lines, which is used to derive the corresponding surface distributions. As described in Section 6.8, the transverse momentum distributions are reconstructed for several energy bins separately. Thus, the corresponding effective areas are only given for these energy bins. The effective areas are suppressed towards low transverse momenta due to the lateral separation cut applied during event selection, which favors large transverse momenta.

The statistical uncertainties of the LSMuonSim simulations are significantly smaller compared to the available CORSIKA simulations used in this work. Moreover, the transverse momentum information of laterally separated muons from CORSIKA simulations is unknown. Hence, the effective areas based on LSMuonSim, shown in Figure 6.17 and Figure 6.18, are used throughout this work in order to derive all surface distributions. However, the effective areas as function of the lateral separation derived from CORSIKA simulations can be found in Appendix C.12.

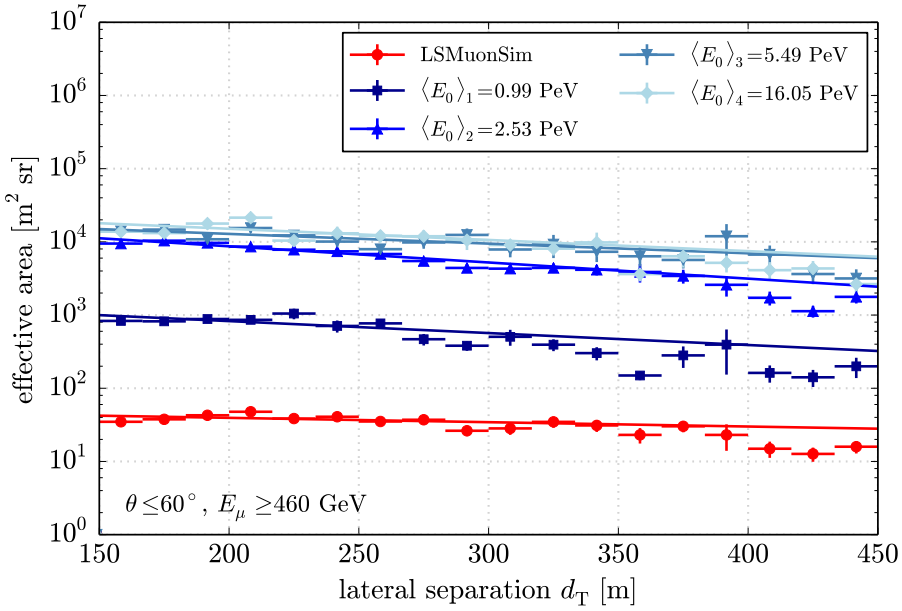

Figure 6.17: Effective areas obtained from LSMuonSim (EPOS-LHC) as function of the lateral separation of events at final filter level (L5).

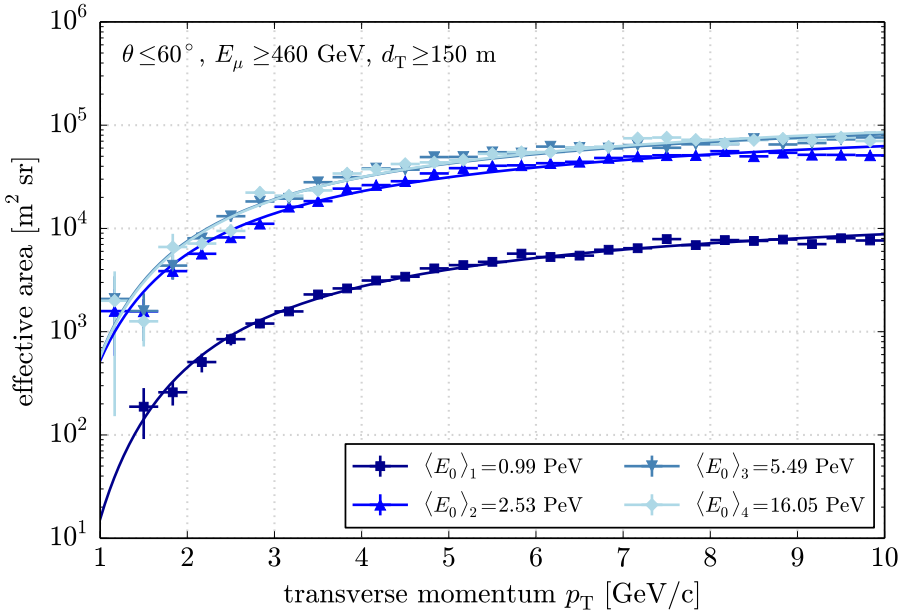

Figure 6.18: Effective areas obtained from LSMuonSim (EPOS-LHC) as function of the transverse momentum of LS Muons at final filter level (L5).

7 RESULTS

"Results! Why, man, I have gotten a lot of results!
I know several thousand things that don't work!"

– Thomas A. Edison *

After applying the reconstructions and selection criteria, as described in Chapter 6, 80951 events are left at final analysis level. The data, taken between May 2012 and May 2015, covers 960 days of livetime, with the burnsample removed from the data. The event rate consequently corresponds to 30765 ± 108 events per year ($(9.76 \pm 0.03) \cdot 10^{-4}$ per second). The resulting distributions and subsequent discussions are presented in the following.

The primary energy spectrum on final analysis level is shown in Section 7.1, including a discussion on the final energy binning used throughout this analysis. Several distributions of the lateral separation of LS Muon events in IceCube are studied in detail in Section 7.2 and a dedicated discussion on the corresponding zenith angle distribution is given in Section 7.3. Results of the transverse momentum estimation, the underlying cosmic ray composition, and seasonal variations of the measured LS Muon fluxes are shown in Section 7.4, Section 7.5, and Section 7.6 respectively. Finally, systematic uncertainties of the final distributions are discussed in Section 7.7, with special emphasis on the lateral separation and zenith angle distributions of LS Muons.

7.1 PRIMARY ENERGY SPECTRUM

The estimation of the primary energy of events at final filter level (L5) relies on the truncated energy method, introduced in Section 6.7. In the following, only events with zenith angle directions below $\theta_{max} = 60°$ are considered for in order to avoid unwanted effects at large inclinations, as discussed in Section 5.5 and Section 7.3. The resulting reconstructed primary energy spectrum is shown in Figure 7.1, using the 960 days of unblinded data. The reconstructed primary energy, as well as the corresponding true MC expectations, obtained from CORSIKA and LSMuonSim, are also shown for comparison.

The final energy binning is optimized in order to improve the statistics of each energy bin for further studies. The optimazation is done by dividing the final dataset into two sub-samples, separated by the mean reconstructed energy $\langle E_0 \rangle_{tot} = 4.08^{+16.32}_{-2.12}$ PeV. These sub-samples are then divided into two further sub-samples, where one contains 68.3% of the events close to $\langle E_0 \rangle$ and the second bin contains all other events. The resulting final energy binning is shown in Figure 7.2 and used for all subsequent energy-dependent studies performed

*As quoted by F. L. Dyer, T. C. Martin, in *"Edison: His Life and Inventions"* (2006).

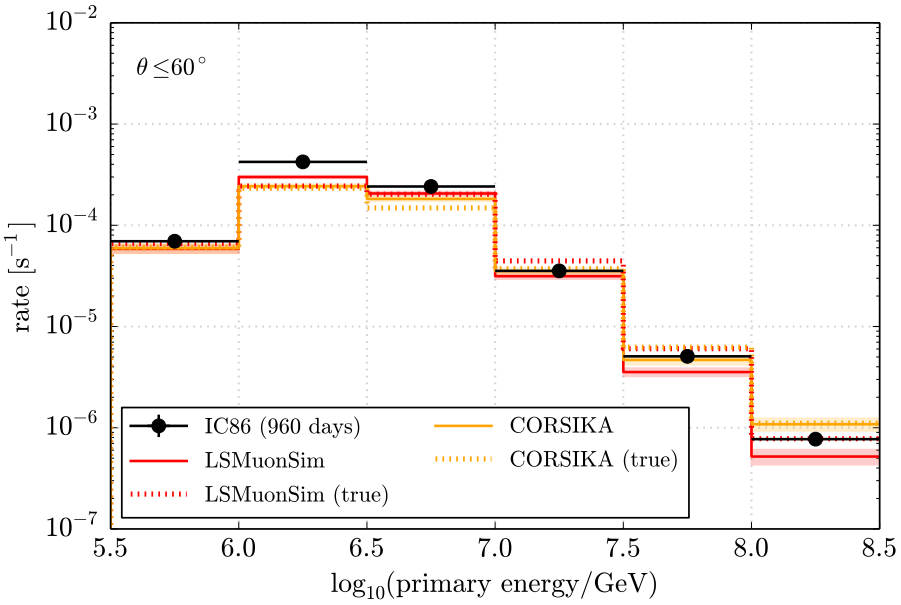

Figure 7.1: Reconstructed primary energy spectrum of events with zenith angle directions $\theta \leqslant 60°$, obtained from 960 days of data and MC simulations, at final filter level (L5).

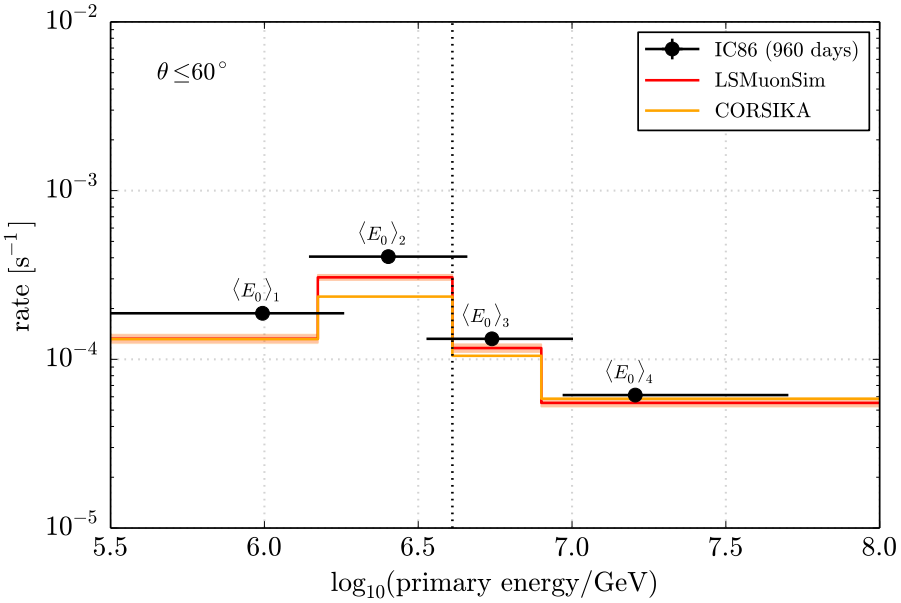

Figure 7.2: Final binning of the primary energy of events with zenith angle directions $\theta \leqslant 60°$ at final filter level (L5), obtained from experimental data and MC simulations. The data points represent the mean energy in each bin and the dotted line the total mean energy $\langle E_{0,tot} \rangle$.

$\langle E_0 \rangle_{tot}$ [PeV]	$\langle E_0 \rangle_1$ [PeV]	$\langle E_0 \rangle_2$ [PeV]	$\langle E_0 \rangle_3$ [PeV]	$\langle E_0 \rangle_4$ [PeV]
$4.08^{+16.32}_{-2.12}$	$0.99^{+0.83}_{-0.85}$	$2.53^{+2.04}_{-1.13}$	$5.49^{+4.58}_{-2.13}$	$16.05^{+34.44}_{-6.73}$

Table 7.1: Mean reconstructed primary energies for each energy bin on final filter level (L5). Only events with zenith angle directions up to $\theta_{max} = 60°$ are considered. The statistical uncertainties represent the interval containing 68.3% of the events, as previously described in Section 6.6.

in this work. Each energy bin is characterized by its mean energy throughout this work, which are given in Table 7.1. To get an estimate of the resulting distributions at surface level, the corresponding surface MC distributions for each energy bin are chosen such that the mean energies at surface level agree with the reconstructed energies obtained from the in-ice sample. These distributions are then used to derive the effective areas, as described in Section 6.9. This is done in order to avoid any energy-dependent biases due to a different energy spectrum of the events at surface level and in the ice.

The energy uncertainty estimates of data correspond to the interval containing ±34.15% of the events around the mean, obtained from LSMuonSim, as previously described in Section 6.6. The positive error of the mean in the highest energy bin $\langle E_0 \rangle_4$ is very large because it includes events up to the highest energies. This is also true for the mean of the total energies $\langle E_0 \rangle_{tot}$ for the same reason. However, the accuracy is sufficiently large to get a broad estimate of the mean energies of each energy bin. Therefore, conclusions on the energy dependence of the lateral separation distribution of muons can be drawn, as described in the following. Additional distributions of the true primary energy as function of the reconstructed energy, representing the accuracy of the energy estimate, can be found in Appendix C.11. Systematic effects on the reconstructed energies are discussed in Section 7.7.

7.2 LATERAL SEPARATION DISTRIBUTION

The lateral separation of events passing all selection criteria (L5) is shown in Figure 7.3, using 940 days of IceCube data. The corresponding distribtutions obtained from MC simulations are also shown. The resulting distributions are fit with a Hagedorn function of the form

$$\frac{d\Phi}{d(d_T)} = \alpha \cdot \left(1 + \frac{d_T}{d_0}\right)^{\beta} + C\,, \tag{7.1}$$

where α, β, and d_0 are free parameters, as described in Equation (2.34). C is an additional parameter, accounting for a constant background contribution, shown as blue dashed line in Figure 7.3. This constant background is caused by multiple showers triggering within the same time window, forming an irreducible background in this analysis. Using a fit of the form Equation (7.1), this irreducible background is then bin-wise subtracted by the resulting parameter

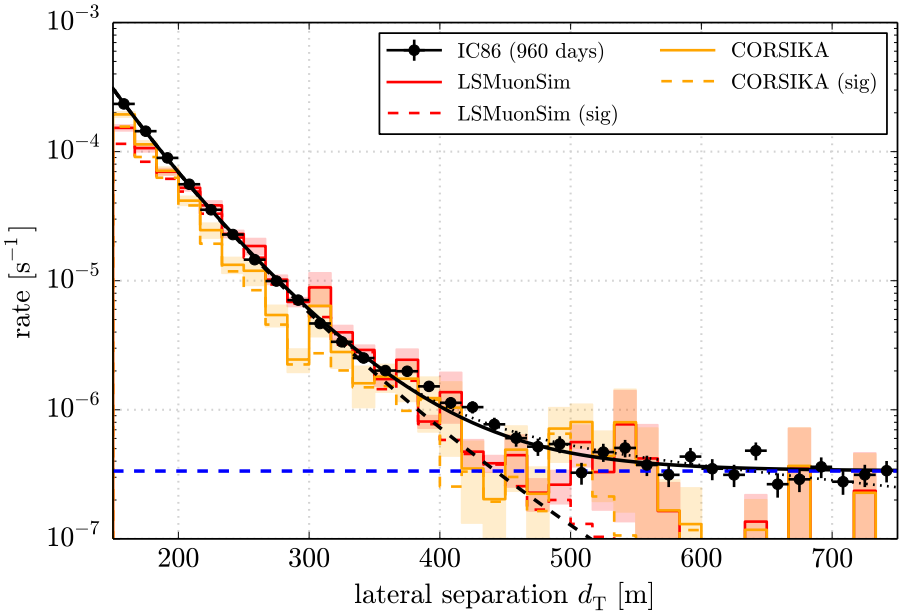

Figure 7.3: Lateral separation distribution on final filter level (L5), using 960 days of IceCube data and obtained from MC simulations. The Hagedorn function from Equation (7.1) is shown as solid black line. The black dashed line represents the Hagedorn part of Equation (7.1) ($C = 0$) and the estimate of the constant background contribution C is shown separately as blue dashed line. The black dotted line indicates the fit used in Ref. [83].

$C = (3.24 \pm 0.21) \cdot 10^{-7}\,\mathrm{s}^{-1}$. Corresponding to this fit, the background starts dominating the event sample at lateral separations of $d_T = 442\,\mathrm{m}$. Hence, although the background is subtracted from the final distributions, the following discussions focus on lateral separations below 450 m, where the event sample is highly signal-dominated.

A comparison to a previous measurement of LS Muons, using one year of data from IceCube in its 59-string configuration (IC59) [83], is shown in Figure 7.4. The resulting lateral separation distributions are in good agreement and the MC simulations describe the data well within the statistical uncertainties. A *Kolmogorov-Smirnov test* (KS test) [215, 216] yields p-values of 0.99 (LSMuonSim) and 0.94 (CORSIKA), indicating a very good description of the experimental data by the MC predictions.

A fit of the form previously used in Ref. [83], for the IC59 analysis of LS Muon events in IceCube, is shown as black dotted line in Figure 7.3 and is in agreement with previous results within the statistical uncertainties. As previously described in Section 6.4, the event rate of multiple showers, obtained from CORSIKA, underestimates the data rate. However, it still adequately describes experimental data, given the rather large statistical uncertainties towards large separations.

Figure 7.5 shows the lateral separation distribution of events at final filter level for zenith angle directions below $\theta_{max} = 60°$. In order to remove the irreducible background, the distribution is fit with a function of the form of Equation (7.1)

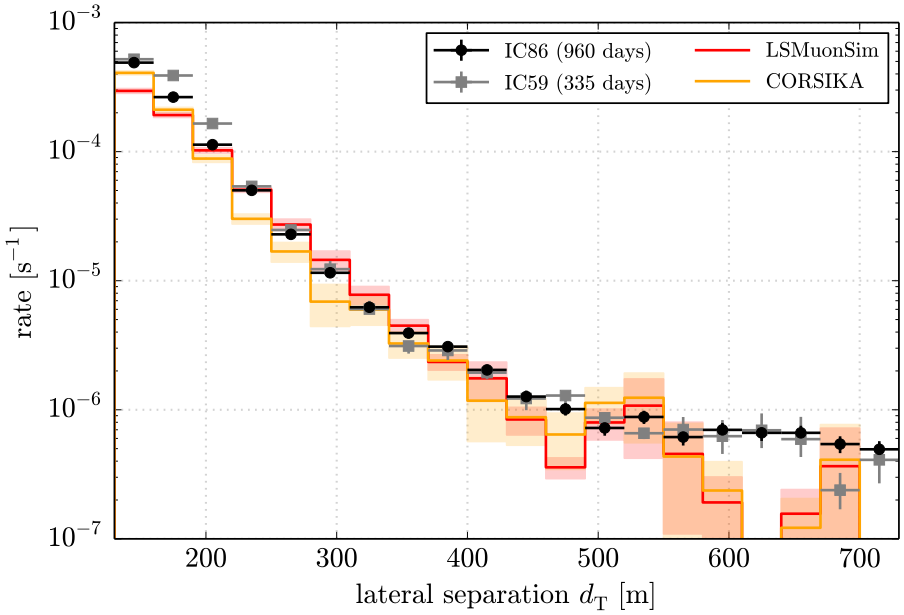

Figure 7.4: Lateral separation distribution of events after applying all selection criteria of this work (IC86) and taken from a previous analysis using IC59 data [83].

and the resulting parameter C is subtracted. The distribution is then re-fit, using Equation (7.1) with $C = 0$. The resulting best fit is shown in Figure 7.5 as solid line. The (true) MC predictions are also shown. The corresponding fit parameters are given in Table 7.2 with the p-values given in Appendix C.1.

The corresponding background-subtracted lateral separation distributions for each energy bin, as introduced in Section 7.1, are shown in Figure 7.6. Only events with reconstructed zenith angle directions of $\theta \leqslant 60°$ are considered. The resulting Hagedorn fits ($C = 0$) are shown as solid lines, with the best fit parameters given in Table 7.2. The dotted lines represent the corresponding Hagedorn fits with d_0 fixed to 237 m, as obtained from the total distribution. As described in Ref. [60] and Section 2.4, the Hagedorn function is not unique

	α [$10^{-3} \cdot m^{-1}s^{-1}$]	β	d_0 [m]	C [$10^{-7} \cdot m^{-1}s^{-1}$]
$\langle E_0 \rangle_{tot}$	75.1 ± 21.0	-11.7 ± 1.1	237.7 ± 43.5	3.2 ± 0.2
$\langle E_0 \rangle_1$	5.1 ± 2.6	-10.1 ± 1.1	$142.3.0 \pm 26.1$	1.4 ± 0.2
$\langle E_0 \rangle_2$	1.6 ± 0.5	-14.0 ± 2.1	322.3 ± 81.3	1.8 ± 0.5
$\langle E_0 \rangle_3$	0.3 ± 0.1	-12.9 ± 2.7	315.1 ± 113.6	0.2 ± 0.2
$\langle E_0 \rangle_4$	0.1 ± 0.1	-12.3 ± 3.9	336.1 ± 174.3	0.1 ± 0.2

Table 7.2: Lateral separation best fit parameters of the fits shown in Figure 7.5 and Figure 7.6 for all energy bins $\langle E_0 \rangle_i$ and $\theta \leqslant 60°$.

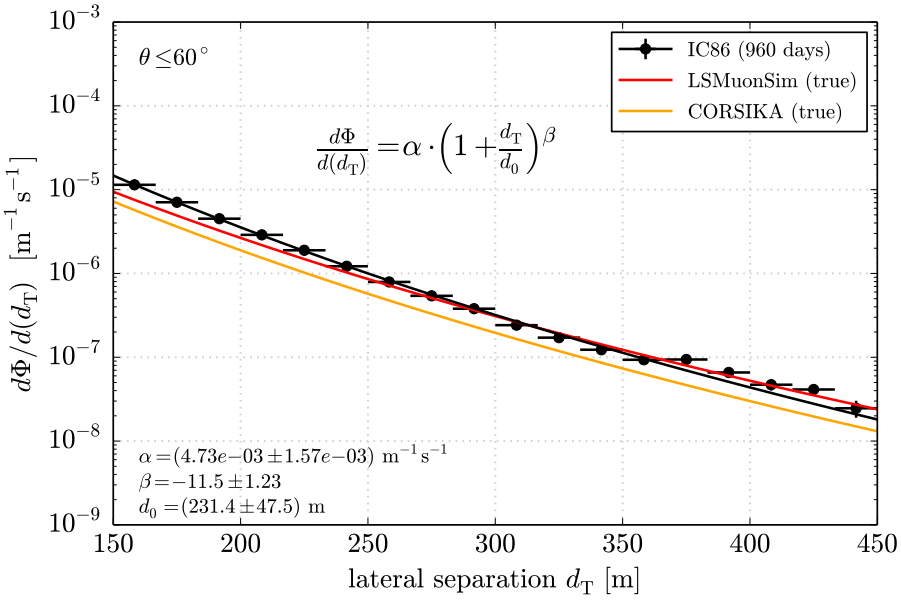

Figure 7.5: Lateral separation distribution of all events after background subtraction at final filter level (L5), measured in ice up to zenith angles of $\theta_{max} = 60°$.

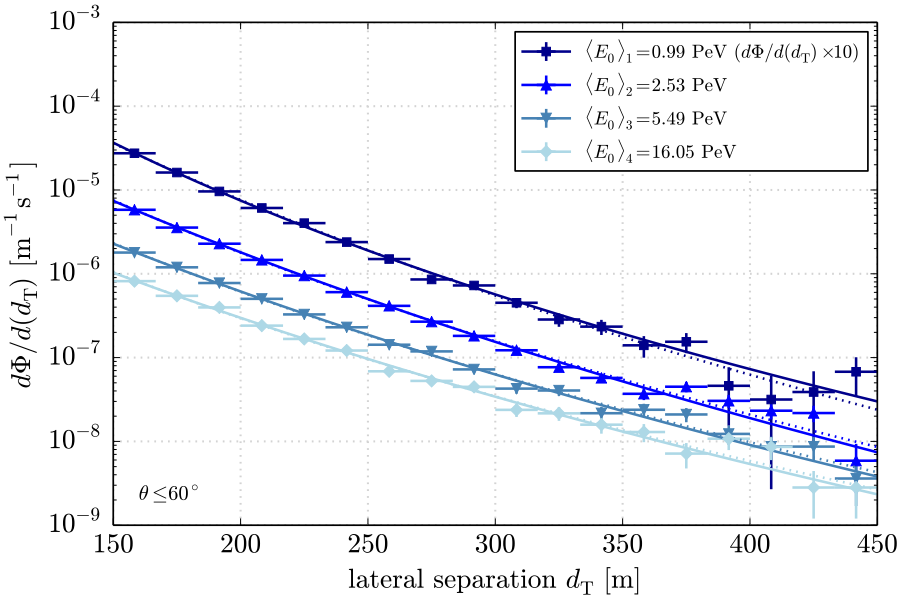

Figure 7.6: Lateral separation distribution for several primary energy bins after background subtraction, measured at final filter level (L5) in ice, up to zenith angles of $\theta_{max} = 60°$. Notice that the distribution for $\langle E_0 \rangle_1$ is scaled by a factor of 10.

when using d_0 as a free parameter. Hence, the latter fits enable comparison of the steepness of the distributions directly, based on the spectral index β.

Studies on systematic effects on the final lateral separation distributions, including dedicated discussions on hadronic models, the primary flux assumption, and the efficiency of DOMs, are presented in Section 7.7.1. Additional distributions of the lateral separation of muons, measured in the ice at final filter level, can be found in Appendix C.1.

Using the effective areas obtained from LSMuonSim (EPOS-LHC), as introduced in Section 6.9, the resulting lateral separation distributions on the surface are estimated. This is done after subtracting the constant background contribution, as described above. The effective areas obtained from CORSIKA simulations can be found in Appendix C.12 for comparison. The resulting distribution of events passing all filter levels (L5), and with zenith angle directions of $\theta \leqslant 60°$, is shown in Figure 7.7. The corresponding Hagedorn fits for data and MC simulations are shown as solid lines, with the fit parameters given in Table 7.3. Figure 7.8 shows the resulting lateral separation distributions at surface level separately for each energy bin with the corresponding Hagedorn fits. The dotted lines indicate Hagedorn fits with the transition parameter d_0 fixed to 156 m, as described for the in-ice distributions before.

As previously discussed in Section 5.5, the CORSIKA simulations at surface level show a steeper lateral separation distribution compared to the experimental data. The distributions obtained from LSMuonSim, using EPOS-LHC as hadronic model, agree better with data, although they overestimate the event rate towards large separations. This is related to the underlying simulated zenith angle distributions, which are discussed in more detail in the following Section 7.3. Further distributions can be found in Appendix C.1.

7.3 ZENITH ANGLE DISTRIBUTION AND INTERACTION HEIGHT

The reconstructed zenith angle distribution of events passing all selection criteria is shown in Figure 7.9. The expectations from MC simulations are also shown for comparison, with the resulting data/MC-ratio displayed in the lower panel.

	α [$10^{-6} \cdot m^{-3} sr^{-1} s^{-1}$]	β	d_0 [m]
$\langle E_0 \rangle_{tot}$	236.3 ± 145.3	-9.7 ± 1.1	157.3 ± 43.0
$\langle E_0 \rangle_1$	1.55 ± 1.23	-10.2 ± 1.9	186.6 ± 77.4
$\langle E_0 \rangle_2$	0.12 ± 0.10	-8.1 ± 1.7	167.5 ± 81.6
$\langle E_0 \rangle_3$	0.03 ± 0.03	-8.1 ± 1.9	170.9 ± 93.5
$\langle E_0 \rangle_4$	0.01 ± 0.01	-6.9 ± 1.8	133.8 ± 97.4

Table 7.3: Lateral separation Hagedorn fit parameters at surface level, for the fits shown in Figure 7.7 and Figure 7.8.

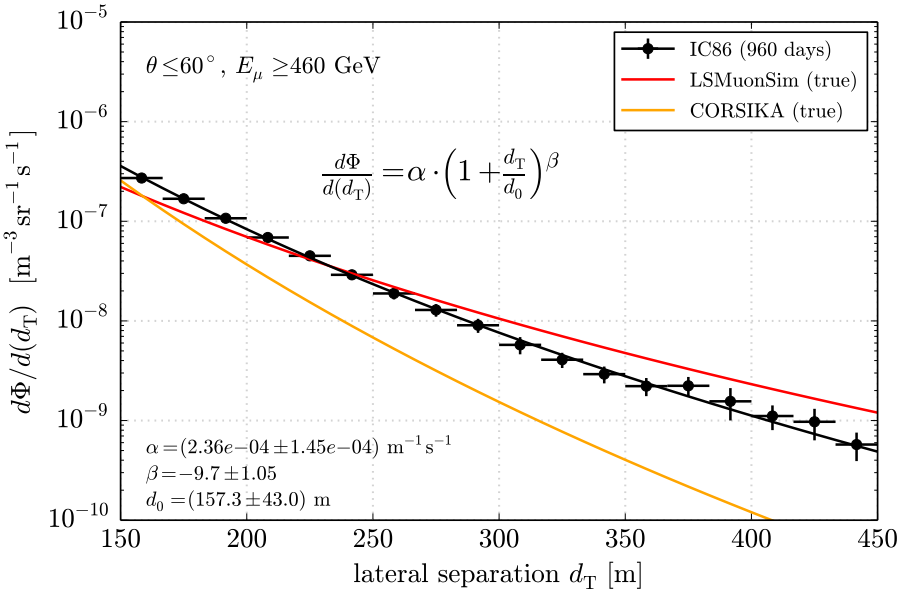

Figure 7.7: Lateral separation distribution at surface, estimated using the effective areas introduced in Section 6.9. The corresponding Hagedorn fits are also shown, for experimental data and MC simulations.

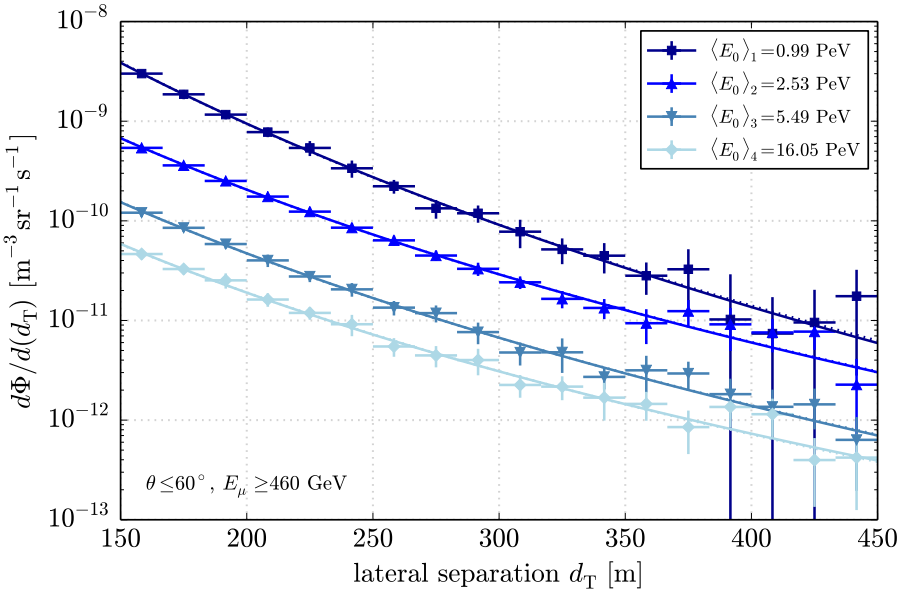

Figure 7.8: Lateral separation distribution at surface for several primary energy bins, estimated using the effective areas shown in Section 6.9.

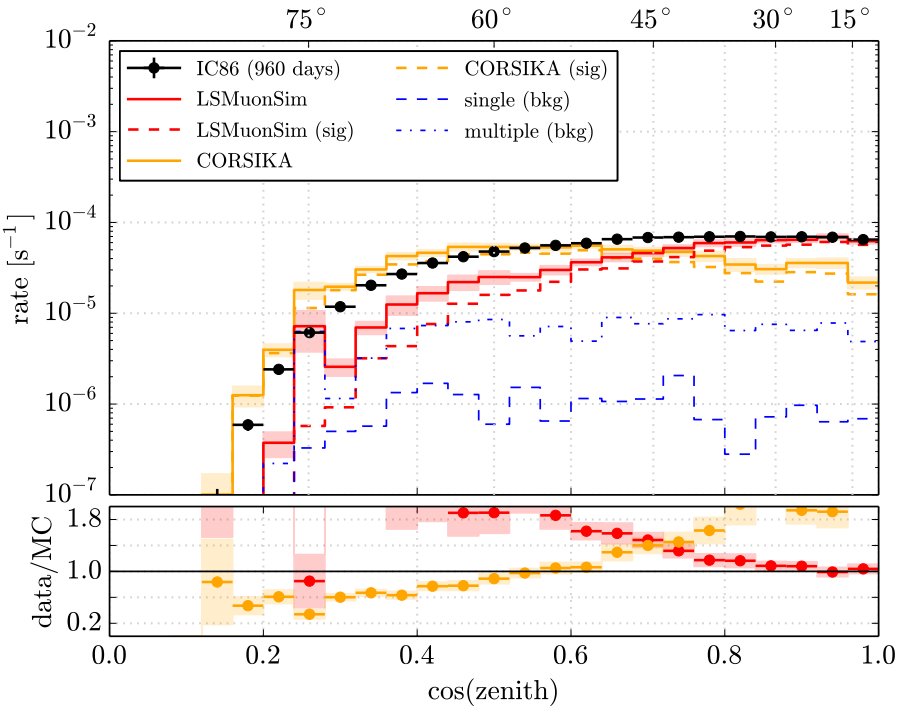

Figure 7.9: Zenith angle distribution of events at final filter level (L5), obtained from 960 days of IceCube data and from MC simulations. Background contributions are shown separately as blue lines. The lower panel shows the corresponding data/MC-ratios.

While the LSMuonSim predictions agree fairly well with data for vertical zenith angle directions ($\theta < 40°$), the LS Muon event rate towards large inclinations is significantly underestimated. This is somewhat expected due to the atmospheric model used, as discussed in Section 5.4.5 and Section 5.5. In addition, towards large zenith angles the distance between the production vertex and the detector becomes very large and lateral separations above $\sim 100\,\mathrm{m}$ can be potentially produced from lower transverse momenta, below $p_{T,min} = 1.0\,\mathrm{GeV/c}$. This contribution is not simulated in the context of LSMuonSim, which presumably causes further underestimation of the simulated LS Muon rate towards large zenith angle directions.

In contrast, CORSIKA significantly underestimates the rate of vertical showers and overestimates the event rate towards horizontal arrival directions. The resulting data/MC discrepancy is on the order of $\pm 80\%$, in agreement with previous results using data from IceCube in its 59-string configuration [83]. In addition, similar effects have been reported by various analyses of high-energy atmospheric muons measured in IceCube [52, 54], with data/MC discrepancies on the order of roughly $\sim 20\%$. These zenith angle discrepancies of simulated atmospheric muons, compared to experimental data observed in IceCube, are not yet understood.

Figure 7.10 shows the resulting LS Muon zenith angle distributions at final filter level for various first interaction heights of the incident cosmic ray nuclei,

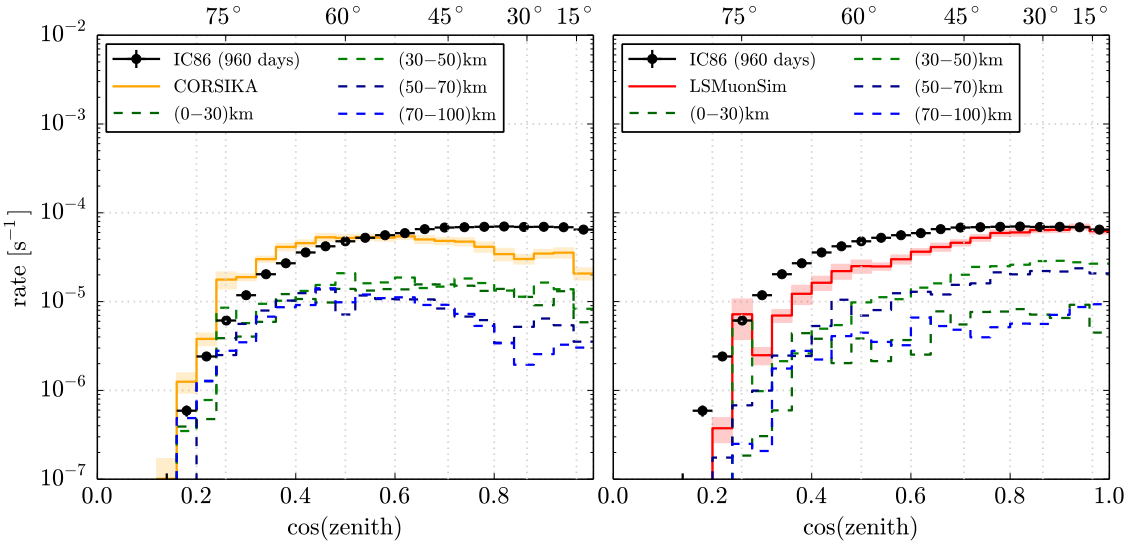

Figure 7.10: Zenith angle distribution from various altitudes, obtained from 960 days of data and CORSIKA (left) and LSMuonSim simulations (right) at final filter level. Dashed lines show the contributions of LS Muon events ($d_{T,true} \geqslant 100\,m$) from different interaction heights.

obtained from simulations. The dashed lines show the contributions from signal events ($d_{T,true} \geqslant 100\,m$) only. The simulated distributions show significant differences between CORSIKA (left) and LSMuonSim (right) simulations. While the CORSIKA predictions show a unnatural suppression of events around $\theta \simeq 30°$, especially towards large altitudes, the distributions obtained from LSMuonSim do not show any unexpected behaviour. Moreover, the CORSIKA distributions show an excess of events from high altitudes ($H > 50\,m$) towards large zenith angle directions.

As described in Section 2.2.1, the atmospheric muon flux depends on the underlying atmospheric model and thus on the height of production. Due to the selection of large separations, the distributions of LS Muons additionally depend on the zenith angle and height of production according to Equation (2.36). The interaction height distributions of events at final analysis level, obtained from CORSIKA (left) and LSMuonSim (right) simulations, are shown in Figure 7.11.

As expected from the relation between lateral separation and height of production, given in Equation (2.36), the selection of LS Muon events causes a selection of showers from high altitudes. This is because the high-p_T muon has more time to separate from the shower core while traveling to the detector. The mean altitude of the first interaction of the events at final filter level is expected to be about ~ 52 km (~ 49 km), based on LSMuonSim (CORSIKA) predictions. Hence, this dataset enables unique studies of extensive air showers initiated at very high altitudes and consequently yields information about the upper atmospheric layers.

However, the CORSIKA simulations once more show an unnatural behaviour for altitudes above ~ 50 km, especially towards horizontal zenith angle direc-

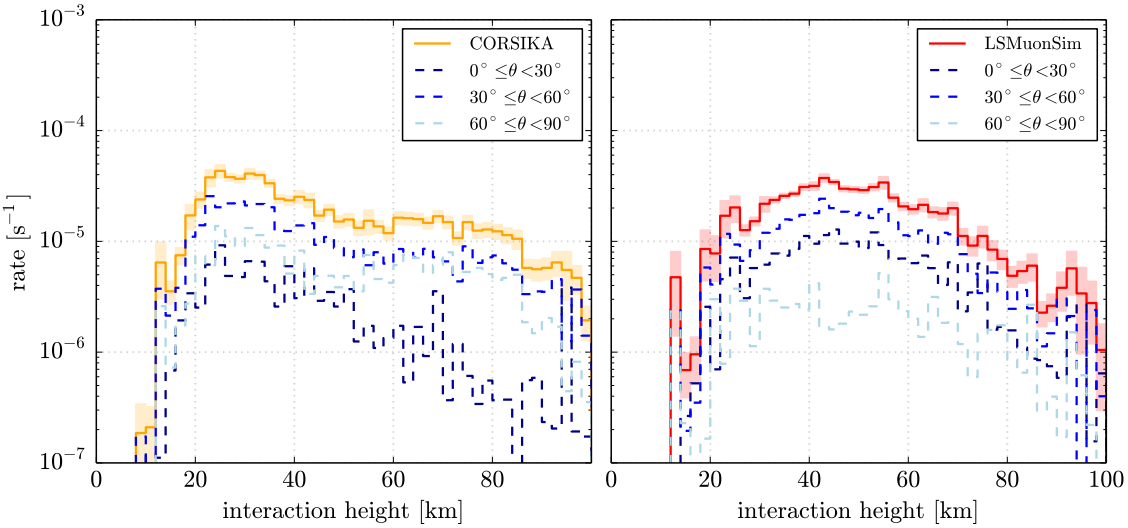

Figure 7.11: Interaction height distribution for various zenith angle directions, obtained from 960 days of data and from CORSIKA (left) and LSMuonSim (right) simulations at final filter level. Dashed lines show the contributions of LS Muon events ($d_{T,true} \geqslant 100\,m$) from different zenith angle regions.

tions. As described in Chapter 5, CORSIKA uses the MSIS 5-layer model of the South Pole atmosphere. In contrast, LSMuonSim uses a mixed model with the first interaction probability obtained from the underlying CORSIKA shower, which is based on the MSIS models, and a simple isothermal model in order to calculate the re-interaction and decay probabilities of hadrons in the atmosphere (see Section 5.4.5). Moreover, CORSIKA explicitly accounts for the curvature of the atmosphere, while LSMuonSim uses the approximation introduced in Section 2.2.1. Hence, there are significant differences in the modeling of the atmosphere between both MC approaches, which is one possible explanation for the zenith angle discrepancy between CORSIKA and LSMuonSim predictions. In turn, the data/MC discrepancies observed in various analyses of atmospheric muons may also be related to the atmospheric model, which has not yet been seriously considered in previous analyses. Several additional distributions of the simulated interaction height can be found in Appendix C.10.

Figure 7.12 shows the zenith angle distributions for the four annual seasons used in CORSIKA simulations and described in Section 2.2.1 and Section A.2. The corresponding data/MC-ratios are shown in Figure 7.13, with linear fits of the form $R(\theta) = \alpha \cdot \cos(\theta) + \beta$ shown as colored dashed lines. The MC distributions agree best with data taken between February and May. The discrepancies for data taken between November and February in the total rate, as well as in the slope of the ratios, are clearly the largest. Hence, the zenith angle discrepancies show a relation to the annual variations which depend on the underlying atmospheric model. However, for none of the annual seasons the MC simulations describe the corresponding data within uncertainties. Studies on further MC

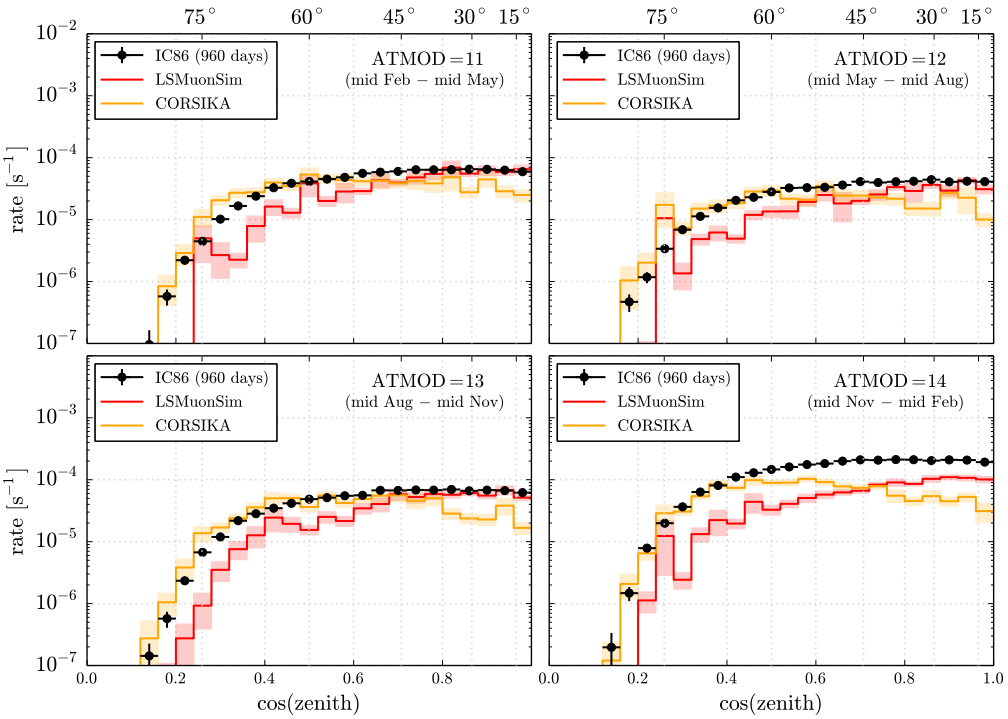

Figure 7.12: Zenith angle distributions for the seasons, obtained from experimental data, as well as LSMuonSim and CORSIKA, at final filter level. The ATMOD parameter corresponds to the identifier used within the CORSIKA package.

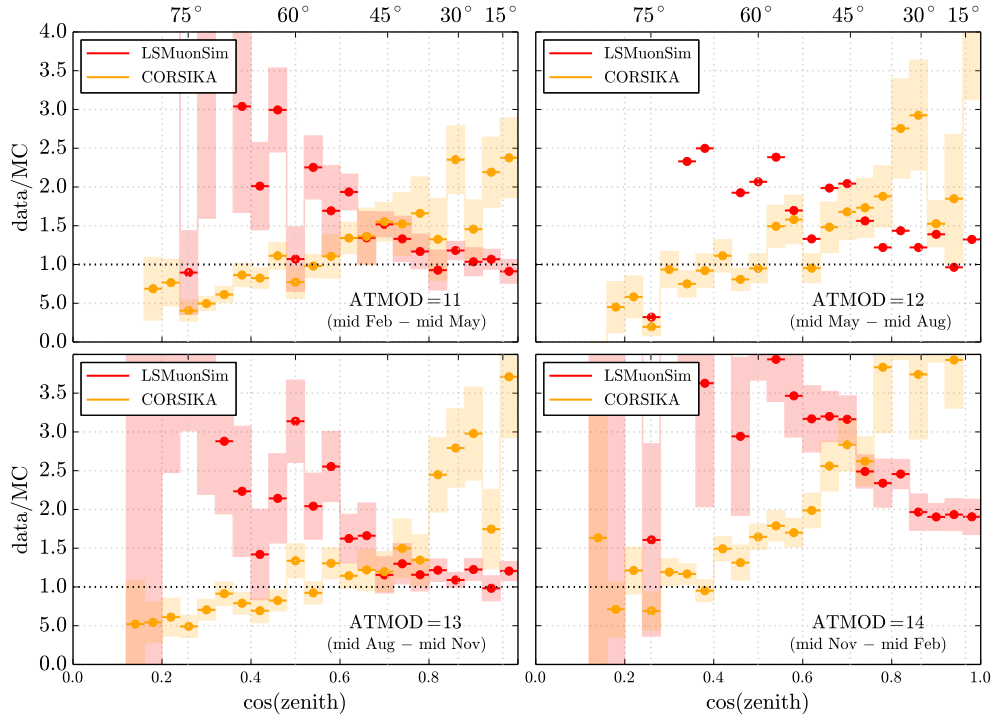

Figure 7.13: Data/MC-ratio of the zenith angle distribution for the seasons, obtained from LSMuonSim and CORSIKA, at final filter level.

model assumptions, potentially effecting the zenith angle distributions at final analysis level, are discussed in Section 7.7.2.

The contributions from various primary nuclei, using the H3A flux assumption, are shown in Appendix C.2, where no significant effect of different primary nuclei on the zenith angle distribution is observed. Further distributions of the zenith angle distributions at several filter levels, as well as on the surface, can also be found in Appendix C.2.

7.4 TRANSVERSE MOMENTUM

As described in Section 6.8, the estimation of the underlying transverse momentum of LS MUONS in ICECUBE relies on an estimate of energy and height of production. Therefore, the height of production $\langle H(\theta) \rangle$ of high-p_T hadrons is approximated with the mean interaction height as a function of the zenith angle direction, as described in Section 6.8. The mean LS MUON energies $\langle E_\mu \rangle_i$ are obtained from LSMUONSIM (EPOS-LHC), for each energy bin i separately, and they are given in Table 7.4. In order to derive the transverse momentum distributions, all events at final analysis level and with zenith angle directions below $\theta_{max} = 60^\circ$ are used.

The resulting transverse momentum distributions, measured in the ice, are shown in Figure C.48, for each energy bin separately. The reconstructed p_T spectra show a suppression towards low transverse momenta, which is caused by the lateral separation cut of $d_T \geqslant 135\,\text{m}$. Therefore, the corresponding Hagedorn fits of the form of Equation (2.34) are applied to events with transverse momentum above $p_{T,min} = 2.5\,\text{GeV/c}$ only. The distributions are fit with the transition parameter fixed to $p_0 = 2\,\text{GeV/c}$ in a first step, where α and β are free parameters (dotted lines). This is done in order to ensure that the minimalization procedure converges during fitting. In a second step the distributions are re-fit with the normalization parameter α fixed to the value obtained from the previous fit and with β and p_0 as free parameters. Figure C.48 shows the resulting Hagedorn fits (solid lines), as well as the corresponding fits applied to the (true) simulated distributions, obtained from LSMUONSIM using EPOS-LHC (dashed lines). The resulting best fit parameters are given in Appendix C.7.

The transverse momentum distributions at surface level are estimated, using the effective areas introduced in Section 6.9. The resulting Hagedorn fits, derived from the two-step procedure described above, accounting for events above $p_{T,min} = 2.0\,\text{GeV/c}$, are shown in Figure 7.15 (left panel, solid lines). The

	$\langle E_0 \rangle_{tot}$	$\langle E_0 \rangle_1$	$\langle E_0 \rangle_2$	$\langle E_0 \rangle_3$	$\langle E_0 \rangle_4$
$\langle E_\mu \rangle$ [TeV]	1.04 ± 0.32	1.06 ± 0.37	1.02 ± 0.34	1.01 ± 0.36	1.01 ± 0.37

Table 7.4: Mean LS MUON energies for each energy bin, used for the transverse momentum estimator, as described in the text ($\theta \leqslant 60^\circ$). The means are obtained from LSMUONSIM, using EPOS-LHC as hadronic model.

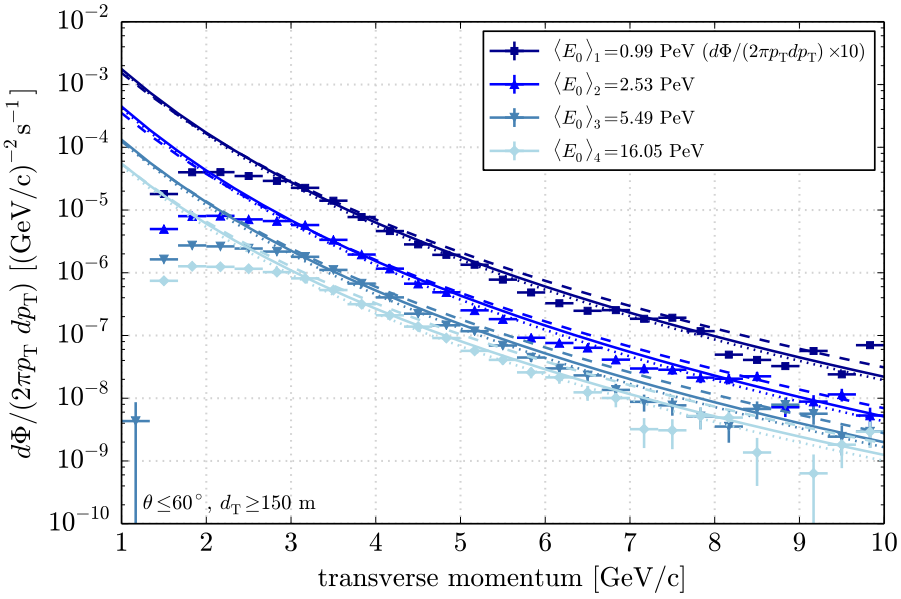

Figure 7.14: Transverse momentum distribution at final filter level (L5) in the ice for several primary energy bins. The Hagedorn fits shown as solid lines are applied for events above $p_{T,min} = 2.5\,GeV/c$. The fits using $p_0 = 2\,GeV/c$ (dotted) and for the true LSMuonSim distributions (L5) are also shown.

fit parameters are given in Table C.2. The corresponding fits obtained from the true MC distributions of LSMuonSim are also shown (dashed lines), as well as the data fits using $p_0 = 2\,GeV/c$ (dotted lines). The right-hand panel shows the corresponding fits applied to transverse momentum distributions of hadrons, produced at various accelerator experiments [66–69]. While the LS Muon distributions are produced from hadronic nucleus-nucleus collisions at various primary energies, involving heavy nuclei, these measurements represent hadron distributions from proton-proton collisions at center-of-mass energies $\sqrt{s}$. The resulting fit parameters for ATLAS data are given in Table 7.6 and they are qualitatively in good agreement with the fits obtained from the LS Muon distributions. LS Muon distributions favor a transition from an exponential to a power law at about $p_0 \simeq (2.1 \pm 0.2)\,GeV/c$. This is in correspondence to the mea-

Primary energy	α [(GeV/c)$^{-2}$m^{-2}sr^{-1}s^{-1}]	β	p_0 [GeV/c]
$\langle E_0 \rangle_1$	142.7 ± 26.4	-10.3 ± 0.5	2.08 ± 0.15
$\langle E_0 \rangle_2$	9.3 ± 2.6	-9.2 ± 0.8	2.14 ± 0.27
$\langle E_0 \rangle_3$	2.3 ± 0.6	-9.2 ± 0.7	2.13 ± 0.24
$\langle E_0 \rangle_4$	1.1 ± 0.3	-9.1 ± 0.6	2.13 ± 0.23

Table 7.5: Transverse momentum Hagedorn fit parameters for the fits of the form Equation (2.34), applied to LS Muon events above $p_{T,min} = 2.0\,GeV/c$, as shown in Figure 7.15.

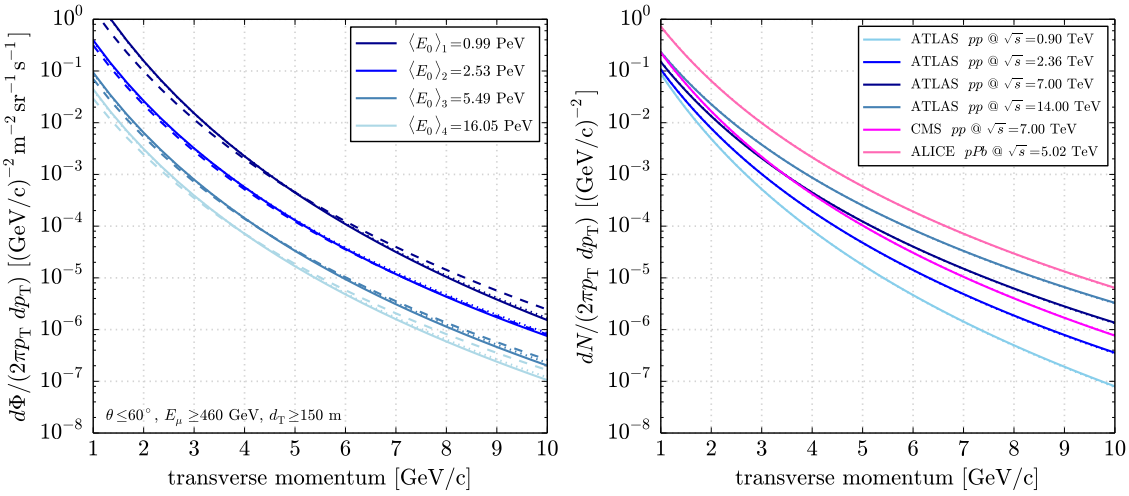

Figure 7.15: Hagedorn fits applied to the reconstructed p_T distributions at surface level for several primary energy bins (left). The fits are shown for 960 days of data (solid) and obtained from the true LSMuonSim distributions (dashed). The fits using $p_0 = 2\,\text{GeV/c}$ are also shown (dotted). Various Hagedorn distributions, obtained from accelerator data [66–69], are also shown (right).

surements at collider experiments. In addition, the spectral indices are on the order of $\beta = -10.3 \pm 0.5$ to $\beta = -9.1 \pm 0.6$, increasing towards higher collision energies, as expected from PQCD (see Section 2.4). This is also observed for the accelerator data, as shown in Table 7.6. Since the spectral indices depend on the mass of the initial particle, the systematically steeper LS Muon distributions, compared to the collider data, may be related to heavier primary cosmic ray nuclei, especially towards larger primary energies where the cosmic ray spectrum is expected to become heavier.

Due to the suppression towards low p_T, the resulting fits strongly depend on the region where the fit is applied. Moreover, the reconstruction of the transverse momentum may be significantly improved using more sophisticated reconstructions, such as likelihood methods, and by including improved estimates of the LS Muon energies and the hadron production height. Further systematic studies are needed in order to analyze the final uncertainties of the method in more detail.

$\sqrt{s}$	α [(GeV/c)$^{-2}$]	β	p_0 [GeV/c]
0.9 TeV	5.2 ± 0.7	-10.0 ± 0.3	1.97 ± 0.08
2.36 TeV	4.3 ± 1.4	-9.1 ± 0.6	1.98 ± 0.23
7.0 TeV	4.6 ± 0.5	-8.3 ± 0.2	1.97 ± 0.07
14.0 TeV	6.1 ± 0.5	-8.0 ± 0.2	1.97 ± 0.06

Table 7.6: Transverse momentum Hagedorn fit parameters for the fits of the form Equation (2.34), as shown in Figure 7.15, applied to ATLAS data [66, 67].

7.5 COSMIC RAY MASS COMPOSITION

As described in Section 2.4, the transverse momentum of hadrons generally depends on the incident particle and the resulting distributions therefore depend on the elementary mass composition of cosmic rays. Consequently, the corresponding lateral separation distributions also depend on the incident primary cosmic ray since, to a certain degree, they follow the p_T distributions of the parent hadrons. Hence, the LS MUON data sample at final analysis level can be used to derive the mass composition of cosmic rays. The contribution from different primary particles to the lateral separation distributions at final filter level, measured in the deep ice detector and assuming the H3A primary flux, using LSMUONSIM, are shown in Figure 7.16. The distributions are shown for each energy bin separately, with the background subtraction as introduced in Section 7.2. The corresponding distributions using various primary flux assumptions, as well as distributions at surface level, can be found in Appendix C.1. As expected from the H3A flux parametrization introduced in Section 2.1.4, at the lowest energies the the mean mass composition is rather light, strongly dominated by helium, while it becomes heavier towards high energies, where the mean composition is dominated by iron nuclei.

In order to derive the primary composition from the LS MUON data sample at final analysis level, the MC distributions are re-weighted to a pure composition assumption, as described in Section 5.3. A simple broken power law of the form Equation (2.9) is assumed, where the parameters are taken from Ref. [46]. The resulting distributions after background subtraction can be found in Figure 7.17, shown for each primary energy bin separately. The corresponding distributions at surface level can be found in Appendix C.1.

The distributions of each individual element are fit with a Hagedorn function of the form Equation (7.1) with $C = 0$, shown in Figure 7.17 as lines, and normalized to one in order to reflect the corresponding probability distributions $d\Phi_{i,\text{norm}}/d(d_T)$ for each primary type i. Only events with lateral separations above 250 m are considered because the distributions show a suppression towards smaller separations for all elements shown in Figure 7.17. The simulated distributions are not properly described by Hagedorn functions towards small lateral separations below 250 m. Assuming that the data represents a superposition of these five primary elements, a least-square fit of the form

$$\frac{d\Phi_{\text{data}}}{d(d_T)} = \sum_i \alpha_i \cdot \frac{d\Phi_{i,\text{norm}}}{d(d_T)} \tag{7.2}$$

is applied, for the $i = 1, \ldots, 5$ primary mass components. The resulting α_i give the normalization of each primary particle type and therefore they represent the abundance of each individual element considered. This approach is used to derive the resulting mean logarithmic mass number $\langle \ln A \rangle$, which best describes the experimental data. The resulting $\langle \ln A \rangle$ measured in-ice is shown in Figure 7.18 for each reconstructed primary energy bin separately (black squares). The mean mass number obtained from LSMUONSIM, using the H3A primary

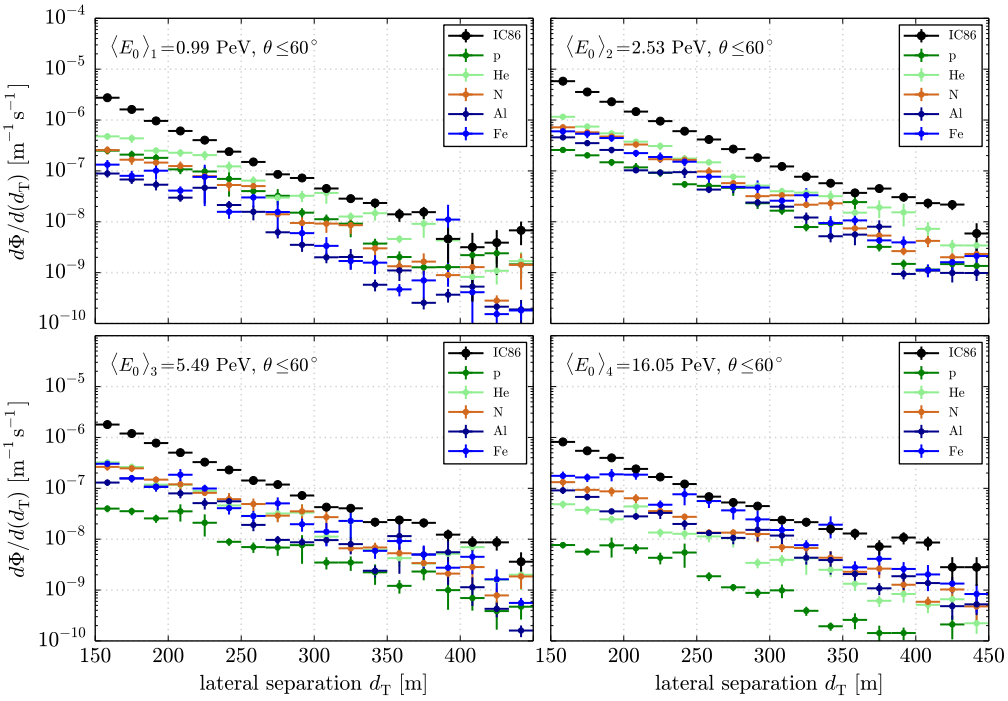

Figure 7.16: Cosmic ray mass composition of all events with $\theta \leqslant 60°$ at final filter level, assuming the H3a primary flux assumption, obtained from LSMuonSim (EPOS-LHC).

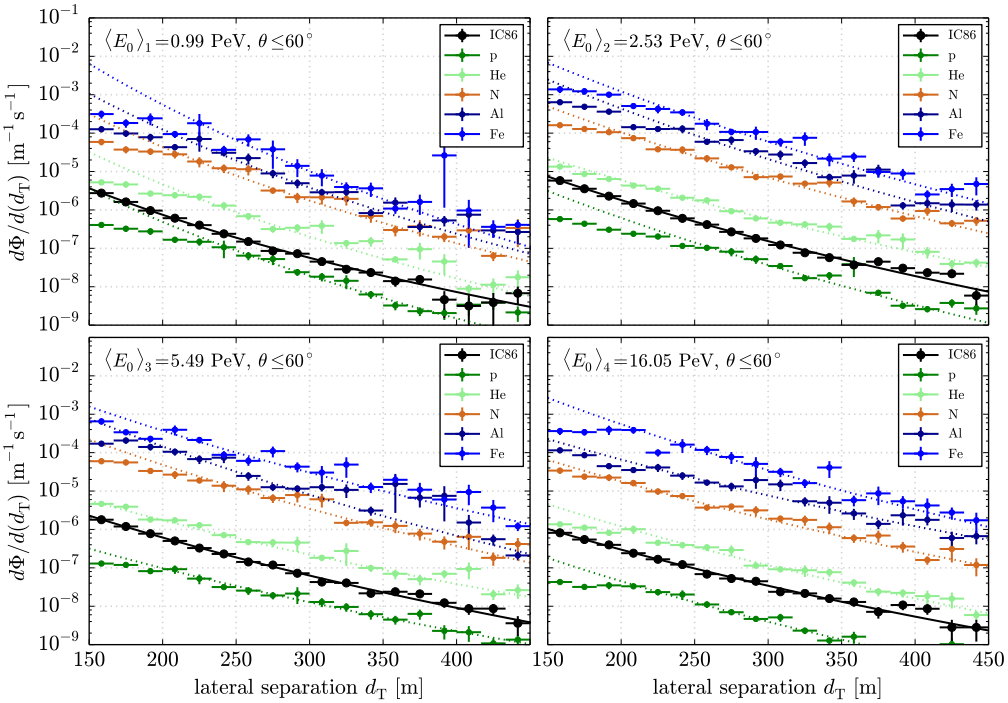

Figure 7.17: Cosmic ray mass composition of all events with $\theta \leqslant 60°$ at final filter level, assuming pure composition flux assumptions, as described in Ref. [46]. See text for details.

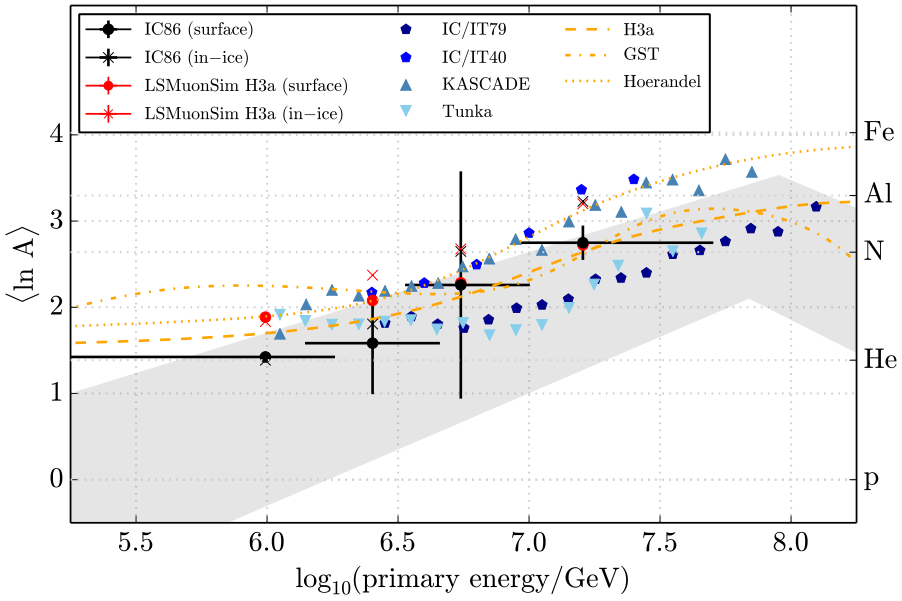

Figure 7.18: Mean mass number $\langle \ln A \rangle$ obtained from LS Muon events at final filter level, as well as from other experiments and theoretical flux assumptions. The external data is taken from Refs. [43, 217, 218] and does not include error estimates. The grey band represents compiled results from various optical measurements, as described in Ref. [43].

flux assumption as shown in Figure 7.16, is also shown for the distributions in the ice (crosses) and on the surface (circles). The MC in-ice predictions show a shift towards higher mass numbers with increasing energy. Thus, the resulting composition estimate is corrected by a factor $s = \langle \ln A \rangle_{\text{surface}} / \langle \ln A \rangle_{\text{in-ice}}$ in order to reflect the cosmic ray mass composition at surface level (black circles). Thereby it is assumed that the shift of the measured data between surface level and the deep ice detector corresponds to a shift obtained from MC distributions using the H3a flux assumption. The mean elementary mass of cosmic ray nuclei increases with increasing primary energies in the range of roughly $10^{5.5}$ GeV to $10^{8.0}$ GeV. As discussed in Section 7.7.3, the systematic uncertainties on the correction factor s, using different flux assumptions, are on the order of roughly 6%. Hence, there is no significant change in the surface correction expected due to different composition assumptions. The correction factors for several primary flux models are also shown in Section 7.7.3.

Previous results from IceCube in its 40-string and 79-string configurations [217, 218], using the in-ice detector together with the surface array IceTop, are also shown in Figure 7.18 (IC/IT). In addition, results from the KASCADE, and the Tunka experiments are shown, as well as a combined uncertainty band from various optical measurements, all taken from Ref. [43]. Several primary flux assumptions, as described in Section 2.1.4 and taken from Refs. [13, 38, 39], are also shown (orange lines). The mean logarithmic mass spectrum, derived from

the LS MUON events at final analysis level, is qualitatively in agreement with other measurements, as well as with various flux model predictions.

However, due to the limited statistics of the underlying MC distributions, the uncertainties of the measured $\langle \ln A \rangle$ spectrum are rather large with $\Delta\langle \ln A \rangle \simeq 1$. In addition, the results strongly depend on the goodness of the Hagedorn fits and on the range where the fits are applied. Moreover, to get an estimate of the mass composition at surface level, the effect of the in-ice propagation on the $\langle \ln A \rangle$ needs to be systematically studied in more detail, for example using various primary flux assumptions and energy binnings. Thus, in order to draw final conclusions on the robustness of this method and to get an estimate of the potentially very large systematic uncertainties, further studies are needed. However, this preliminary result agrees with previous measurements and theoretical flux predictions within uncertainties and represents the first estimate of the cosmic ray mass composition using laterally separated muons in ICECUBE.

This measurement can be further improved for future analyses by using higher MC statistics in order to improve, for example, the robustness of the Hagedorn fits for each element. Moreover, the estimation of the underlying primary energies is based on a fit applied to a mixed composition, assuming an H3A spectrum, as described in Section 6.7. Since the deposited energy of the air shower in ICECUBE is expected to depend on the mass of the primary nucleus, this can lead to a mass dependence of the reconstructed primary energy and may consequently influence the mass composition within each energy bin. Hence, a more sophisticated energy estimator, accounting for different primary particle types, will further enhance the precision of the reconstructed energy in future analyses and would thereby improve subsequent composition studies using LS MUONS.

7.6 SEASONAL VARIATIONS

As discussed in Section 2.2.2 and Section 2.3, the hadron production in the atmosphere depends on the atmospheric density profile. Therefore, the subsequent flux of muons is effected by seasonal variations in the atmosphere. According to Equation (2.21), a lower atmospheric density, and in turn a lower temperature, leads to a larger number of mesons decaying into muons. The seasonal variations of the atmospheric muon flux has been previously measured by various deep underground experiments, such as AMANDA [219], ICECUBE [220], BOREXINO [221], and MACRO [222]. These fluctuations are typically on the order of about $\pm 10\%$.

The seasonal variations of the three year data sample at final level (L5) of this analysis are shown in Figure 7.19. In addition the predictions from CORSIKA and LSMUONSIM simulations are displayed. The CORSIKA simulations use the 5-layer parametrizations of the MSIS atmospheric model, as described in Section 5.1 and Appendix A.2. LSMUONSIM uses a mixed model, where the first interaction is obtained from CORSIKA and therefore also uses the MSIS models,

while the propagation and decay, resulting in the production of an LS MUON, is based on a simple isothermal model (see Section 5.4.5). The resulting distribution is fit with a sinus function of the form

$$f(x) = a \cdot \sin(\varphi \cdot x + b) + c \,, \tag{7.3}$$

where a, b, and c are free parameters. The phase parameter $\varphi = 2\pi/12$ is fixed to the seasonal phase of one year. The seasonal variations at final filter level are on the order of $\pm 50\%$, which is significantly larger than the fluctuations observed in other analyses of atmospheric muons. This is because LS MUONS are typically produced at very high altitudes in order to produce large lateral separations from the shower core. Based on LSMUONSIM, the mean first interaction height in this analysis is roughly 51 km, as shown in Figure 7.11 and Figure 6.15, and LS MUONS are then typically produced early during shower development. The resulting seasonal variations are also shown in Figure 7.20 (top panel), where in addition the temperature fluctuations in the atmosphere at the South Pole are shown for various atmospheric layers (center panel). The temperature data, shown in this work, is taken from the NASA AIRS experiment [223], and further details can be found in Appendix A.6. The layers are given by their atmospheric pressure, which is directly related to the altitude, as described in Appendix A.6. The resulting fluctuations of the LS MUON rate, as well as of the temperatures at different atmospheric altitudes, are shown in Figure 7.20 (bottom panel).

As described in Refs. [98, 220], the relation of muon fluxes and temperature of the atmosphere are related through a *atmospheric temperature coefficient* α_T, which is given by

$$\frac{\Delta\Phi}{\langle\Phi\rangle} = \alpha_T \cdot \frac{\Delta T}{\langle T\rangle} \,, \tag{7.4}$$

where $\Delta x = x - \langle x\rangle$, with $\langle x\rangle$ the mean value of $x \in \{\Phi, T\}$. Figure 7.21 shows the variation of the LS MUON event rate on final analysis level $\Delta\Phi/\langle\Phi\rangle$ as a function of the temperature fluctuations $\Delta T/\langle T\rangle$ in different atmospheric layers. The resulting linear best fits of the form Equation (7.4) are also shown, with the corresponding temperature coefficients of the different layers given in Table 7.7.

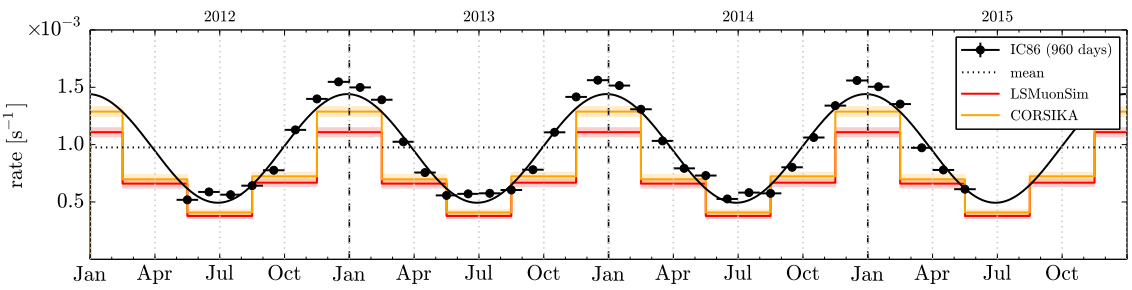

Figure 7.19: Seasonal variations of the event rate at final filter level (L5) obtained from 960 days of data and from MC simulations. The mean event rate at final level (dotted line) is also shown.

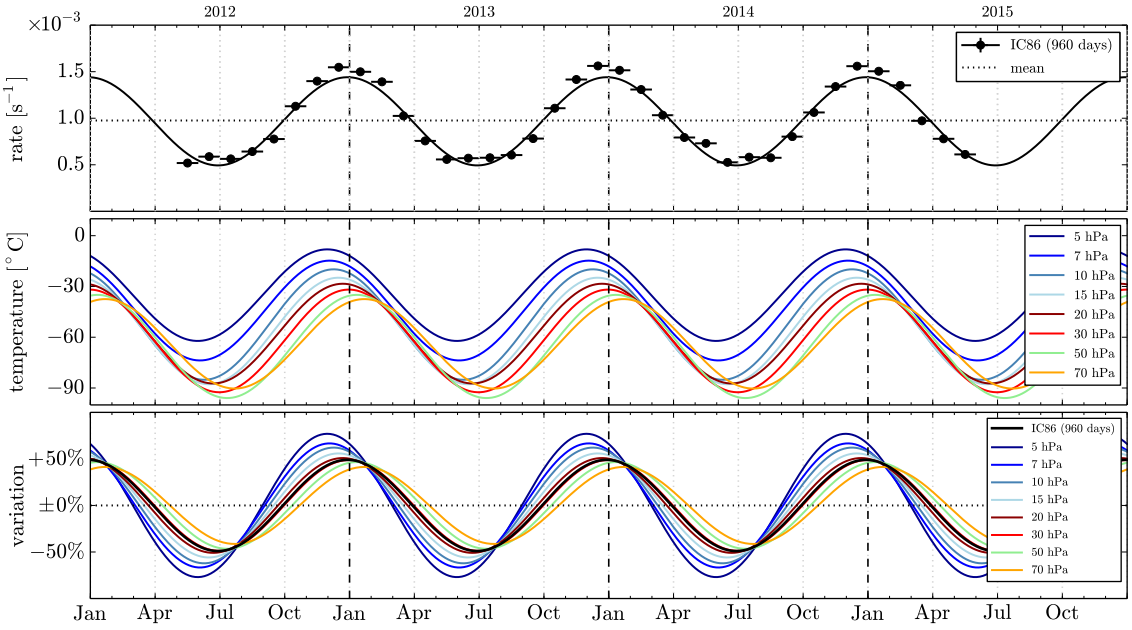

Figure 7.20: Seasonal variations of the event rate at final filter level (L5) obtained from 960 days of data (top), as well as temperature variations in various atmospheric layers (center). The corresponding variations are combined in the bottom panel.

The highest correlation is observed for temperature data approximately in the 30 hPa layer.

Figure 7.22 shows the time at which the maxima of temperature variations for different atmospheric layers occur, obtained from the sinus fits shown in Figure 7.20. The resulting distribution is fit with an exponential (solid line). Using this fit, the maximum of the LS MUON rate fluctuations is used to derive a corresponding atmospheric pressure for the experimental data. This is done at final filter level (L5), as well as for events passing the pre-selection (L0). The variation maximum at final level appears earlier in the year, compared to the variations at L0. This corresponds to a shift of the LS MUON production height towards higher atmospheric altitudes around 30 hPa, as generally expected from previous discussions. The corresponding altitudes are calculated, using a simple barometric formula [33] (Figure 7.22, right axis). Based on this approximation, the resulting estimated mean hight of LS MUON production is roughly 30.1 km. As shown in Appendix C.10, the mean height of production of LS MUONS, ob-

layer	15 hPa	20 hPa	30 hPa	50 hPa	70 hPa
α_T	0.86 ± 0.05	0.95 ± 0.05	1.02 ± 0.05	1.09 ± 0.06	1.17 ± 0.09

Table 7.7: Atmospheric temperature coefficients obtained from final level events, as defined in Equation (7.4) and shown in Figure 7.21.

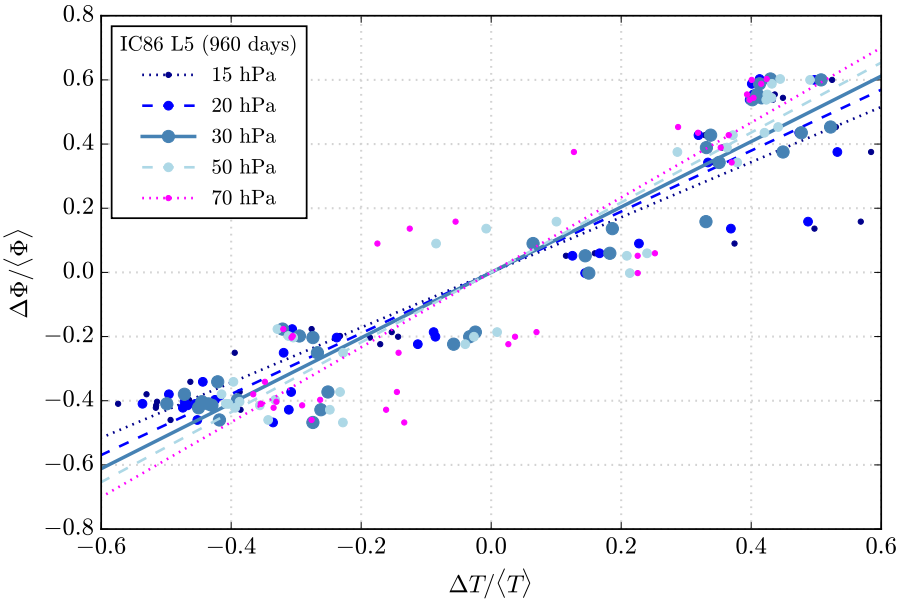

Figure 7.21: Temperature coefficients for various atmospheric layers, as defined in Equation (7.4) (see text for details). The corresponding coefficients are given in Table 7.7.

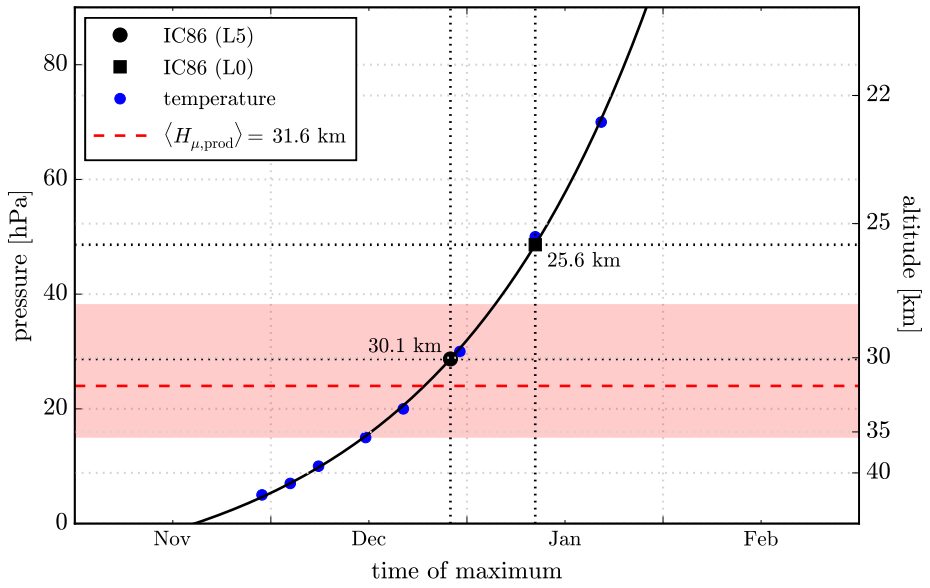

Figure 7.22: Time of the maximum temperature variations, obtained from the sinus fits, shown in Figure 7.21 (blue points). The solid line represents an exponential fit and black points show the time of the maximum data rate at L5 (circle) and L0 (square). The right axis shows the corresponding altitudes, obtained using a simple barometric formula. The height of LS MUON production is also shown, obtained from LSMUONSIM and including error bands.

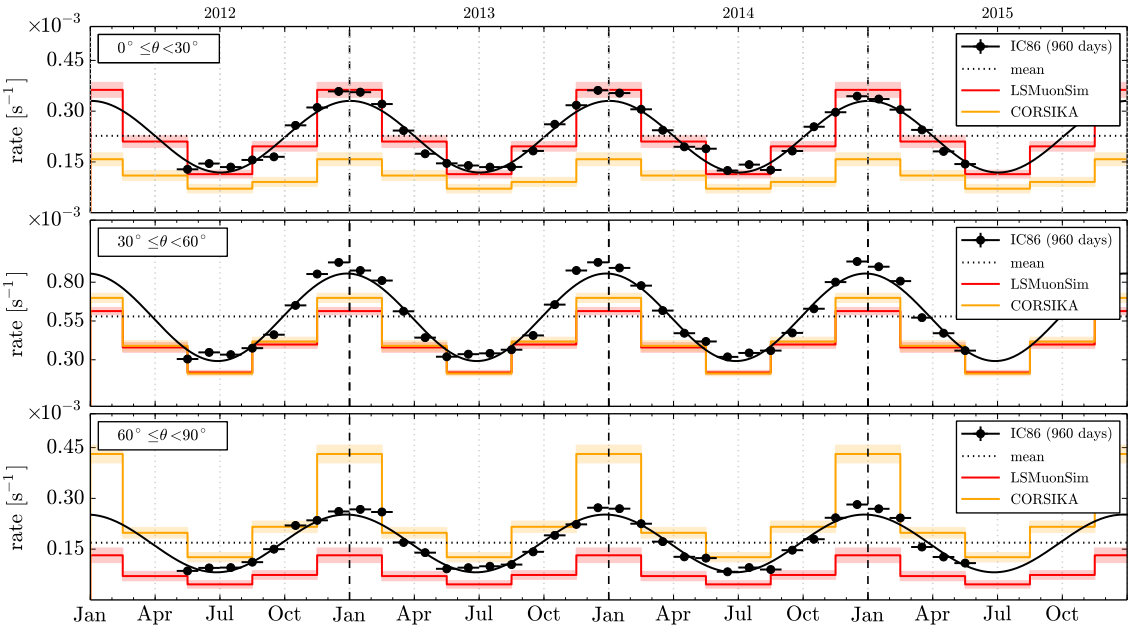

Figure 7.23: Seasonal variations of the event rate at final filter level (L5) obtained from 960 days of data, as well as from MC simulations, for various zenith angle regions. The center panel shows a different y-scale than top and bottom panel.

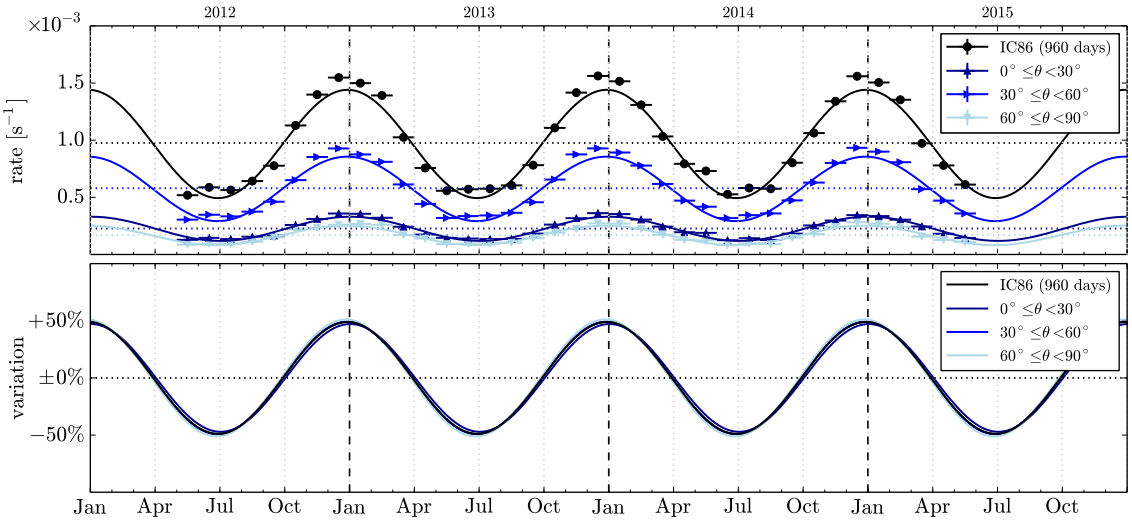

Figure 7.24: Seasonal variations of the event rate at final filter level (L5), obtained from 960 days of data for various zenith angle regions (top). The resulting percentile seasonal variations are shown in the bottom panel and are in good agreement for all zenith angle directions.

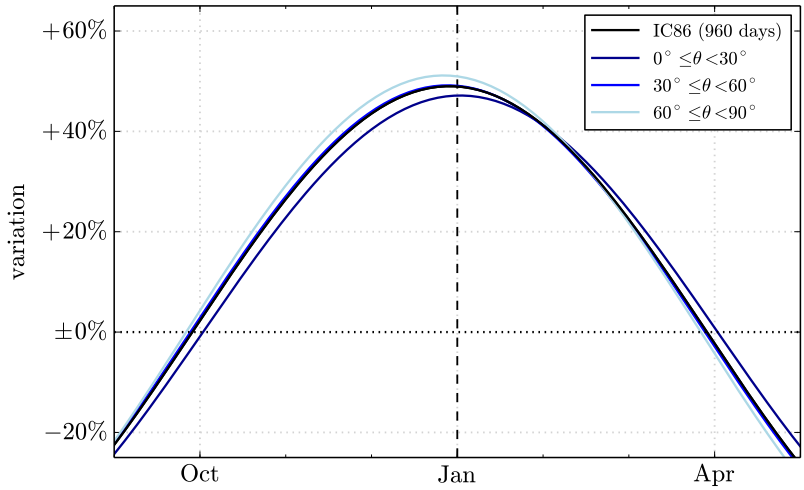

Figure 7.25: Seasonal variations of the total event rate at final filter level (L5), obtained from 960 days of data (dotted), and for various zenith angle regions, between October and April (blue lines).

tained from LSMuonSim, is approximately $\langle H_{\mu,\text{prod}} \rangle = (31.6 \pm 3.9)$ km. Within uncertainties this is in agreement with the production height obtained using the maxima of the seasonal variations, as shown in Figure 7.22. The somewhat smaller production heights obtained from the seasonal variations may be caused by background events, which are not included in the MC estimate from LSMuonSim. However, the barometric formula assumes a constant temperature, constant composition, and an ideal gas for the atmosphere. Hence, in order to draw final conclusions on the LS Muon production height, further studies are needed, using for example experimental data of the atmospheric pressure as a function of the altitude.

A comparison between the observed annual fluctuations for various zenith angle directions and the corresponding predictions from MC simulations can be found in Figure 7.23. As expected from previous discussions in Section 7.3, the variations of more vertical LS Muon fluxes are in very good agreement with LSMuonSim predictions, while the rate is significantly underestimated towards large inclinations. CORSIKA shows significant differences in the total rates, compared to experimental data, for all angular regions and the zenith angle distributions strongly depend on the season, as also shown in Figure 7.12. Hence, observation of the seasonal variations qualitatively favor an atmospheric model, as described by LSMuonSim, especially towards vertical angles. However, as discussed above, further studies on the modeling of the atmosphere are necessary in order to draw final conclusions on the data/MC discrepancies observed in this and other analyses of atmospheric muons in IceCube.

Figure 7.24 shows the resulting seasonal variations of the observed LS Muon flux at final filter level for several zenith angle regions (top panel), as well as the corresponding percentile fluctuations (bottom panel). A closer view of the variations between October and April is shown in Figure 7.25, where a shift of

the maxima and different amplitudes for various zenith angles can be observed. This is because the hadrons travel larger distances in higher atmospheric layers towards large zenith angles and thus the resulting muons are produced at higher altitudes. These experimentally observed fluctuations are in correspondence with increasing first interaction heights towards large zenith angles, as previously discussed for the MC predictions in Figure 6.15.

7.7 SYSTEMATIC UNCERTAINTIES

In order to account for systematic uncertainties of the distributions at final filter level, various effects are studied, which may cause systematic shifts in the observed distributions. The DOM efficiency is studied in detail to get an estimate on the light yield measured in the ice. In addition, the influence of the hadronic models, used in LS MUON simulations are discussed. Finally, various primary flux assumptions are studied. These systematic effects are discussed in the following, with special emphasis on the lateral separation in Section 7.7.1 and on the zenith angle distributions in Section 7.7.2. The systematics are only studied for the LS MUON signal contribution ($d_{T,true} \geqslant 100\,m$), obtained from LSMUONSIM, because there are no dedicated background simulations from CORSIKA available at final filter level to produce meaningful systematic results. However, when it is possible to use a simple re-weighting rather than dedicated simulations, systematic uncertainties are also derived for CORSIKA simulations. The baseline background contribution is shown in the following figures in order to compare to experimental data.

7.7.1 LATERAL SEPARATION

Systematic uncertainties on the lateral separation distribution are discussed in the following. The resulting uncertainties on the Hagedorn fits are given in Table 7.8. The total uncertainty estimates are calculated by adding the individual uncertainties quadratically.

DOM Efficiency

The efficiency model of the ICECUBE DOMs is determined from *in-situ* measurements, using the Cherenkov light produced by muons in the ice [224]. It includes effects of the cable shadowing, as well as the properties of the refrozen ice surrounding the DOMs. Using these measurements, the uncertainties of the baseline DOM efficiency, used in MC simulations, is measured to be roughly $\pm 10\%$. In order to study the effect of the DOM efficiency, the simulations are therefore performed with efficiencies modified by $\pm 10\%$. Existing systematic datasets produced with CORSIKA are rather small and only a few events remain at final filter level of this analysis. Thus, the following studies are mainly based on LSMUONSIM.

Systematics	$\Delta\alpha/\alpha$	$\Delta\beta/\beta$	$\Delta d_0/d_0$	$\Delta\langle E_0\rangle/\langle E_0\rangle$
CORSIKA (L2)				
DOMeff +10%	+24.4%	–	–	+19.5%
DOMeff −10%	−35.7%	–	–	−14.1%
LSMuonSim (L5)				
DOMeff +10%	+4.5%	$< +1\%$	$< +1\%$	+1.6%
DOMeff −10%	−28.2%	−5.5%	−1.1%	$< -1\%$
Hadronic model	–	–	–	+7.4% ($< \pm 2\%$)
Primary flux	–	–	–	$< \pm 1\%$
Total	+24.8%	+1.0%	+1.0%	+20.9%
	−45.5%	−5.5%	−1.1%	−14.3%

Table 7.8: Systematic uncertainties on the Hagedorn fit parameters, as well as on the primary energy estimator, as described in the text.

The lateral separation distributions, obtained from CORSIKA and LSMuonSim, using the baseline DOM efficiency, are shown in Figure 7.26. The resulting distributions for LSMuonSim, using systematic uncertainties of ±10%, are also shown. The uncertainties on the corresponding Hagedorn fit parameters, as well as on the primary energy reconstruction, are shown in Table 7.8. For the normalization parameter α and the energy reconstruction, uncertainties obtained from CORSIKA are also included. This is done by deriving the uncertainties at a lower filter level (L2) due to the lack of statistics at higher levels. The uncertainties on the α parameter are derived from the total flux estimates.

Hadronic Interaction Model

Figure 7.27 shows the lateral separation obtained from LSMuonSim, using various hadronic models, which are described in Section 5.2. Thereby only the generation of the LS Muon is effected while the muon bundle remains unchanged. While EPOS-LHC describes the data well, Sibyll 2.1 underestimates the rate of LS Muon events. QGSJet II-4 on the other hand highly overestimates the event rate, especially towards large separations. This is due to significantly flatter transverse momentum distributions, as shown in Figure 5.5 and as expected from the spectral indices given in Appendix B.1. Although LSMuonSim seems to underestimate the event rate for low separations below ~ 200 m, the agreement between CORSIKA (Sibyll 2.1) and LSMuonSim, using Sibyll as hadronic model, is remarkably good. The uncertainties from the hadronic models on the primary energy estimator, which depends on MC simulations, can be found in Table 7.8. They are below 2% while the differences between CORSIKA and LSMuonSim are 7.4%. Hence, the latter is taken as systematic uncertainty on the energy estimator used in this work.

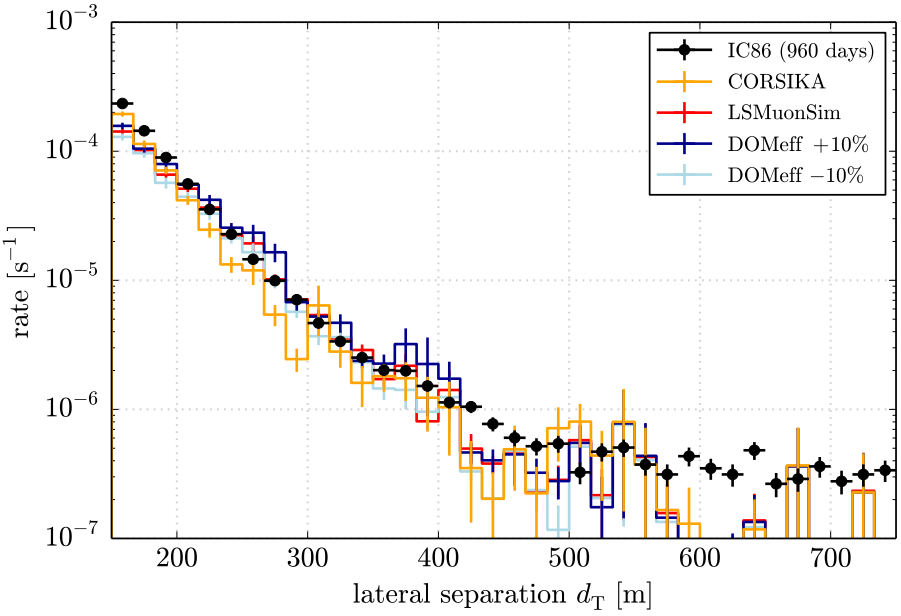

Figure 7.26: Lateral separation distribution at final filter level, obtained from LSMuonSim and CORSIKA, as well as from experimental data. The corresponding distributions from LSMuonSim, assuming modified DOM efficiencies, are also shown. See text for details.

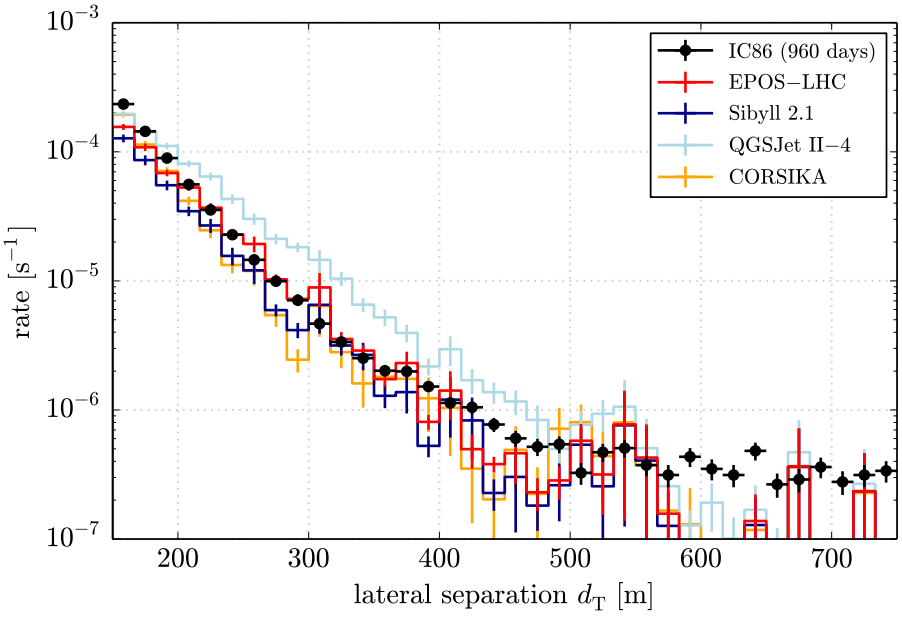

Figure 7.27: Lateral separation distribution at final filter level, obtained from LSMuonSim, using various hadronic models. Corresponding distributions, obtained from data and CORSIKA (Sibyll 2.1), are also shown.

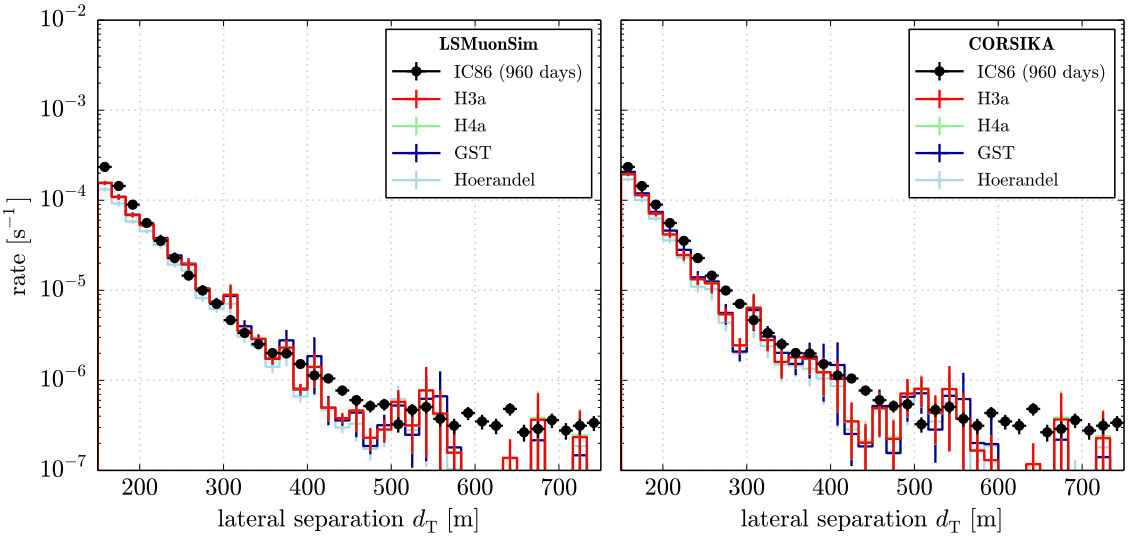

Figure 7.28: Lateral separation distribution at final filter level, assuming various primary flux assumptions, using LSMuonSim and CORSIKA.

Primary Flux

The lateral separation distributions, using various primary flux assumptions, as introduced in Section 2.1.4 and given in Appendix A.1, are shown in Figure 7.28. The distributions are obtained from LSMuonSim (left) and CORSIKA (right). The resulting uncertainties on the Hagedorn fit parameters, as well as on the primary energy estimate, are given in Table 7.8. In general, the effect of different primary flux assumptions on the MC simulations is rather small with deviations of only a few percent. In any case, the measured data distributions are independent from the MC flux assumptions and they are therefore not accounted for in the final results. However, since the energy estimator relies on MC simulations, the uncertainties on the primary energy reconstruction are taken into account. They are below 1%, as given in Table 7.8.

7.7.2 ZENITH ANGLE

The systematic uncertainties on the zenith angle distributions at final level are discussed in the following. This is done with emphasis on the zenith angle discrepancies between experimental data and simulations, shown in Section 7.3.

DOM Efficiency

The DOM efficiency uncertainties, as previously described in Section 7.7.1, on the zenith angle distributions at final filter level, are shown in Figure 7.29. Similarly to the lateral separation distributions, the uncertainty contribution to the zenith angle due to DOM efficiency is rather small. In addition, no significant effect on the form of the distributions can be seen. Hence, no relation between the DOM

efficiency and the zenith angle discrepancies is observed, which is in agreement with previous results of high-energy muons in IceCube [52].

Hadronic Interaction Model

The zenith angle distributions, using LSMuonSim with various hadronic models, are shown in Figure 7.30. Although there are differences between the models, especially towards vertical angles, the general shape of the resulting distributions does not change significantly. The excess towards large inclination, observed in CORSIKA simulations, is not reproduced by any hadronic model using LSMuonSim. Hence, the zenith angle MC discrepancies observed in this analysis can not be explained by the underlying hadronic model. This is in correspondence with previous studies, using high-energy atmospheric muons in IceCube [52].

In addition, the lateral separation distribution of QGSJet II-4 simulations, shown in Figure 7.27, shows significant differences to other models. As previously discussed, this is caused by large differences in the underlying transverse momentum distributions. However, QGSJet simulations do not show an effect on the zenith angle distribution, which could be related to the discrepancies observed between data and MC. Moreover, the lateral separation distribution, obtained from LSMuonSim with Sibyll 2.1, agree very well with CORSIKA predictions, which also use Sibyll 2.1 as hadronic model, while the corresponding zenith angle distributions show significant differences. Hence, the zenith angle discrepancies are not related to the underlying p_T distributions.

Primary Flux

The effect of the primary flux assumption on the zenith angle distributions at final analysis level is shown in Figure 7.31. As previously discussed for the lateral separation, the effect of the flux assumption is very small. A relation between the zenith angle discrepancies and the primary flux assumption is not observed. Similar results have also been reported in Ref. [52].

Further Uncertainties

Further systematic uncertainties effecting the zenith angle distributions of high-energy atmospheric muons in IceCube, have been studied in Refs. [52, 54]. As previously described, these analyses observed similar differences in the zenith angle distributions obtained from experimental data and CORSIKA. The resulting data/MC discrepancies are observed on a $\sim 20\%$ level. Dedicated studies on the photon propagation simulation in the ice, including the effects on various ice properties and the DOM angular acceptance, did not show any significant effect on the zenith angle distributions of high-energy muons. Moreover, the zenith angle discrepancy is reproduced using independent approaches for the the photon propagation simulation in the ice.

In addition, the data/MC discrepancies are not significant at trigger level [52], where data is dominated by low-energy muons. On the other hand, they are

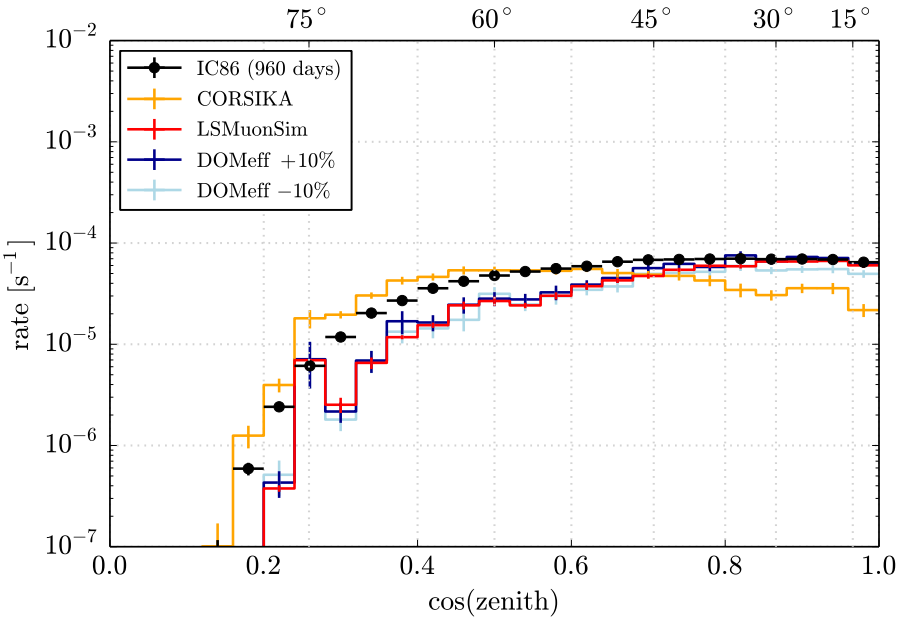

Figure 7.29: Zenith angle distribution at final filter level, obtained from LSMuonSim and CORSIKA, as well as from experimental data. The corresponding distributions from LSMuonSim, assuming modified DOM efficiencies, are also shown. See text for details.

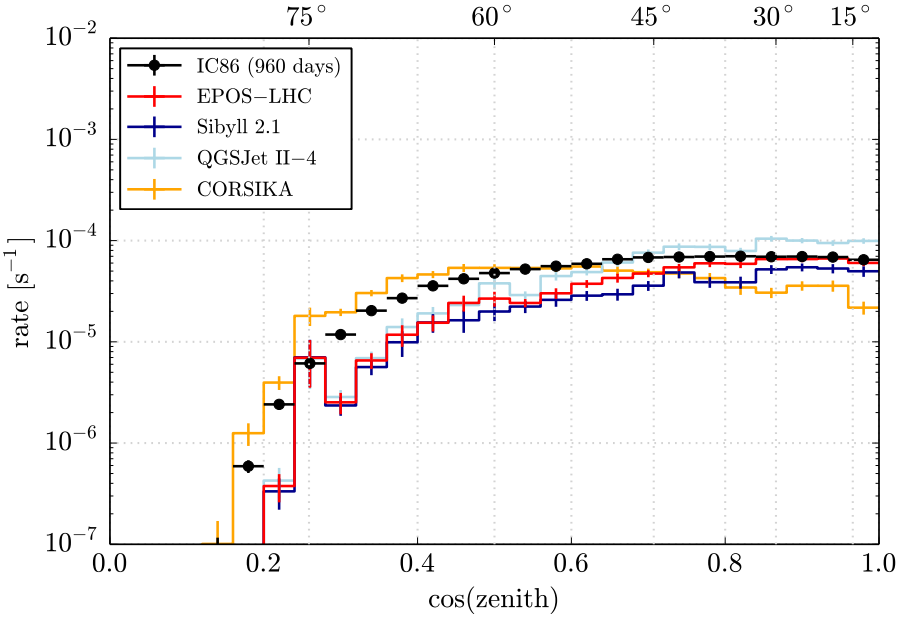

Figure 7.30: Zenith angle distribution at final filter level, obtained from LSMuonSim, using various hadronic models. Corresponding distributions, obtained from data and CORSIKA (Sibyll 2.1), are also shown.

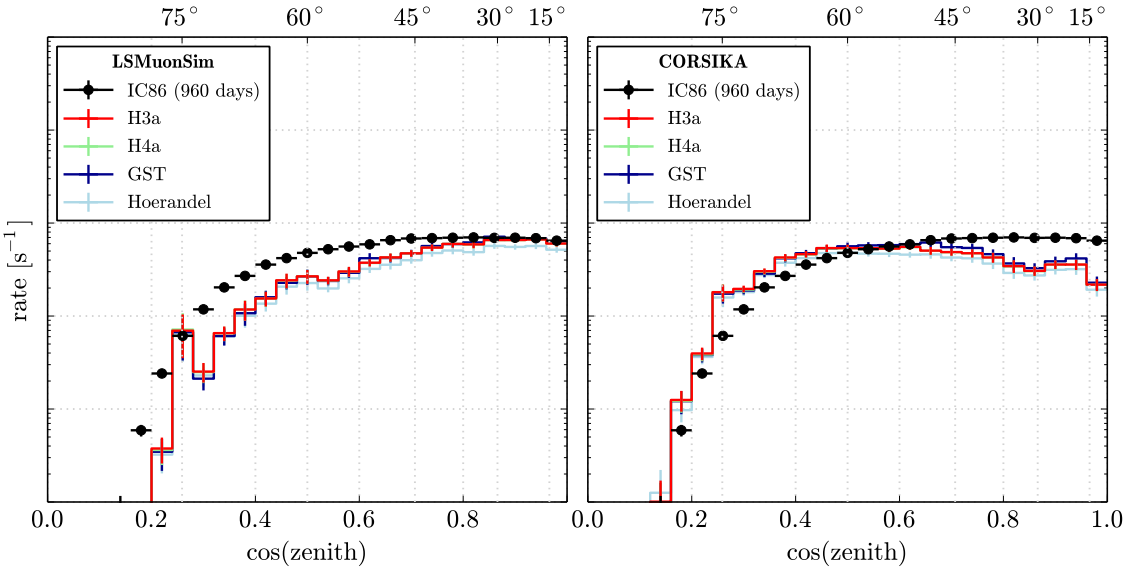

Figure 7.31: Zenith angle distribution at final filter level, assuming various primary flux assumptions, using LSMuonSim and CORSIKA.

smaller for high-energy muons up to the PeV range, compared to the results from LS Muons, which typically have energies of a few TeV (see Appendix C.9). Hence, no systematic effect due to the underlying muon energy can be identified.

However, the mean interaction height of showers observed at trigger level is lower than for high-energy muon events, and the first interaction of LS Muon events is shifted towards even higher altitudes. This observation is qualitatively compatible with the zenith angle discrepancies potentially arising from the MC interaction height distributions, as previously discussed in Section 7.3.

Summary

The zenith angle discrepancies between experimental data of atmospheric muons and MC predictions have been discussed in previous analyses [52, 54, 83] and throughout this work. In the following, the various potential effects on the zenith angle distributions are summarized in order to draw conclusions on the underlying reasons for those discrepancies. The following MC studies do not show any significant systematic effects on the zenith angle distribution of LS Muon events, and they are therefore disfavored as the cause of the observed discrepancies:

- DOM efficiency and angular acceptance
- Primary flux assumption and mass composition
- Hadronic model
- Transverse momentum distribution
- Photon propagation and ice model

In contrast, systematic effects have been observed for events from different interaction heights. This determines the height of production of LS MUONS and had not been considered as the source for these discrepancies in previous analyses. As shown in Section 7.3, the form of the zenith angle distributions clearly depends on the altitude at which the underlying air shower was initiated. The excess towards horizontal directions, as well as the suppression of vertical events, observed in CORSIKA simulations, can be related to the altitude. In addition, the differences between LSMUONSIM and CORSIKA are expected to be influenced by the underlying atmospheric model and the discrepancies show a dependence on the annual seasons, used in simulations. The distributions of the first interaction height of events at final analysis level, obtained from MC simulations, also show significant discrepancies between CORSIKA and LSMUONSIM, as discussed in Section 7.3. Moreover, selecting high-energy muons naturally selects events from higher altitudes, and the selection of LS MUONS is dominated by air shower events from even greater heights. Hence, the increasing discrepancies observed for LS MUONS, compared to the high-energy muons analyses [52, 54], suggest an explanation related to the atmospheric models used in CORSIKA.

In order to draw final conclusions, the effects of the atmospheric models used in CORSIKA simulations need to be further studied. This can be done in future analyses, for example, by producing systematic MC simulations with different atmospheric model parameters. An experimental estimate on the height of production of measured showers can further constrain the effects of the atmospheric models used in MC simulations. Studies of the seasonal variations, as discussed in Section 7.7, or measurements of the shower maximum X_{max} based on hybrid measurements, for example using air Cherenkov telescopes, can contribute to a better understanding of atmospheric effects. This would enable the derivation of the dependencies between the zenith angle distributions and the underlying height of muon production directly. Thereby, it would be possible to systematically study the data/MC discrepancies of the zenith angle distributions related to the height of production of atmospheric muons in detail.

7.7.3 COMPOSITION MEASUREMENT

As described in Section 7.5, the estimation of the mean mass number $\langle \ln A \rangle$ is done using a surface correction factor $s = \langle \ln A \rangle_{\text{surface}} / \langle \ln A \rangle_{\text{in-ice}}$, which is obtained from MC simulations. The factor s therefore depends on the underlying composition assumption. Figure 7.32 shows the mean logarithmic mass in the ice at final filter level and at surface level, obtained from LSMUONSIM, using various primary flux models, as described in Section 2.1.4. The resulting correction factors s are given in Table 7.9, where the relative uncertainties with respect to the H3A primary flux are also shown. As discussed in Section 7.5, in order to derive final conclusions on the total systematic uncertainties of the estimated logarithmic mass number further studies are needed, including systematic effects due to the primary energy estimator and the choice of the energy binning.

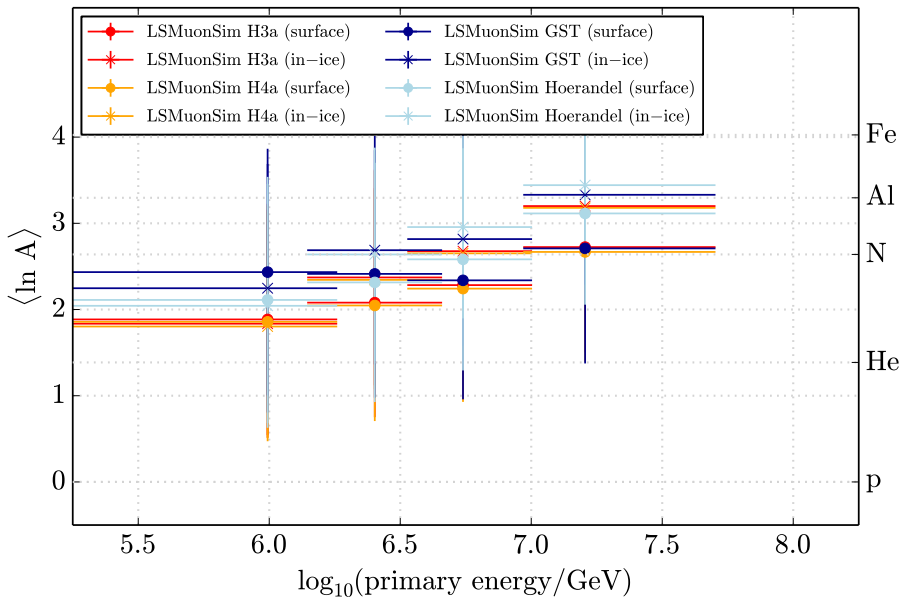

Figure 7.32: Mean mass number $\langle \ln A \rangle$ for various primary flux assumptions, obtained from simulated in-ice distributions, obtained from LSMuonSim, at final filter level (crosses), as well as at surface level (circles).

	Energy bin	H3a	H4a	GST	Hoerandel	Total
Factor s	$\langle E_0 \rangle_1$	1.03	1.03	1.08	1.03	
	$\langle E_0 \rangle_2$	0.88	0.87	0.90	0.88	
	$\langle E_0 \rangle_3$	0.85	0.85	0.83	0.87	
	$\langle E_0 \rangle_4$	0.85	0.84	0.81	0.90	
Rel. uncert.	$\langle E_0 \rangle_1$		+0.3%	+5.5%	+0.6%	+5.5%
	$\langle E_0 \rangle_2$		−0.4%	+2.4%	+0.1%	(+2.4/−0.4)%
	$\langle E_0 \rangle_3$		−0.9%	−2.7%	+2.4%	(+2.4/−2.6)%
	$\langle E_0 \rangle_4$		−1.4%	−4.5%	+6.3%	(+6.3/−4.7)%

Table 7.9: Surface correction factors s, as defined in the text, for several primary flux assumptions (top), as well as corresponding relative uncertainties with respect to the H3a flux (bottom).

8

EXOTIC DOUBLE-TRACKS FROM COSMIC RAY AIR SHOWERS

"I have done a terrible thing,
I have postulated a particle that cannot be detected."
*– Wolfgang E. Pauli**

ALTHOUGH the standard model of particle physics is one of the most successful and experimentally best tested theories of today, many fundamental questions, that cannot be described in the context of the standard model, remain still open. After Maxwell successfully described the phenomena of electricity and magnetism in a unified theory, called *quantum electrodynamics* (QED), in the 1960's a unified description of the electrodynamic and weak interactions, the *electroweak theory* was formulated. The energy-dependent (running) coupling constants of the fundamental forces of the the SM [58, 225], as given in Equation (2.32) for QCD, are shown in Figure 8.1 (left). They approximately match at energies around 10^{16} GeV. This led to the idea that (at least) the three fundamental forces, can be described within an underlying unified theory, a *grand unified theory* (GUT), which unifies electroweak and strong forces. A good match for the running couplings at a GUT scale of $M_{GUT} \simeq 10^{16}$ GeV can for example be accomplished in the context of *supersymmetry* (SUSY), as shown in Figure 8.1 (right), an extension of the standard model that will be described as an example in the following.

A more technical problem is caused by quantum loop corrections to the Higgs mass from virtual effects of every particle that couples to the (scalar) Higgs field [226]. Assuming a theory is valid up to a ultraviolet cutoff Λ_{UV} in the order of the GUT scale M_{GUT}, couplings of fermions with the Higgs field cause quantum corrections that lead to a quadratically divergent Higgs mass-squared term of the form [227]

$$\delta m_H^2 = -\frac{|\lambda_f|^2}{8\pi^2}\left(\Lambda_{UV}^2 + \dots\right) . \tag{8.1}$$

Hence, these virtual corrections should cause a very large Higgs mass. The experimentally measured Higgs mass on the other hand is $m_H \simeq 125\,\text{GeV}$ [34]. This problem is referred to as the *(gauge) hierarchy problem* or the *naturalness problem* in physics and can also be solved by supersymmetry. Due to the presence of new (hypothetical) SUSY particles, so-called *superpartners*, the divergent terms would roughly cancel out, preventing the Higgs mass from getting too large [227].

* As quoted by F. Reines, in *"Spaceship Neutrino"* by C. Sutton (1992).

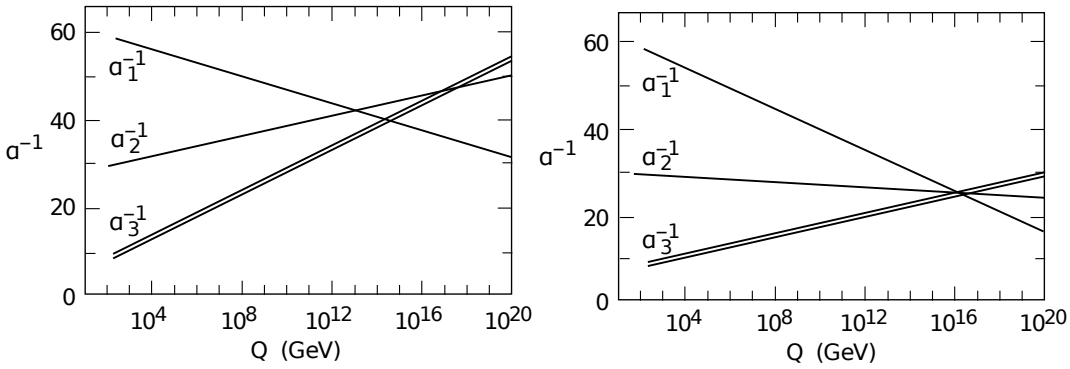

Figure 8.1: Running coupling constants as described by the SM (left) and in the context of SUSY (right). Taken from [225].

Moreover, many SUSY theories predict the existence of a stable *lightest supersymmetric particle* (LSP). Since recent experimental SUSY mass limits typically favor masses in the TeV range or above, these LSPs are very good dark matter candidates. Although several different approaches to explain these and other open questions have been made during the last six decades, and experimental limits on the parameter space of different theories have been set, neither of them have been experimentally confirmed. It was previously proposed in literature [5, 6, 228–230] that high energy cosmic ray and neutrino interactions can produce supersymmetric and other exotic particles which, under favorable conditions, can produce distinctive double-track signatures in km^3-scale neutrino telescopes.

In the following the concept of searches for exotic double-tracks is introduced using the example of supersymmetry. The production of supersymmetric particles in cosmic ray air showers is described and the expected SUSY fluxes in IceCube are discussed. This is done in comparison with a previous analysis of exotic neutrino-induced double-tracks in IceCube [151]. Although in the following the example of supersymmetry is used, the basic principles and discussions can be applied analogously or similar to other theories *beyond the standard model* (BSM) causing double-track signatures proposed in literature, such as *Kaluza-Klein* (KK) theories [230].

8.1 (MINIMAL) SUPERSYMMETRIC MODELS

Supersymmetric models are based on an additional spacetime symmetry, called *supersymmetry* (SUSY), that relates fermionic particle states with bosonic states. Thereby, each particle is assiociated with a *superpartner*, whos spin differs by a half-integer. This symmetry can be described by supersymmetry operators $\mathcal{Q}$ that relate the fermionic and bosonic states by [226]

$$\begin{aligned} \mathcal{Q}|\text{boson}\rangle &= |\text{fermion}\rangle \\ \mathcal{Q}|\text{fermion}\rangle &= |\text{boson}\rangle \end{aligned} \tag{8.2}$$

The simplest supersymmetric extension of the standard model is the *minimal supersymmetric model* (MSSM) [231], which introduces one superpartner for

each SM particle and one additional Higgs-doublet in the Higgs sector. These supersymmetric partners are referred to by adding a *"s"* to the beginning of the name of a particle, i.e. slepton, squark, sfermion, stau, etc., and using a "~" indicating a SUSY particle, i.e. $\tilde{l}$, $\tilde{q}$, $\tilde{f}$, $\tilde{\tau}$, etc. For all bosons, the superpartner is indicated by adding a "ino" to the end of a particle's name, i.e. Wino, photino, gravitino, etc.

The additional Higgs-doublet introduces an additional Higgs field. One of the Higgs-doublets couples to up-type particles while the other one couples to down-type particles. This doubles the degrees of freedom in the Higgs sector and leads to five Higgs particles after weak symmetry breaking [226, 227]: two scalar particles, h_0 and H_0, a pseudo-scalar A_0, and the two charged $H^{\pm}$. These additional Higgs particles also have superpartners. The charged Higgsinos $\tilde{H}^{\pm}$ and the gauge bosinos (the supersymmetric partner of the SM gauge bosons), as well as the neutral Higgsinos $\tilde{h}_0$ and $\tilde{H}_0$ and the gauge bosinos can mix, leading to six different mass eigenstates [227]: the two charginos $\tilde{\chi}^{\pm}_{1,2}$ (Dirac fermions) and the four neutralinos $\tilde{\chi}^0_{1,2,3,4}$ (Majorana fermions).

Although the MSSM is the simplest supersymmetric extension of the standard model, the parameter space is tremendous compared to the SM. The standard model has 19 free parameters [58, 226]: three gauge couplings and the QCD vacuum angle θ_{QCD}, two parameters from the Higgs potential, and 13 parameters in the flavor sector. The MSSM on the other hand contains 124 parameters: the 19 parameters of the SM, five gaugino masses, three additional parameters in the Higgs sector, and 97 additional free parameters in the flavor sector (for a detailed discussion see for example Ref. [226]). Therefore, the variety of phenomenological models is huge while the parameter space of experimental searches is usually rather limited, which makes searches for supersymmetric particles very challenging.

Thus, the parameter space of the MSSM is usually further constrained to simplify phenomenological calculations. This can be done, for example, by avoiding *flavor changing neutral currents* (FCNCs) and CP violations that are expected not being realized in nature. The *phenomenological MSSM* (pMSSM) thereby reduces the parameter space to 19 real parameters [232]. However, this parameter space can be further constrained by some theoretical assumptions, such as R-parity conservation or an underlying supersymmetry breaking mechanism, as superficially described in the following. A comprehensive description can be found for example in Ref. [226].

8.1.1 R-PARITY AND (N)LSP

Simple SUSY models, such as the MSSM, assume *R-parity* conservation, with R defined as

$$R = (-1)^{3(B-L)+2S} \,. \tag{8.3}$$

B and L are the baryon and lepton numbers and S is the spin of the particle, i.e. standard model particles have an even R-parity, while their superpartners

have odd R-parity. It is worthwhile to note that it is also possible to construct phenomenologically viable models with R-parity violations (see for example Ref. [226]), but these models are beyond the scope of this work and are not considered here. An important consequence of R-parity conservation is that SUSY particles are always produced in pairs. Moreover, R-parity immediately implies that the *lightest supersymmetric particle* (LSP) cannot decay into SM particles and must be stable. Assuming the LSP is weakly interacting it forms a good candidate for dark matter. The SUSY particle which is the LSP is determined by a SUSY breaking mechanism, as described in Section 8.1.2. A stable LSP has significant implications for cosmology: assuming that (stable) relic LSPs left over from Big Bang can account for the dark matter density of the universe, supersymmetric models are constrained by astrophysical measurements. Thus, almost all cases of electromagnetically charged or colored LSPs are ruled out because such relics would have been bound into atoms and would have already been detected in searches for anomalous nuclei [226]. Additionally, the lightest sneutrino as the LSP can also be ruled out by cosmological considerations and data from direct dark matter detection experiments [226]. Thus, depending on the actual breaking mechanism, the LSP is typically the lightest neutralino or the gravitino.

In models where the gravitino is the LSP, the *next-to-lightest supersymmetric particle* (NLSP) is usually a charged lepton, typically the right-handed stau $\tilde{\tau}_R$. The lifetime of the NLSP can be large and these particles can be *meta-stable* [228] because the NLSP decays into the gravitino very weakly.

High energy cosmic ray interactions and neutrino interactions can, in principle, produce a pair of SUSY particles which decay into LSPs via two meta-stable NLSPs. In SUSY models with electrically charged NLSP, for example the supersymmetric stau, it is possible for the NLSP to produce Cherenkov-light while traveling through water or ice, as described in Section 3.1.4. Thus, under these conditions SUSY particles produced in cosmic ray or neutrino interactions decay into two meta-stable, charged NLSPs, that can produce distinctive double-track signatures in neutrino telescopes. This enables direct measurement of supersymmetric sleptons in large scale neutrino observatories, forming a complementary approach to typical accelerator SUSY searches.

8.1.2 SUPERSYMMETRY BREAKING

If a perfect supersymmetry is realized in nature, the supersymmetric partners have the same charges (electrical, weak, etc.) and masses as the corresponding SM particles [226]. Thus, an excited atom could, in principle, emit a massless photino turning an electron into a supersymmetric selectron. This can happen for all electrons of the atom. Now being bosonic, the Pauli principle does not hold anymore for these selectrons that could consequently all go into the ground state. This would clearly change the atomic structure and properties of chemical processes and is obviously not realized in nature. Moreover, these rather light SUSY particles could be easily produced at current collider experiments and would have have been observed in experimental data.

Therefore, supersymmetry must be broken causing much higher SUSY particle masses. Additionally, to solve for example the fine-tuning problem described above, the SUSY masses can not be too high in order to cancel out the divergencies. Generally, the mass differences between SM and SUSY particles are expected to be in the order of $\mathcal{O}(1\,\text{TeV})$ to avoid further theoretical difficulties [226].

There are various approaches describing the supersymmetry breaking mechanism in a theoretical framework, but the actual dynamics of supersymmetry breaking are, due to the large parameter space and no experimental evidence, unknown. However, all realistic SUSY models assume a *hidden sector* that somehow breaks the supersymmetry spontaneously and that couples only indirectly and very weakly to SM particles and their superpartners. This sector interacts with the observable sector via extremely heavy messenger fields and it causes a soft SUSY breaking at a scale $M^2_{\text{SUSY}} \gg M^2_W$. The actual dynamics of the supersymmetry breaking, and thus the resulting SUSY model, depend on the nature of these mediating fields.

An obvious choice for a hidden sector that couples weakly to standard model particles and their superpartners, causing the SUSY breaking, is gravity. Since gravity generally couples to energy, some gravity mediated effects must be present, causing the supersymmetry being spontaneously broken. These models are described in the context of *supergravity* (SUGRA) [233–235]. In the *minimal supergravity* (MSUGRA) model, the resulting parameter space is thereby dramatically reduced, compared to that of the MSSM, and typically characterized by only four parameters and a sign: the scalar mass parameter m_0, the gaugino mass parameter $m_{1/2}$, a trilenear coupling A_0, the ratio of the Higgs vacuum expectation values (VEVs) $\tan(\beta)$, where $\beta = v_2/v_1$ with the two Higgs VEVs v_1 and v_2, and the sign of the Higgs mass parameter μ.

Another possible scenario is the spontaneous breaking of supersymmetry due to usual gauge interactions. These *gauge-mediated supersymmetry breaking* (GMSB) models are based on new messenger fields that couple directly to the hidden sector and also have SM gauge couplings. These interactions cause the SUSY breaking effects and also reduce the parameter space to only four parameters and a sign [236, 237]: the mass of the messenger fields M_{mess}, the messenger index N_{Mess}, the SUSY breaking mass scale Λ, as well as $\tan(\beta)$ and $\text{sign}(\mu)$.

There are several further possible SUSY breaking scenarios, such as *anomaly-mediated supersymmetry breaking* (AMSB) [238, 239]. Since typically MSUGRA and GMSB models have the supersymmetric stau as NLSP, these are used in this work as an example. A detailed description of the theoretical concepts of these and other models are beyond the scope of this work. A detailed discussion can be found in for example Refs. [226, 227, 233–235, 237]. In the following, the most important implications from some SUSY benchmark models, that can produce long-lived staus, are described.

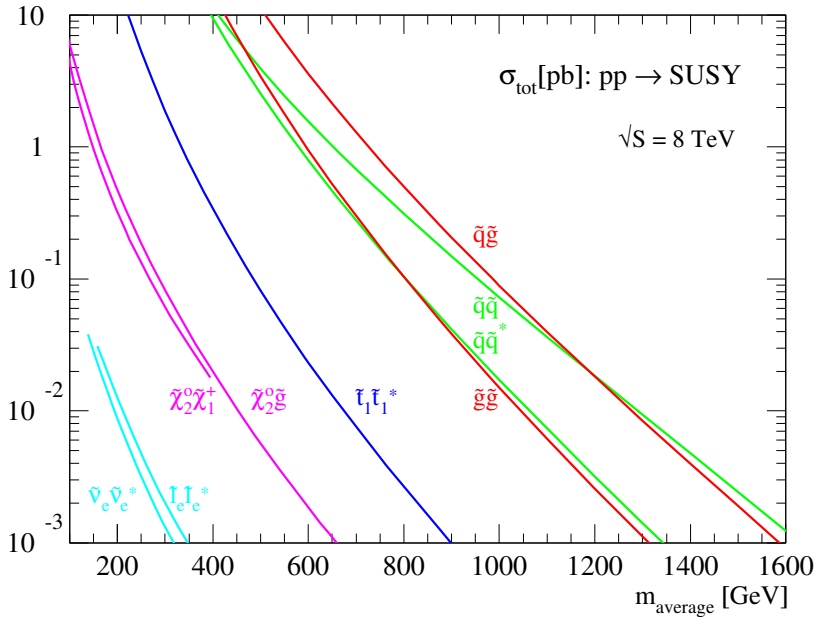

Figure 8.2: Proton-proton cross-sections to produce different SUSY particle pairs as a function of the average particle masses for a center-of-mass energy of 8 TeV. Taken from Ref. [34].

8.1.3 CONSTRAINED MSSM BENCHMARK MODELS

The cross-sections for production of supersymmetric particles must depend on the collision energy, but are also highly mass dependent [240]. The proton-proton cross-sections for production of different SUSY pairs for a center-of-mass energy of 8 TeV are shown in Figure 8.2 [34]. Since these cross-sections decrease with increasing SUSY masses, any phenomenological calculations strongly depend on the mass spectrum of the underlying model, and therefore on the choice of the SUSY breaking parameters.

In this work, the *Snowmass Points and Slopes* (SPS) are used, which are a set of benchmark points and parameters in the MSSM parameter space, assuming several SUSY breaking mechanisms, taken from [236]. Four of these SPS models yield a supersymmetric stau as NLSP and are therefore considered in the following. The parameters for these models are summarized in Table 8.1. Based on these parameters, the mass spectrum of the theory can be derived using the software package SPheno [241]. The resulting SUSY mass spectrum for the GMSB SPS-7 model can be found in Figure 8.3.

Using the mass spectrum shown in Figure 8.3, the proton-proton cross-sections are obtained from PYTHIA 6 [187]. They are shown in Figure 8.4, together with the neutrino-proton cross-sections, taken from [151].

mSUGRA	$M_{1/2}$ [GeV]	m_0 [GeV]	$\tan(\beta)$	A_0 [GeV]
I	280	10	11	0
ϵ	440	20	15	−25
GMSB	M_{mess} [TeV]	Λ [TeV]	$\tan(\beta)$	N_{mess}
II	70	35	15	3
SPS-7	80	40	15	3

Table 8.1: SUSY SPS benchmark models used in this work, as described in Ref. [236].

8.2 SUSY FLUX ESTIMATES

The production of supersymmetric particles for collision energies below 100 TeV is highly suppressed due to the decreasing SUSY cross-sections towards lower energies, as shown in Figure 8.4. Therefore, assuming that SUSY particles are predominantly produced in the first interaction of a cosmic ray air shower is a valid first approximation. In order to estimate the flux of supersymmetric stau pairs in IceCube, it is also assumed that any supersymmetric particle, which is pair-produced in a primary interaction of a cosmic ray nucleus N, decays into meta-stable NLSPs (the supersymmetric staus), which are stable while traveling to the detector. The maximal flux of stau pairs produced in an air shower is then given by

$$\frac{d\Phi_{\tilde{\tau}\tilde{\tau},max}}{dE_N} \approx \frac{d\Phi_{SUSY}}{dE_N} = A \cdot \frac{\sigma_{SUSY,N}}{\sigma_{SM,N} + \sigma_{SUSY,N}} \cdot \frac{d\Phi_N}{dE_N} , \tag{8.4}$$

where $A \simeq \langle A \rangle = 14.5$ is the average number of nucleons in an air target nucleus, as described in Section 2.2.1. Thereby, the detector and filter efficiencies are not considered and Equation (8.4) represents an optimistic maximum estimate. The cross-sections are approximated by the proton-proton cross-sections, obtained from PYTHIA 6, using SPheno to calculate different mass spectra, as described in Section 8.1.3. The resulting cross-sections for the GMSB SPS-7 model are shown in Figure 8.4. The flux of supersymmetric particles is clearly suppressed by the small ratio $\sigma_{SUSY,N}/(\sigma_{SM,N} + \sigma_{SUSY,N})$, which is shown in Figure 8.5, assuming the GMSB SPS-7 model. At energies of around 100 TeV for example, the SUSY flux from hadronic interactions is suppressed by a factor of $\sim 10^{-18}$.

The estimated SUSY fluxes for different SPS benchmark models, are shown in Figure 8.6, assuming a pure-proton primary flux following a simple broken power law of the form of Equation (2.10) (shown as dotted line).

Analogously, assuming all SUSY particles decay into the meta-stable NLSP, the flux of supersymmetric stau pairs produced in neutrino interactions is given by

$$\frac{d\Phi_{\tilde{\tau}\tilde{\tau},max}}{dE_\nu} = \mathcal{P} \cdot \frac{\sigma_{SUSY,\nu}}{\sigma_{SM,\nu} + \sigma_{SUSY,\nu}} \cdot \frac{d\Phi_\nu}{dE_\nu} , \tag{8.5}$$

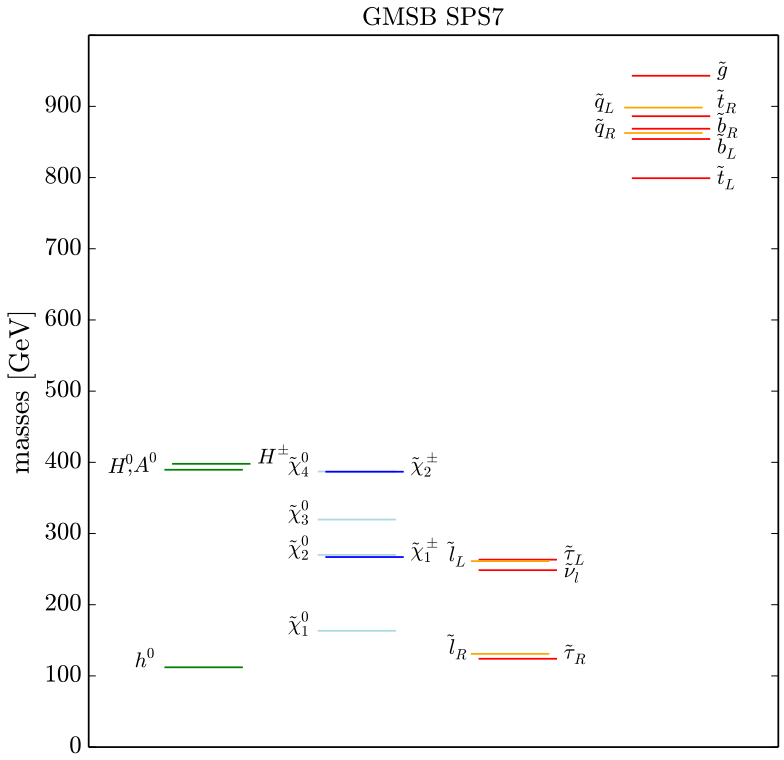

Figure 8.3: Mass spectrum for the GMSB SPS-7 benchmark model, calculated with the SPHENO software package [241]. squark and slepton flavors not explicitly noted here have very small mass differences and are indicated by the $\tilde{q}$ and $\tilde{l}$ lines.

where the probability $\mathcal{P}$ of a neutrino to interact with a nucleus within the Earth is [151]

$$\mathcal{P} = 1 - \exp\left(-(\sigma_{SM,\nu} + \sigma_{SUSY,\nu}) \cdot N_0 \cdot \int \rho_{Earth}(l)\,dl\right) , \tag{8.6}$$

with $N_0 = 6.022 \cdot 10^{23}\,g^{-1}$. The Earth's density profile $\rho(l)_{Earth}$ is described by the PREM model [203] as shown in Ref. [151]. The ratio of the neutrino cross-sections are also shown in Figure 8.5. Due to the generally small SM cross-sections $\sigma_{SM,\nu}$, the ratio is about 4 to 10 orders of magnitude larger compared to the proton ratios, given in Equation (8.4).

Assuming a cylindrical detector volume with height 1000 m and radius 500 m, and a pure-proton primary flux following a simple broken power law, the expected (hadronic) SUSY fluxes in ICECUBE are calculated. The resulting total SUSY fluxes per year, based on various SPS benchmark models, are shown in Table 8.2. The fluxes produced by high energy neutrino interactions are taken from Ref. [150]. The resulting SUSY fluxes are in agreement with the flux estimates from Ref. [242], where the same SPS benchmark models are used. However, recent results from the ATLAS and CMS experiments [243–246], have excluded large regions of the SUSY parameter space, which results in

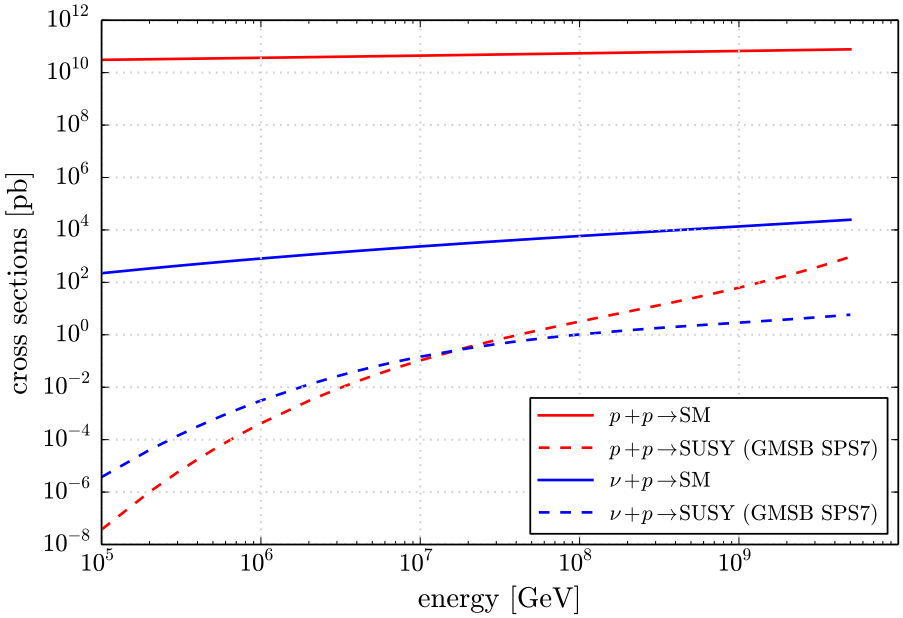

Figure 8.4: Proton-proton and neutrino-proton Standard Model and SUSY cross-sections using the mass spectrum from the SPS-7 benchmark model.

strong constraints on the expected squark and gluino masses between 600 GeV – 1 TeV. Hence, the MSSM models used in this work are strongly disfavored due to their low SUSY masses and therefore represent very optimistic scenarios. Assuming higher SUSY masses, which are not experimentally excluded yet, the cross-sections further decrease, as shown in Figure 8.2. Subsequently, the resulting SUSY fluxes are expected to further decrease for more realistic SUSY scenarios, which do not conflict with the latest accelerator measurements. For a comprehensive discussion on the latest experimental results, see for example Refs. [243–246].

MODEL	HADRONIC [events/yr]	NEUTRINO [events/yr]
mSUGRA I	$1.7 \cdot 10^{-3}$	1.7
mSUGRA ϵ	$1.3 \cdot 10^{-4}$	0.5
GMSB II	$6.9 \cdot 10^{-4}$	0.8
GMSB SPS-7	$3.3 \cdot 10^{-4}$	0.5

Table 8.2: Estimated SUSY events per year in IceCube from hadronic cosmic ray and neutrino interactions, assuming various benchmark models, as given in Table 8.1. The flux estimates from neutrino interactions are taken from Ref. [150].

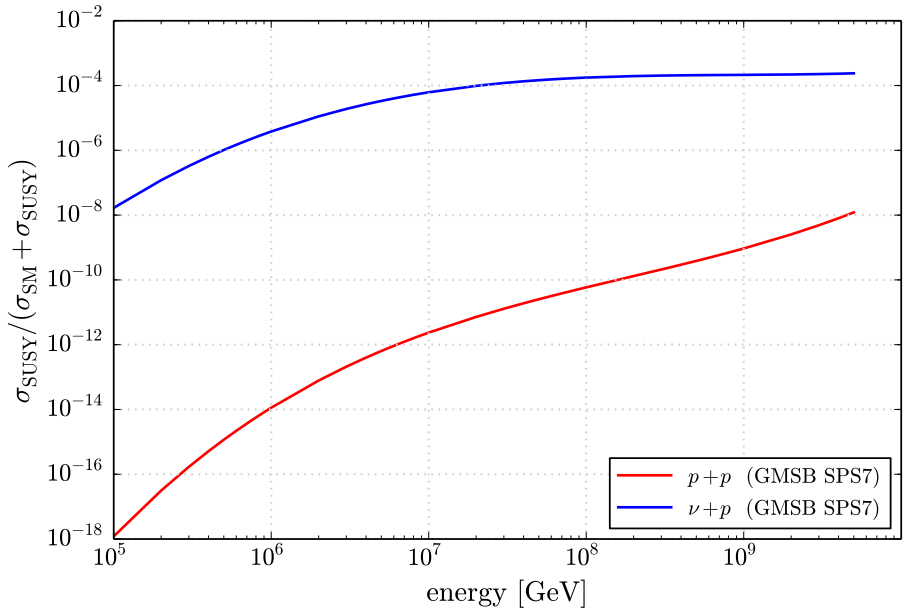

Figure 8.5: Ratio of SUSY and standard model cross-sections assuming the SPS-7 model.

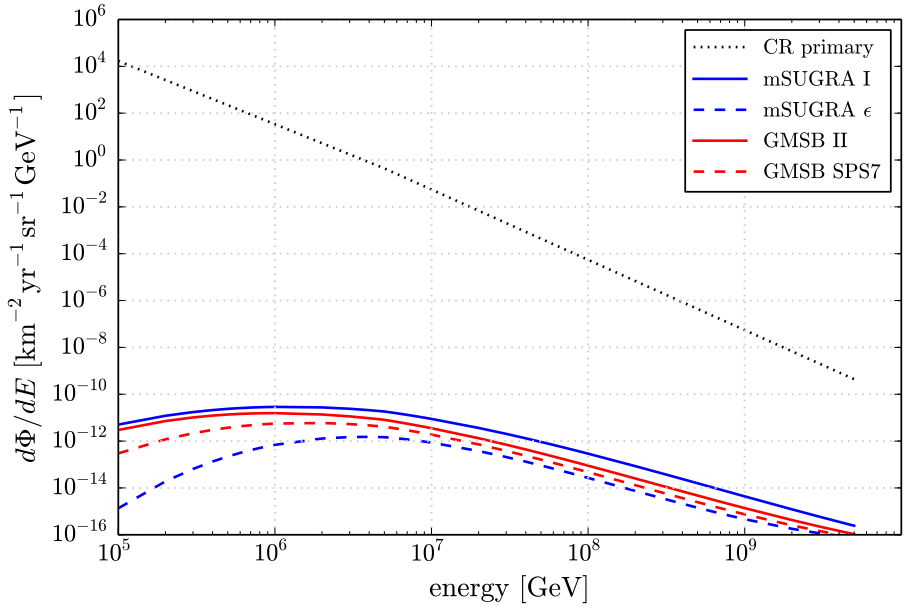

Figure 8.6: Estimated SUSY fluxes from cosmic ray interactions using Equation (8.4) based on the various SPS benchmark models shown in Table 8.1.

8.3 DISCUSSION

While the expected SUSY fluxes in IceCube from neutrino interactions are in the order of few events per year, even assuming most optimistic SPS scenarios, the corresponding SUSY event rates from hadronic cosmic ray interactions are on the order of 10^{-4} to 10^{-3} events per year. Moreover, these flux estimates are based on minimal supersymmetric models, which are experimentally highly disfavored by recent accelerator data [243–246], and do not account for any detector and filter efficiencies in IceCube. Hence, realistic scenarios result in even lower flux estimates for experimental SUSY searches in existing neutrino telescopes.

However, the observation of up-going neutrino induced double-tracks would still be a distinctive signature of BSM physics, because there is no significant background contribution which can mimic such signatures [151]. In contrast, the distinction between down-going SUSY double-tracks and LS Muon events, or events from multiple neutrinos and air showers, is experimentally very challenging. Thus, the resulting effective areas are expected to be significantly smaller than for the LS Muon analysis, as discussed in Section 6.9.

Therefore, considering recent SUSY mass limits, the experimental search for supersymmetric double-tracks from cosmic ray air showers, using existing neutrino telescopes, as proposed in Refs. [5, 6, 228, 229], is not feasible in the context of existing SUSY models. Although the phase space of Kaluza-Klein models is less constrained by recent collider experiments, current KK limits are significantly higher than assumed in Ref. [230]. Thus, these scenarios face similar problems as SUSY models, because the expected flux decreases with increasing KK masses. Although future detector prospects, such as an extended detector volume or denser instrumentation, would enhance the expected fluxes, the background contribution for potential BSM double-tracks would also increase. Hence, the ability to detect BSM double-track signatures, produced by cosmic ray air showers in large neutrino telescopes, would not significantly improve by potential detector upgrades.

9 SUMMARY AND DISCUSSION

"Uh-huh! Who would've guessed
reading and writing would pay off..?"
– Homer J. Simpson *

In this work, the measurement of laterally separated muons was presented, using data from IceCube in its 86-string configuration, taken between May 2012 and May 2015. Dedicated reconstruction methods and filter criteria have been developed in order to select LS Muon events with separations above 135 m from the shower core within IceCube data. After applying all selection criteria, 80951 events were left in 960 days of lifetime, corresponding to a rate of 30765 ± 208 events per year. In addition, a method to produce high-statistics Monte Carlo simulations of LS Muon events was devolped, which enables sophisticated studies on the transverse momentum of hadrons in air showers and the mass composition of the initial cosmic ray nuclei. The measured lateral separation distribution is in good agreement with previous IC59 results [83] and is well described by the MC simulations used in this work. A Hagedorn fit applied to the data after background subtraction yields a spectral index of $\beta_{\text{in-ice}} = -11.7^{+1.1}_{-1.1}\,(\text{stat.})\,^{+0.1}_{-0.6}\,(\text{sys.})$ and implies a transition from an exponential behaviour to a power law at $d_{0,\text{in-ice}} = 237.7^{+43.5}_{-43.5}\,(\text{stat.})\,^{+2.4}_{-2.6}\,(\text{sys.})\,\text{m}$.

In addition, a method for the estimation of the primary energies of events at final filter level was presented, which allows energy-dependent studies of the resulting distributions. The primary energies of showers considered in this work are between approximately 100 TeV and 100 PeV, with a reconstructed mean primary energy of $\langle E_0 \rangle_{\text{tot}} = 4.08^{+16.32}_{-2.12}\,(\text{stat.})\,^{+0.85}_{-0.58}\,(\text{sys.})\,\text{PeV}$. The final data was divided into four energy bins and the resulting lateral separation distributions were individually fit with Hagedorn functions. Based on these fits, it was shown that the lateral separation distributions become flatter with increasing primary energies, as expected from PQCD. This is the first energy-dependent measurement of laterally separated muons in IceCube.

Based on simulations, the effective areas for LS Muon events in IceCube have been derived and the lateral separation distributions at surface level were estimated. The resulting separation distribution of LS Muons on the surface was also fit with a Hagedorn function, yielding a spectral index of $\beta_{\text{surface}} = -9.7^{+1.1}_{-1.1}\,(\text{stat.})\,^{+0.1}_{-0.5}\,(\text{sys.})$. From this fit, the transition from an exponential to a power law appears at $d_{0,\text{surface}} = 157.3^{+43.0}_{-43.0}\,(\text{stat.})\,^{+1.6}_{-1.7}\,(\text{sys.})\,\text{m}$ at surface level.

Based on MC simulations, the transverse momentum distributions of laterally separated muons were also derived at surface level, using corresponding effective areas. The resulting Hagedorn fits for each energy bin result in spectral

* In *"The Simpsons – Mr. Lisa Goes to Washington"*, by G. Meyer (1993).

indices between $\beta = -10.3^{+0.5}_{-0.5}\,(\mathrm{stat.})\,^{+0.1}_{-0.6}\,(\mathrm{sys.})$ and $-9.1^{+0.6}_{-0.6}\,(\mathrm{stat.})\,^{+0.1}_{-0.5}\,(\mathrm{sys.})$. As expected from PQCD, the distributions become flatter with increasing collision energy. The transition from an exponential to a power law behaviour is favored to appear at around $p_0 \simeq 2.1^{+0.2}_{-0.2}\,(\mathrm{stat.})\,^{+0.1}_{-0.1}\,(\mathrm{sys.})\,\mathrm{GeV/c}$. These results are qualitatively in agreement with hadron spectra from recent collider data.

The zenith angle distribution of LS Muon events at final filter level shows significant discrepancies between experimental data and the MC simulations, used in this work. This issue has been previously reported by the IC59 analysis of laterally separated muons [83], as well as in analyses of high-energy atmospheric muons [52, 54]. Studies have been performed in these analyses, which did not find meaningful conclusions on this issue. Given that these existing zenith angle discrepancies are also present in this analysis, dedicated studies have been performed, considering effects of DOM efficiency, hadronic models, and primary flux assumptions. No significant relation between these effects and the zenith angle distribution was found. In contrast, studies on the first interaction height of cosmic ray air showers, performed in this work, have shown a relation between the zenith angle distribution and atmospheric altitude, which had not been considered in previous analyses. It was discussed, that this relation may suggest that the modeling of the atmosphere within simulations is a possible explanation for the discrepancies observed. However, in order to draw final conclusions on the zenith angle discrepancies between data and MC simulations, additional studies need to be performed in future work. Measurements of the height of production of atmospheric muons, for example using hybrid detectors, can contribute to understanding of the underlying uncertainties, and may thus solve the zenith angle problem.

In order to study atmospheric effects on the flux of laterally separated muons, the seasonal variations at final analysis level, as well as at lower levels, were discussed. At final filter level, seasonal variations of the LS Muon flux are on the order of approximately $\pm 50\%$, significantly larger than at lower analysis levels and for other analyses of atmospheric muons. This is due to the selection of events from high altitudes, where temperature fluctuations are very large. Hence, the analysis of laterally separated muons provides a unique possibility to investigate atmospheric effects at very high altitudes. A mean production height of approximately 30 km was estimated from temperature profiles and the phases of seasonal flux variations. This estimate agrees within uncertainties with MC predictions. Thus, seasonal variations of the laterally separated muon flux may help to draw further conclusions on the average height production of LS Muons in future analyses.

Moreover, it was shown that the lateral separation distribution of muons depends on the cosmic ray mass composition and a method to derive the mean logarithmic mass composition of cosmic rays was presented. The resulting $\langle \ln A \rangle$ spectrum agrees with other measurements of the cosmic ray mass composition and various model predictions within uncertainties. It was shown, that the mass composition of cosmic ray nuclei increases with increasing energies in the energy range of roughly $10^{5.5}$ GeV to $10^{8.0}$ GeV. However, the corresponding

uncertainties are rather large due to limited MC statistics and potentially very large systematic uncertainties. Hence, further studies on the systematics of this approach are required in order to draw final conclusions on the mass composition of cosmic ray nuclei.

Finally, the prospects for the observation of exotic double-track signatures were studied. These signatures can be generated by particles, which are predicted by theories beyond the standard model, and may be produced in cosmic ray air showers. The expected event rates for various supersymmetric SPS benchmark models were calculated. The models used in this analysis reflect very optimistic scenarios, particularly considering recent experimental limits on the SUSY masses from accelerator measurements. In addition, perfect trigger and filter efficiencies were assumed in order to derive upper limits on the expected fluxes. The resulting event rates of SUSY double-tracks from air showers in IceCube are below $\Phi^{\text{max}}_{\text{SUSY}} \simeq 10^{-3}$ events per year. Considering the experimental challenges of this search, originating from background contributions of LS Muon events and from multiple air showers within the same time window, it was concluded that a search for down-going SUSY double-tracks is not feasible. Although other scenarios proposed in literature, such as Kaluza-Klein models, are experimentally less constrained by recent accelerator data, these models face similar problems of low flux expectations. This is due to their decreasing production cross-sections with increasing particle masses. Hence, it was concluded that the direct detection of exotic double-tracks from cosmic ray air showers is not feasible using existing neutrino telescopes, given current BSM models and recent experimental mass limits.

ACKNOWLEDGMENTS

"That was a great time [...]
- I can't remember it, but I'll never forget it!"
– Ian F. Kilmister[*]

First of all I would like to thank my supervisor, Klaus Helbing for giving me the opportunity to work in the IceCube collaboration, for many helpful and inspiring discussions, and for his trust, which made this work possible. I would also like to thank Ingrid Schaarwächter for her excellent administrative and organizational support during my time in Wuppertal. Also, I thank Karl-Heinz Kampert for his useful input and support in many aspects. Very special thanks to Sandro Kopper who helped me to get started in IceCube, who introduced me to various software packages and analysis methods, and who was always open for many lively discussions regarding this work and beyond. I would also like to thank Stephanie Hickford for her endless support and many useful discussions with respect to this thesis, also for providing me with accommodation during the last few weeks of my time in Wuppertal, and especially for the great times outside of work. Moreover, I thank Anna Pollmann and Eric Mayotte who helped me in many aspects of this work, as well as Julian Rautenberg and Christian Pauly for many interesting discussions. I would also like to thank everyone in the IceCube cosmic ray working group, especially Hermann Kolanoski, who volunteered to review my work, and Timo Karg for always being available for any questions and for giving me useful input regarding this analysis. I would also like to thank the *friends of atmospheric muons*, Serap Tilav, Anatoli Fedynitch, and Patrick Berghaus for enlightening discussions and great times during various conferences.

Special thanks go to my friends Cornelius Thiem, Christopher Huber, and Martin Stürtzer, without whom this work would not have been possible. Thank you for the countless hours we spent together and the unforgettable experiences we had. I would also like to thank everyone else in my band *Royal Street Orchestra* who made the last eight years unforgettable: Christopher Esch, Nikolaos Rondelis, Dragan Burmazovic, Armin Alic, Max Klaas, Christian Mohrhenn, and Jan Kreienkamp. In addition, I would like to thank Max Pensel, Johannes Klement, Gero Kosack, Björn Bogs, and Marc Munz, as well as Ilka Lancelle and the Zweistein crew for all the enjoyable times over more than 15 years. Last but not least, many thanks to my parents, Birgit and Klaus-Peter Soldin, as well as my brother Marcel, for their love and support through all my life. In this respect, I would also like to thank Wolfgang Soldin for many enjoyable conversations and discussions. Finally, very special thanks to Tante Helga, who triggered my interest in physics and set me on the path towards this work.

[*] In *"White Line Fever"* (2002).

A

SUPPLEMENTS

"Morgenstund' hat Gold im Mund,
doch Abendstund' macht Platin-Platten"
*– Beginner**

Various supplementary material is shown in the following. The cosmic ray flux parametrizations, assumed in this work, are given in Appendix A.1 and the atmospheric MSIS models, used by CORSIKA, are shown in Section A.2. Appendix A.3 discusses the different random number generators, used in LSMuonSim. A definition of the Pearson correlation coefficients is given in Appendix A.4 and additional Feynman diagrams are shown in Appendix A.5. The temperature data, used in order to study the seasonal variations in this analysis, are shown in Appendix A.6.

A.1 COSMIC RAY FLUX PARAMETRIZATIONS

Using the parametrization from Equation (2.12)

$$\Phi_i(E_0) = \sum_j a_{i,j} \cdot E_0^{-\gamma_{i,j}} \cdot \exp\left(-\frac{E_0}{Z_i R_{c,j}}\right) , \tag{A.1}$$

the parameters for different cosmic ray flux assumptions from Ref. [38] and Ref. [39], used in this work, can be found in Table A.2 and Table A.1 respectively.

A.2 ATMOSPHERIC MODEL PARAMETRIZATIONS

The MSIS-90-E atmospheric models [47, 48] use a 5-layer parametrization of the atmosphere where the mass overburden $T(H)$ of the i-th layer is given by

$$T(H) = a_i + b_i^{H/c_i} , \tag{A.2}$$

for the lower four layers, $i = 1, \ldots, 4$. The fifth layer is parametrized linearly by

$$T(H) = a_5 - b_5 \frac{H}{c_5} . \tag{A.3}$$

For the South Pole models used in this work the borders of the different layers are given by $H = (4, 10, 40, 100)$ km and the mass overburden vanishes at $H = 112.8$ km. The parameters a, b, and c are given in Table A.3. Further models can be found in Ref. [47, 48]

* In *"Foxy Music"*, Advanced Chemistry (2016).

H3a / H4a	R_c		p	He	N	Al	Fe
Z			1	2	7	13	26
Population 1	4 PV	a	7860	3550	2200	1430	2120
		γ	1.66	1.58	1.63	1.67	1.63
Population 2	30 PV	a	20	20	13.4	13.4	13.4
		γ	1.4	1.4	1.4	1.4	1.4
Population 3	2 EV	a	1.7	1.7	1.14	1.14	1.14
		γ	1.4	1.4	1.4	1.4	1.4
Population 4	60 EV	a	200				
		γ	1.6				

Table A.1: Parameters for the H3A/H4A flux parametrizations used in this work [38].

GST	R_c		p	He	C	O	Fe
Z			1	2	6	14	26
Population 1	120 TV	a	7000	3200	100	130	60
		γ	1.66	1.58	1.4	1.4	1.3
Population 2	4 PV	a	150	65	6	7	2.3
		γ	1.4	1.3	1.3	1.3	1.2
Population 3	1.3 EV	a	14				0.0025
		γ	1.4				1.2
Population 2*	4 PV	a	150	65	6	7	2.1
		γ	1.4	1.3	1.3	1.3	1.2
Population 3*	1.5 EV	a	12				0.011
		γ	1.4				1.2
Population 4*	40 EV	a	1.2				
		γ	1.4				

Table A.2: Parameters for the GST flux parametrization used in this work [39].

LAYER i	H (km)	a_i (g/cm^2)	b_i (g/cm^2)	a_i (cm)
Mar. 31, 1997				
1	$0-4$	-137.7	1130.7	867358
2	$4-10$	-37.9	1052.1	741208
3	$10-40$	0.2	1137.2	633846
4	$40-100$	-0.0006	442.5	759850
5	>100	0.0021	1.0	$5.43 \cdot 10^9$
Jul. 1, 1997				
1	$0-4$	-163.3	1183.7	875221
2	$4-10$	-65.4	1108.1	753213
3	$10-40$	0.4	1424.0	545846
4	$40-100$	-0.0005	207.6	793043
5	>100	0.0019	1.0	$5.98 \cdot 10^9$
Oct. 1, 1997				
1	$0-4$	-142.8	1177.2	861745
2	$4-10$	-70.2	1125.1	765925
3	$10-40$	1.1	1304.8	581351
4	$40-100$	-0.0009	433.8	775155
5	>100	0.0015	1.0	$7.41 \cdot 10^9$
Dec. 31, 1997				
1	$0-4$	-128.6	1139.9	861813
2	$4-10$	-39.6	1073.8	744955
3	$10-40$	1.1	1052.9	675928
4	$40-100$	-0.0026	492.5	829627
5	>100	0.0019	1.0	$5.86 \cdot 10^9$

Table A.3: Parameters for the MSIS-90-E atmospheric models used in this work [47, 48].

A.3 RANDOM NUMBER GENERATION

For the generation of LS MUON events in LSMUONSIM, many pseudo-random number generators are used. The general concept of pseudo-random number generation from a given probability density function is described in the following. In addition, the different generators used in LSMUONSIM are described.

A.3.1 GENERAL CONCEPT

In order to obtain a spectrum from a given distribution or probability function, the following steps have to be performed:

(a) Assuming a simple power law spectrum, the probability density function is given by

$$\frac{d\Phi}{dE} = \alpha \cdot E^{\beta} \tag{A.4}$$

with $E_{min} \leqslant E < E_{max}$. This probability function is shown in Figure A.1 (a), using $\beta = -1$ and normalized to 1.

(b) The corresponding cumulative distribution function is given by

$$\Phi(E) = \int_{E_{min}}^{E} \alpha \cdot E' \, dE' = \frac{\alpha}{\beta + 1} \left(E^{\beta+1} - E_{min}^{\beta+1} \right) , \tag{A.5}$$

which is shown in Figure A.1 (b).

(c) The inverted CDF

$$E(\Phi) = \left(\frac{\beta + 1}{\alpha} \cdot \Phi + E_{min}^{\beta+1} \right)^{1/(\beta+1)} \tag{A.6}$$

is shown in Figure A.1 (c).

(d) The desired spectrum can be generated by replacing Φ with uniformly distributed values between 0 and $\Phi(E_{max})$ (see Figure A.1 (d)).

A simple realization of a pseudo-random number generator, using the python programing language, is shown below. The function `sampling()` generates a pseudo-random number between `xmin` and `xmax` from any given probability function of the form `pdf(param,x)`, as described above, where `param` is a corresponding list of parameters (here $\alpha = 1$, $\beta = -1$).

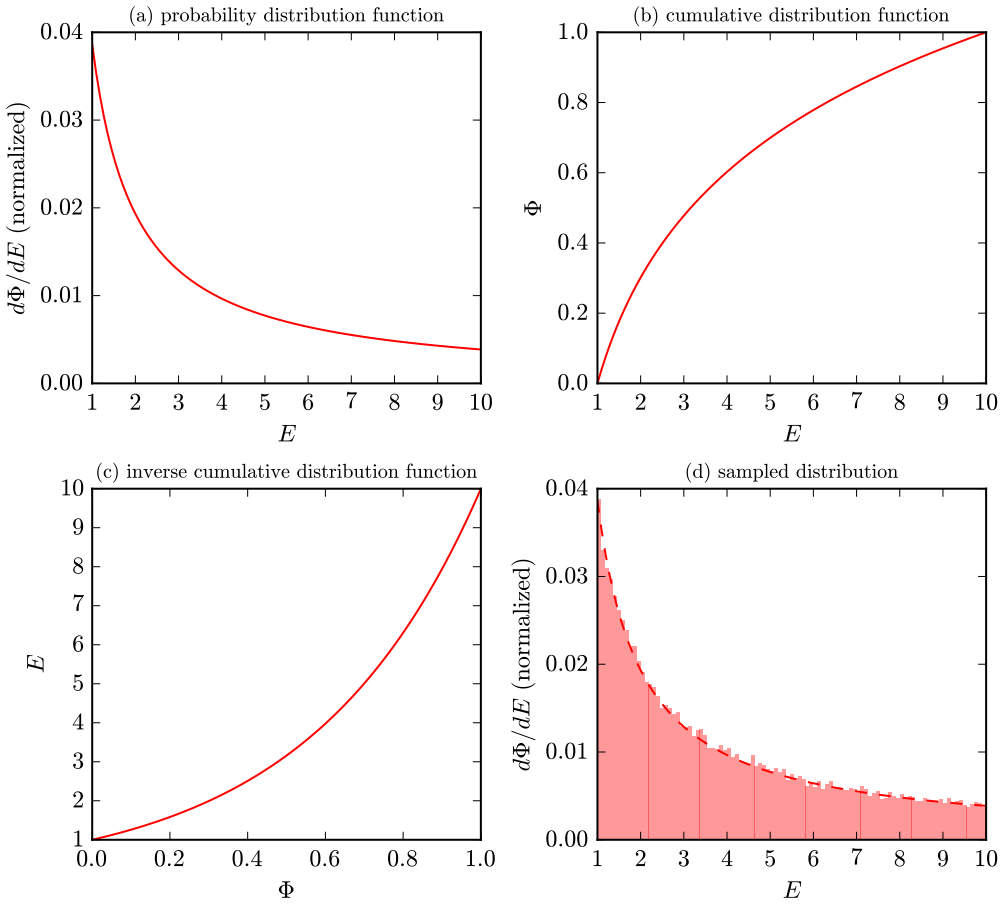

Figure A.1: Random number generation based on the probability density function Equation (A.4), as described in the text.

```
import numpy
from scipy import interpolate

param = [1, -1]
pdf = lambda p, x: p[0] * x**p[1]

def sampling(pdf, param, xmin, xmax):
   steps=1000
   binning = numpy.linspace(xmin, xmax, steps)
   y_data = pdf(param, binning)
   y_data = y_data[:-1] / numpy.sum(y_data[:-1])
   cum_values = numpy.zeros(binning.shape)
   cum_values[1:] = numpy.cumsum(y_data)
   inv_cdf = interpolate.interp1d(cum_values, binning)
   r = numpy.random.uniform()

   return inv_cdf(r)
```

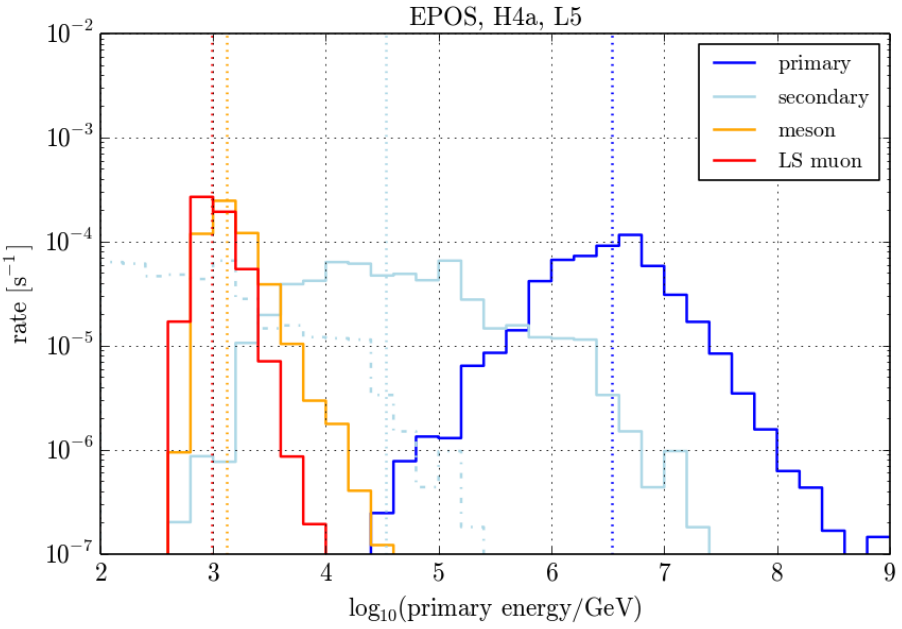

Figure A.2: Energy spectrum of particles produced in the first two interactions during shower development, obtained from LSMuonSim at final analysis level. Dotted, vertical lines indicate the corresponding mean energies for each distribution.

A.3.2 FURTHER PARTICLE GENERATIONS

The energy spectrum of hadrons produced during the first two hadronic interactions during the air shower development, obtained from LSMuonSim as described in Section 5.4.4, are shown in Figure A.2. The contribution of hadrons produced in the *Primary* production channel is defined in Section 5.4.2. The energy spectrum of *Secondary* hadrons includes mesons produced in the production channels *Secondary I* and *Secondary II*, also described in Section 5.4.2.

As shown in Figure A.2, the mean energy of hadrons (dotted, vertical lines) produced in a secondary interaction is approximately two orders of magnitude smaller than the primary collision energy. Assuming the same scaling for the next interaction, the resulting hadron spectrum can be approximated with an energy spectrum, indicated by the dashed-dotted line. The mean energy of the resulting LS Muons can then be estimated to be typically below ~ 100 GeV. Since the threshold energy a vertical muon to reach the deep IceCube detector is about 460 GeV, the contribution of LS Muons from further re-interactions during the shower development can be neglected in this work.

A.3.3 TRANSVERSE MOMENTUM

As described in Section 5.4.3, in LSMUONSIM the transverse momentum for each event is generated, using the probability density function Equation (5.4)

$$\frac{dN}{dp_T} = 2\alpha\pi p_T \cdot \left(1 + \frac{p_T}{p_0}\right)^{\beta}, \tag{A.7}$$

with fixed spectral index $\beta = -3.0$, $\alpha = 1.0$, and $p_0 = 2.0\,\text{GeV}$. The transverse momentum for each event is randomly generated between $p_{T,min} = 1.0\,\text{GeV}$ and $p_{T,max} = 10.0\,\text{GeV}$ using the inverse of the Cumulative Distribution Function (CDF).

$$\begin{aligned}\Phi(p_T) &\equiv \int_{p_{T,min}}^{p_T} 2\pi p'_T \cdot \left(1 + \frac{p'_T}{p_0}\right)^{-3} dp'_T \qquad (A.8)\\ &= \left[-\frac{\pi p_0^3 \cdot (p_0 + 2p'_T)}{(p_0 + p'_T)^2}\right]_{p_{T,min}}^{p_T}\\ \Rightarrow p_T(\Phi) &= \frac{-p_0 A - \sqrt{1 + p_0 A} - 1}{A}, \qquad (A.9)\\ A &\equiv \frac{RD \cdot \Phi(p_{T,max})}{\pi p_0^3} - \frac{p_0 + 2p_{T,min}}{(p_0 + p_{T,min})^2},\end{aligned}$$

where RD is a random number between 0 and 1.

In order to account for a realistic p_T spectrum, each event is re-weighted as described in Section 5.4.3, by applying the weight

$$\begin{aligned}\omega_{p_T}(E, p_T) &= \frac{\text{expected } p_T \text{ spectrum}}{\text{generated } p_T \text{ spectrum}}\\ &= N_0 \cdot \left(1 + \frac{p_T}{p_0}\right)^{\beta(E_0)+3}\end{aligned} \tag{A.10}$$

to each LS MUON event. The generated and the expected spectrum are normalized to 1 by applying the normalization factor

$$N_0 \equiv \frac{\int_{p_{T,min}}^{p_{T,max}} p'_T \cdot \left(1 + \frac{p'_T}{p_0}\right)^{-3} dp'_T}{\int_{p_{T,min}}^{p_{T,max}} p'_T \cdot \left(1 + \frac{p'_T}{p_0}\right)^{\beta(E_0)} dp'_T}. \tag{A.11}$$

A.3.4 PATH LENGTHS

Decay

To simulate the decay of unstable hadrons h, produced at altitude H, only the decay term of the cascade equations (Equation (2.21)) needs to be taken into account. With the decay length defined in Equation (2.18) they reduce to Equation (5.10)

$$\frac{d\Phi_h(E, X)}{dX} = -\frac{\Phi_h(E, X)}{\lambda_{dec,h}} = -\frac{\Phi_h(E, X)}{c\beta\gamma\tau_h\rho(H)}. \tag{A.12}$$

The next decay vertex of the hadron is then generated by calculating the inverse CDF. Assuming the atmospheric density given in Equation (2.17) and that a hadron h was produced at slant depth $X(H)$, that decays at $X(H_h)$:

$$\begin{aligned}
\int \frac{1}{\Phi} d\Phi = \ln(\Phi) &= -\frac{h_0}{c\beta\gamma\tau_h \cos(\theta)} \cdot \int_{X(H_h)}^{X(H)} \frac{1}{X'} dX' \\
\Rightarrow -\frac{c\beta\gamma\tau_h \cos(\theta) \ln(\Phi)}{h_0} &= \ln(X(H)) - \ln(X(H_h)) \\
&= \ln(X_0 \cdot e^{-H_h/h_0}) - \ln(X_0 \cdot e^{-H/h_0}) \\
&= \frac{H - H_h}{h_0} \\
\Rightarrow -c\beta\gamma\tau_h \ln(\Phi) &= \frac{H - H_h}{\cos(\theta)} \equiv L_{dec,h}(E_h) \,, \qquad \text{(A.13)}
\end{aligned}$$

where the mean lifetime of hadrons is taken from the Particle Data Group (PDG) [34]. The resulting path length $L_{dec,h}$ to the decay vertex of each hadron with energy E_h is now generated randomly by replacing Φ with a uniformly distributed number RD between 0 and 1:

$$\begin{aligned}
L_{h,dec}(E_h) &= -c\beta\gamma\tau_h \cdot \ln(RD) \\
&= -c \cdot \frac{\sqrt{E_h^2 - m_h^2}}{m_h} \tau_h \cdot \ln(RD) \,. \qquad \text{(A.14)}
\end{aligned}$$

Interaction

The same approach is used for any hadron produced at height H that re-interacts in the atmosphere at height H_h. Neglecting the decay and regeneration terms, the cascade Equation (2.21) reduce to Equation (5.12)

$$\frac{d\Phi_h(E,X)}{dX} = -\frac{\Phi_h(E,X)}{\lambda_{int,h}} \,, \qquad \text{(A.15)}$$

with the (inverse) CDF

$$\begin{aligned}
\int \frac{1}{\Phi} d\Phi = \ln(\Phi) &= -\int_{X(H_h)}^{X(H)} \frac{1}{\lambda_{int,h}} dX' \\
\Rightarrow -\lambda_{int,h} \ln(\Phi) &= X(H) - X(H_h) \\
&= X_0 \cdot e^{-H/h_0} - X_0 \cdot e^{-H_h/h_0} \\
\Rightarrow H_h &= -h_0 \ln\left(e^{-H/h_0} - \frac{\lambda_{int,h} \cdot \ln(\Phi)}{X_0}\right) \qquad \text{(A.16)}
\end{aligned}$$

By replacing Φ with a random uniform number RD between 0 and 1, the traveled path length $L_{int,h}$ of the hadron before interacting is then given by

$$\begin{aligned}
L_{int,h}(E_h, \theta, H) &\equiv \frac{H - H_h}{\cos\theta} \\
&= \frac{H}{\cos(\theta)} + \frac{h_0}{\cos(\theta)} \cdot \ln\left(e^{-H/h_0} - \frac{\lambda_{int,h} \cdot \ln(RD)}{X_0}\right) \,, \qquad \text{(A.17)}
\end{aligned}$$

with $\lambda_{\text{int,h}}$ given in Equation (2.19). The cross-sections of hadrons are obtained from the underlying hadronic model and can be found in Appendix B.4.

A.4 PEARSON CORRELATION COEFFICIENT

The *Pearson (product-moment) correlation coefficient* is a measure of the linear correlation between two variables x and y and given by [193]

$$r_p(x, y) = \frac{\text{cov}(x, y)}{\sigma_x \cdot \sigma_y}, \tag{A.18}$$

where $\text{cov}(x, y)$ is the covariance and σ_x, σ_y are the standard deviations of x and y. It has a value of $+1$ in case of a total positive correlation and -1 for a total negative correlation. The two values are linearly uncorrelated if $r_p(x, y) = 0$.

A.5 FEYNMAN DIAGRAMS

The Feynman diagrams for the inelastic bremsstrahlung process, as described in Section 3.1, are shown in Figure A.3.

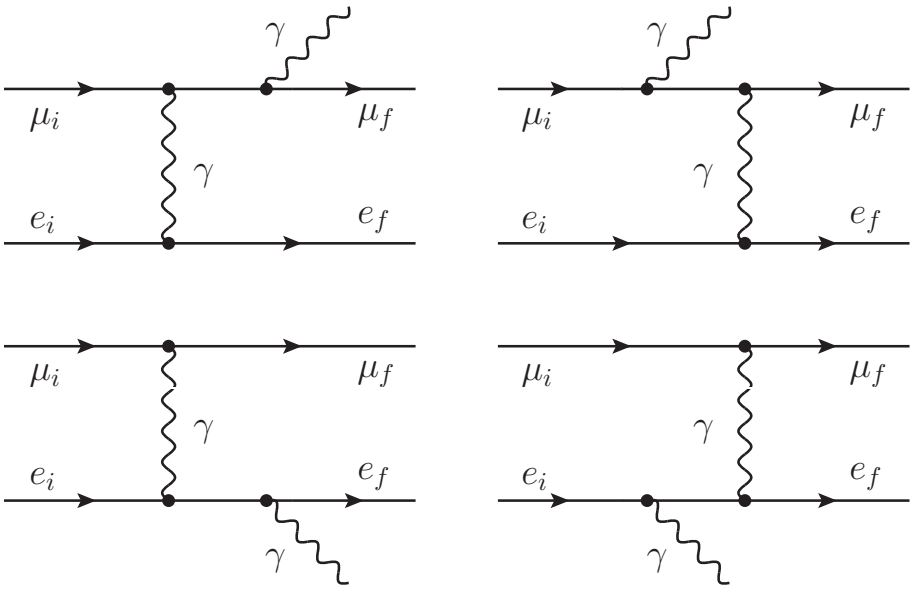

Figure A.3: Feynman diagrams of the inelastic bremsstrahlung process, as described in Section 3.1.

A.6 SEASONAL VARIATIONS

The temperature data, taken by the NASA AIRS project [223], is shown in Figure A.4 (top panel). The corresponding temperature variations are also shown (bottom panel). For comprehensive discussions on atmospheric temperature data, see for example Refs. [223, 247]. The corresponding heights of the atmospheric pressure layers are shown in Figure A.5 as a function of the annual season. The data is taken from Ref. [248]. Figure A.6 shows the seasonal variations of events after pre-filtering (Lo), which are used in Section 7.6.

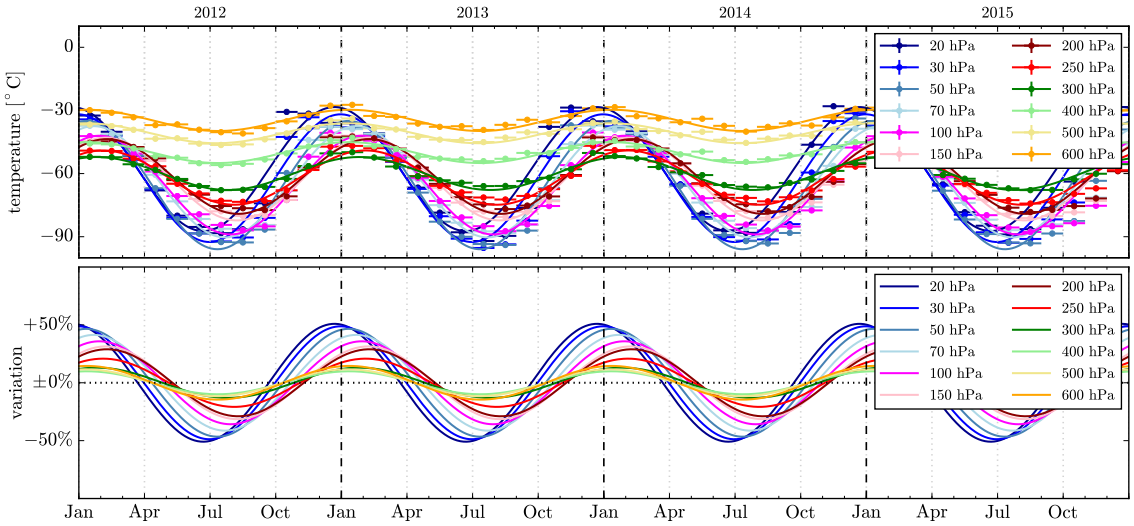

Figure A.4: Seasonal temperature variations measured by the AIRS experiment, taken from Ref. [223].

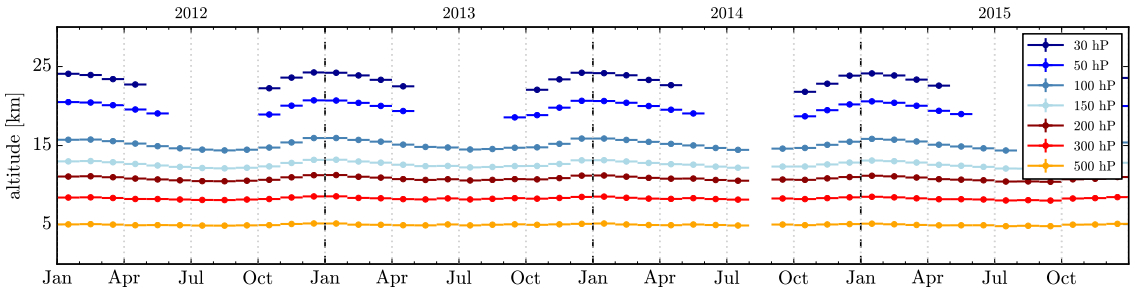

Figure A.5: Altitudes of the atmospheric pressure layers as a function of the annual season. Taken from Ref. [223]

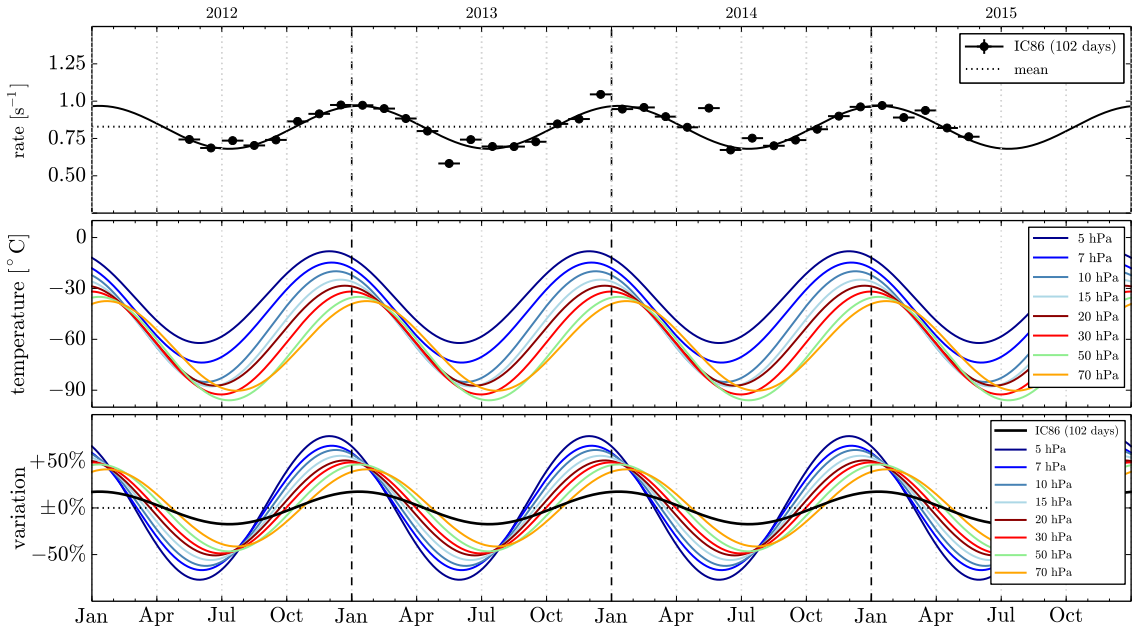

Figure A.6: Seasonal variations of the event rate after pre-filtering (Lo) obtained from 102 days of burnsample data (top), as well as temperature variations in various atmospheric layers (center). The corresponding variations are combined in the bottom panel.

B

SIMULATION INPUTS

"The inside of a computer is as dumb as hell
but it goes like mad!"
– Richard P. Feynman *

In the following, the input distributions used in LSMuonSim, as described in Section 5.4, are shown. A collection of various spectral indices of the transverse momentum distributions, obtained from different hadronic models, is presented in Appendix B.1. The corresponding energy spectra of hadrons, obtained from EPOS-LHC (only), are shown in Appendix B.2. In Appendix B.3 the hadron generation probabilities are shown and the cross-sections used in LSMuonSim are given in Appendix B.4. Finally, pearson coefficients between hadron energy and transverse momentum, obtained from EPOS-LHC (only), are shown in Appendix B.5.

B.1 SPECTRAL INDICES

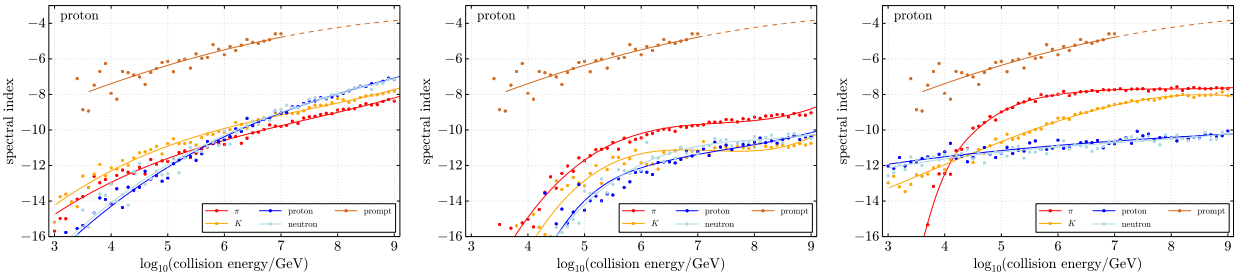

Figure B.1: Spectral indices β obtained from Hagedorn fits of the form Equation (2.34) for proton-nitrogen collisions at various energies using EPOS-LHC (left), Sibyll 2.1 (center), and QGSJet II-4 (right) as hadronic model.

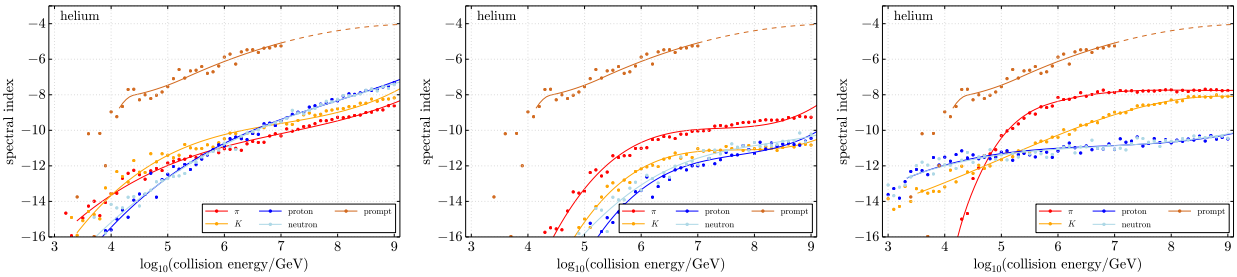

Figure B.2: Spectral indices β obtained from Hagedorn fits of the form Equation (2.34) for helium-nitrogen collisions at various energies using EPOS-LHC (left), Sibyll 2.1 (center), and QGSJet II-4 (right) as hadronic model.

* In *"Feynman Lectures on Computation"* (1964).

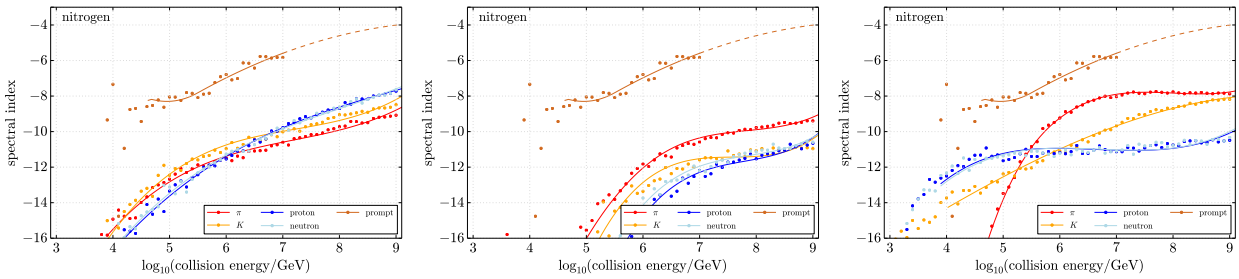

Figure B.3: Spectral indices β obtained from Hagedorn fits of the form Equation (2.34) for nitrogen-nitrogen collisions at various energies using EPOS-LHC (left), SIBYLL 2.1 (center), and QGSJET II-4 (right) as hadronic model.

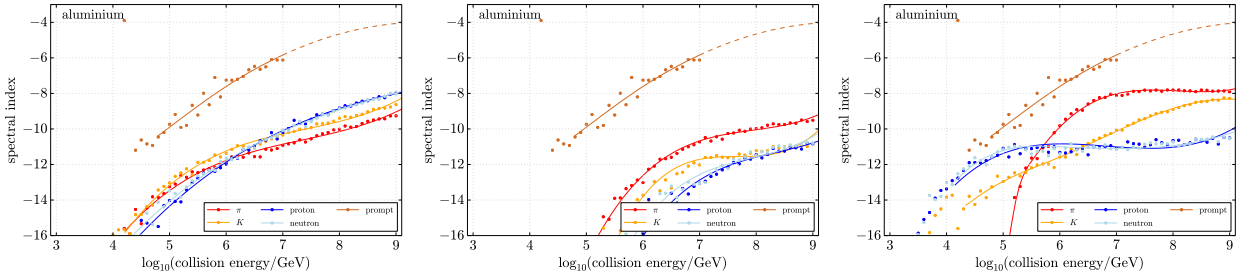

Figure B.4: Spectral indices β obtained from Hagedorn fits of the form Equation (2.34) for aluminium-nitrogen collisions at various energies using EPOS-LHC (left), SIBYLL 2.1 (center), and QGSJET II-4 (right) as hadronic model.

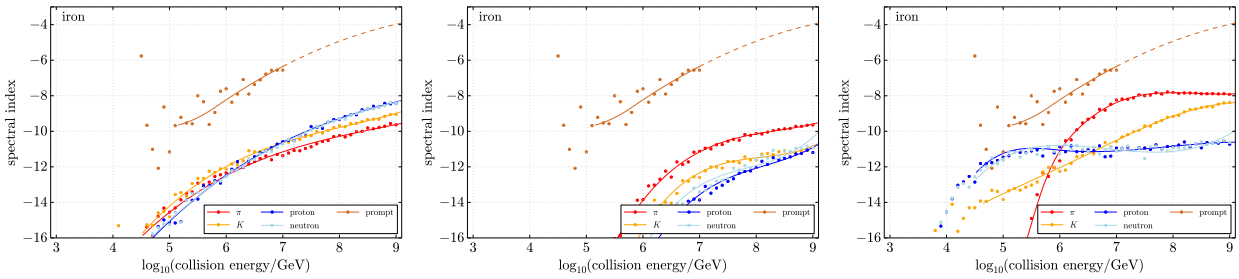

Figure B.5: Spectral indices β obtained from Hagedorn fits of the form Equation (2.34) for iron-nitrogen collisions at various energies using EPOS-LHC (left), SIBYLL 2.1 (center), and QGSJET II-4 (right) as hadronic model.

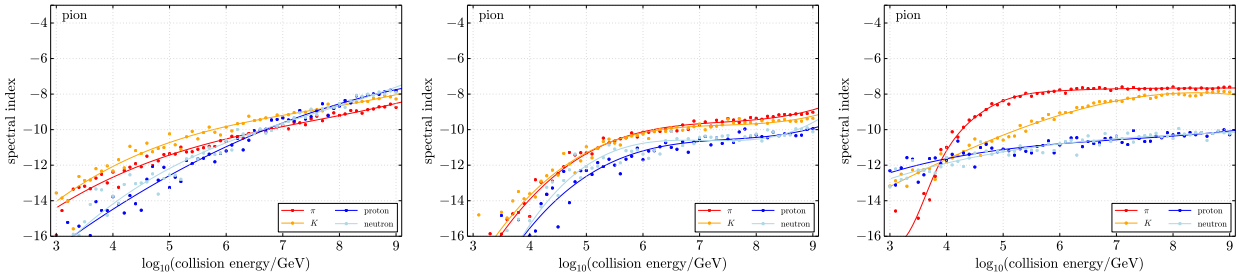

Figure B.6: Spectral indices β obtained from Hagedorn fits of the form Equation (2.34) for pion-nitrogen collisions at various energies using EPOS-LHC (left), SIBYLL 2.1 (center), and QGSJET II-4 (right) as hadronic model.

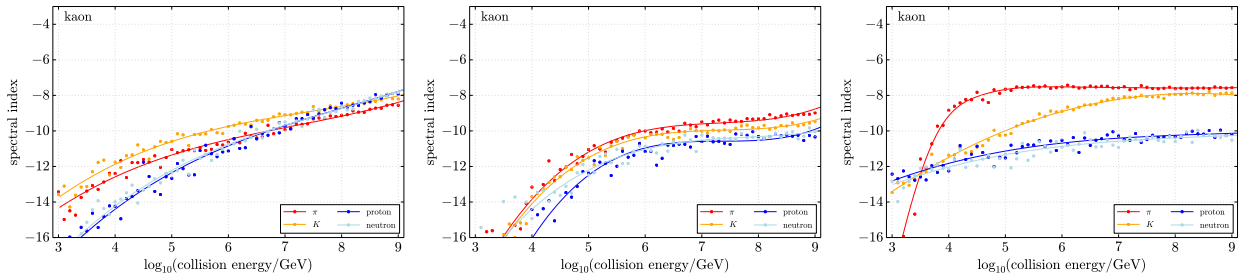

Figure B.7: Spectral indices β obtained from Hagedorn fits of the form Equation (2.34) for kaon-nitrogen collisions at various energies using EPOS-LHC (left), SIBYLL 2.1 (center), and QGSJET II-4 (right) as hadronic model.

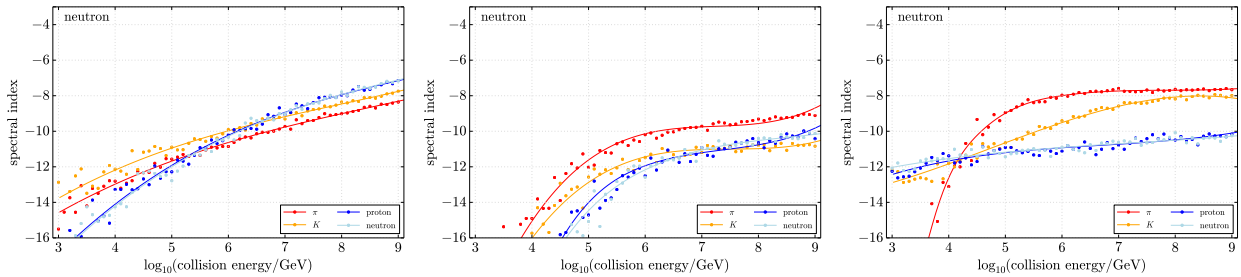

Figure B.8: Spectral indices β obtained from Hagedorn fits of the form Equation (2.34) for neutron-nitrogen collisions at various energies using EPOS-LHC (left), SIBYLL 2.1 (center), and QGSJET II-4 (right) as hadronic model.

B.2 ENERGY SPECTRA

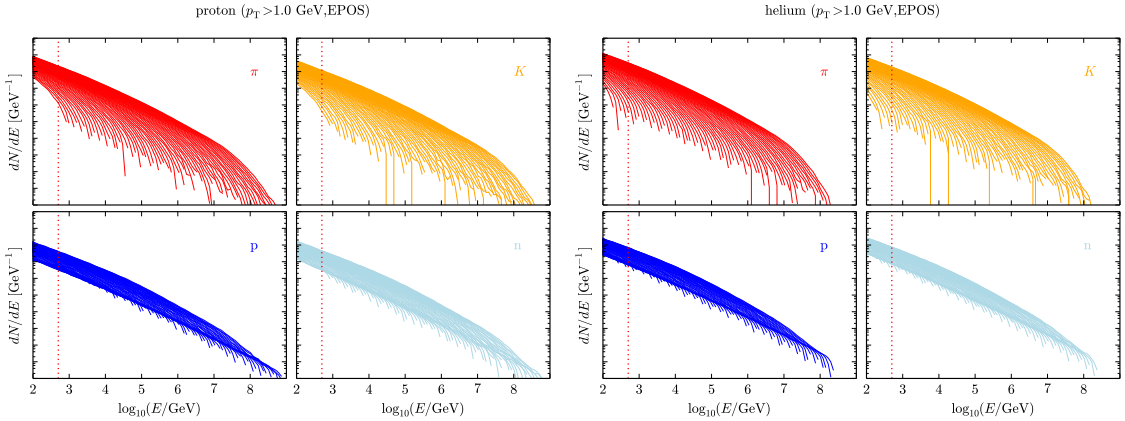

Figure B.9: High p_T hadron energy spectra obtained from proton-nitrogen (left) and helium-nitrogen (right) collisions at various energies using EPOS-LHC.

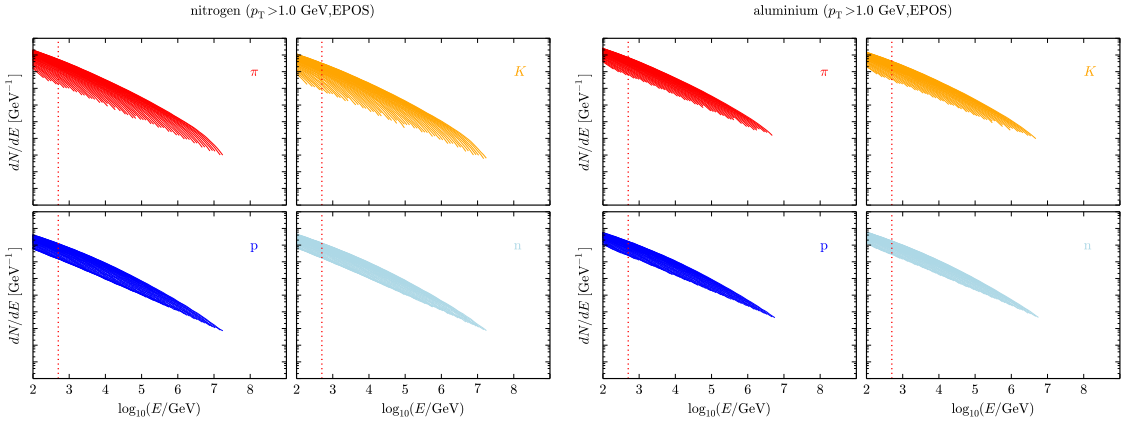

Figure B.10: High p_T hadron energy spectra obtained from nitrogen-nitrogen (left) and aluminium-nitrogen (right) collisions at various energies using EPOS-LHC.

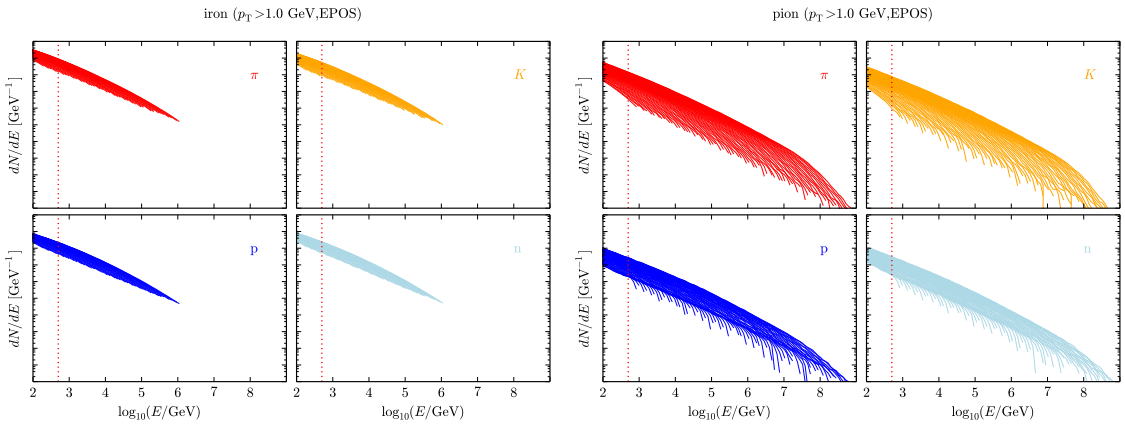

Figure B.11: High p_T hadron energy spectra obtained from iron-nitrogen (left) and pion-nitrogen (right) collisions at various energies using EPOS-LHC.

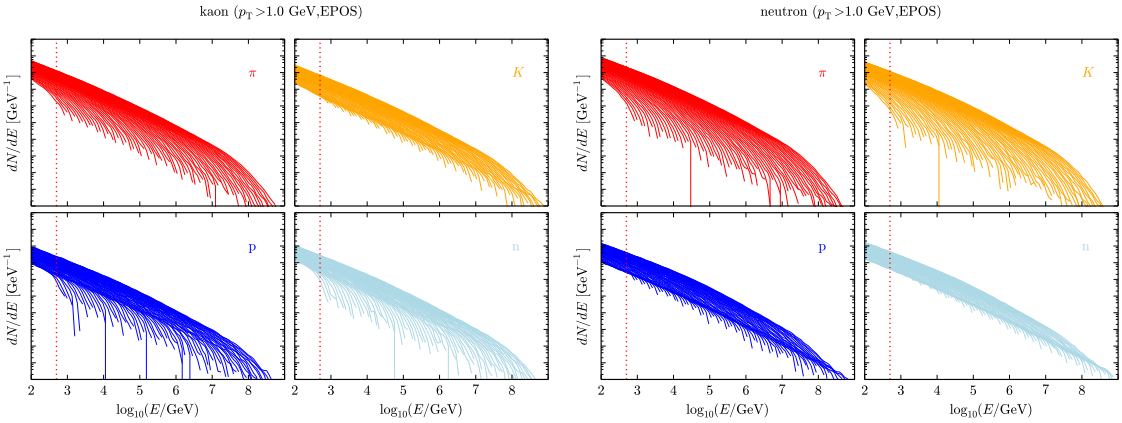

Figure B.12: High p_T hadron energy spectra obtained from kaon-nitrogen (left) and neutron-nitrogen (right) collisions at various energies using EPOS-LHC.

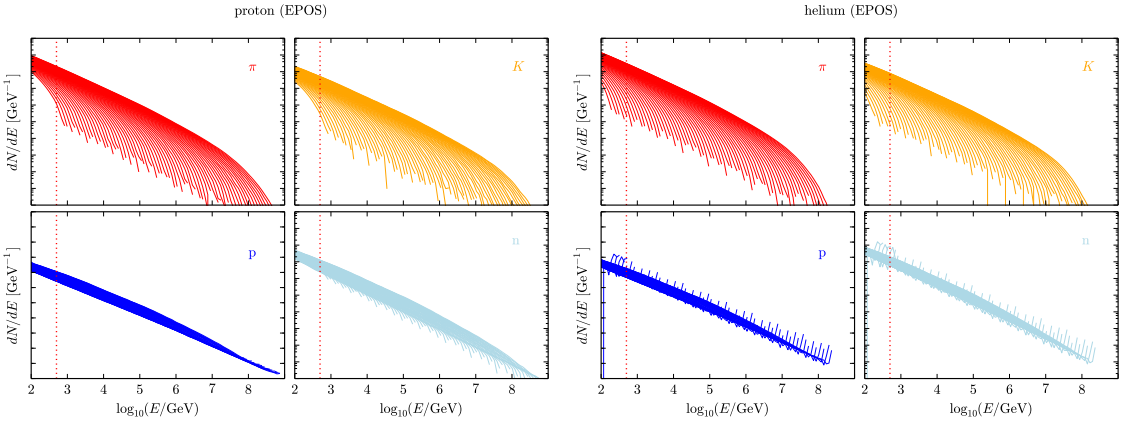

Figure B.13: All hadron energy spectra obtained from proton-nitrogen (left) and helium-nitrogen (right) collisions at various energies using EPOS-LHC.

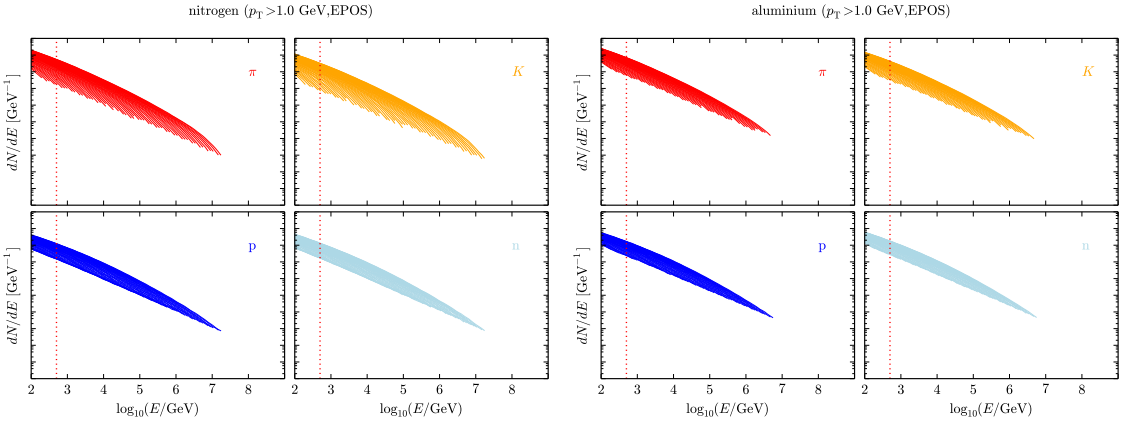

Figure B.14: All hadron energy spectra obtained from nitrogen-nitrogen (left) and aluminium-nitrogen (right) collisions at various energies using EPOS-LHC.

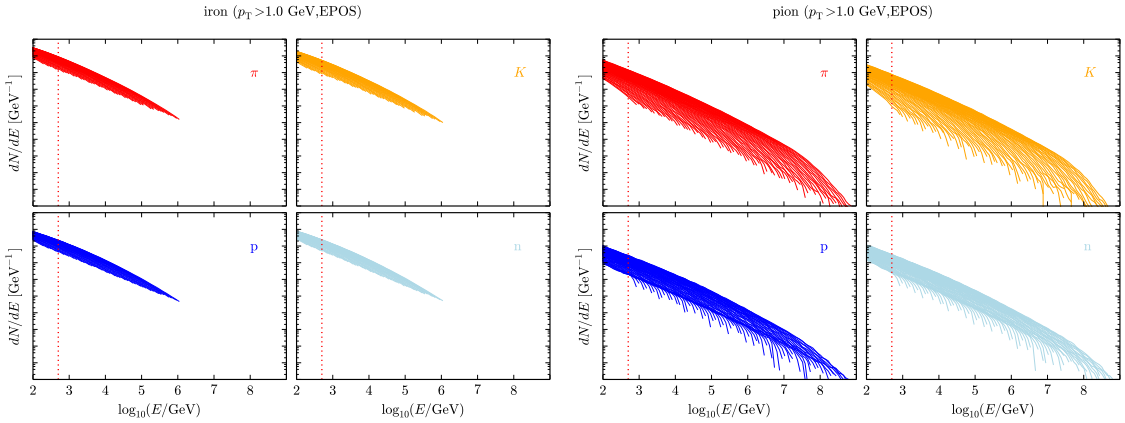

Figure B.15: All hadron energy spectra obtained from iron-nitrogen (left) and pion-nitrogen (right) collisions at various energies using EPOS-LHC.

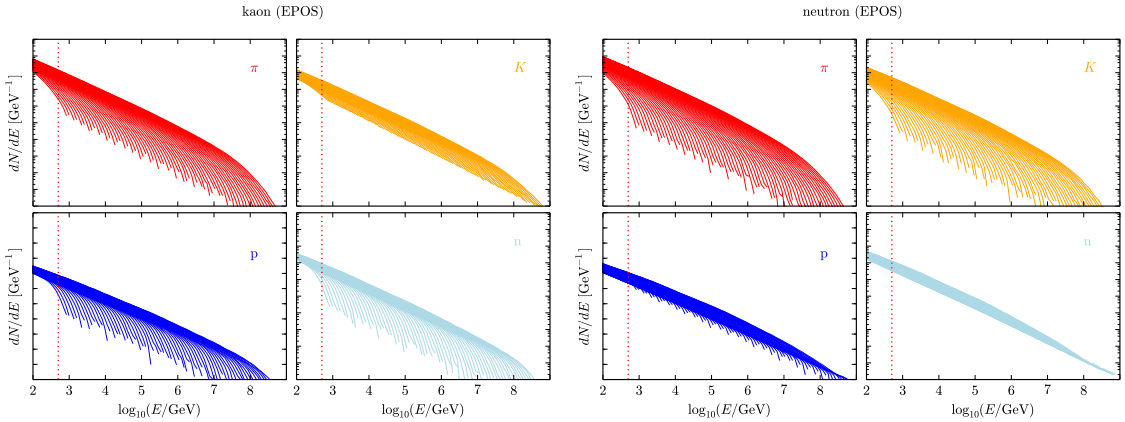

Figure B.16: All hadron energy spectra obtained from kaon-nitrogen (left) and neutron-nitrogen (right) collisions at various energies using EPOS-LHC.

B.3 GENERATION PROBABILITIES

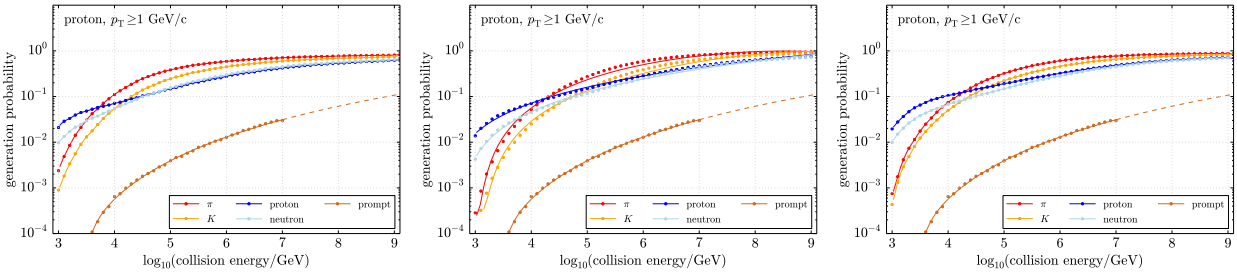

Figure B.17: High p_T generation probabilities obtained from proton-nitrogen collisions at various energies using EPOS-LHC (left), SIBYLL 2.1 (center), and QGSJET II-4 (right) as hadronic model.

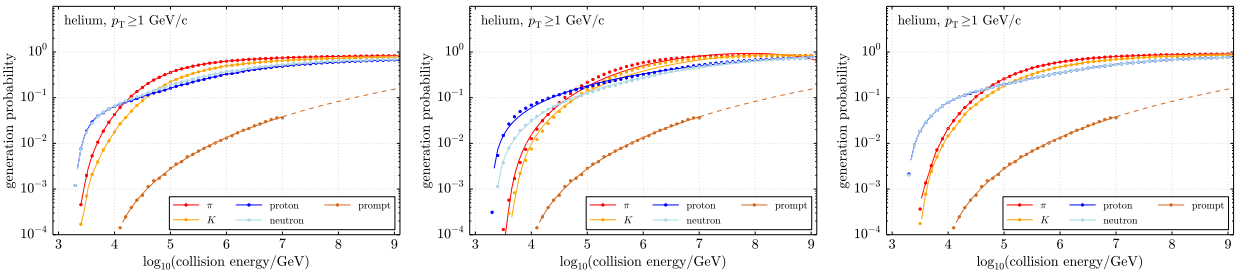

Figure B.18: High p_T generation probabilities obtained from helium-nitrogen collisions at various energies using EPOS-LHC (left), SIBYLL 2.1 (center), and QGSJET II-4 (right) as hadronic model.

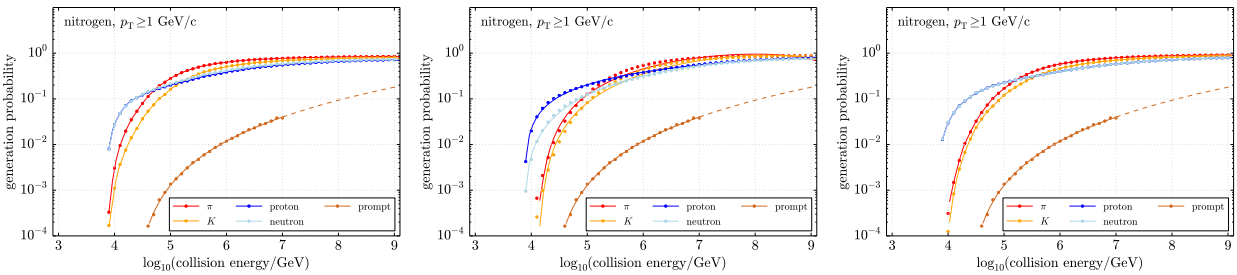

Figure B.19: High p_T generation probabilities obtained from nitrogen-nitrogen collisions at various energies using EPOS-LHC (left), SIBYLL 2.1 (center), and QGSJET II-4 (right) as hadronic model.

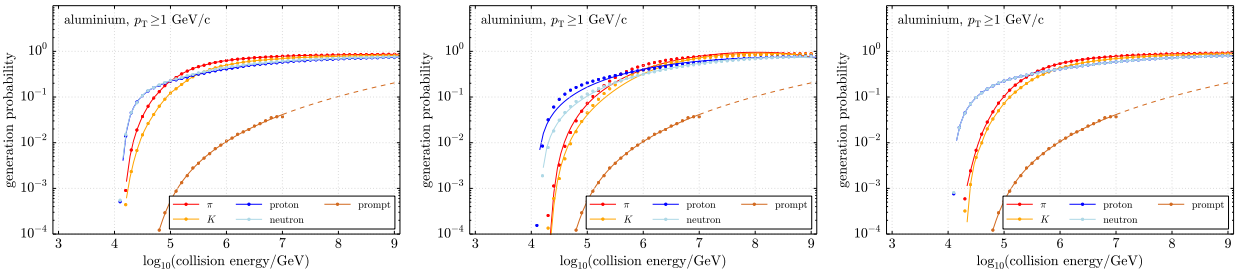

Figure B.20: High p_T generation probabilities obtained from aluminium-nitrogen collisions at various energies using EPOS-LHC (left), SIBYLL 2.1 (center), and QGSJET II-4 (right) as hadronic model.

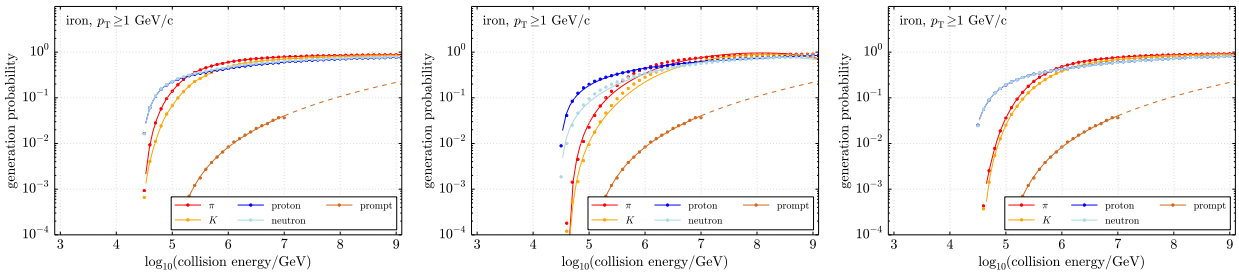

Figure B.21: High p_T generation probabilities obtained from iron-nitrogen collisions at various energies using EPOS-LHC (left), SIBYLL 2.1 (center), and QGSJET II-4 (right) as hadronic model.

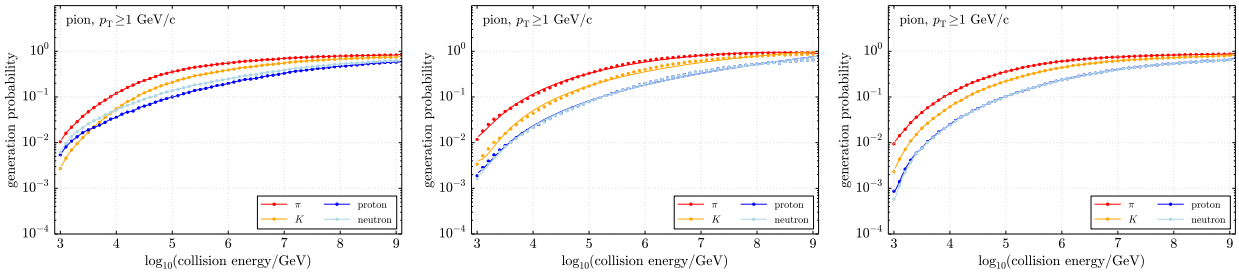

Figure B.22: High p_T generation probabilities obtained from pion-nitrogen collisions at various energies using EPOS-LHC (left), SIBYLL 2.1 (center), and QGSJET II-4 (right) as hadronic model.

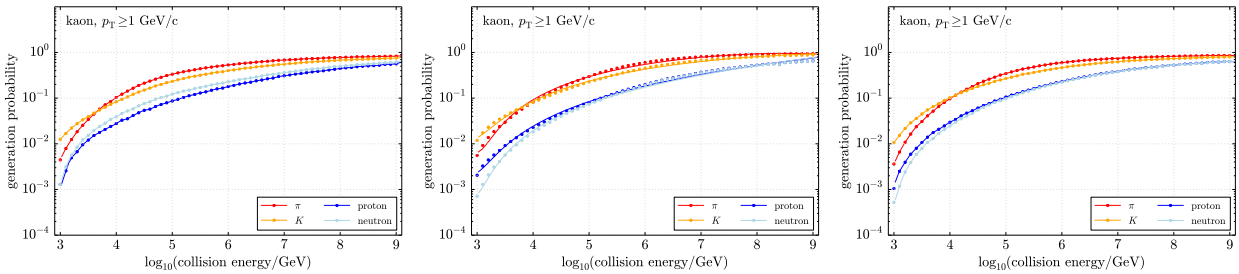

Figure B.23: High p_T generation probabilities obtained from kaon-nitrogen collisions at various energies using EPOS-LHC (left), SIBYLL 2.1 (center), and QGSJET II-4 (right) as hadronic model.

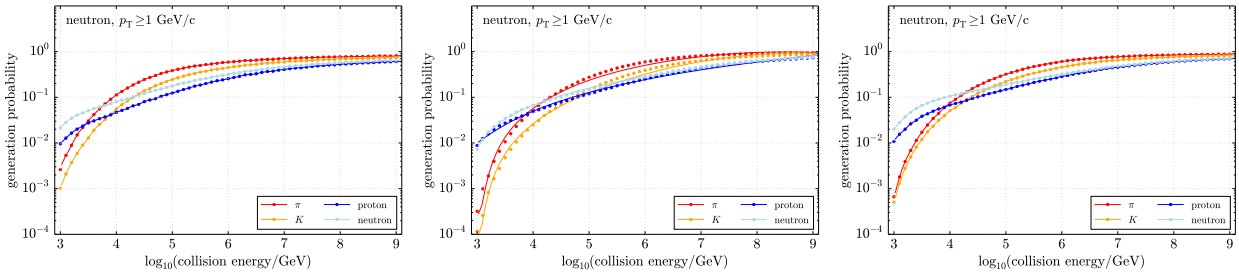

Figure B.24: High p_T generation probabilities obtained from neutron-nitrogen collisions at various energies using EPOS-LHC (left), SIBYLL 2.1 (center), and QGSJET II-4 (right) as hadronic model.

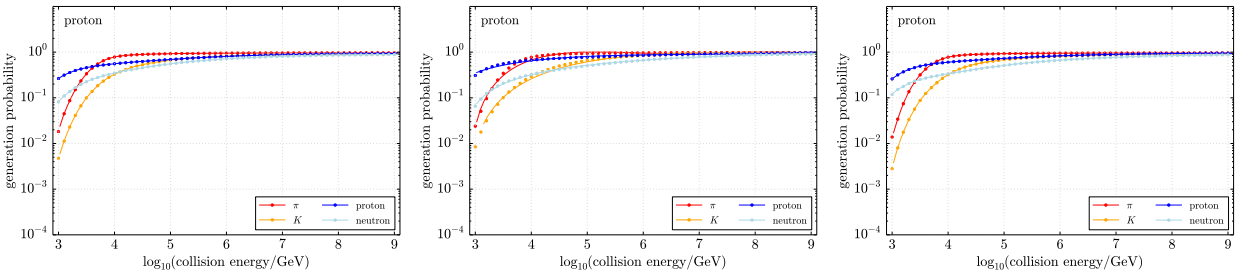

Figure B.25: All hadron generation probabilities obtained from proton-nitrogen collisions at various energies using EPOS-LHC (left), SIBYLL 2.1 (center), and QGSJET II-4 (right) as hadronic model.

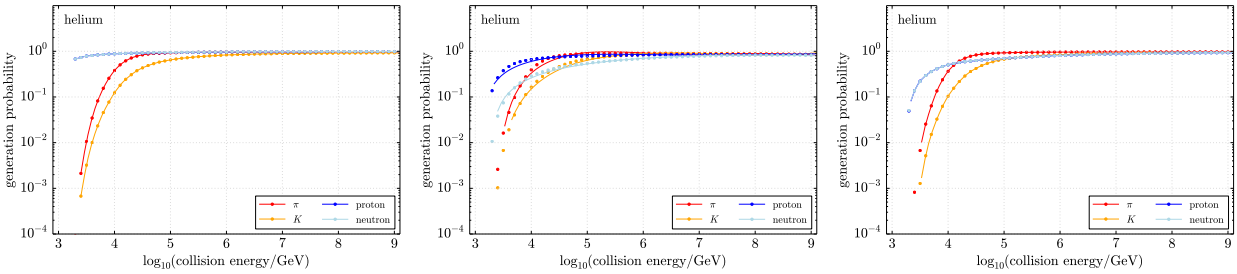

Figure B.26: All hadron generation probabilities obtained from helium-nitrogen collisions at various energies using EPOS-LHC (left), SIBYLL 2.1 (center), and QGSJET II-4 (right) as hadronic model.

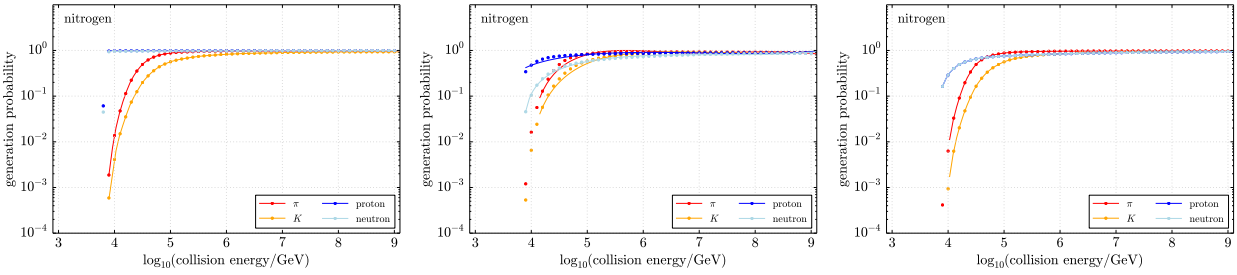

Figure B.27: All hadron generation probabilities obtained from nitrogen-nitrogen collisions at various energies using EPOS-LHC (left), SIBYLL 2.1 (center), and QGSJET II-4 (right) as hadronic model.

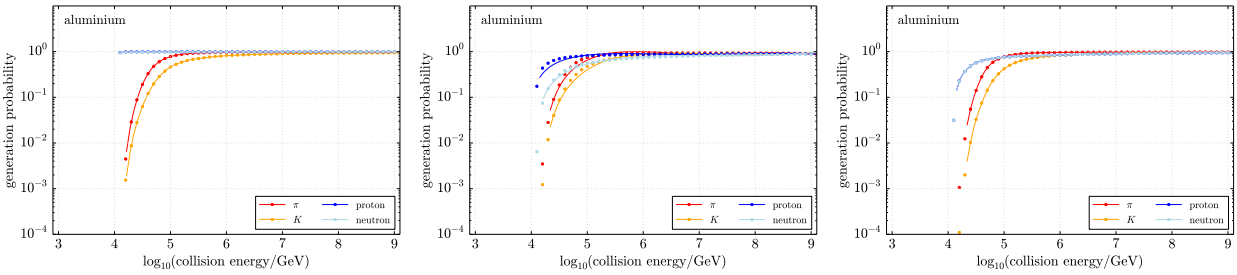

Figure B.28: All hadron generation probabilities obtained from aluminium-nitrogen collisions at various energies using EPOS-LHC (left), SIBYLL 2.1 (center), and QGSJET II-4 (right) as hadronic model.

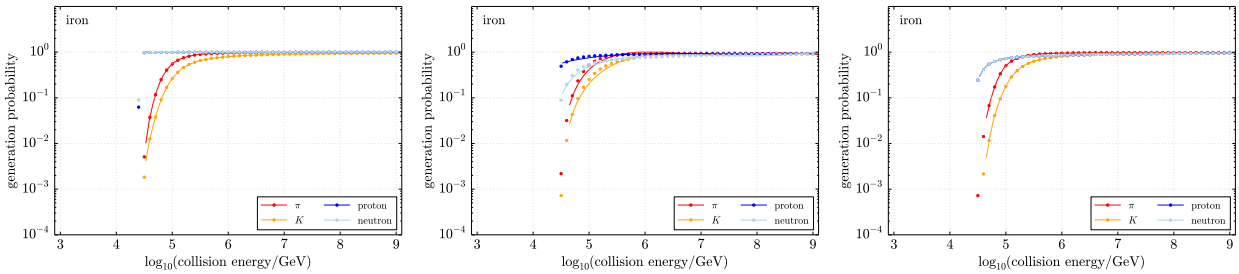

Figure B.29: All hadron generation probabilities obtained from iron-nitrogen collisions at various energies using EPOS-LHC (left), SIBYLL 2.1 (center), and QGSJET II-4 (right) as hadronic model.

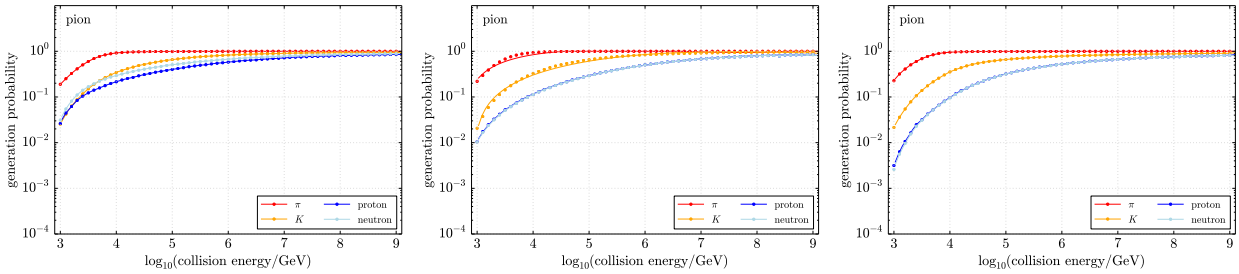

Figure B.30: All hadron generation probabilities obtained from pion-nitrogen collisions at various energies using EPOS-LHC (left), SIBYLL 2.1 (center), and QGSJET II-4 (right) as hadronic model.

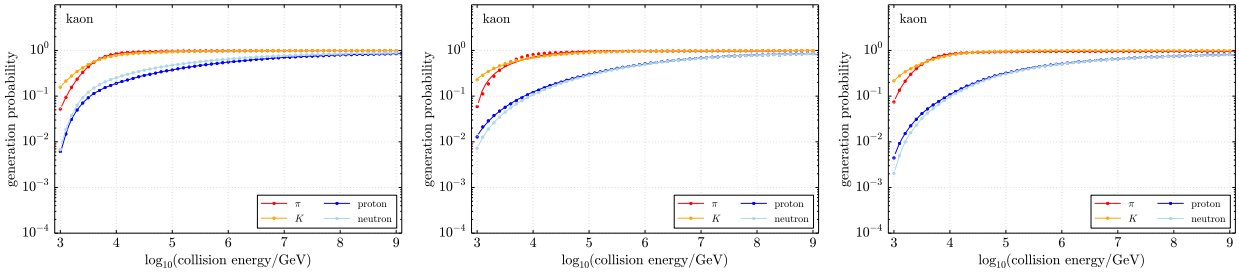

Figure B.31: All hadron generation probabilities obtained from kaon-nitrogen collisions at various energies using EPOS-LHC (left), SIBYLL 2.1 (center), and QGSJET II-4 (right) as hadronic model.

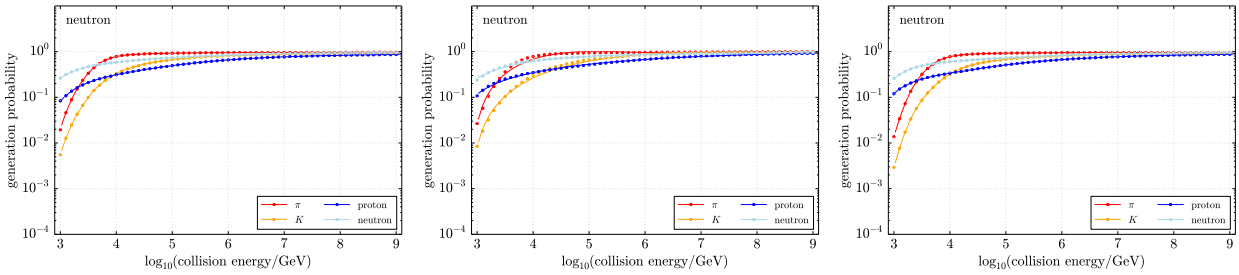

Figure B.32: All hadron generation probabilities obtained from neutron-nitrogen collisions at various energies using EPOS-LHC (left), SIBYLL 2.1 (center), and QGSJET II-4 (right) as hadronic model.

B.4 CROSS SECTIONS

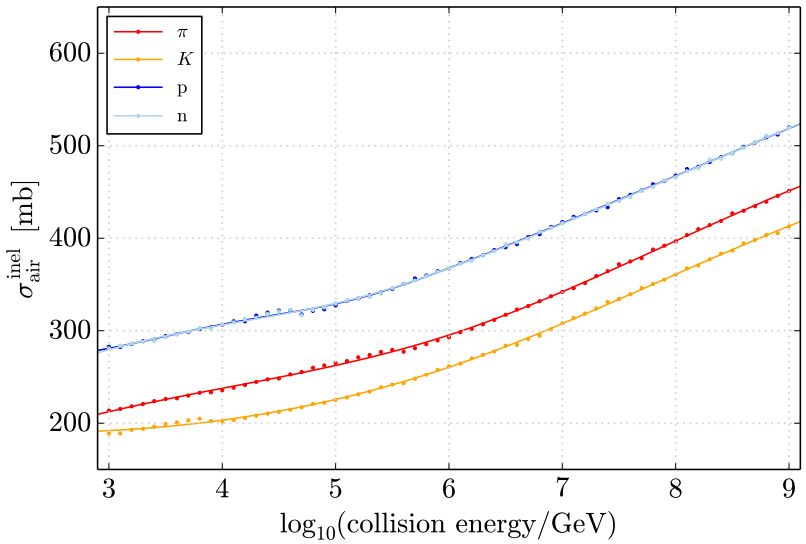

Figure B.33: Inelastic hadron-air cross-section obtained from EPOS-LHC.

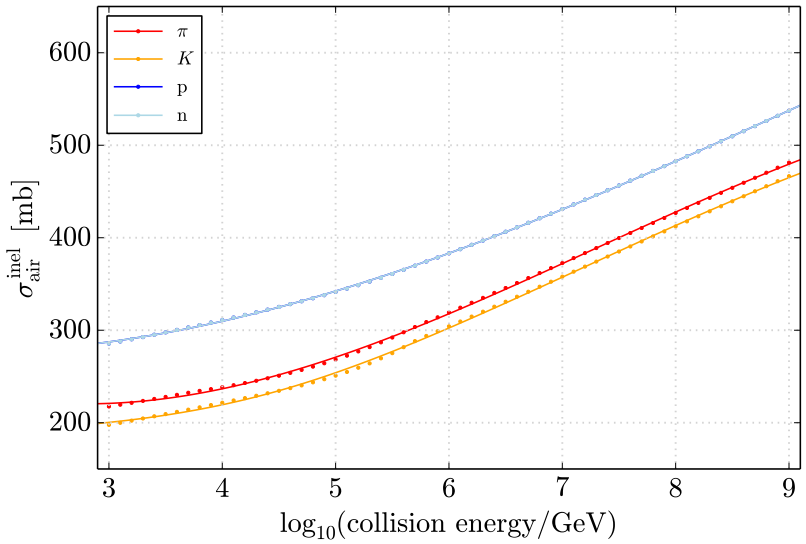

Figure B.34: Inelastic hadron-air cross-section obtained from SIBYLL 2.1.

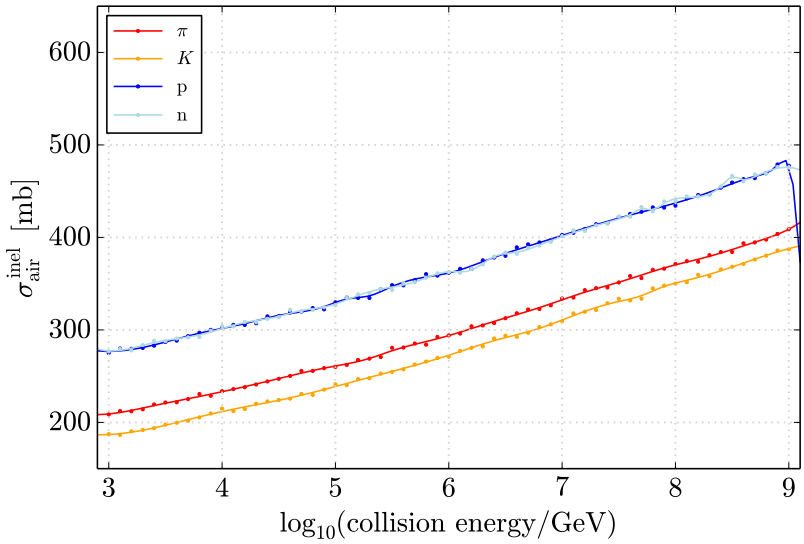

Figure B.35: Inelastic hadron-air cross-section obtained from QGSJET II-4.

B.5 CORRELATIONS

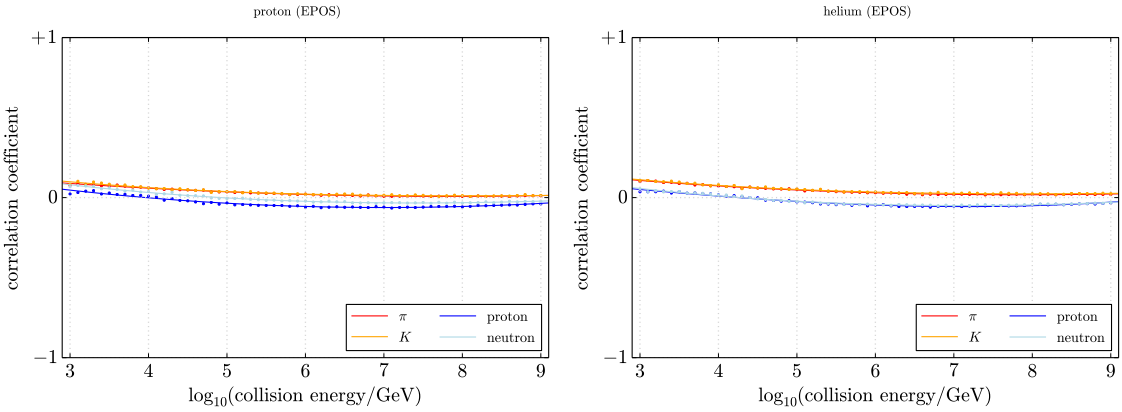

Figure B.36: Pearson correlation coefficients with respect to energy and transverse momentum produced in proton-nitrogen (left) and helium-nitrogen (right) collisions, obtained from EPOS-LHC.

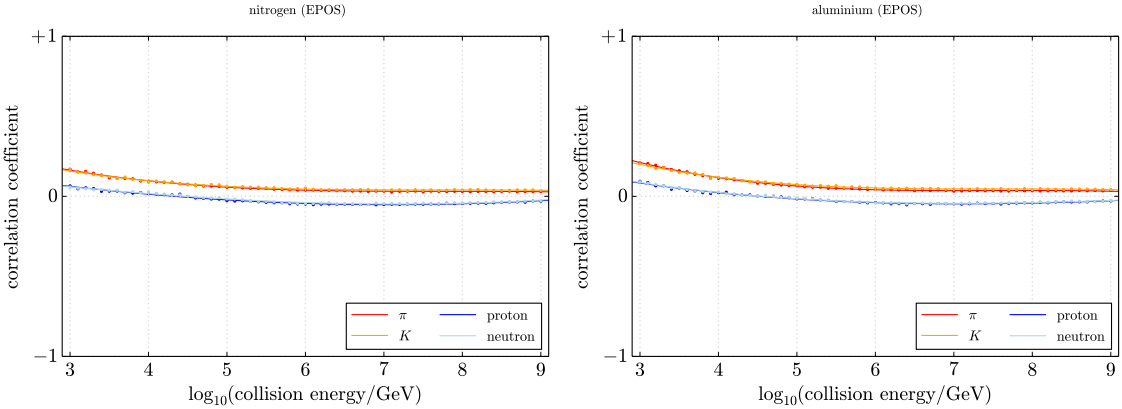

Figure B.37: Pearson correlation coefficients with respect to energy and transverse momentum produced in nitrogen-nitrogen (left) and aluminium-nitrogen (right) collisions, obtained from EPOS-LHC.

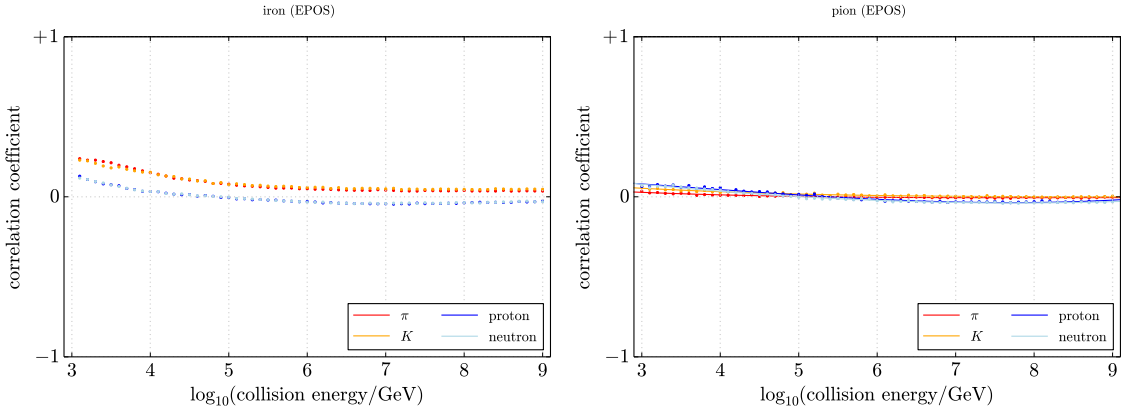

Figure B.38: Pearson correlation coefficients with respect to energy and transverse momentum produced in iron-nitrogen (left) and pion-nitrogen (right) collisions, obtained from EPOS-LHC.

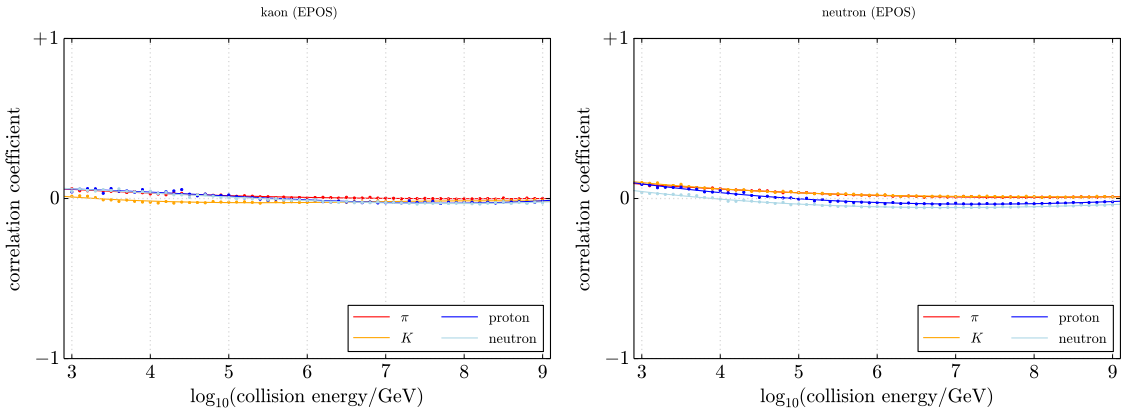

Figure B.39: Pearson correlation coefficients with respect to energy and transverse momentum produced in pion-nitrogen (left) and neutron-nitrogen (right) collisions, obtained from EPOS-LHC.

C

ADDITIONAL DISTRIBUTIONS

"Count what is countable, measure what is measurable, and what is not measurable, make measurable."

*– Galileo Galilei**

Additional distributions, relevant for this analysis, are shown in the following. Several lateral separation distributions for various filter levels are presented in Appendix C.1. In Appendix C.2 various additional zenith angle distributions, at different filter levels. Distributions of the cut variables for all filter levels are shown in Appendix C.3, Appendix C.4, Appendix C.5, and Appendix C.6. Various MC distributions of the transverse momentum, primary energy, LS Muon energy, and the interaction height, are shown in Appendix C.7, Appendix C.8, Appendix C.9, and Appendix C.10. Finally, further studies on the reconstruction accuracies of this analysis are discussed in Appendix C.11 and additional distributions of the effective areas are shown in Appendix C.12.

C.1 LATERAL SEPARATION

Various distributions of the lateral separation at different filter levels, are shown in the following.

In-Ice

The lateral separation distributions of burnsample events (102 days) at several analysis levels, as described in Section 6.4, are shown in Figure C.1 (L2), Figure C.2 (L3), and Figure C.3 (L4). The corresponding distributions obtained from MC simulations are also shown, as well as the resulting data/MC ratio (lower panels).

Figure C.5, Figure C.6, Figure C.7, and Figure C.8 show the reconstructed lateral separation distribution of final level events, using 960 days of IceCube data after background reduction ($\theta \leqslant 60°$). The corresponding Hagedorn fits, as described in Section 7.2 (Equation (7.1), using $C = 0$), are shown as solid lines. The MC predictions represent the corresponding Hagedorn fits applied to the true lateral separation distributions obtained from CORSIKA and LSMuonSim. The resulting p-values of the fits, obtained from KS-tests, are given in Table C.1. Figure C.9, Figure C.10, and Figure C.11 show the lateral separation distributions for various primary energy bins and primary flux assumptions.

* As quoted in *"Institute of Public Administration"* (1967).

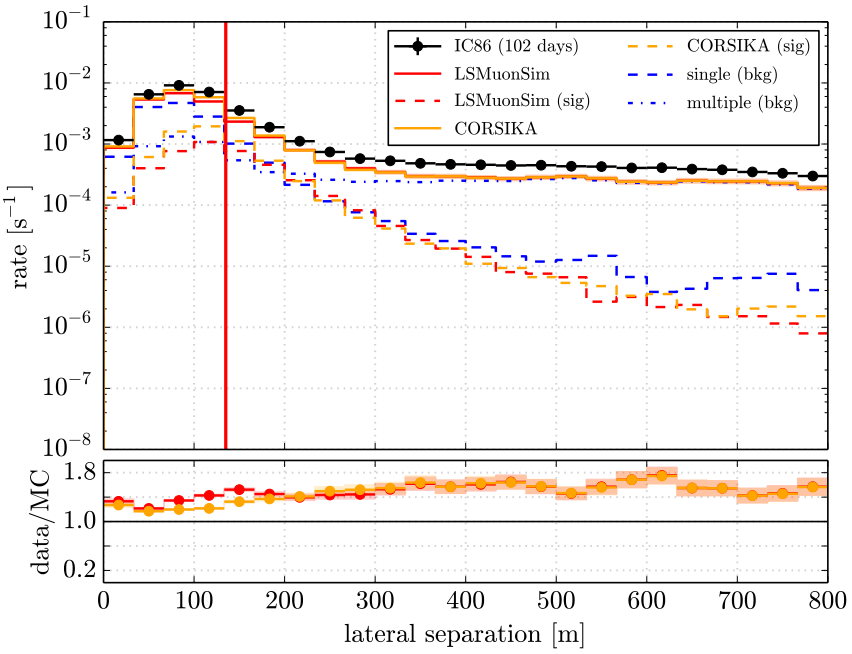

Figure C.1: Lateral separation distribution at L2 filter level.

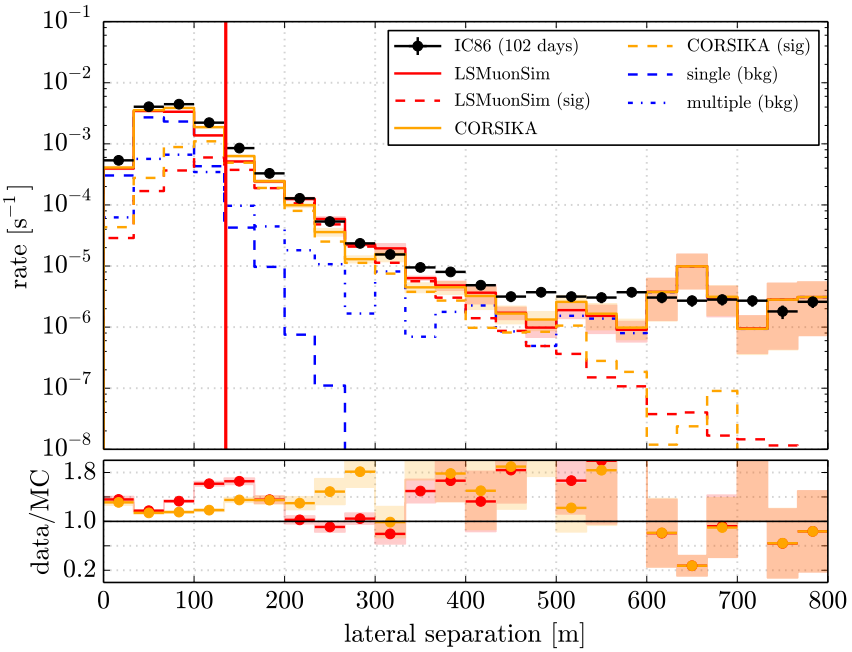

Figure C.2: Lateral separation distribution at L3 filter level.

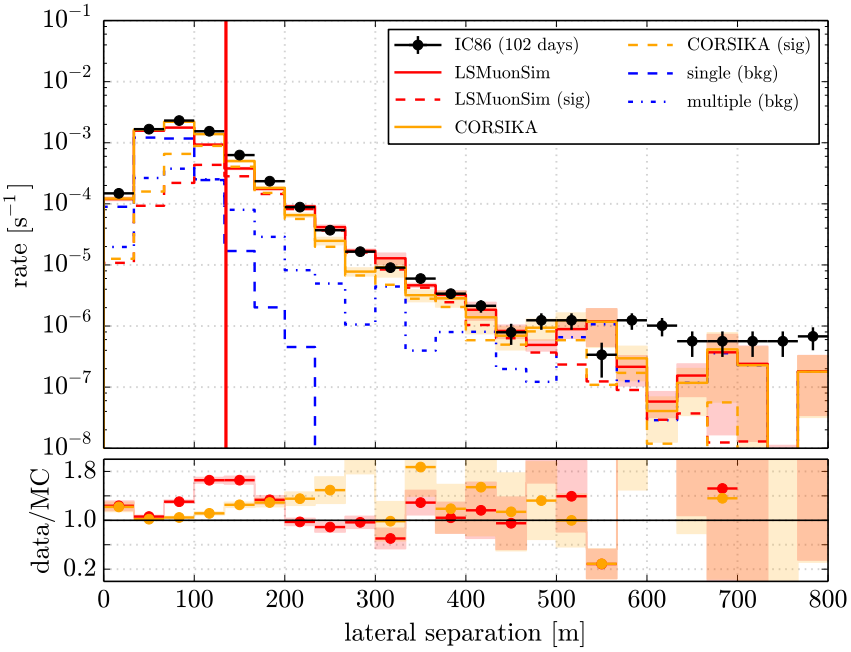

Figure C.3: Lateral separation distribution at L4 filter level.

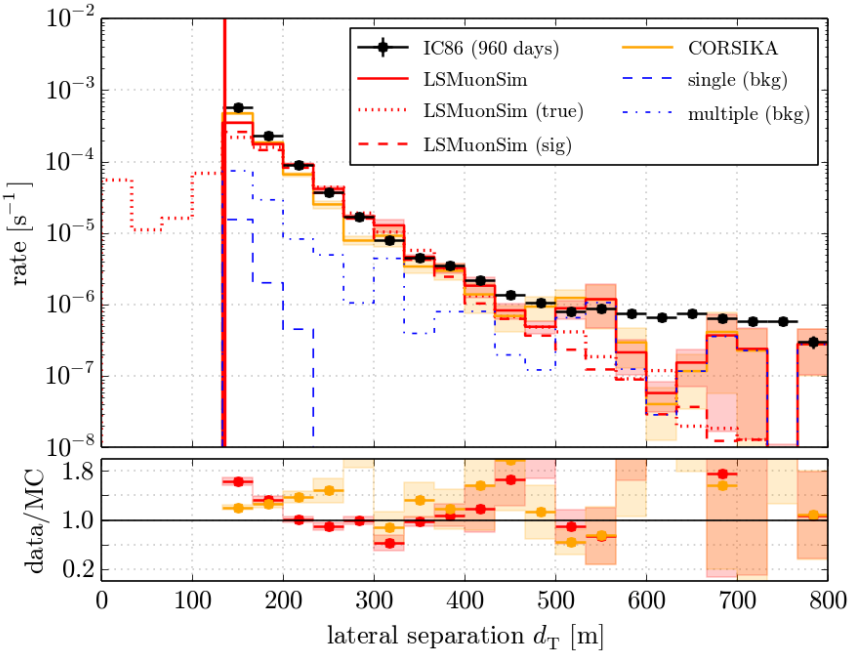

Figure C.4: Lateral separation distribution at L5 filter level.

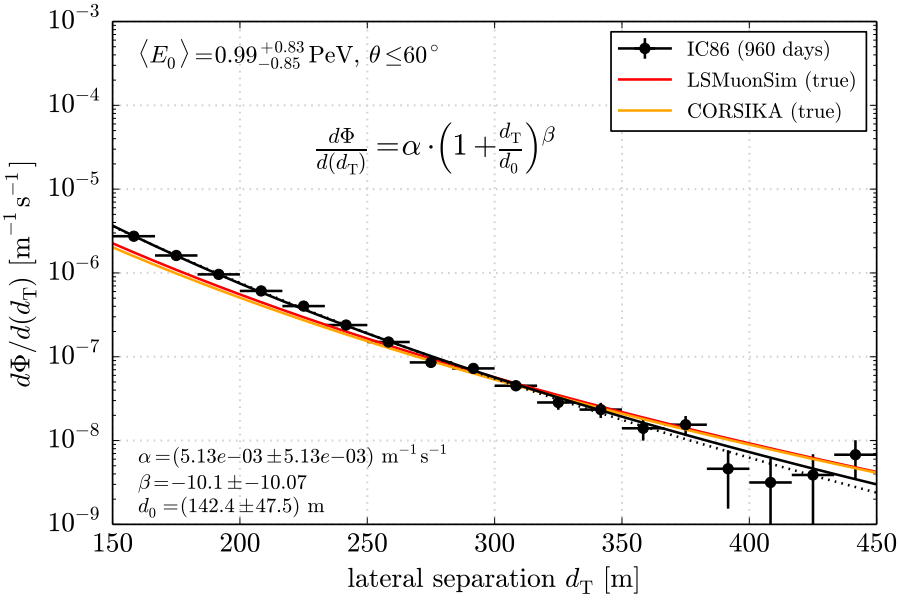

Figure C.5: Lateral separation distribution energy bin 1.

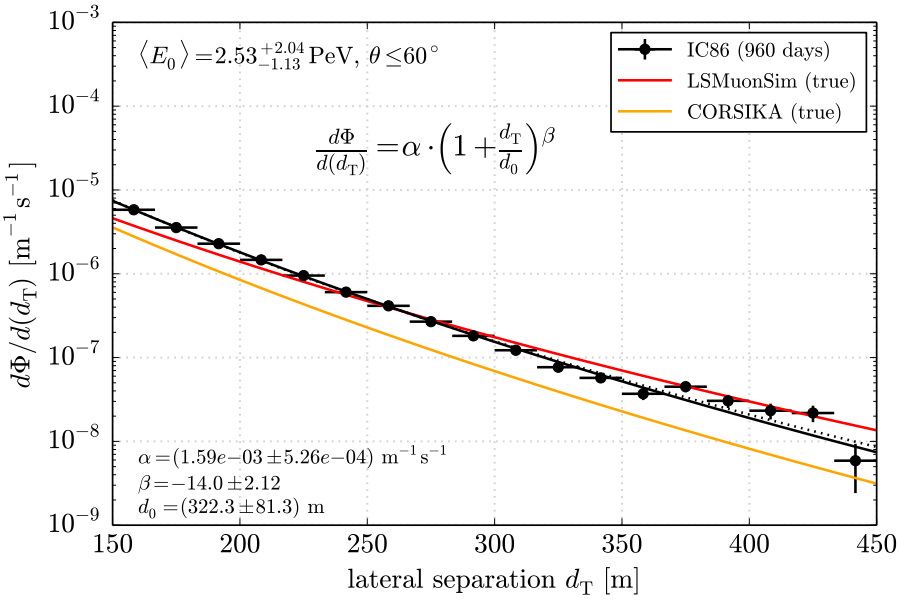

Figure C.6: Lateral separation distribution energy bin 2.

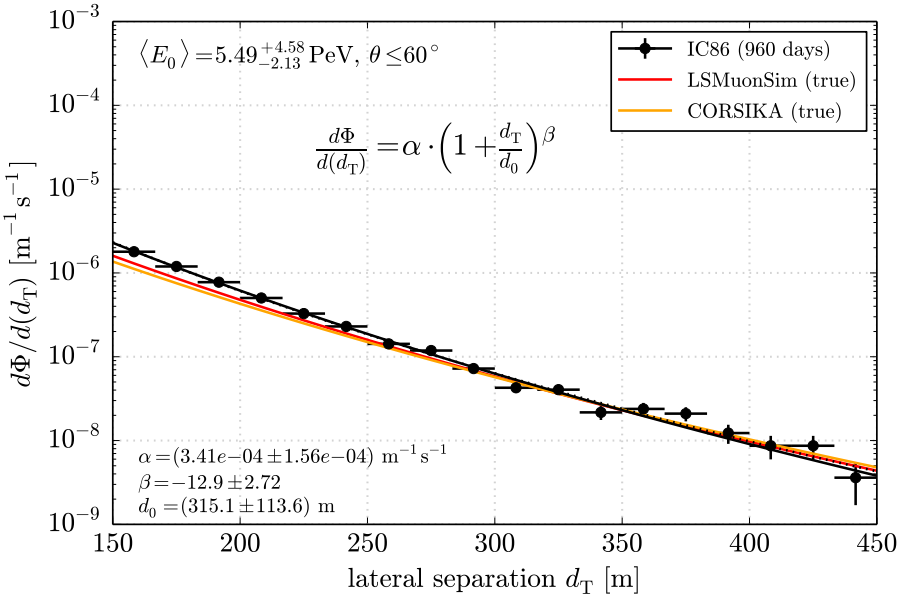

Figure C.7: Lateral separation distribution energy bin 3.

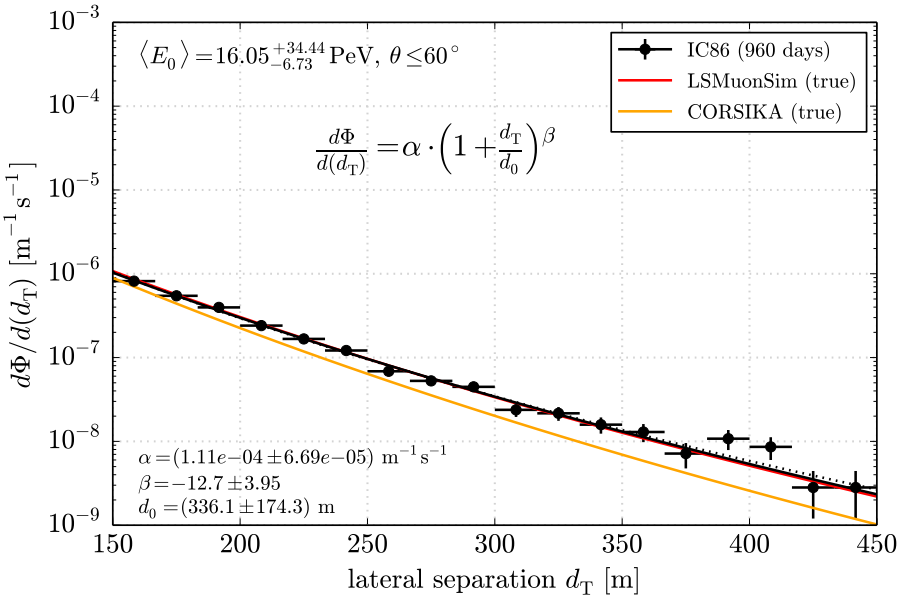

Figure C.8: Lateral separation distribution energy bin 4.

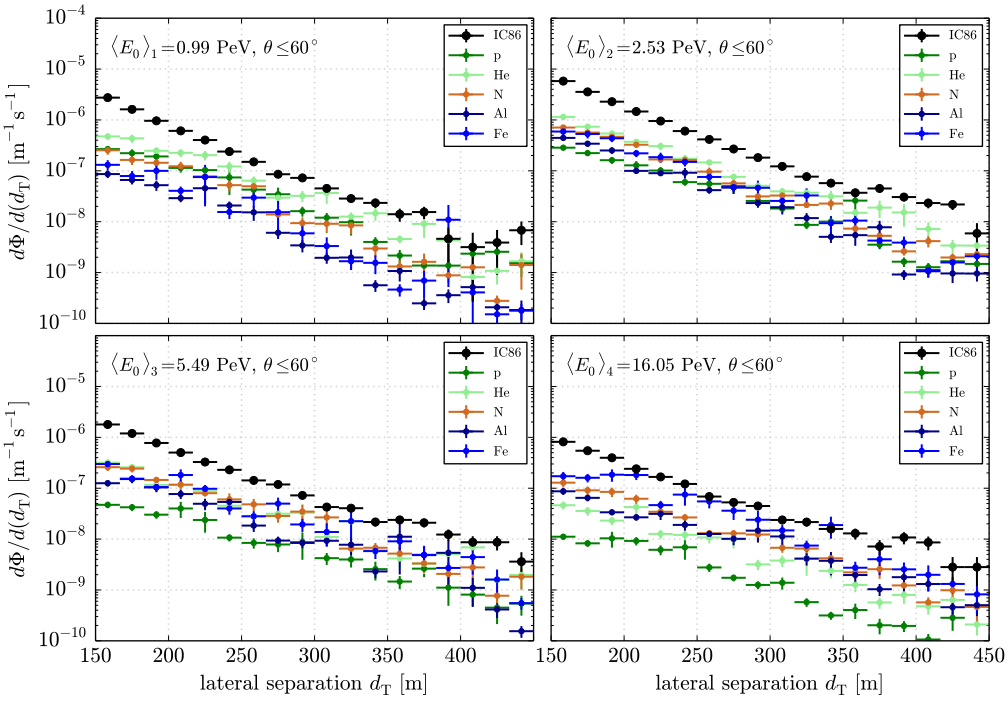

Figure C.9: Cosmic ray mass composition obtained from LSMuonSim at final filter level for $\theta \leqslant 60°$, assuming a H4a primary flux.

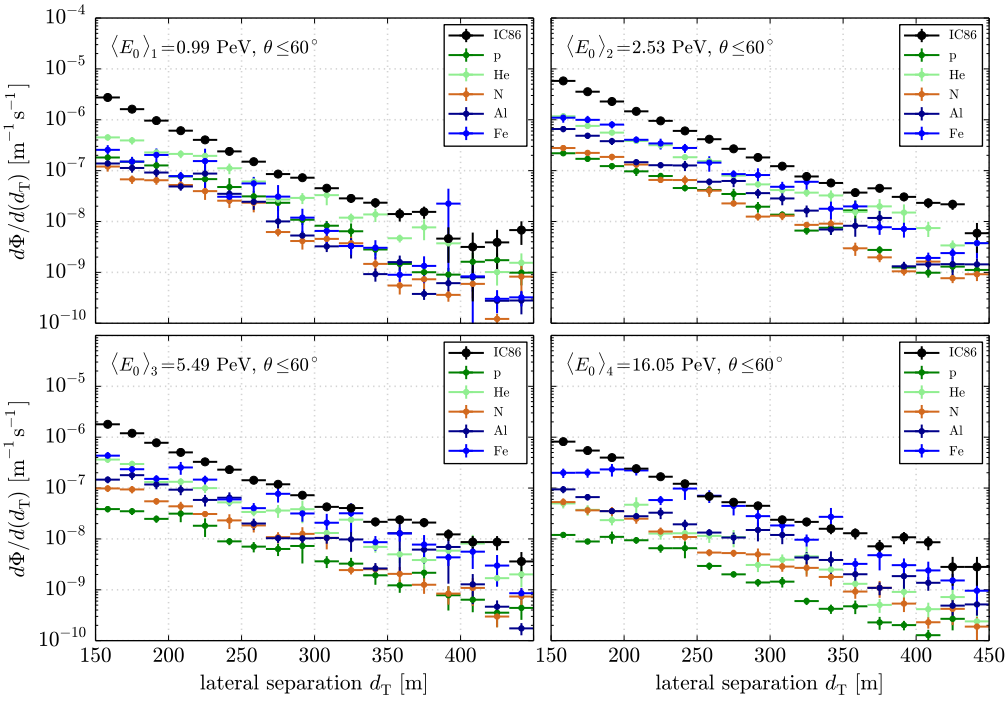

Figure C.10: Cosmic ray mass composition obtained from LSMuonSim at final filter level for $\theta \leqslant 60°$, assuming a GST primary flux.

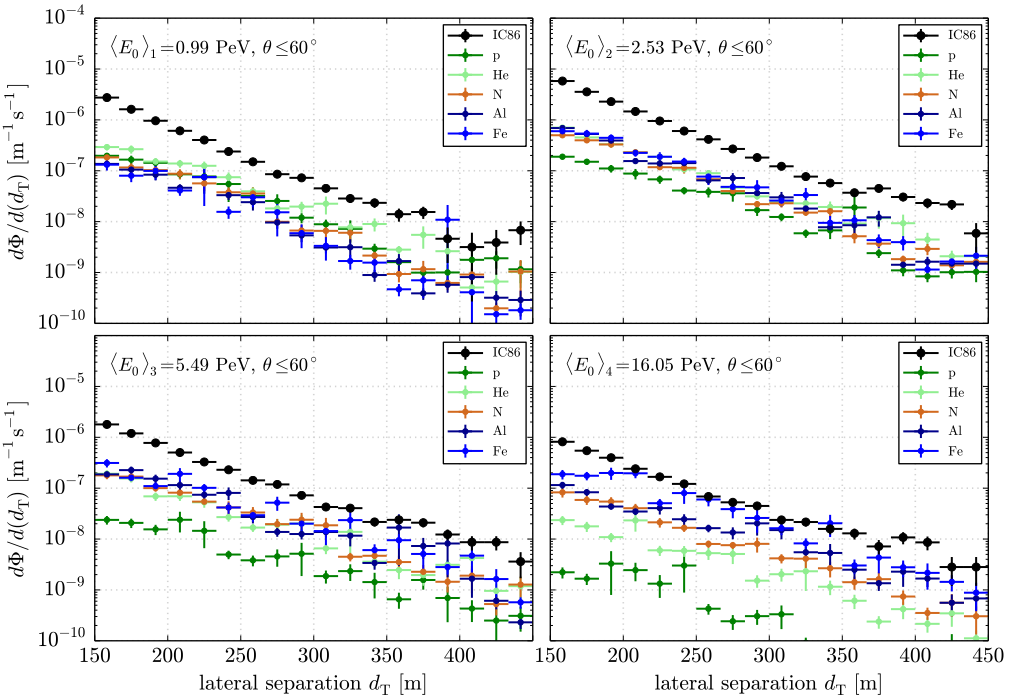

Figure C.11: Cosmic ray mass composition obtained from LSMuonSim at final filter level for $\theta \leqslant 60°$, assuming a Hoerandel primary flux.

Surface

Figure C.12, Figure C.13, Figure C.14, and Figure C.15 show the reconstructed lateral separation distribution of final level events at surface level, using 960 days of IceCube data after background reduction ($\theta \leqslant 60°$). The effective areas used for the surface estimation are given in Section 6.9 (Figure 6.17).

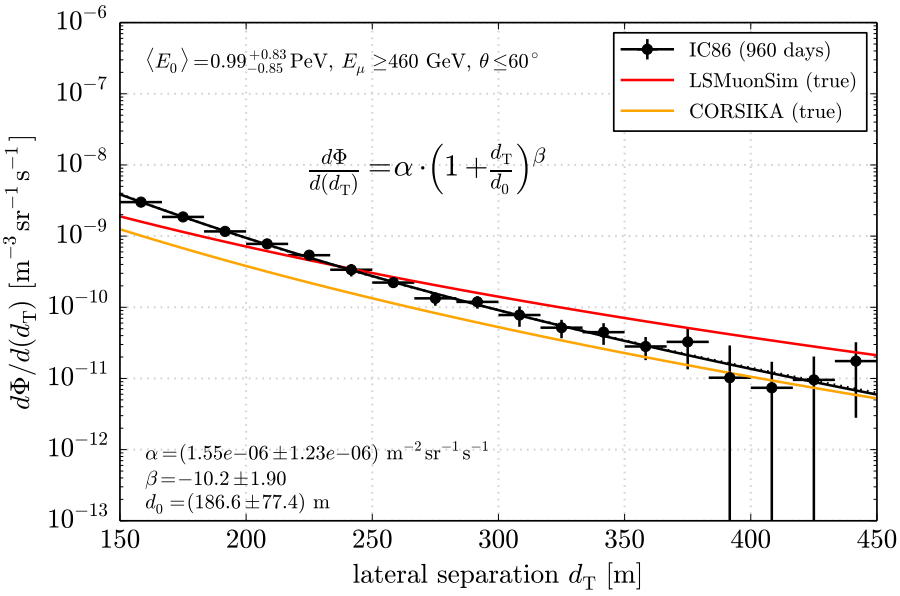

Figure C.12: Lateral separation distribution energy bin 1 at surface level.

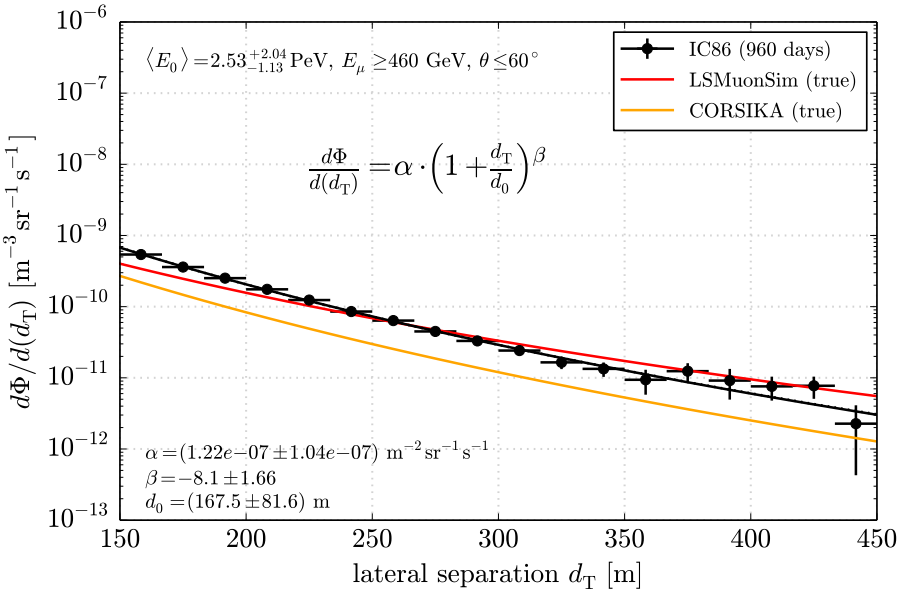

Figure C.13: Lateral separation distribution energy bin 2 at surface level..

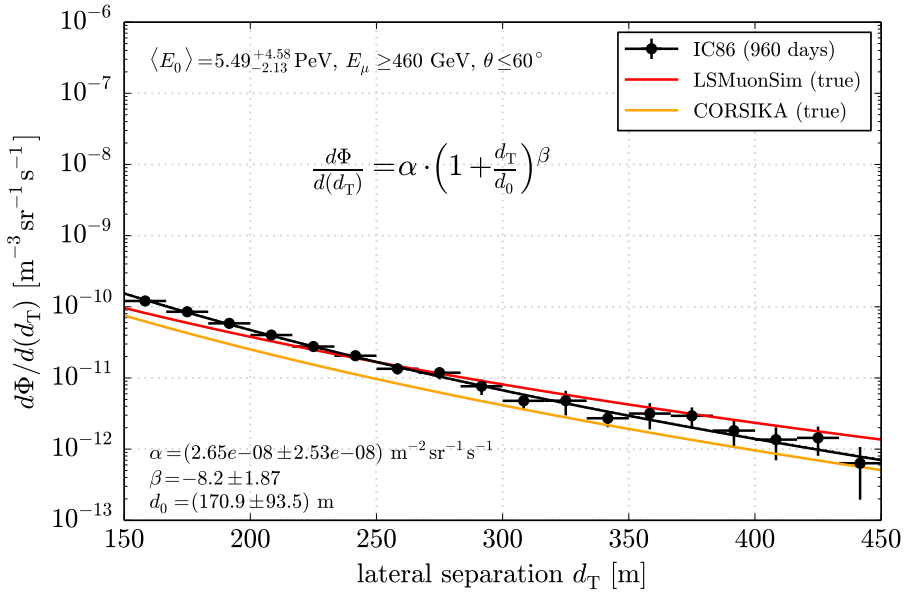

Figure C.14: Lateral separation distribution energy bin 3 at surface level..

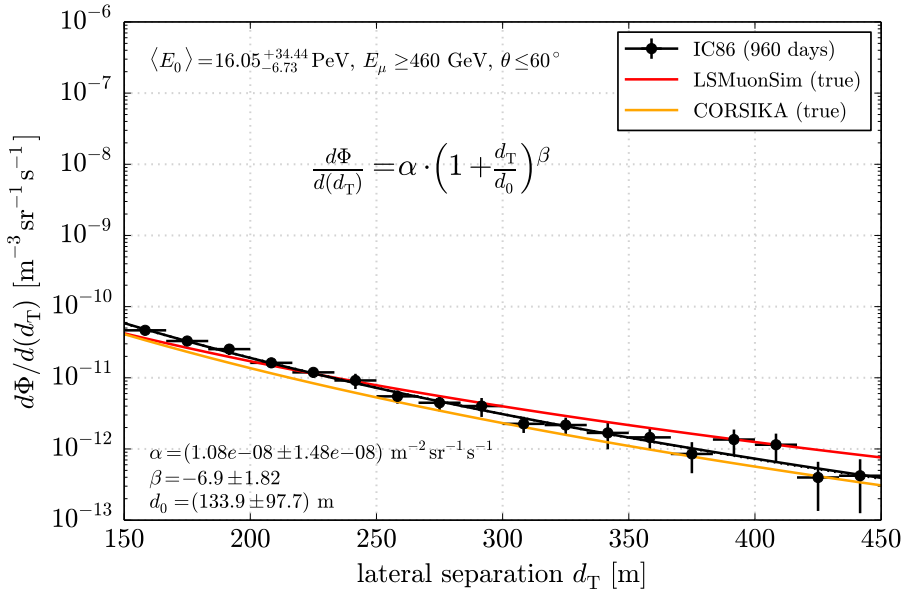

Figure C.15: Lateral separation distribution energy bin 4 at surface level..

ENERGY BIN	$\langle E_0 \rangle_{tot}$	$\langle E_0 \rangle_1$	$\langle E_0 \rangle_2$	$\langle E_0 \rangle_3$	$\langle E_0 \rangle_4$
In-ice	0.460	0.003	0.006	0.156	0.168
Surface	0.297	0.002	0.006	0.085	0.096

Table C.1: p-values of the Hagedorn fits applied at final filter level, with the best fit parameters given in Table 7.2 (in-ice) and Table 7.3 (surface).

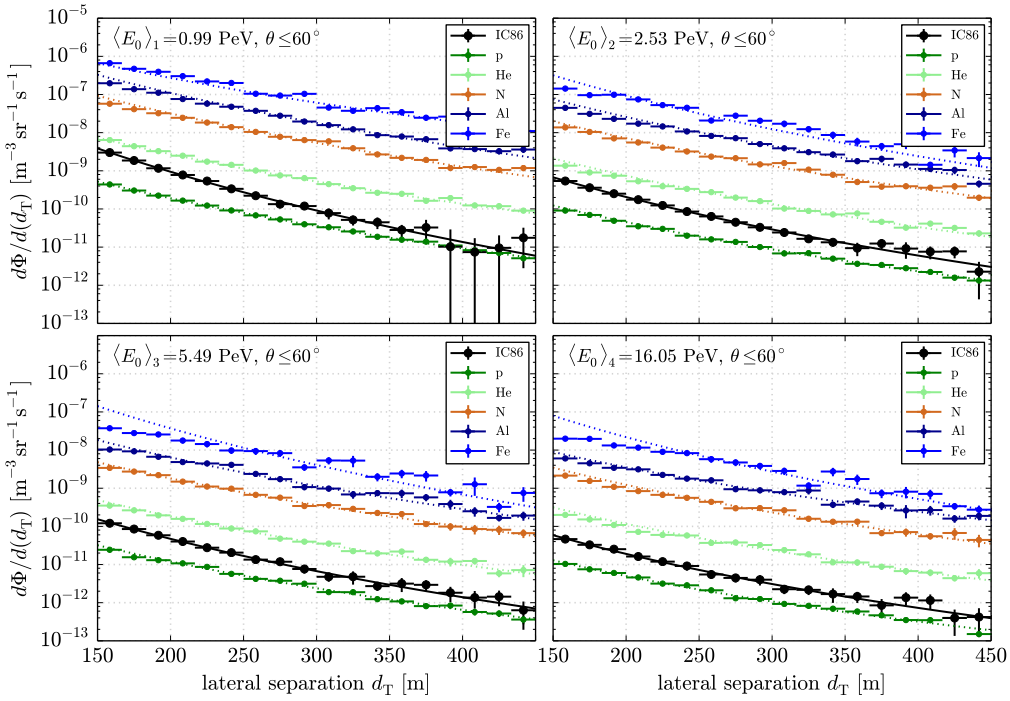

Figure C.16: Cosmic ray mass composition obtained from LSMuonSim at surface level for $\theta \leqslant 60°$, assuming pure flux assumptions, as described in Ref. [46].

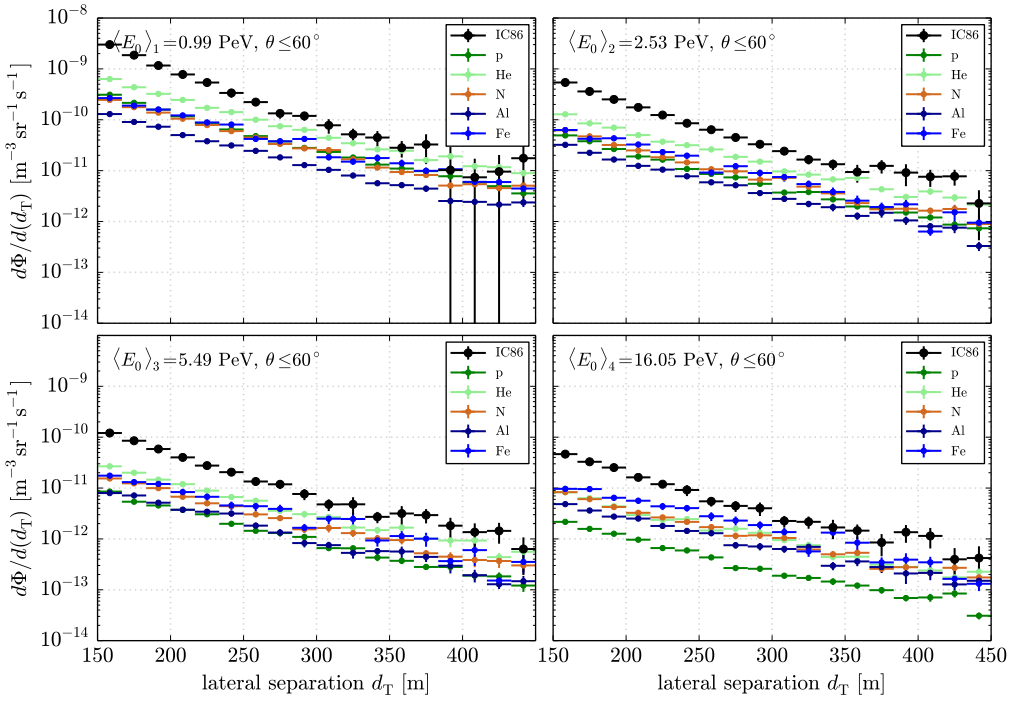

Figure C.17: Cosmic ray mass composition obtained from LSMuonSim at surface level for $\theta \leqslant 60°$, assuming a H3a primary flux.

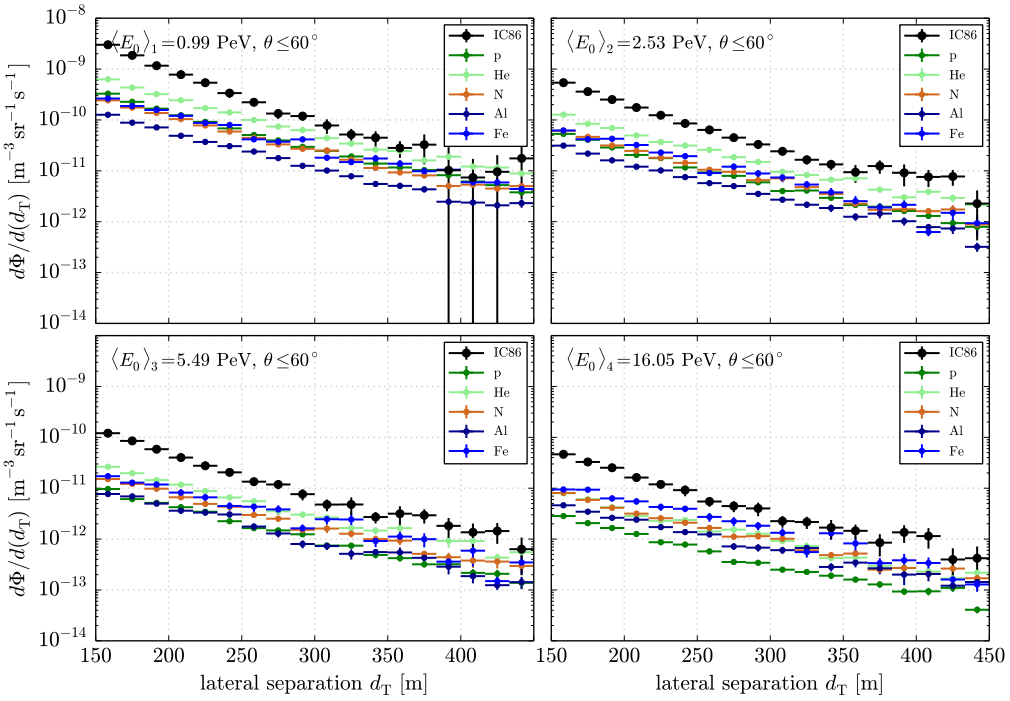

Figure C.18: Cosmic ray mass composition obtained from LSMuonSim at surface level for $\theta \leqslant 60°$, assuming a H4a primary flux.

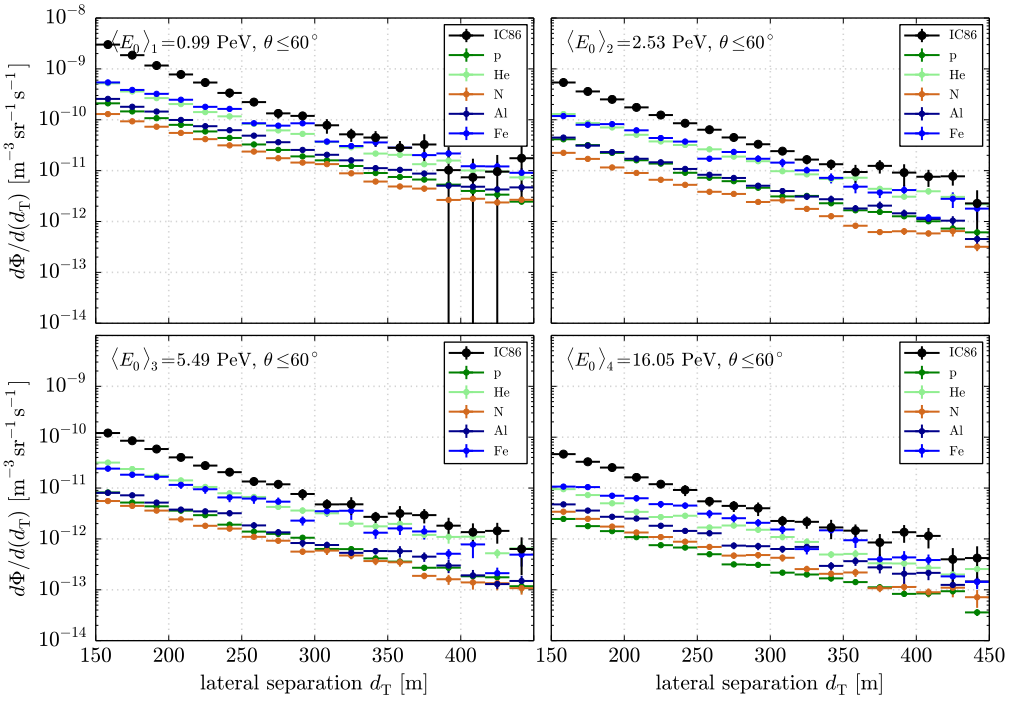

Figure C.19: Cosmic ray mass composition obtained from LSMuonSim at surface level for $\theta \leqslant 60°$, assuming a GST primary flux.

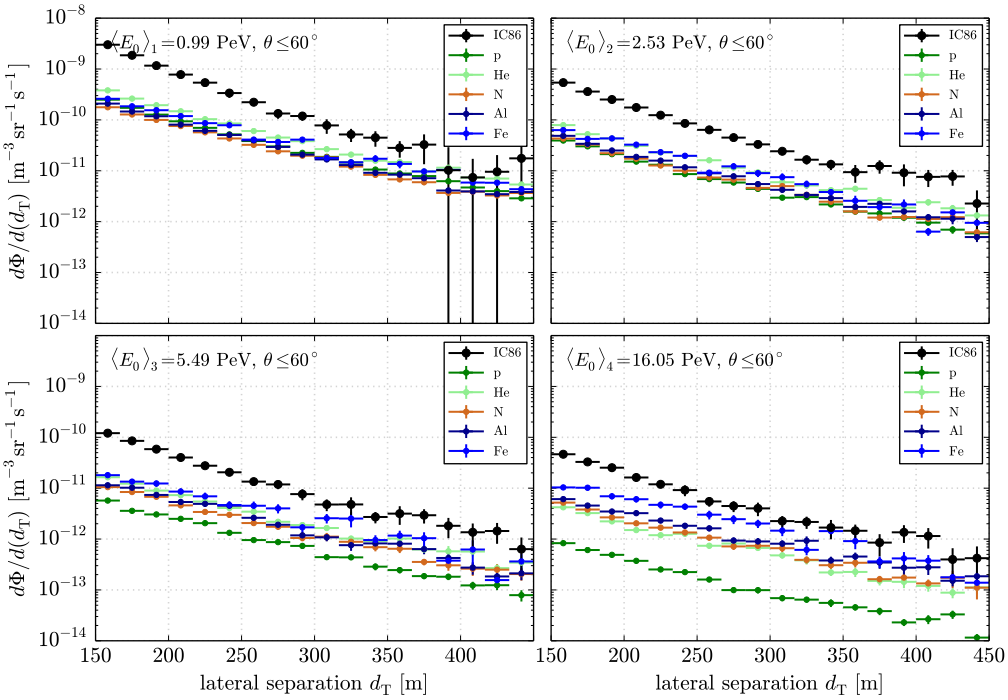

Figure C.20: Cosmic ray mass composition obtained from LSMuonSim at surface level for $\theta \leqslant 60°$, assuming a Hoerandel primary flux.

C.2 ZENITH ANGLE

In-Ice

The zenith angle distributions of burnsample events (102 days) at several analysis levels, as described in Section 6.4, are shown in Figure C.21 (L2), Figure C.22 (L3), and Figure C.23 (L4). The corresponding distributions obtained from MC simulations are also shown, as well as the resulting data/MC ratio (lower panels).

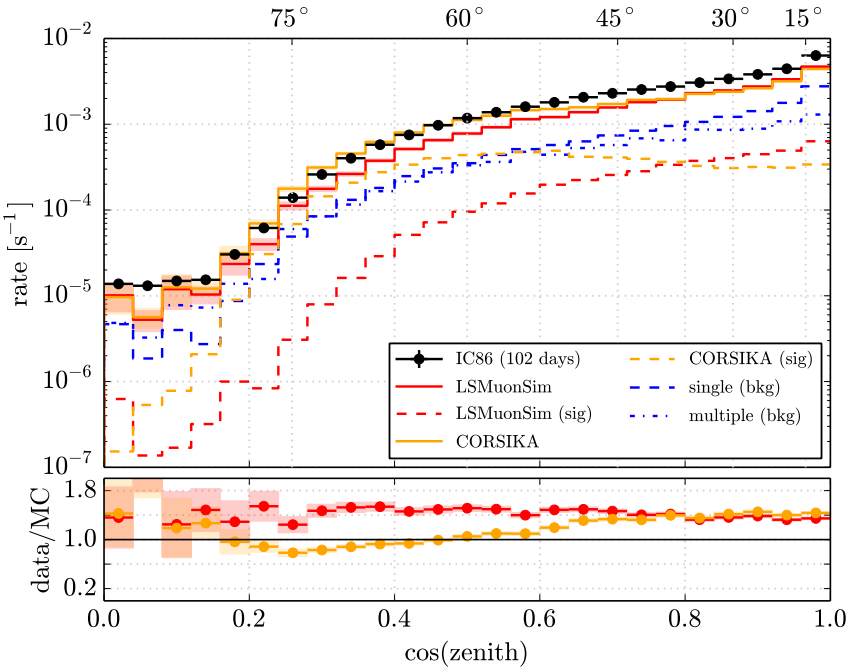

Figure C.21: Zenith angle distribution at L2 filter level.

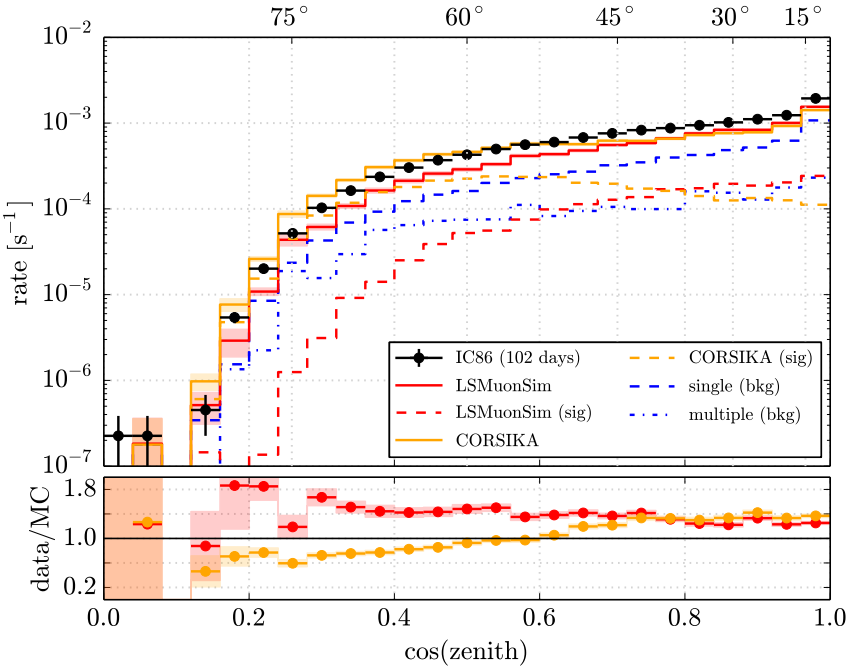

Figure C.22: Zenith angle distribution at L3 filter level.

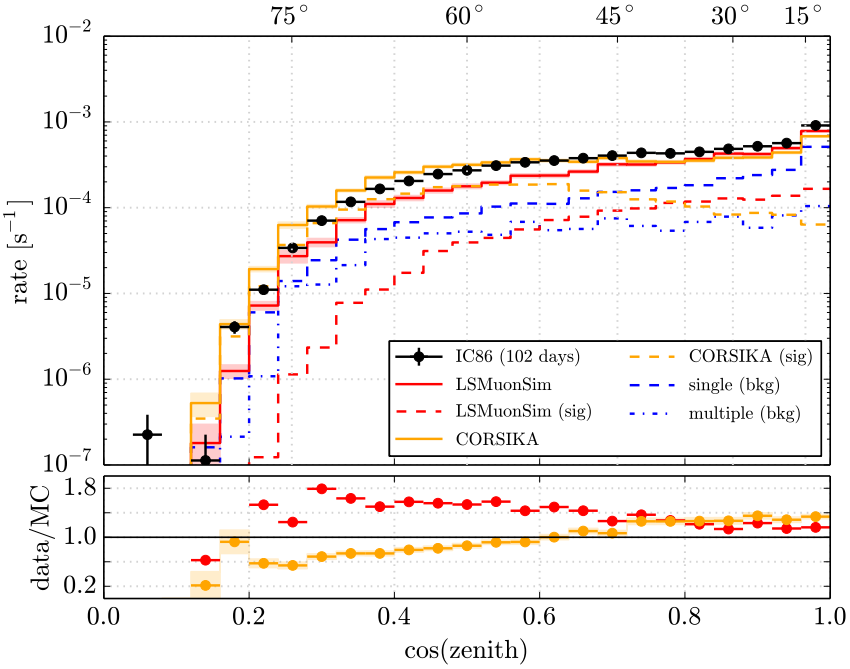

Figure C.23: Zenith angle distribution at L4 filter level.

The reconstructed zenith angle distributions at final analysis level (L5) for various primary particle types, using the H3a primary flux assumption, are shown in Figure C.24 (L5). The distributions are shown for CORSIKA (left) and LSMuonSim simulations (right) separately. The contributions from different primaries (dashed lines) only include LS Muon events ($d_T \geqslant 100\,m$). No significant effect of different primary nuclei on the zenith angle distribution is observed.

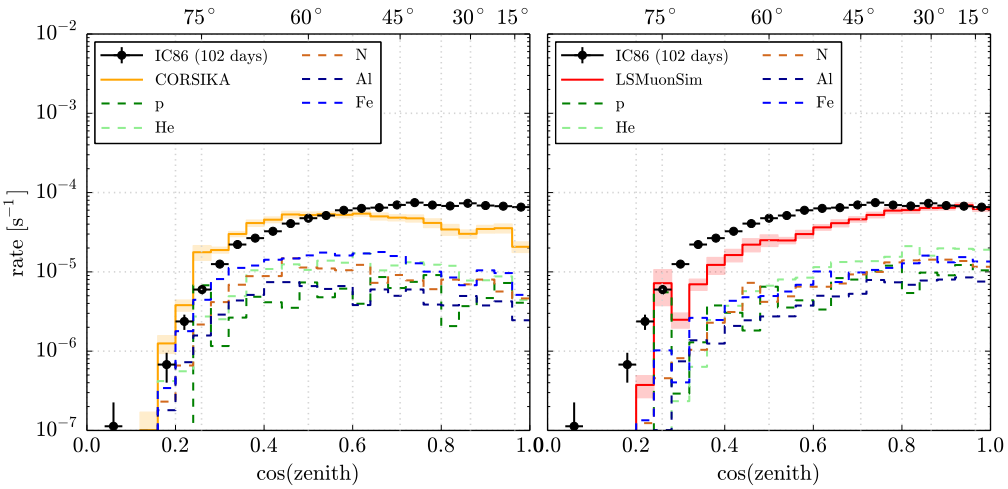

Figure C.24: Zenith angle distribution, assuming the H3a flux assumption, obtained CORSIKA (left) and LSMuonSim simulations (right) at final filter level. Dashed lines show the contributions of LS Muon events ($d_{T,true} \geqslant 100\,m$) for various primary particle types.

Surface

The zenith angle distribution at surface level is shown in Figure C.25, for (all) simulated events from various altitudes separately.

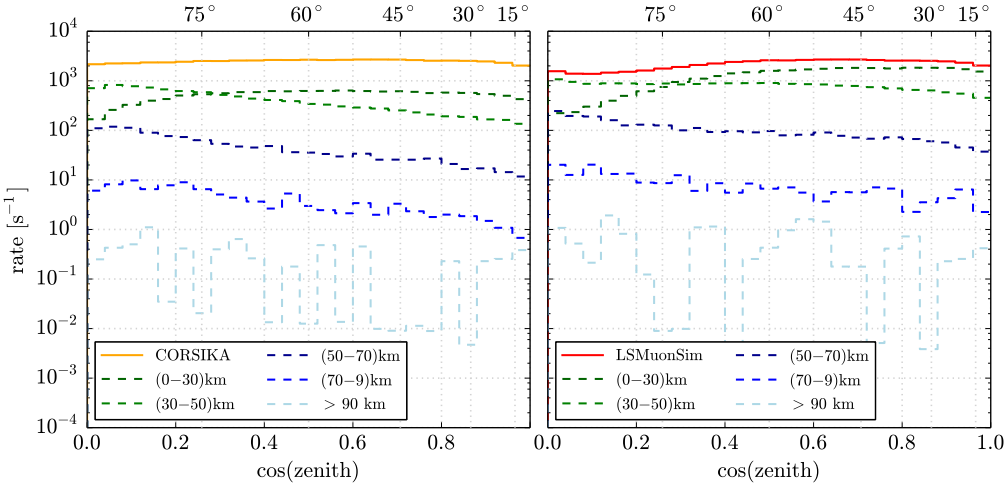

Figure C.25: Simulated zenith angle distribution of all events at surface level from various altitudes, obtained from CORSIKA (left) and LSMuonSim (right).

C.3 TOTAL CHARGE

The total charge distributions of burnsample events (102 days) at all analysis levels, as described in Section 6.4, are shown in Figure C.26 (L0), Figure C.27 (L1), Figure C.28 (L2), Figure C.29 (L3), Figure C.30 (L4), and Figure C.31 (L5). The corresponding distributions obtained from MC simulations are also shown.

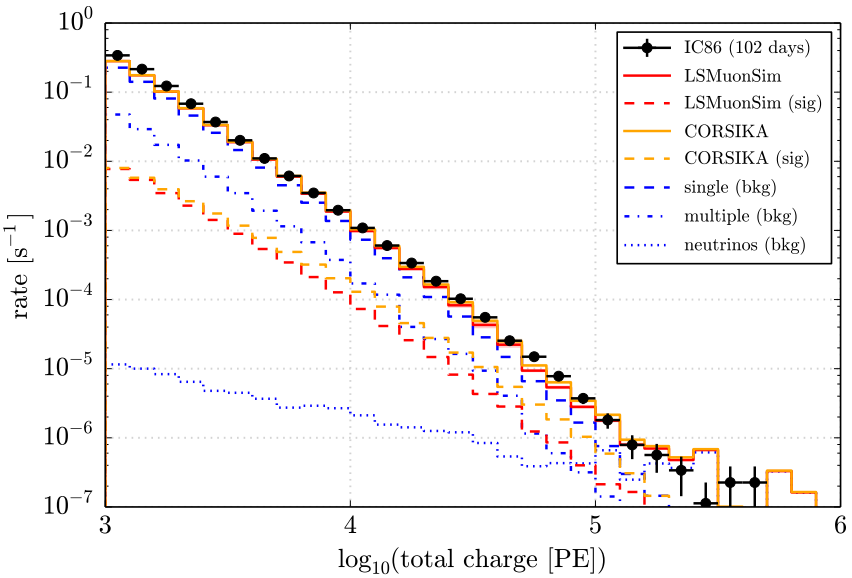

Figure C.26: Total charge distribution at L0 filter level.

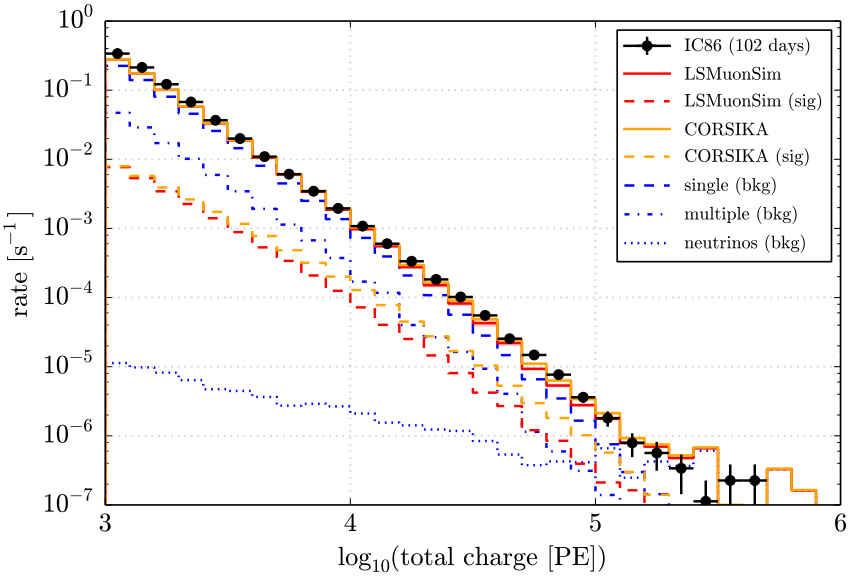

Figure C.27: Total charge distribution at L1 filter level.

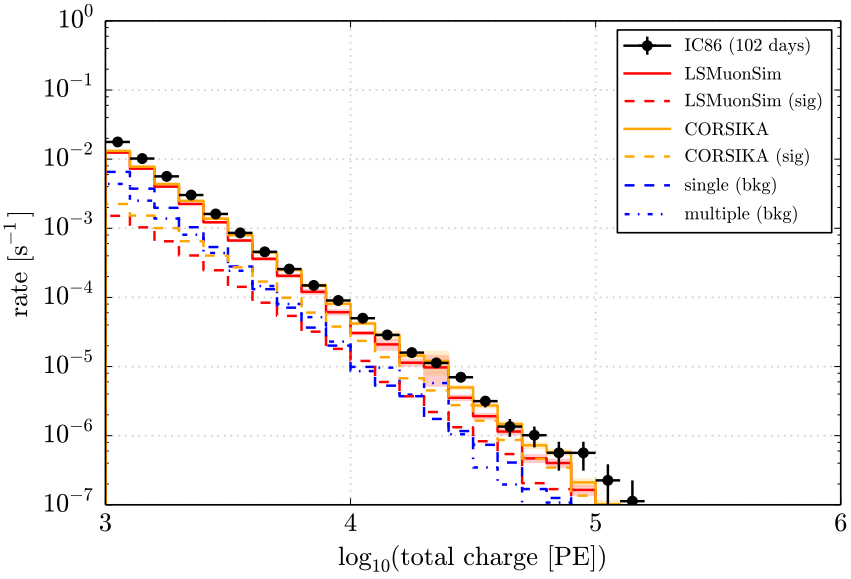

Figure C.28: Total charge distribution at L2 filter level.

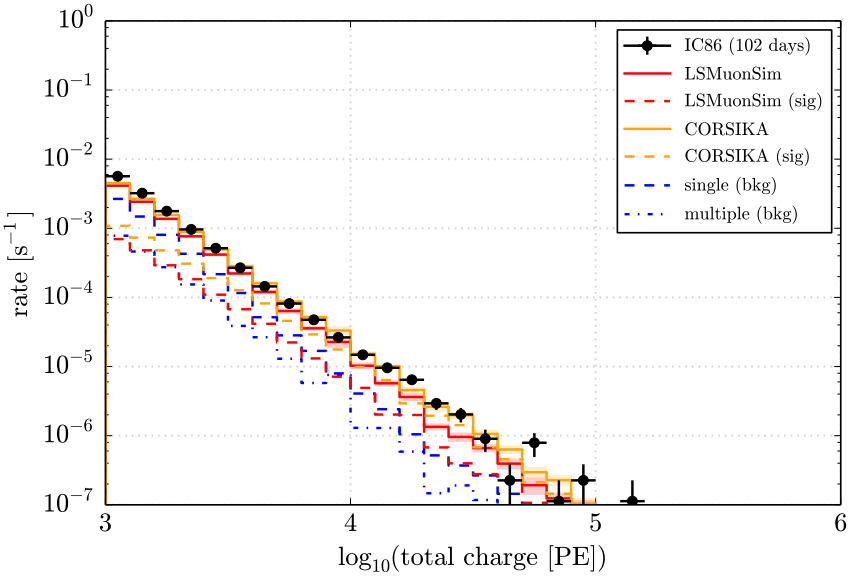

Figure C.29: Total charge distribution at L3 filter level.

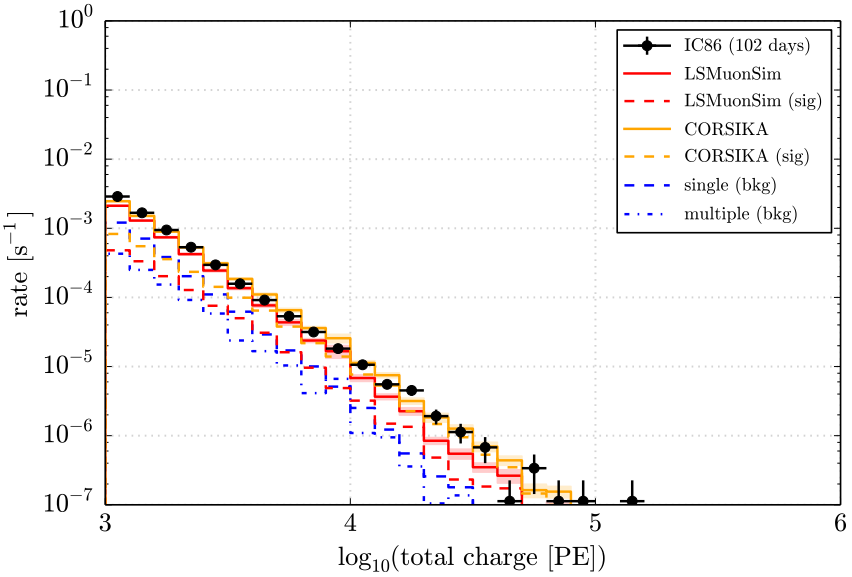

Figure C.30: Total charge distribution at L4 filter level.

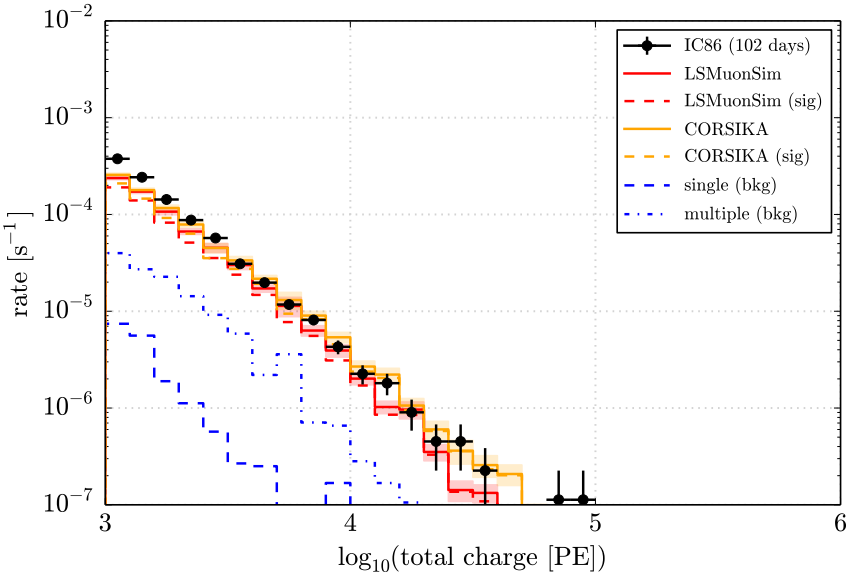

Figure C.31: Total charge distribution at L5 filter level.

C.4 OPENING ANGLE

The distributions of the reconstructed opening angles of burnsample events (102 days) at several analysis levels, as described in Section 6.4, are shown in Figure C.32 (L2), Figure C.33 (L3), Figure C.34 (L4), and Figure C.35 (L5). The corresponding distributions obtained from MC simulations are also shown.

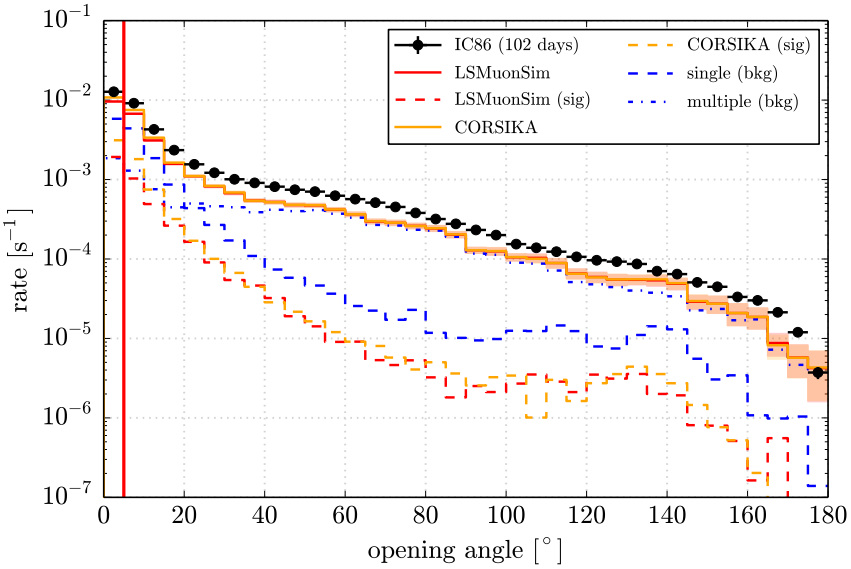

Figure C.32: Reconstructed opening angle distribution at L2 filter level.

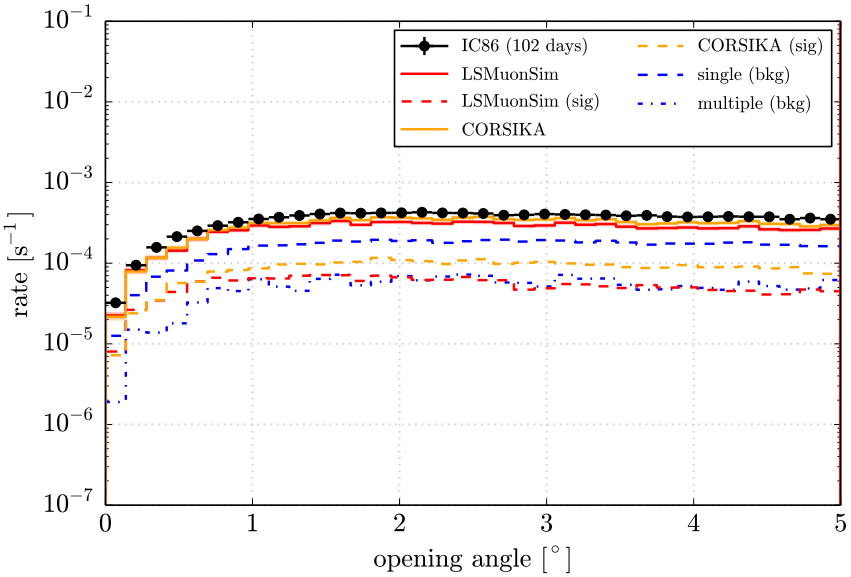

Figure C.33: Reconstructed opening angle distribution at L3 filter level.

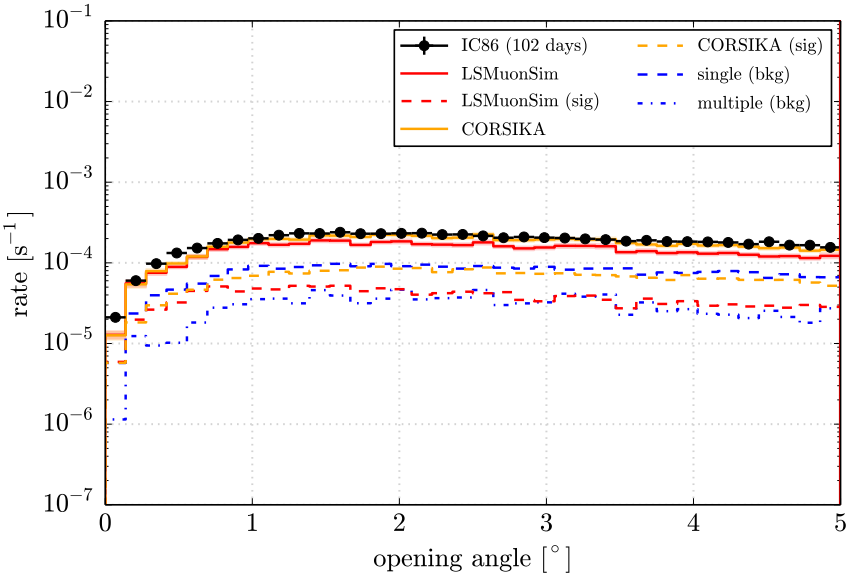

Figure C.34: Reconstructed opening angle distribution at L4 filter level.

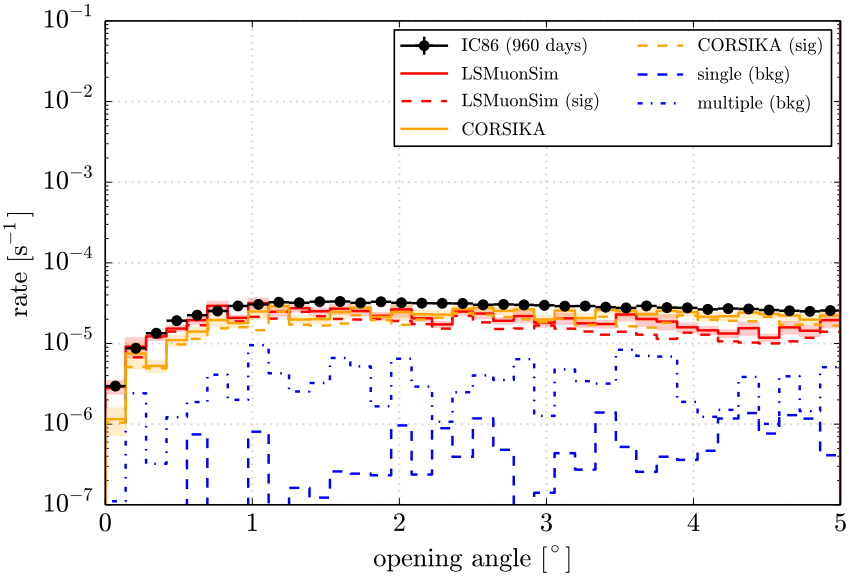

Figure C.35: Reconstructed opening angle distribution at L5 filter level.

C.5 TIME DIFFERENCE

The time difference between the reconstructed bundle and muon track, obtained from burnsample events (102 days) at various filter levels, as described in Section 6.4, are shown in Figure C.36 (L2), Figure C.37 (L3), Figure C.38 (L4), and Figure C.39 (L5). The corresponding distributions obtained from MC simulations are also shown.

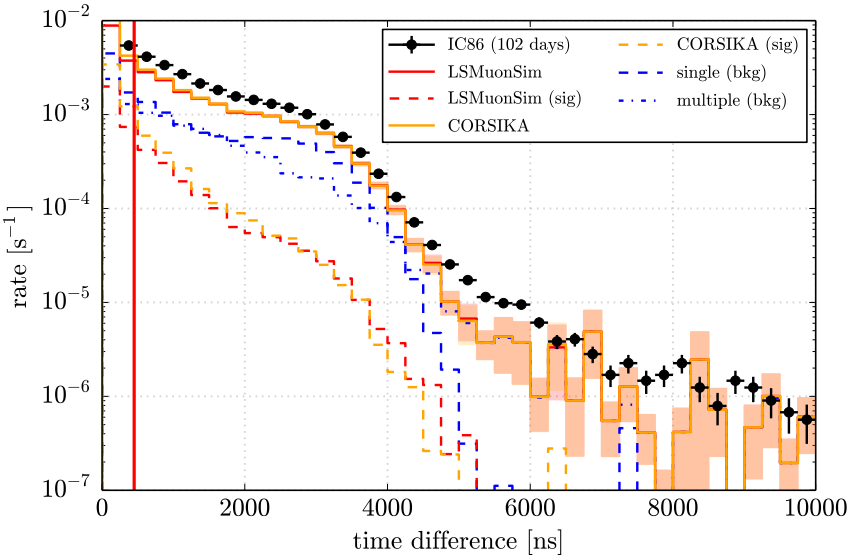

Figure C.36: Time difference between reconstructed bundle and LS Muon track at L2 filter level.

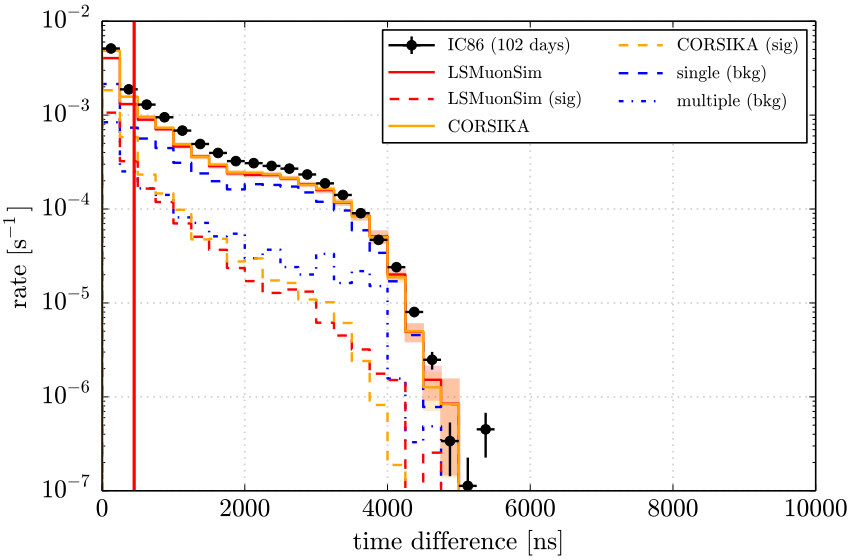

Figure C.37: Time difference between reconstructed bundle and LS Muon track at L3 filter level.

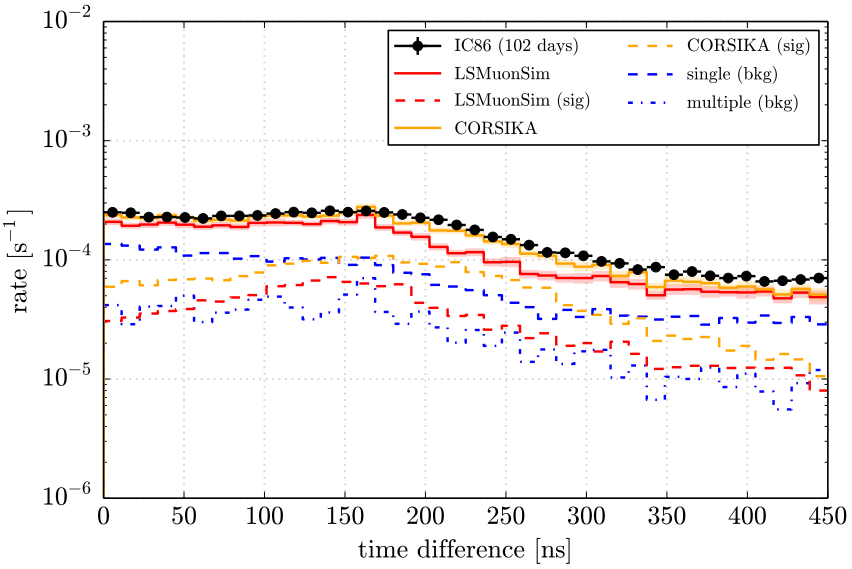

Figure C.38: Time difference between reconstructed bundle and LS MUON track at L4 filter level.

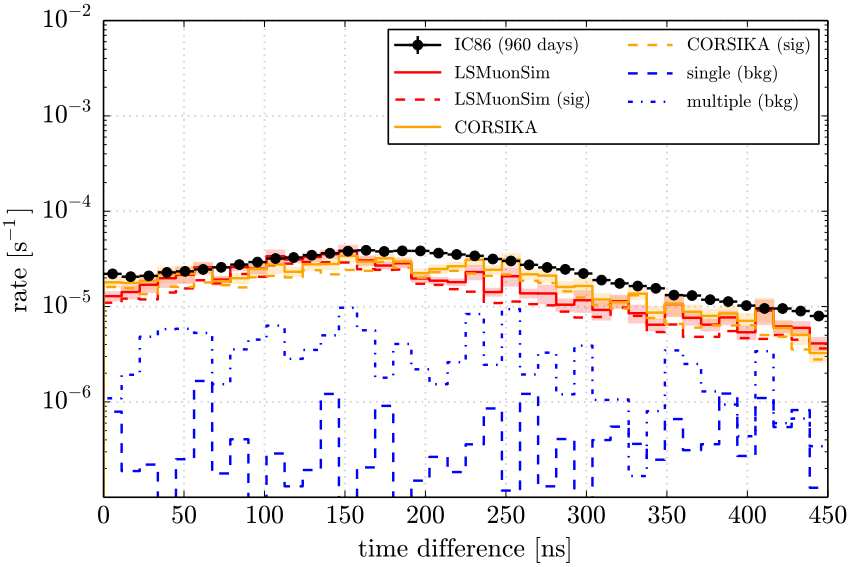

Figure C.39: Time difference between reconstructed bundle and LS MUON track at L5 filter level.

C.6 REDUCED LOG-LIKELIHOOD

The distribution of the reduced likelihood value of the first-guess LLH fit, obtained from burnsample events (102 days) at all filter levels, as described in Section 6.4, are shown in Figure C.40 (L0), Figure C.41 (L1), Figure C.42 (L2), Figure C.43 (L3), Figure C.44 (L4), and Figure C.45 (L5). The corresponding distributions obtained from MC simulations are also shown.

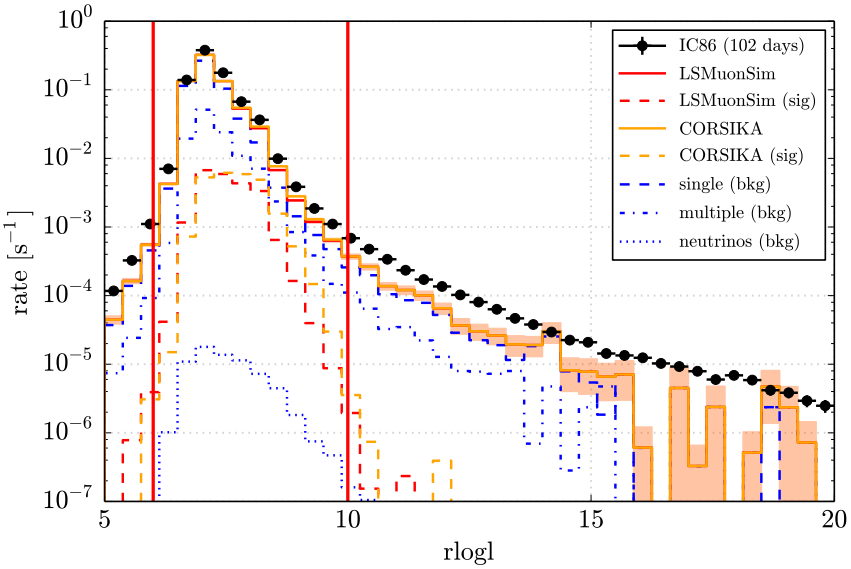

Figure C.40: Reduced likelihood value of the first-guess LLH fit at L0 filter level.

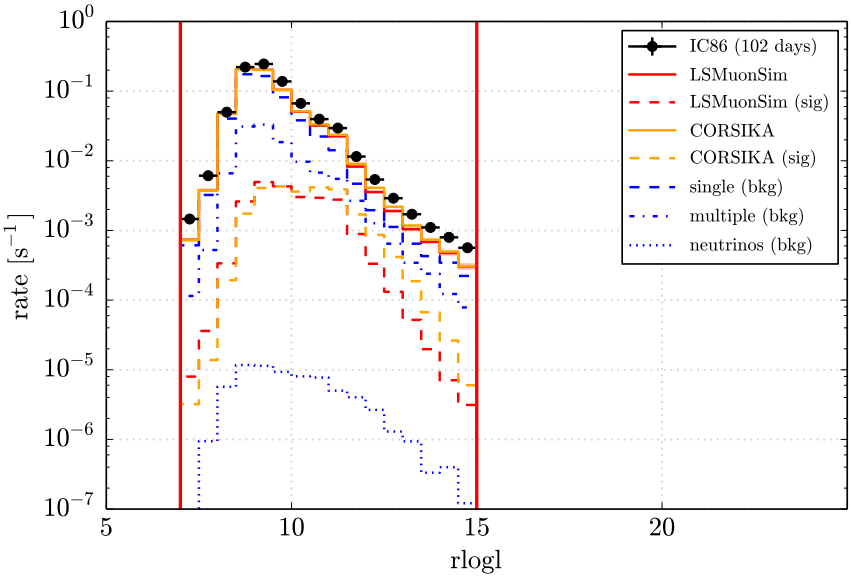

Figure C.41: Reduced likelihood value of the first-guess LLH fit at L1 filter level.

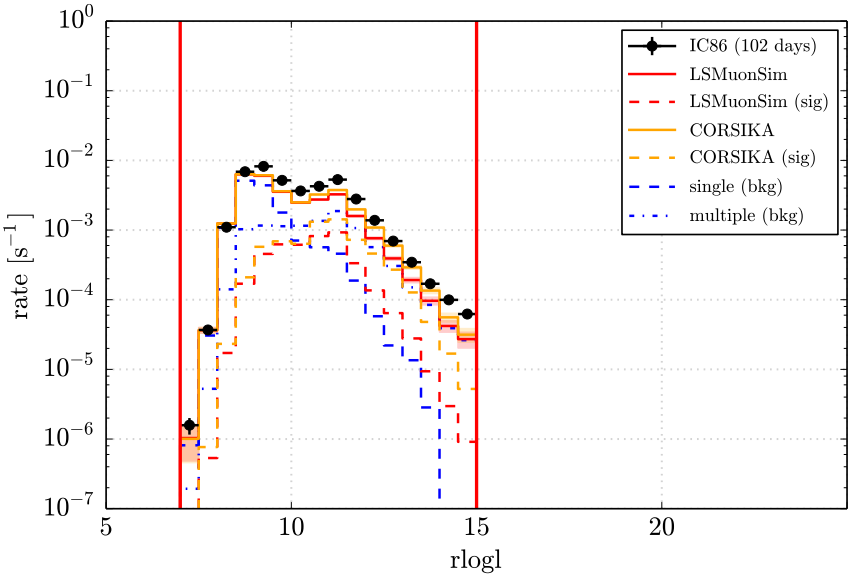

Figure C.42: Reduced likelihood value of the first-guess LLH fit at L2 filter level.

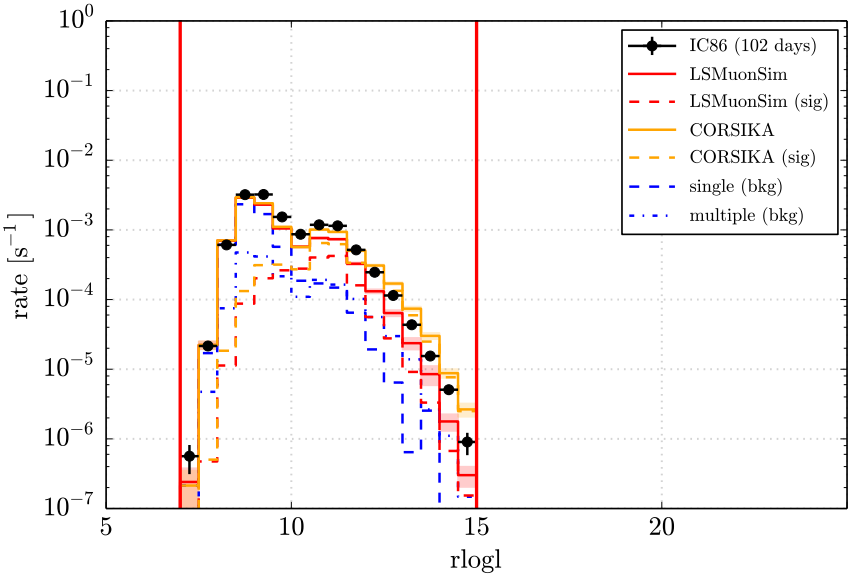

Figure C.43: Reduced likelihood value of the first-guess LLH fit at L3 filter level.

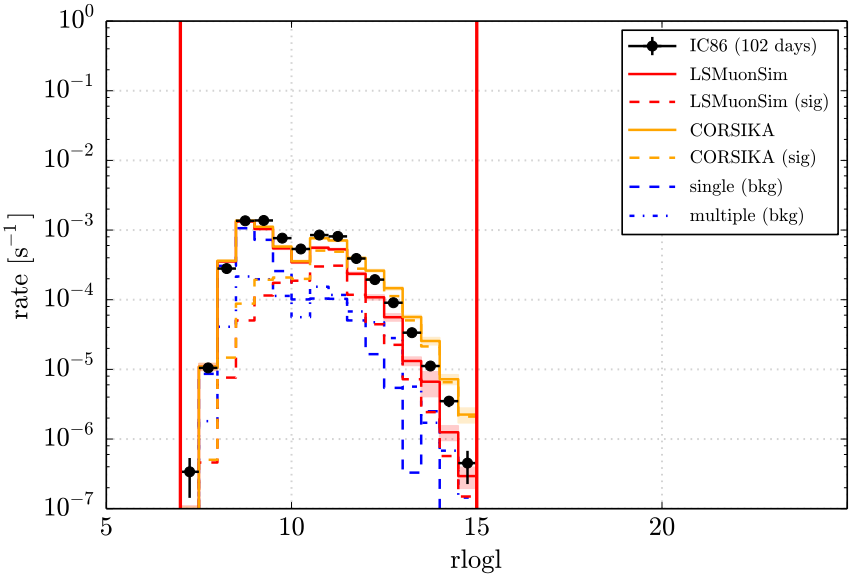

Figure C.44: Reduced likelihood value of the first-guess LLH fit at L4 filter level.

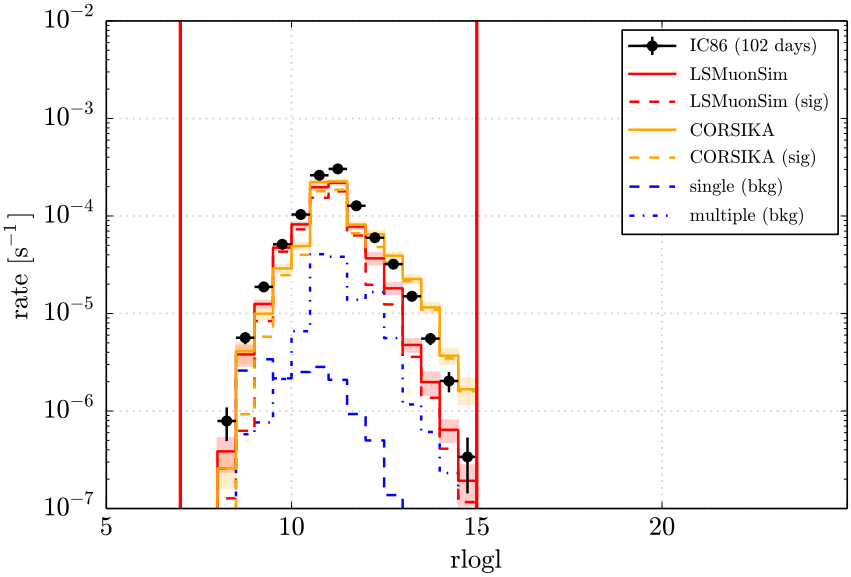

Figure C.45: Reduced likelihood value of the first-guess LLH fit at L5 filter level.

C.7 TRANSVERSE MOMENTUM

In-Ice

The transverse momentum distributions of LS MUON events at final filter level are shown in Figure C.46 (left), in comparison to collider data (right). The corresponding fit parameters of the Hagedorn fits, also previously shown in Figure C.48, are given in Table C.2.

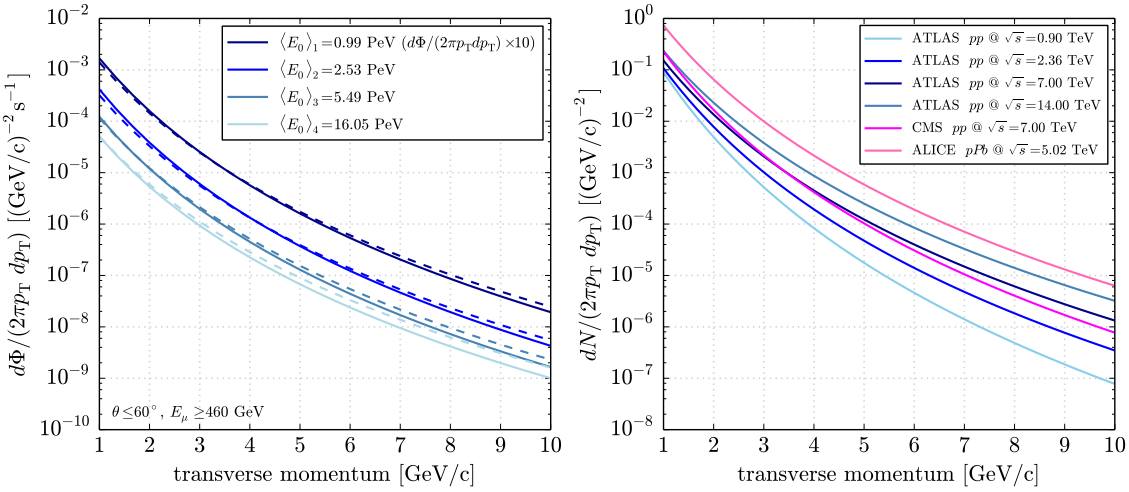

Figure C.46: Hagedorn fits applied to the reconstructed p_T distributions in ice at final filter level for several primary energy bins (left). The fits are shown for 960 days of data (solid lines) and obtained from the true MC distributions using LSMUONSIM. Various Hagedorn distributions, obtained from accelerator data, are also shown (right).

Primary energy	$10^{-3} \cdot \alpha$ [(GeV/c)$^{-2}$s^{-1}]	β	p_0 [GeV/c]
$\langle E_0 \rangle_1$	4.6 ± 0.9	-8.2 ± 0.4	2.04 ± 0.17
$\langle E_0 \rangle_2$	11.9 ± 3.1	-8.4 ± 0.5	2.05 ± 0.21
$\langle E_0 \rangle_3$	3.3 ± 0.8	-8.2 ± 0.5	2.05 ± 0.20
$\langle E_0 \rangle_4$	1.2 ± 0.3	-8.0 ± 0.6	2.07 ± 0.20

Table C.2: Transverse momentum Hagedorn fit parameters for the fits of the form Equation (2.34), as shown in Figure 7.15.

Surface

The simulated transverse momentum distributions of LS Muon events at surface level (in-ice), obtained from LSMuonSim, are shown in Figure C.47. Figure C.48 shows the corresponding reconstructed p_T distributions at surface level, as well as the resulting Hagedorn fits, with the fit parameters discussed in Section 7.4.

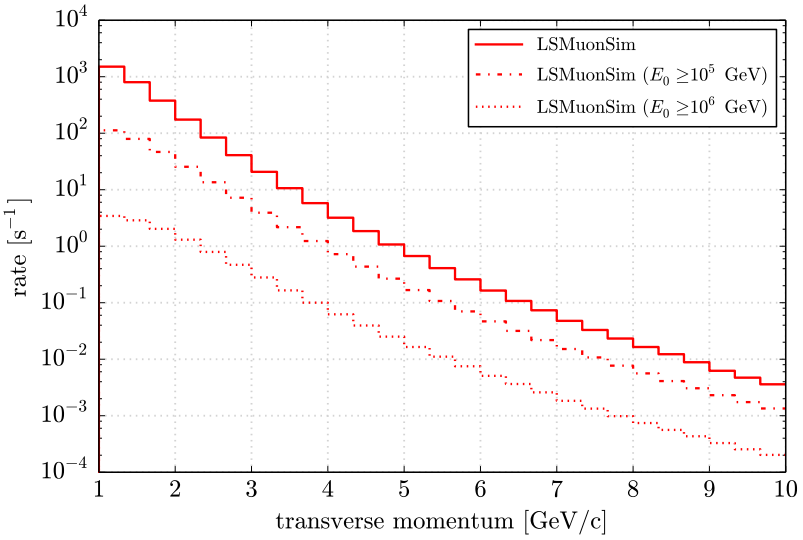

Figure C.47: Simulated (true) transverse momentum distributions of LS Muons at surface level, obtained from LSMuonSim. The individual contributions from different primary energy regions are shown separately.

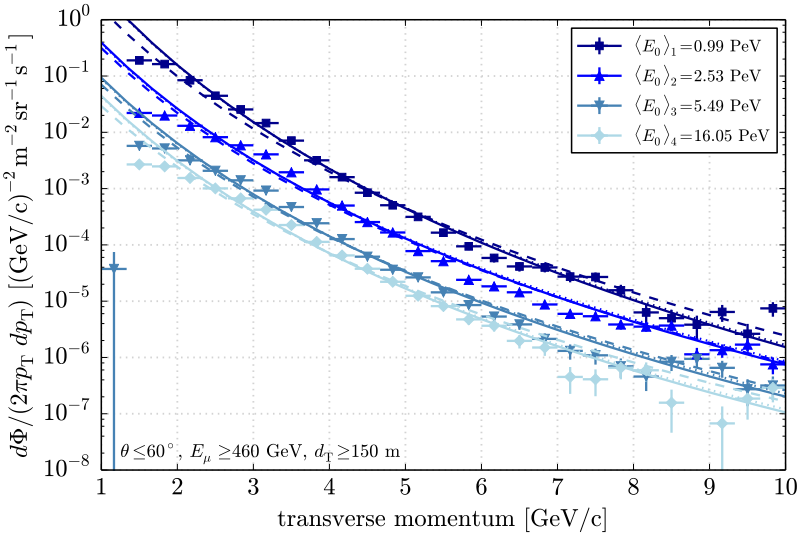

Figure C.48: Transverse momentum distribution at surface level for several primary energy bins. The Hagedorn fits shown as solid lines are applied for events above $p_{T,min} = 2\,GeV/c$

C.8 PRIMARY ENERGY

In-Ice

The simulated primary energy spectra for all analysis levels are shown in Figure C.49 (L0), Figure C.50 (L1), Figure C.51 (L2), Figure C.52 (L3), Figure C.53 (L4), Figure C.54 (L5). The spectra are obtained from LSMUONSIM and CORSIKA simulations.

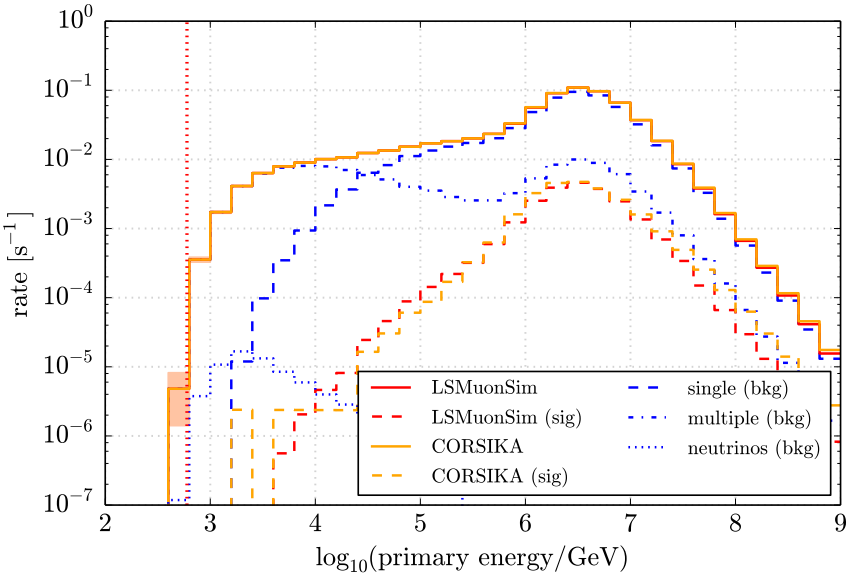

Figure C.49: Simulated primary energy spectrum at filter level L0.

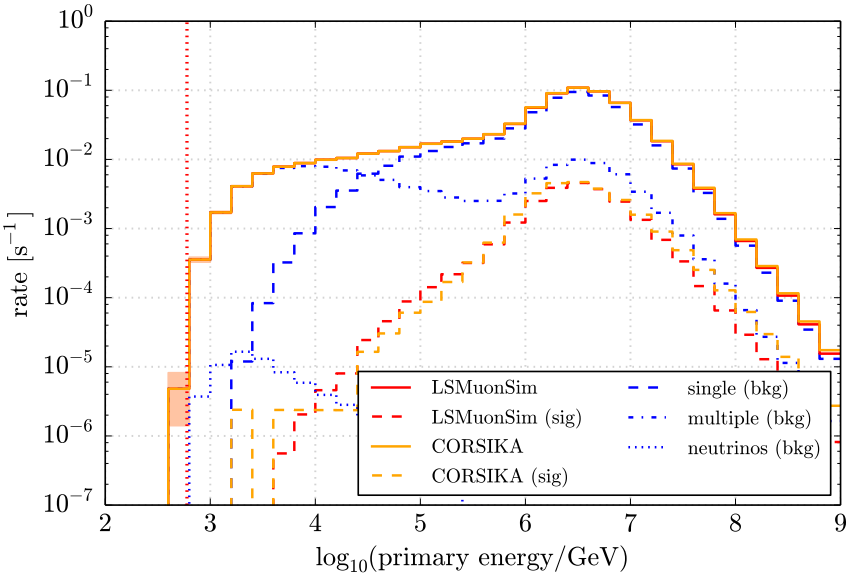

Figure C.50: Simulated primary energy spectrum at filter level L1.

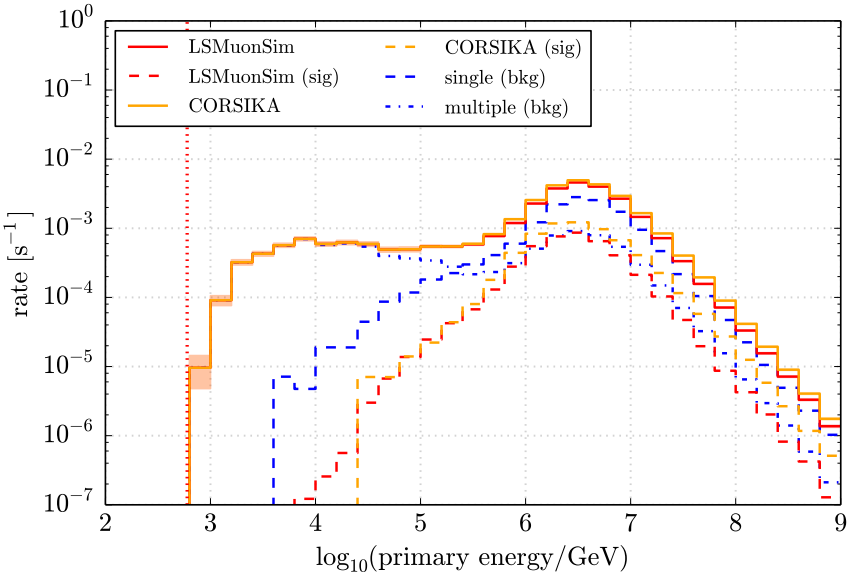

Figure C.51: Simulated primary energy spectrum at filter level L2.

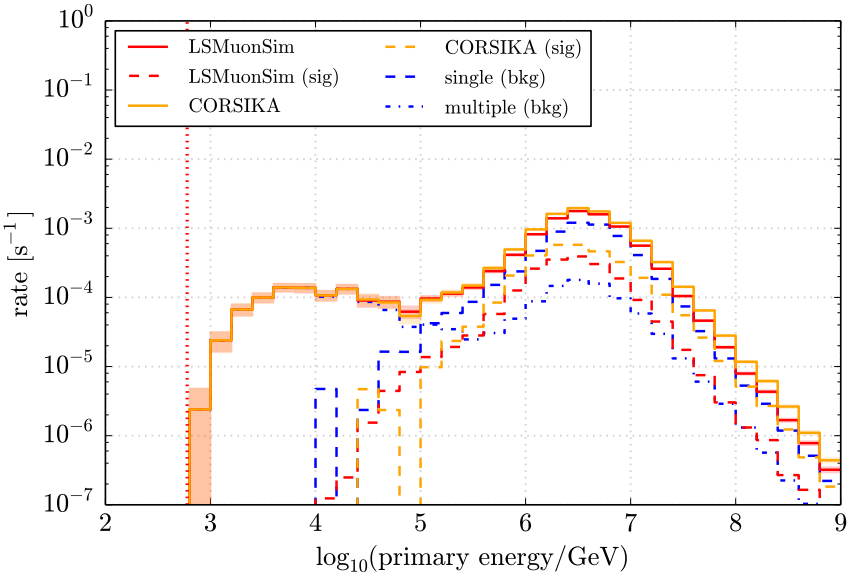

Figure C.52: Simulated primary energy spectrum at filter level L3.

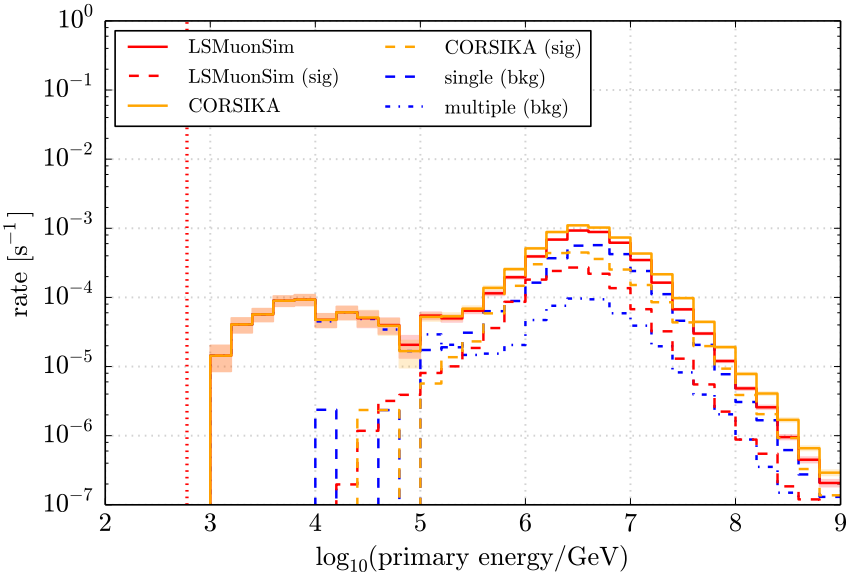

Figure C.53: Simulated primary energy spectrum at filter level L4.

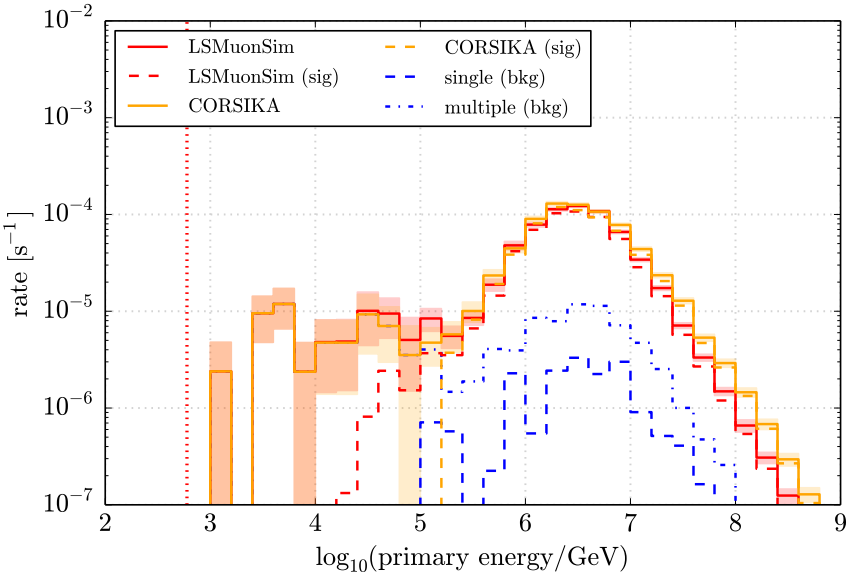

Figure C.54: Simulated primary energy spectrum at final filter level L5.

C.9 LS MUON ENERGY

In-Ice

The simulated energy spectra of muons with the larges lateral separation of the shower, for all analysis levels, are shown in Figure C.55 (L0), Figure C.56 (L1), Figure C.57 (L2), Figure C.58 (L3), Figure C.59 (L4), Figure C.60 (L5). The spectra are obtained from LSMuonSim and CORSIKA simulations.

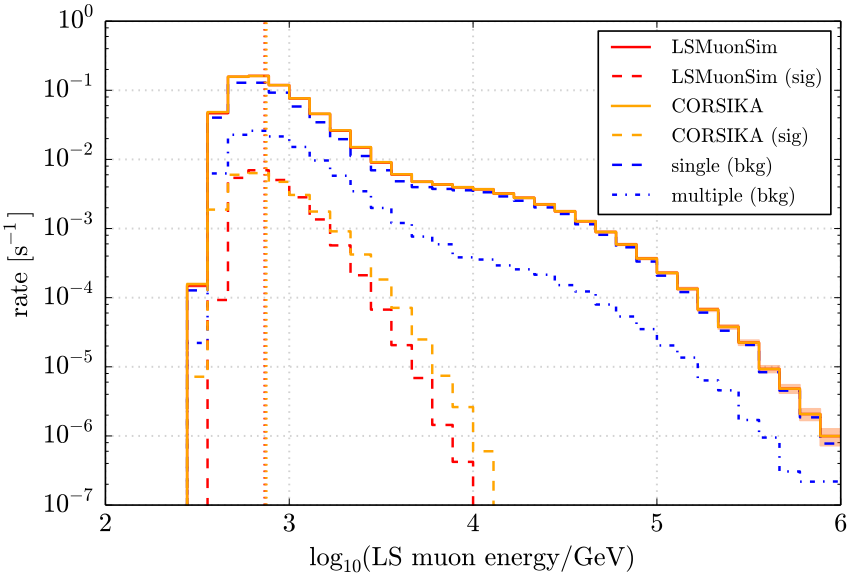

Figure C.55: Simulated LS Muon energy spectrum at filter level L0.

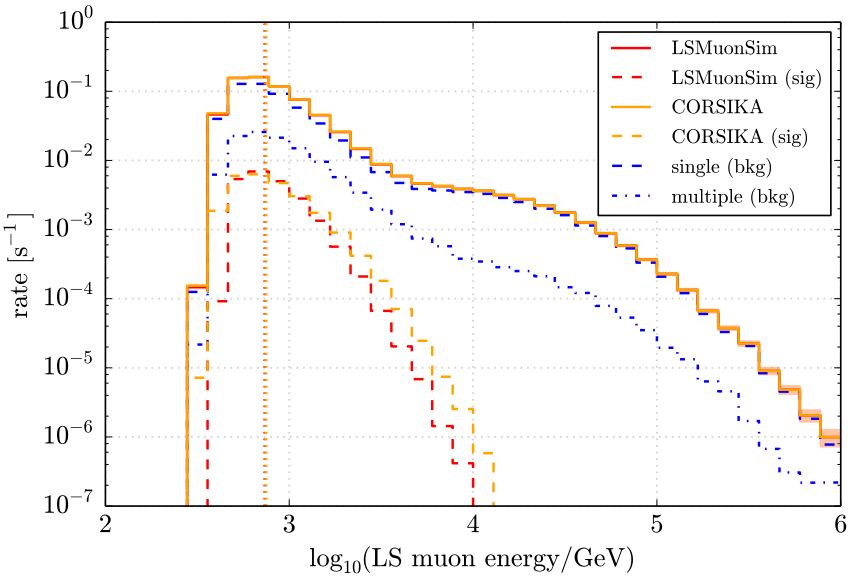

Figure C.56: Simulated LS Muon energy spectrum at filter level L1.

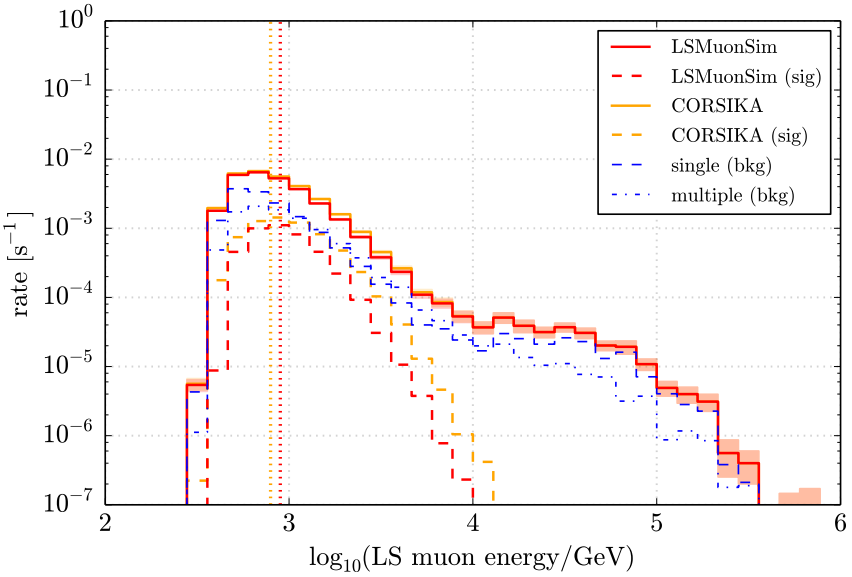

Figure C.57: Simulated LS MUON energy spectrum at filter level L2.

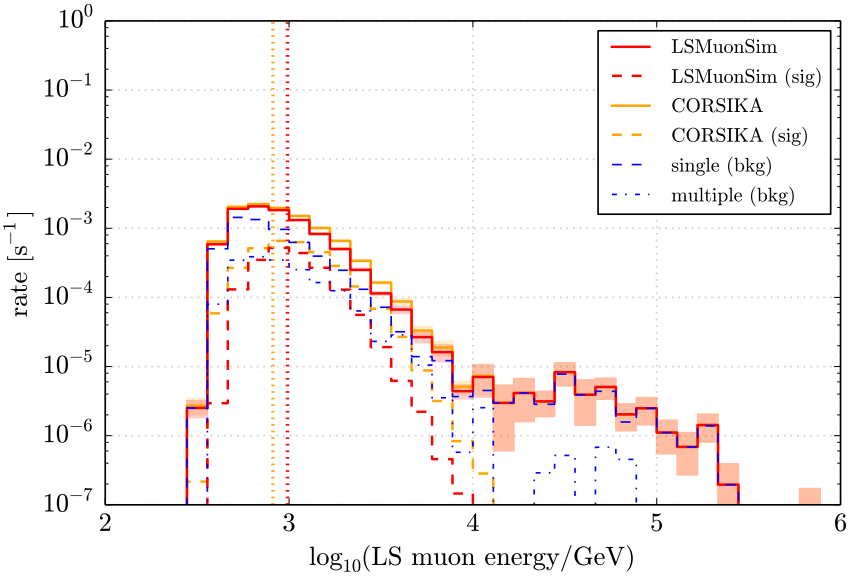

Figure C.58: Simulated LS MUON energy spectrum at filter level L3.

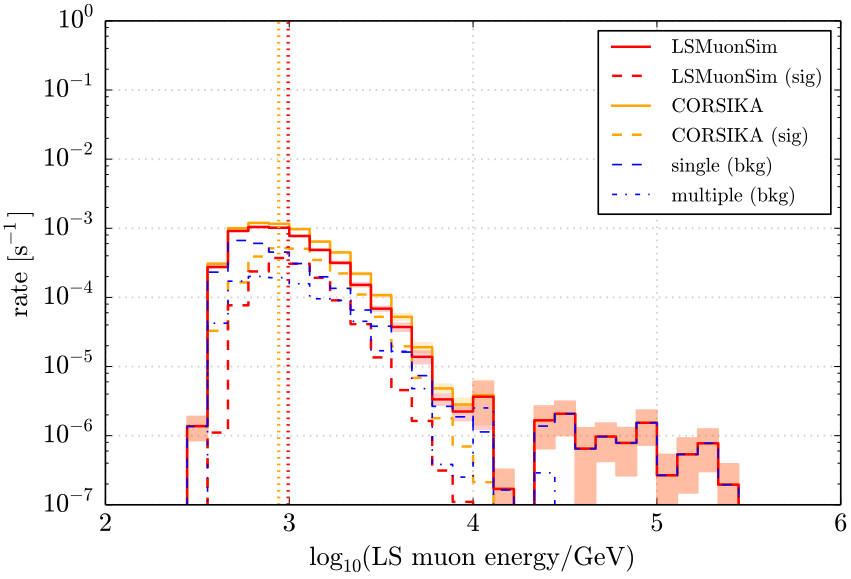

Figure C.59: Simulated LS Muon energy spectrum at filter level L4.

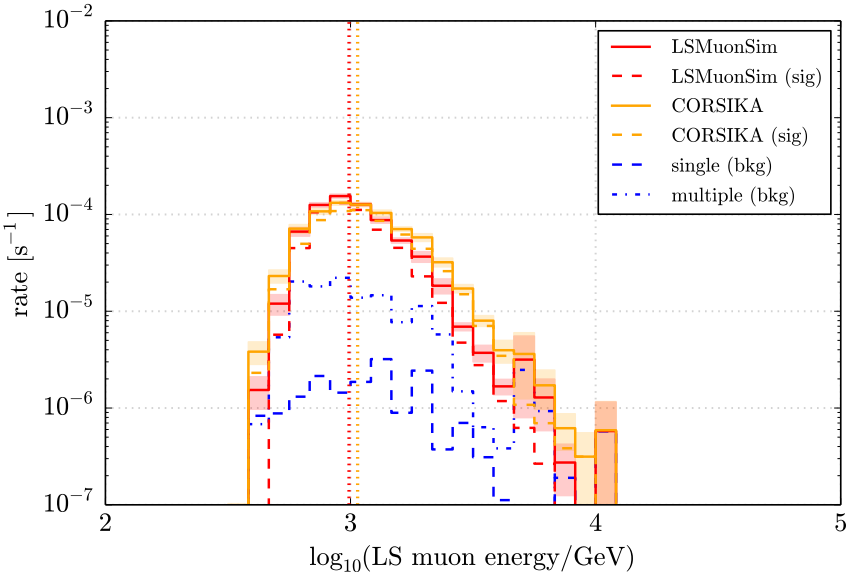

Figure C.60: Simulated LS Muon energy spectrum at final filter level L5.

The simulated energy spectra of muons with the larges lateral separation of the shower, for various zenith angles, are shown in Figure C.61 (L2), Figure C.62 (L3), Figure C.63 (L4), Figure C.64 (L5). The spectra are shown for CORSIKA (left) and LSMuonSim simulations (right) separately. The contributions from different zenith angles only include LS Muon events ($d_T \geqslant 100\,\mathrm{m}$).

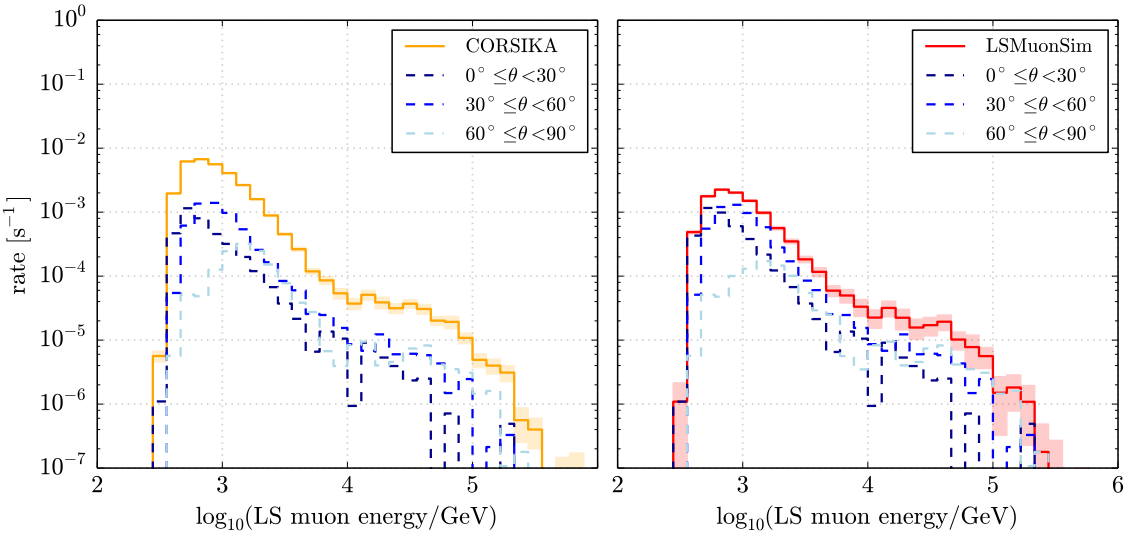

Figure C.61: Simulated LS Muon energy spectrum at filter level L2 for various zenith angle bins.

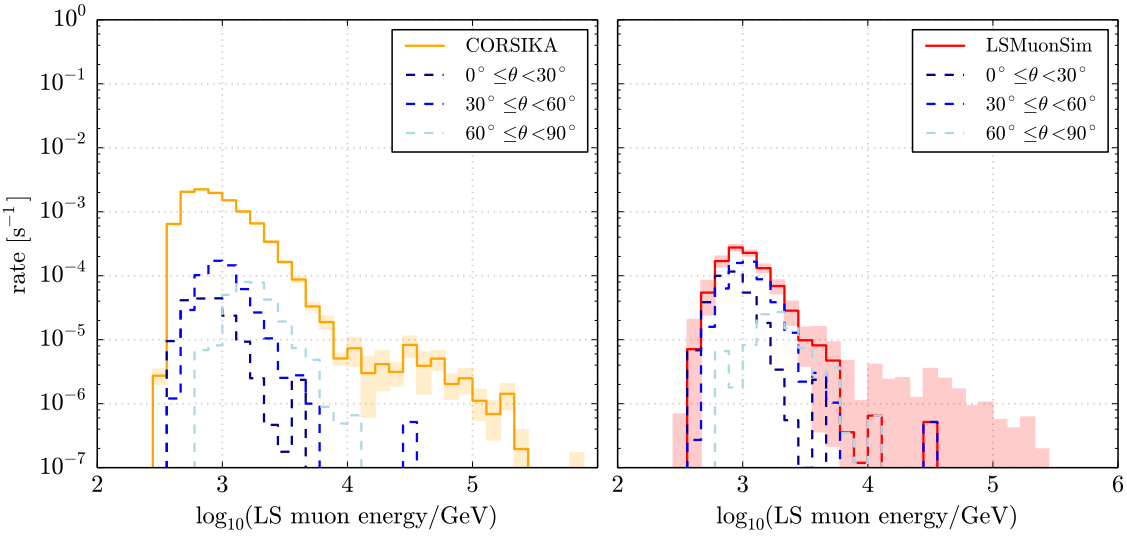

Figure C.62: Simulated LS Muon energy spectrum at filter level L3 for various zenith angle bins.

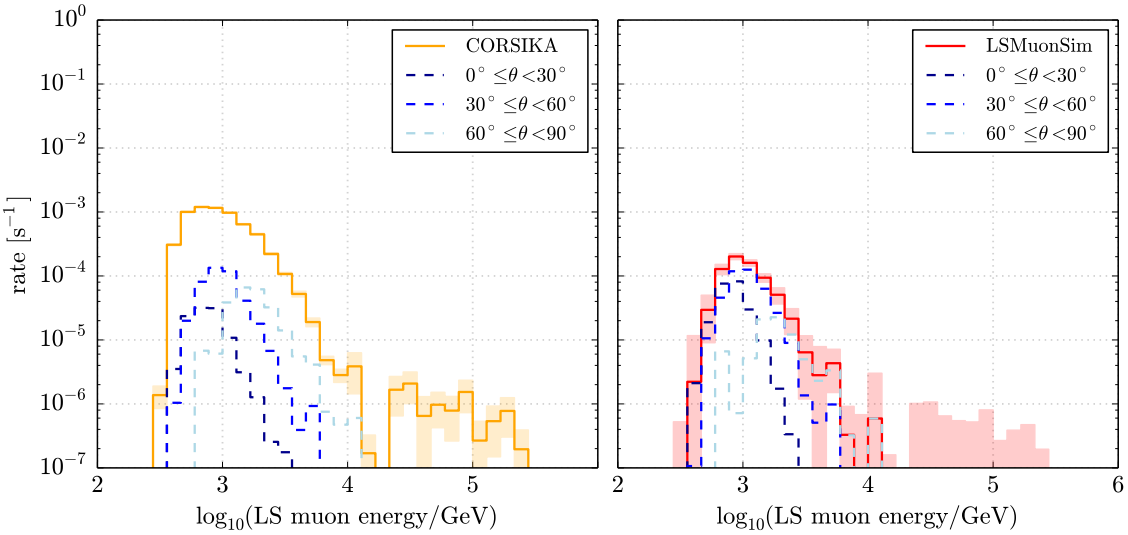

Figure C.63: Simulated LS Muon energy spectrum at filter level L4 for various zenith angle bins.

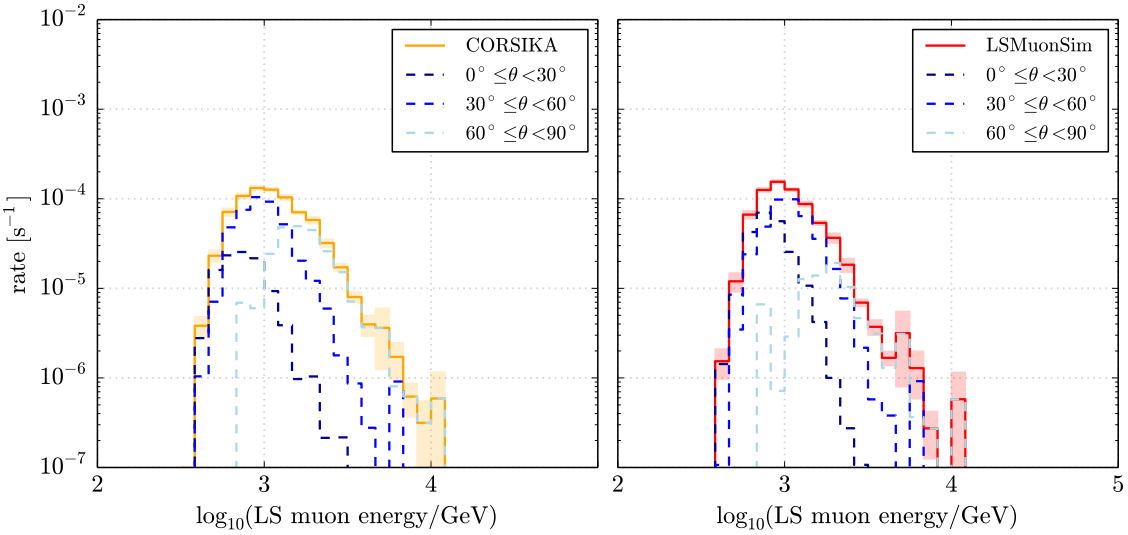

Figure C.64: Simulated LS Muon energy spectrum at final filter level L5 for various zenith angle bins.

Surface

Figure C.65 shows the energy spectrum of the largest separated muon produced in each simulated air shower, with muon energy above $E_\mu \geqslant 460\,\mathrm{GeV}$.

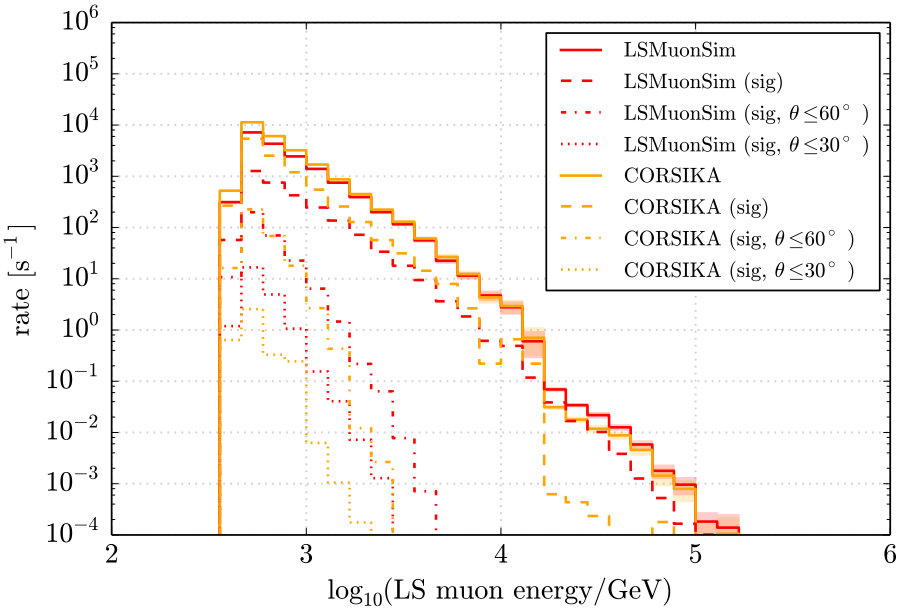

Figure C.65: Simulated (true) energy spectrum of the muon with the largest separation from the shower core and $E_\mu \geqslant 460\,\mathrm{GeV}$ (surface level). LS Muons with $d_T \geqslant 100\,\mathrm{m}$ are shown separately (sig).

C.10 ATMOSPHERIC HEIGHTS

In-Ice

Figure C.66 shows the first interaction height distribution of simulated simulated events at final filter level for the seasons used in MC simulations. The distributions are obtained from CORSIKA and LSMuonSim. The heights of production of LS Muons, obtained from LSMuonSim, are shown in Figure C.67, for various zenith angle directions. The resulting mean LS Muon production height is $\langle H_{\mu,\mathrm{prod}} \rangle = (31.6 \pm 3.9)$ km, shown as dashed line.

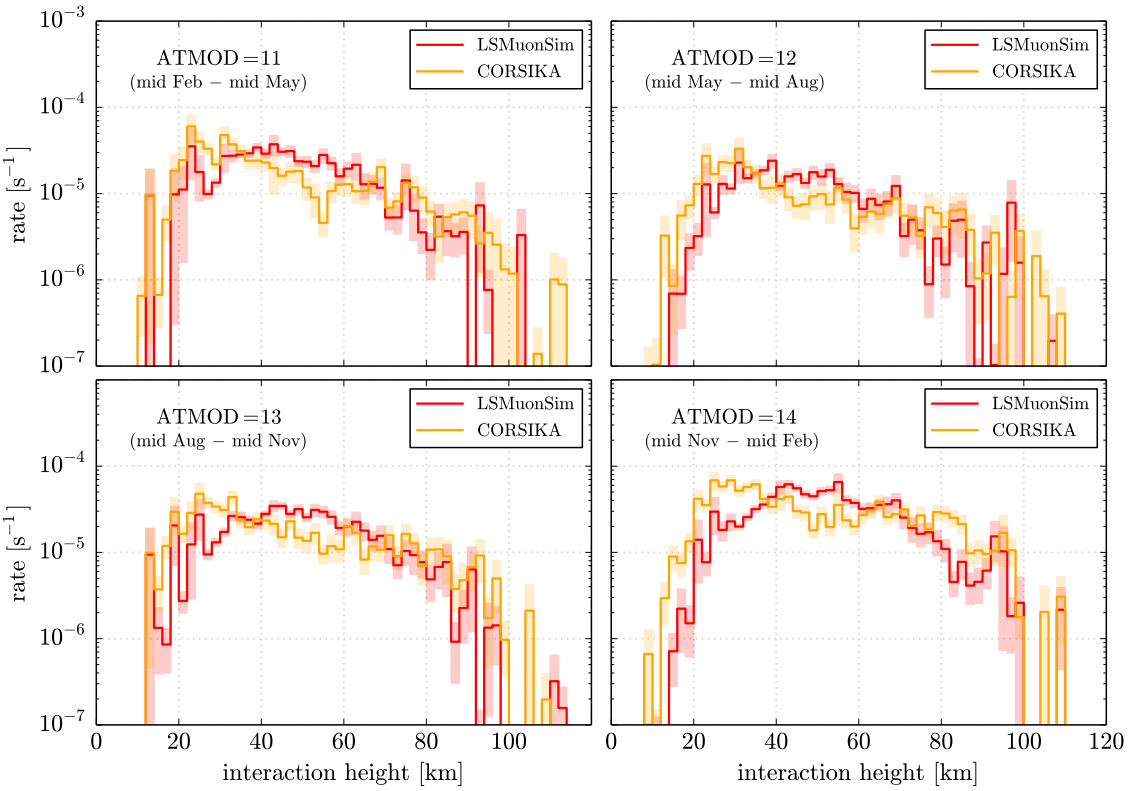

Figure C.66: Interaction height distribution for different seasons.

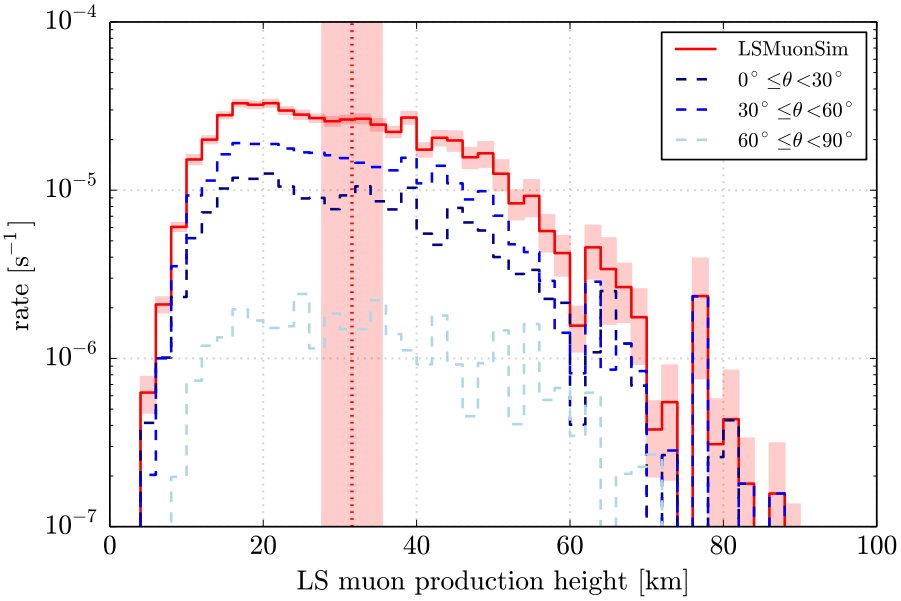

Figure C.67: Production height distribution of LS Muons at final filter level, obtained from LSMuonSim. The mean production height is shown as dotted line with error band.

Surface

Figure C.68 shows the interaction height distribution of simulated air showers at surface level for various zenith angle directions. The distributions are obtained from CORSIKA (left) and LSMuonSim (right).

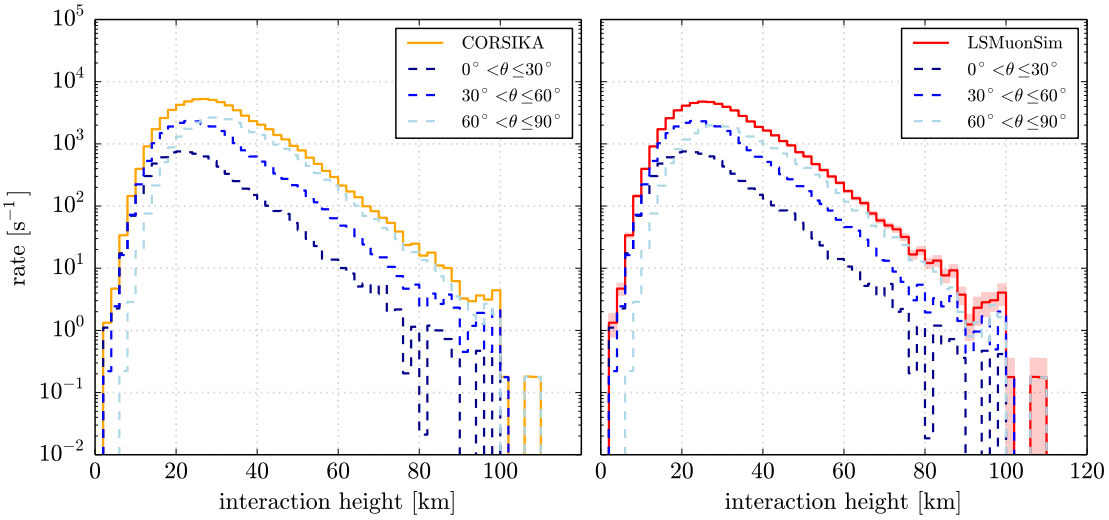

Figure C.68: Simulated distribution of the first interaction height at surface level.

C.11 RECONSTRUCTION ACCURACIES

Figure C.69 shows the true lateral separation as a function of the reconstructed lateral separation. The true primary energy of events at final filter level (L5) is shown in Figure C.71 as function of the reconstructed energy, obtained from LSMuonSim. Figure C.70 shows the true zenith angle as a function of the reconstructed zenith angle direction.

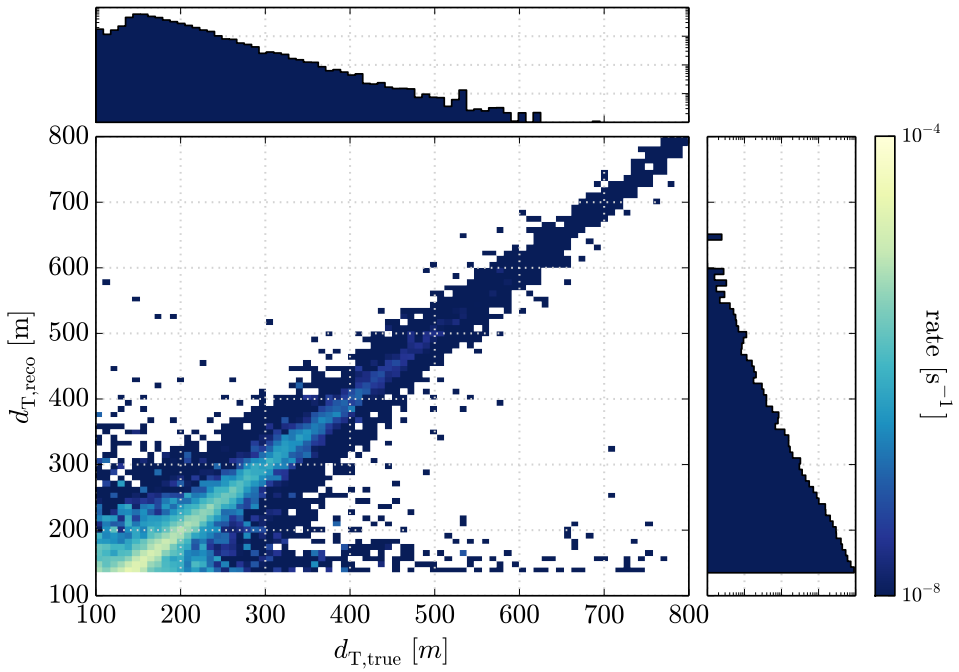

Figure C.69: Lateral separation accuracy of LS Muon events at final filter level (L5).

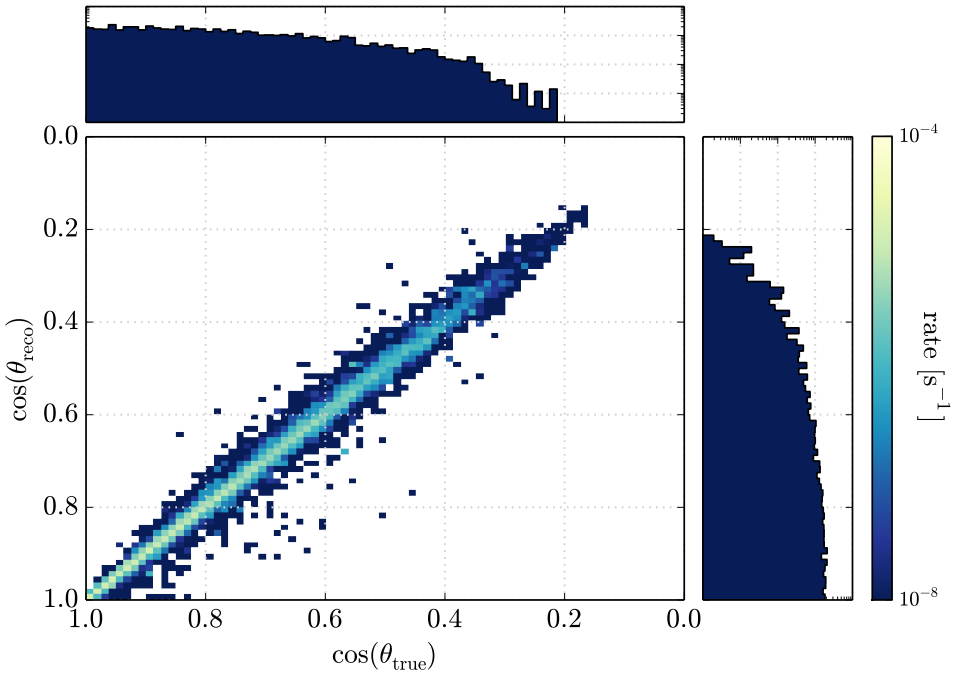

Figure C.70: Zenith angle accuracy of LS MUON events at final filter level (L5).

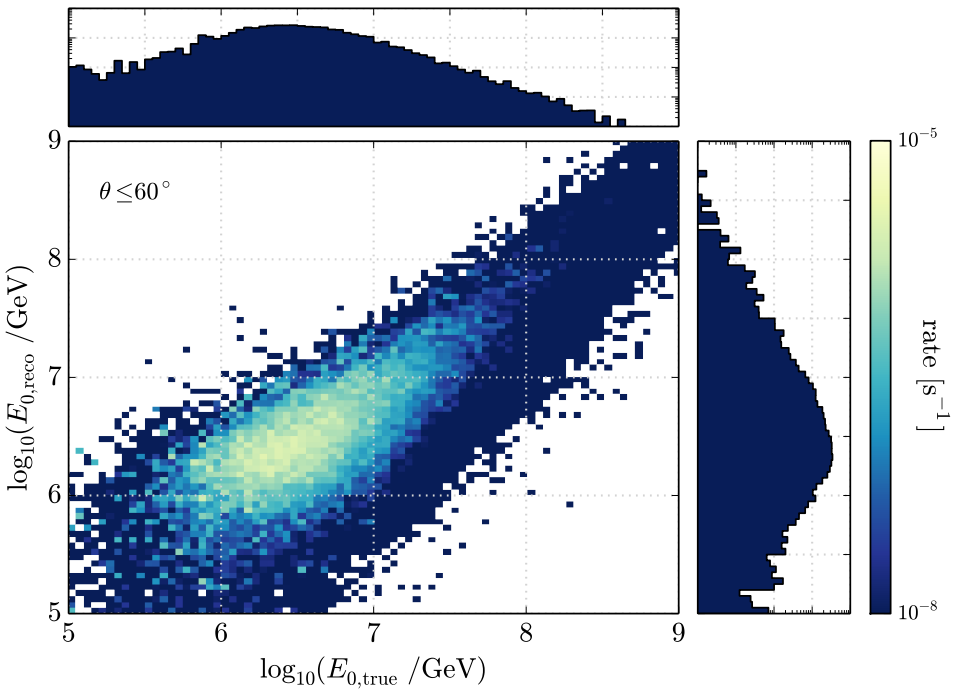

Figure C.71: Reconstructed primary energy as a function of the true primary energy of LS MUON events at final filter level (L5).

C.12 EFFECTIVE AREAS

The effective areas, as described in Section 6.9 and used in this work, obtained from LSMuonSim and CORSIKA, are shown in Figure C.72.

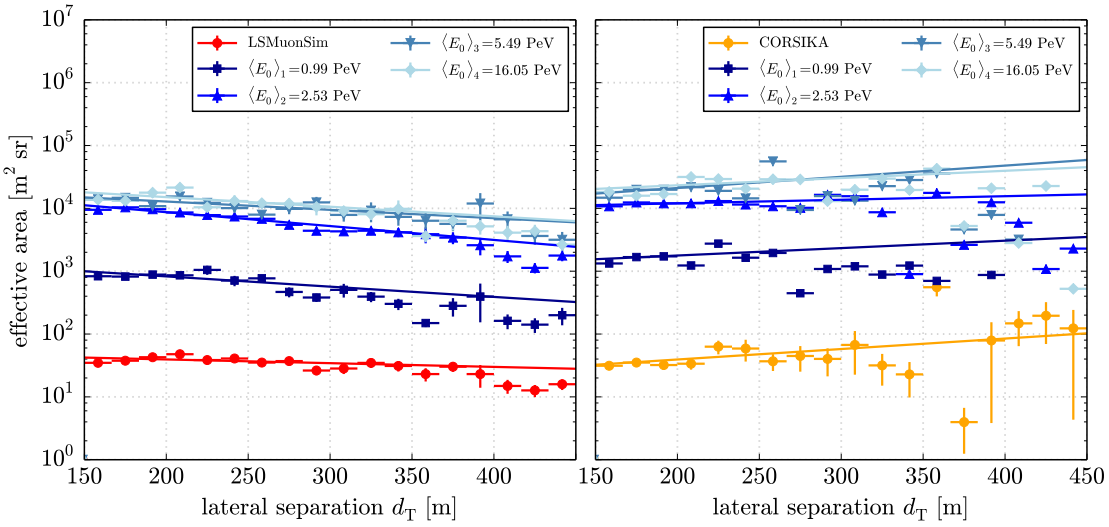

Figure C.72: Effective areas obtained from LSMuonSim (left) and CORSIKA (right).

ABBREVIATIONS AND ACRONYMS

"If I could remember the names of all these particles, I'd be a botanist."

– Enrico Fermi[*]

AGASA	Akeno Giant Air Shower Array
AGN	Active Galactic Nuleus
AIRS	Atmospheric Infrared Sounder
ALICE	A Large Ion Collider Experiment
ANIS	All Neutrino Interaction Simulation
ANTARES	Astronomy with a Neutrino Telescope and Abyss environmental Research
AMANDA	Antarctic Muon And Neutrino Detector Array
AMS	Alpha Magnetic Spectrometer
AMSB	Anomaly-Mediated Supersymmetry Breaking
ARM	Advanced RISC Machines
ATIC	Advanced Thin Ionization Calorimeter
ATLAS	A Toroidal LHC Apparatus
ATWD	Analog Transient Waveform Digitizer
Auger	Pierre Auger Observatory
BOREXINO	Boron Solar Neutrino Experiment
BSM	Beyond Standard Model
CDF	Cumulative Distribution Function
CMB	Cosmic Microwave Background
CMS	Compact Muon Solenoid
CORSIKA	Cosmic Ray Simulations for Kascade
CPU	Central Processing Unit

[*] As quoted by M. Kaku, in *"Hyperspace"* (1995).

CREAM	Cosmic Ray Energetics And Mass instrument
CRMC	Cosmic Ray Monte Carlo
CTEQ5	Coordinated Theoretical/Experimental Project on QCD Phenomenology and Tests of the Standard Model 5
DAQ	Data Acquisition
DC	DeepCore
DOM	Digital Optical Module
DPMJet	Dual Parton Model with Jets
DSB	DOMHub Service Board
DUMAND	Deep Underwater Muon And Neutrino Telescope
EAS	Extensive Air Shower
EHE	Extremely High Energy
EPOS-LHC	EPOS Hadronic Interaction Model
FADC	Fast Analog to Digital Converter
FCNC	Flavor Changing Neutral Current
FPGA	Field Programmable Gate Array
Gheisha	Gheisha Hadronic Interaction Model
GMSB	Gauge-Mediated Supersymmetry Breaking
GPS	Global Positioning System
GRB	Gamma-Ray Burst
GST	Gaisser-Stanev-Tilav
GUT	Grand Unified Theory
GZK	Greisen Zatsepin Kuzmin
H3a	Hillas 3a Model
H4a	Hillas 4a Model
HIJING	Heavy Ion Jet Interaction Generator
HiRes	High Resolution
HLC	Hard Local Coincidence

IC	IceCube (in-ice)
IC59	IceCube 59-string configuration (in-ice)
IC86	IceCube 86-string configuration (in-ice)
IceCube	IceCube Neutrino Observatory
IceTop	IceCube Surface Array
IceTray	IceCube Software Framework
ICL	IceCube Laboratory
ISS	International Space Station
IT	IceTop
KASCADE-Grande	Karlsruhe Shower Core and Array Detector-Grande
KASCADE	Karlsruhe Shower Core and Array Detector
KK	Kaluza-Klein
KM3NeT	Cubic-Kilometer Neutrino Telescope
KS	Kolmogorov-Smirnov
LED	Light Emitting Diode
LHC	Large Hadron Collider
LLH	Log-Likelihood
LQCD	Lattice Quantum Chromodynamics
LS Muon	Laterally Separated Muon
LSMuonSim	LS Muon Simulation Code
LSP	Lightest Supersymmetric Particle
MACRO	Monopole, Astrophysics and Cosmic Rays Observatory
MCEq	Matrix Cascade Equation
MC	Monte Carlo
MIP	Minimum Ionizing Particle
MPE	Multi-Photoelectron
MSIS	Mass Spectrometer and Incoherent Scatter

MSSM	Minimal Supersymmetric Standard Model
mSUGRA	minimal Supergravity
NASA	National Aeronautics and Space Administration
NLSP	Next-to-Lightest Supersymmetric Particle
NuGen	Neutrino Generation Code
PAMELA	Payload for Antimatter Matter Exploration and Light-nuclei Astrophysics
PCI	Peripheral Component Interconnect
PDG	Particle Data Group
PE	Photoelectron
pMSSM	phenomenological Minimal Supersymmetric Standard Model
PMT	Photomultiplier Tube
PPC	Photon Propagation Code
PQCD	Perturbative Quantum Chromodynamics
PREM	Preliminary Reference Earth Model
PROPOSAL	Propagator with Optimal Precision and Optimized Speed for All Leptons
PYTHIA	PYTHIA Event Generator
QCD	Quantum Chromodynamics
QED	Quantum Electrodynamics
QGP	Quark-Gluon Plasma
QGS	Quark-Gluon String
QGSJet	Quark-Gluon String Model with Jets
RapCal	Reciprocal Active Pulsing Calibration
SBC	Single Board Computer
SBM	Statistical-Bootstrap Model
SciPy	Scientific Python Software Package
Sibyll	Sibyll Hadronic Interaction Model

SLC	Soft Local Coincidence
SMT3	Simple Majority Trigger 3
SMT8	Simple Majority Trigger 8
SMT	Simple Majority Trigger
SM	Standard Model
SN	Supernova
SNR	Supernova Remnant
SPE	Single Photoelectron
SPheno	Supersymmetry Phenomenology Event Generator
SPS	Snowmass Points and Slopes
SUGRA	Supergravity
SUSY	Supersymmetry
TA	Telescope Array
TOTEM	Total Elastic and Diffractive Cross Section Measurement
UTC	Coordinated Universal Time
VEM	Vertical Equivalent Muon
VEV	Vacuum Expectation Value
WIMP	Weakly Interacting Massive Particle

BIBLIOGRAPHY

[1] V. S. Hess. "Über Beobachtungen der durchdringenden Strahlung bei sieben Freiballonfahrten." In: *Phys. Z.* 13 (1912), pp. 1084–1091.

[2] W. Kohlhörster. "Messungen der durchdringenden Strahlung im Freiballon in grösseren Höhen." In: *Phys. Z.* 14 (1913), pp. 1153–1156.

[3] K.-H. Kampert and A. A. Watson. "Extensive air showers and ultra high-energy cosmic rays: a historical review." In: *European Physical Journal H* 37 (Aug. 2012), pp. 359–412. DOI: 10.1140/epjh/e2012-30013-x. arXiv: 1207.4827.

[4] T. K. Gaisser. *Cosmic Rays And Particle Physics*. Cambridge University Press, 1990.

[5] I. F. M. Albuquerque, G. Burdman, and Z. Chacko. "Direct detection of supersymmetric particles in neutrino telescopes." In: *Phys. Rev.* D75 (2007), p. 035006. DOI: 10.1103/PhysRevD.75.035006. arXiv: 0605120 [hep-ph].

[6] J. I. Illana, M. Ahlers, M. Masip, and D. Meloni. "Exotic physics with ultrahigh energy cosmic rays." In: *Acta Phys. Polon.* B38 (2007), pp. 3357–3364. arXiv: 0710.0584 [hep-ph].

[7] R. Blandford and D. Eichler. "Particle acceleration at astrophysical shocks: A theory of cosmic ray origin." In: *Physics Reports* 154.1 (1987), pp. 1 –75. ISSN: 0370-1573. DOI: 10.1016/0370-1573(87)90134-7.

[8] W. Baade and F. Zwicky. "Cosmic Rays from Super-Novae." In: *Proceedings of the National Academy of Sciences* 20.5 (1934), pp. 259–263. DOI: 10.1073/pnas.20.5.259.

[9] C. Grupen. *Astroparticle Physics*. Springer, 2005.

[10] Y. Sekido, T. Masuda, S. Yoshida, and M. Wada. "The Crab Nebula as an Observed Point Source of Cosmic Rays." In: *Phys. Rev.* 83 (3 1951), pp. 658–659. DOI: 10.1103/PhysRev.83.658.2.

[11] H. W. Babcock. "Magnetic Variable Stars as Sources of Cosmic Rays." In: *Phys. Rev.* 74 (4 1948), pp. 489–489. DOI: 10.1103/PhysRev.74.489.

[12] J. R. Hörandel. "Models of the knee in the energy spectrum of cosmic rays." In: *Astroparticle Physics* 21.3 (2004), pp. 241 –265. ISSN: 0927-6505. DOI: 10.1016/j.astropartphys.2004.01.004.

[13] J. R. Hörandel. "The Composition of Cosmic Rays at the Knee." In: *Proceedings, Centenary Symposium 2012: Discovery of Cosmic Rays: Denver, CO, USA, June 26-28, 2012*. [AIP Conf. Proc.1516,185(2012)]. 2012. DOI: 10.1063/1.4792566. arXiv: 1212.0739 [astro-ph.HE].

[14] J. R. Hörandel. "Cosmic-ray composition and its relation to shock acceleration by supernova remnants." In: *36th COSPAR Scientific Assembly Beijing, China, July 16-23, 2006*. Vol. 41. 2008, pp. 442–463. DOI: 10.1016/j.asr.2007.06.008. arXiv: 0702370 [astro-ph].

[15] R. U. Abbasi et al. "First observation of the Greisen-Zatsepin-Kuzmin suppression." In: *Phys. Rev. Lett.* 100 (2008), p. 101101. DOI: 10.1103/PhysRevLett.100.101101. arXiv: 0703099 [astro-ph].

[16] Y. Tameda. "Telescope Array Experiment." In: *Nuclear Physics B - Proceedings Supplements* 196 (2009), pp. 74 –79. ISSN: 0920-5632. DOI: 10.1016/j.nuclphysbps.2009.09.011.

[17] J. Abraham et al. "Properties and performance of the prototype instrument for the Pierre Auger Observatory." In: *Nucl. Instrum. Meth.* A523 (2004), pp. 50–95. DOI: 10.1016/j.nima.2003.12.012.

[18] J. Abraham et al. "Observation of the suppression of the flux of cosmic rays above 4×10^{19}eV." In: *Phys. Rev. Lett.* 101 (2008), p. 061101. DOI: 10.1103/PhysRevLett.101.061101. arXiv: 0806.4302 [astro-ph].

[19] G. Henri, G. Pelletier, P. O. Petrucci, and N. Renaud. "Active galactic nuclei as high-energy engines." In: *Astropart. Phys.* 11 (1999), pp. 347–356. DOI: 10.1016/S0927-6505(98)00071-1. arXiv: 9901051 [astro-ph].

[20] J. Arons. "Magnetars in the metagalaxy: an origin for ultrahigh-energy cosmic rays in the nearby universe." In: *Astrophys. J.* 589 (2003), pp. 871–892. DOI: 10.1086/374776. arXiv: 0208444 [astro-ph].

[21] Eli Waxman. "Cosmological Gamma-Ray Bursts and the Highest Energy Cosmic Rays." In: *Phys. Rev. Lett.* 75 (3 1995), pp. 386–389. DOI: 10.1103/PhysRevLett.75.386.

[22] M. Vietri. "On the acceleration of ultrahigh-energy cosmic rays in gamma-ray bursts." In: *Astrophys. J.* 453 (1995), pp. 883–889. DOI: 10.1086/176448. arXiv: 9506081 [astro-ph].

[23] E. Waxman and J. N. Bahcall. "High-energy neutrinos from cosmological gamma-ray burst fireballs." In: *Phys. Rev. Lett.* 78 (1997), pp. 2292–2295. DOI: 10.1103/PhysRevLett.78.2292. arXiv: 9701231 [astro-ph].

[24] F. W. Stecker, C. Done, M. H. Salamon, and P. Sommers. "High-energy neutrinos from active galactic nuclei." In: *Phys. Rev. Lett.* 66 (1991). [Erratum: Phys. Rev. Lett.69,2738(1992)], pp. 2697–2700. DOI: 10.1103/PhysRevLett.66.2697.

[25] F. Halzen, R. A. Vazquez, T. Stanev, and H. P. Vankov. "The highest energy cosmic ray." In: *Physics in collision. Proceedings, 14th International Conference, Tallahassee, USA, June 15-17, 1994*. Vol. 3. 1995, pp. 151–156. DOI: 10.1016/0927-6505(94)00038-5.

[26] M. G. Aartsen et al. "First observation of PeV-energy neutrinos with IceCube." In: *Phys. Rev. Lett.* 111 (2013), p. 021103. DOI: 10.1103/PhysRevLett.111.021103. arXiv: 1304.5356 [astro-ph.HE].

[27] M. G. Aartsen et al. "Observation of High-Energy Astrophysical Neutrinos in Three Years of IceCube Data." In: *Phys. Rev. Lett.* 113 (2014), p. 101101. DOI: 10.1103/PhysRevLett.113.101101. arXiv: 1405.5303 [astro-ph.HE].

[28] M. G. Aartsen et al. "Evidence for High-Energy Extraterrestrial Neutrinos at the IceCube Detector." In: *Science* 342 (2013), p. 1242856. DOI: 10.1126/science.1242856. arXiv: 1311.5238 [astro-ph.HE].

[29] M. G. Aartsen et al. "All-sky search for time-integrated neutrino emission from astrophysical sources with 7 years of IceCube data." In: (2016). arXiv: 1609.04981 [astro-ph.HE].

[30] E. Fermi. "On the Origin of the Cosmic Radiation." In: *Phys. Rev.* 75 (1949), pp. 1169–1174. DOI: 10.1103/PhysRev.75.1169.

[31] F. Halzen. "The Search for the source of the highest energy cosmic rays." In: *New worlds in astroparticle physics. Proceedings, International Workshop, Faro, Portugal, September 8-10, 1996*. 1997, pp. 35–56. arXiv: 9704020 [astro-ph].

[32] B. Peters. "Primary cosmic radiation and extensive air showers." In: *Il Nuovo Cimento (1955-1965)* 22.4 (1961), pp. 800–819. DOI: 10.1007/BF02783106.

[33] H. Kolanoski and N. Wermes. *Teilchendetektoren – Grundlagen und Anwendungen*. Springer Spektum, 2016.

[34] C. Patrignani et al. "Review of Particle Physics." In: *Chin. Phys.* C40.10 (2016), p. 100001. DOI: 10.1088/1674-1137/40/10/100001.

[35] T. Antoni et al. "The Cosmic ray experiment KASCADE." In: *Nucl. Instrum. Meth.* A513 (2003), pp. 490–510. DOI: 10.1016/S0168-9002(03)02076-X.

[36] W. D. Apel et al. "Kneelike Structure in the Spectrum of the Heavy Component of Cosmic Rays Observed with KASCADE-Grande." In: *Phys. Rev. Lett.* 107 (17 2011), p. 171104. DOI: 10.1103/PhysRevLett.107.171104.

[37] A. M. Hillas. "Cosmic Rays: Recent Progress and some Current Questions." In: (2006). arXiv: 0607109 [astro-ph].

[38] T. K. Gaisser. "Spectrum of cosmic-ray nucleons, kaon production, and the atmospheric muon charge ratio." In: *Astropart. Phys.* 35 (2012), pp. 801–806. DOI: 10.1016/j.astropartphys.2012.02.010. arXiv: 1111.6675 [astro-ph.HE].

[39] T. K. Gaisser, T. Stanev, and S. Tilav. "Cosmic Ray Energy Spectrum from Measurements of Air Showers." In: *Front. Phys.(Beijing)* 8 (2013), pp. 748–758. DOI: 10.1007/s11467-013-0319-7. arXiv: 1303.3565 [astro-ph.HE].

[40] K. Greisen. "End to the Cosmic-Ray Spectrum?" In: *Phys. Rev. Lett.* 16 (17 1966), pp. 748–750. DOI: 10.1103/PhysRevLett.16.748.

[41] G. T. Zatsepin and V. A. Kuzmin. "Upper Limit of the Spectrum of Cosmic Rays." In: *Soviet Journal of Experimental and Theoretical Physics Letters* 4 (Aug. 1966), p. 78.

[42] M. Takeda et al. "Energy determination in the Akeno Giant Air Shower Array experiment." In: *Astropart. Phys.* 19 (2003), pp. 447–462. DOI: 10.1016/S0927-6505(02)00243-8. arXiv: 0209422 [astro-ph].

[43] K.-H. Kampert and M. Unger. "Measurements of the cosmic ray composition with air shower experiments." In: *Astroparticle Physics* 35.10 (2012), pp. 660 –678. DOI: 10.1016/j.astropartphys.2012.02.004.

[44] W. Heitler. *The Quantum Theory of Radiation*. Oxford University Press, London, 1954, p. 386.

[45] J. Matthews. "A Heitler model of extensive air showers." In: *Astroparticle Physics* 22.5–6 (2005), pp. 387 –397. DOI: 10.1016/j.astropartphys.2004.09.003.

[46] P. Gondolo, G. Ingelman, and M. Thunman. "Charm production and high-energy atmospheric muon and neutrino fluxes." In: *Astropart. Phys.* 5 (1996), pp. 309–332. DOI: 10.1016/0927-6505(96)00033-3. arXiv: 9505417 [hep-ph].

[47] A.E. Hedin et al. "A global thermospheric model based on mass spectrometer and incoherent scatter data." In: *J. Geophys. Res.* 82 (1977), pp. 2139–2156.

[48] D. Heck, G. Schatz, T. Thouw, J. Knapp, and J. N. Capdevielle. "CORSIKA: A Monte Carlo code to simulate extensive air showers." In: (1998).

[49] J. I. Illana, P. Lipari, M. Masip, and D. Meloni. "Atmospheric lepton fluxes at very high energy." In: *Astropart. Phys.* 34 (2011), pp. 663–673. DOI: 10.1016/j.astropartphys.2011.01.001. arXiv: 1010.5084 [astro-ph.HE].

[50] A. Fedynitch, R. Engel, T K. Gaisser, F. Riehn, and T. Stanev. "Calculation of conventional and prompt lepton fluxes at very high energy." In: *EPJ Web Conf.* 99 (2015), p. 08001. DOI: 10.1051/epjconf/20159908001. arXiv: 1503.00544 [hep-ph].

[51] F. Riehn, R. Engel, A. Fedynitch, T. K. Gaisser, and T. Stanev. "Charm production in SIBYLL." In: *EPJ Web Conf.* 99 (2015), p. 12001. DOI: 10.1051/epjconf/20159912001. arXiv: 1502.06353 [hep-ph].

[52] M. G. Aartsen et al. "Characterization of the Atmospheric Muon Flux in IceCube." In: *Astropart. Phys.* 78 (2016), pp. 1–27. DOI: 10.1016/j.astropartphys.2016.01.006. arXiv: 1506.07981 [astro-ph.HE].

[53] R. Enberg, M. H. Reno, and I. Sarcevic. "Prompt neutrino fluxes from atmospheric charm." In: *Phys. Rev.* D78 (2008), p. 043005. DOI: 10.1103/PhysRevD.78.043005. arXiv: 0806.0418 [hep-ph].

[54] T. Fuchs. "Charmante Myonen im Eis: Messung des hochenergetischen atmosphärischen Myon-Energiespektrums im IceCube in der Detektorkonfiguration IC86-I." PhD thesis. 2016.

[55] R. Hagedorn. "Multiplicities, p_T Distributions and the Expected Hadron $\rightarrow$ Quark - Gluon Phase Transition." In: *Riv. Nuovo Cim.* 6N10 (1983), pp. 1–50. DOI: 10.1007/BF02740917.

[56] C. J. Hamer. "The Statistical Bootstrap Model." PhD thesis. California Institute of Technology, 1972.

[57] R. Gupta. "Introduction to lattice QCD: Course." In: *Probing the standard model of particle interactions. Proceedings, Summer School in Theoretical Physics, NATO Advanced Study Institute, 68th session, Les Houches, France, July 28-September 5, 1997. Pt. 1, 2*. 1997, pp. 83–219. arXiv: 9807028 [hep-lat].

[58] M. E. Peskin and D. V. Schroeder. *An Introduction to Quantum Field Theory*. Westview Press, 1995.

[59] J. Rafelski. *Melting Hadrons, Boiling Quarks - From Hagedorn Temperature to Ultra-Relativistic Heavy-Ion Collisions at CERN*. Springer International Publishing, 2016. DOI: 10.1007/978-3-319-17545-4.

[60] R. Hagedorn. "Thermodynamics of strong interactions." In: (1971). DOI: 10.5170/CERN-1971-012.

[61] G. Arnison et al. "Transverse momentum spectra for charged particles at the CERN proton-antiproton collider." In: *Physics Letters B* 118.1 (1982), pp. 167 –172. ISSN: 0370-2693. DOI: 10.1016/0370-2693(82)90623-2.

[62] S. Borsanyi, G. Endrodi, Z. Fodor, A. Jakovac, S. D. Katz, S. Krieg, C. Ratti, and K. K. Szabo. "The QCD equation of state with dynamical quarks." In: *JHEP* 11 (2010), p. 077. DOI: 10.1007/JHEP11(2010)077. arXiv: 1007.2580 [hep-lat].

[63] S. Borsanyi, Z. Fodor, C. Hoelbling, S. D. Katz, S. Krieg, and K. K. Szabo. "Full result for the {QCD} equation of state with flavors." In: *Physics Letters B* 730 (2014), pp. 99 –104. ISSN: 0370-2693. DOI: http://doi.org/10.1016/j.physletb.2014.01.007.

[64] J. Adams et al. "Centrality and pseudorapidity dependence of charged hadron production at intermediate p_T in Au + Au collisions at $\sqrt{s_{NN}} =$ 130 GeV." In: *Phys. Rev. C* 70 (4 2004), p. 044901. DOI: 10.1103/PhysRevC.70.044901.

[65] A. Adare et al. "Measurement of neutral mesons in p+p collisions at $\sqrt{(s)}$= 200 GeV and scaling properties of hadron production." In: *Phys. Rev.* D83 (2011), p. 052004. DOI: 10.1103/PhysRevD.83.052004. arXiv: 1005.3674 [hep-ex].

[66] G. Aad et al. "Charged-particle multiplicities in pp interactions measured with the ATLAS detector at the LHC." In: *New J. Phys.* 13 (2011), p. 053033. DOI: 10.1088/1367-2630/13/5/053033. arXiv: 1012.5104 [hep-ex].

[67] G. Aad et al. "Charged-particle distributions in $\sqrt{s}$=13 TeV pp interactions measured with the ATLAS detector at the LHC." In: *Phys. Lett.* B758 (2016), pp. 67–88. DOI: 10.1016/j.physletb.2016.04.050. arXiv: 1602.01633 [hep-ex].

[68] V. Khachatryan et al. "Transverse-momentum and pseudorapidity distributions of charged hadrons in pp collisions at $\sqrt{s} = 7$ TeV." In: *Phys. Rev. Lett.* 105 (2010), p. 022002. DOI: 10.1103/PhysRevLett.105.022002. arXiv: 1005.3299 [hep-ex].

[69] B. Abelev et al. "Transverse momentum distribution and nuclear modification factor of charged particles in p-Pb collisions at $\sqrt{s_{NN}} = 5.02$ TeV." In: *Phys. Rev. Lett.* 110.8 (2013), p. 082302. DOI: 10.1103/PhysRevLett.110.082302. arXiv: 1210.4520 [nucl-ex].

[70] B. L. Combridge, J. Kripfganz, and J. Ranft. "Hadron Production at Large Transverse Momentum and QCD." In: *Phys. Lett.* 70B (1977), p. 234. DOI: 10.1016/0370-2693(77)90528-7.

[71] J. Ranft and G. Ranft. "Quark and Gluon Transverse Momenta and QCD Predictions for Large Transverse Momentum Particle Production." In: *Acta Phys. Polon.* B10 (1979), p. 229.

[72] R. Vogt, M. Cacciari, and P. Nason. "QCD predictions of heavy quark production at RHIC." In: *Nucl. Phys.* A774 (2006), pp. 661–664. DOI: 10.1016/j.nuclphysa.2006.06.109.

[73] J. K. Kwang. "QCD prediction of transverse momentum distribution of partons." In: *Physics Letters B* 73.1 (1978), pp. 45 –48. ISSN: 0370-2693. DOI: 10.1016/0370-2693(78)90168-5.

[74] G. Altarelli. "Partons in quantum chromodynamics." In: *Physics Reports* 81.1 (1982), pp. 1 –129. ISSN: 0370-1573. DOI: 10.1016/0370-1573(82)90127-2.

[75] D. J. Gross and F. Wilczek. "Ultraviolet Behavior of Non-Abelian Gauge Theories." In: *Phys. Rev. Lett.* 30 (26 1973), pp. 1343–1346. DOI: 10.1103/PhysRevLett.30.1343.

[76] H. D. Politzer. "Reliable Perturbative Results for Strong Interactions?" In: *Phys. Rev. Lett.* 30 (26 1973), pp. 1346–1349. DOI: 10.1103/PhysRevLett.30.1346.

[77] M. Mekhfi. "Multiparton Processes: An Application to Double Drell-Yan." In: *Phys. Rev.* D32 (1985), p. 2371. DOI: 10.1103/PhysRevD.32.2371.

[78] B. Blok, Yu. Dokshitser, L. Frankfurt, and M. Strikman. "pQCD physics of multiparton interactions." In: *Eur. Phys. J.* C72 (2012), p. 1963. DOI: 10.1140/epjc/s10052-012-1963-8. arXiv: 1106.5533 [hep-ph].

[79] C. Tsallis. "Possible generalization of Boltzmann-Gibbs statistics." In: *Journal of Statistical Physics* 52.1 (1988), pp. 479–487. ISSN: 1572-9613. DOI: 10.1007/BF01016429.

[80] P. K Khandai, P. Sett, P. Shukla, and V. Singh. "Description of hadron p_T spectra with modified Tsallis function." In: *DAE Symp. Nucl. Phys.* 58 (2013), pp. 718–719.

[81] R. Ulrich, C. Baus, and R. Engel. "Relation between hadronic interactions and ultra-high energy extensive air showers." In: *EPJ Web Conf.* 99 (2015), p. 11001. DOI: 10.1051/epjconf/20159911001.

[82] T. Pierog, Iu. Karpenko, J. M. Katzy, E. Yatsenko, and K. Werner. "EPOS LHC: Test of collective hadronization with data measured at the CERN Large Hadron Collider." In: *Phys. Rev.* C92.3 (2015), p. 034906. DOI: 10.1103/PhysRevC.92.034906. arXiv: 1306.0121 [hep-ph].

[83] R. Abbasi et al. "Lateral Distribution of Muons in IceCube Cosmic Ray Events." In: *Phys. Rev.* D87.1 (2013), p. 012005. DOI: 10.1103/PhysRevD.87.012005. arXiv: 1208.2979 [astro-ph.HE].

[84] M. Calicchio et al. "Status report of the MACRO experiment at Gran Sasso." In: *Nucl. Instrum. Meth.* A264 (1988). [Nucl. Phys. Proc. Suppl.13,368(1990)], p. 18. DOI: 10.1016/0168-9002(88)91095-9.

[85] M. Ambrosio et al. "High statistics measurement of the underground muon pair separation at Gran Sasso." In: *Phys. Rev.* D60 (1999), p. 032001. DOI: 10.1103/PhysRevD.60.032001. arXiv: 9901027 [hep-ex].

[86] O. Ganel et al. "Beam tests of the balloon-borne (ATIC) experiment." In: *Nuclear Instruments and Methods in Physics Research Section A: Accelerators, Spectrometers, Detectors and Associated Equipment* 552.3 (2005), pp. 409 –419. ISSN: 0168-9002. DOI: 10.1016/j.nima.2005.06.081.

[87] H. S. Ahn et al. "The Cosmic Ray Energetics And Mass (CREAM) instrument." In: *Nucl. Instrum. Meth.* A579 (2007), pp. 1034–1053. DOI: 10.1016/j.nima.2007.05.203.

[88] P. Picozza et al. "PAMELA: A Payload for Antimatter Matter Exploration and Light-nuclei Astrophysics." In: *Astropart. Phys.* 27 (2007), pp. 296–315. DOI: 10.1016/j.astropartphys.2006.12.002. arXiv: 0608697 [astro-ph].

[89] S. Ting. "The Alpha Magnetic Spectrometer on the International Space Station." In: *Nuclear Physics B - Proceedings Supplements* 243 (2013), pp. 12 –24. ISSN: 0920-5632. DOI: 10.1016/j.nuclphysbps.2013.09.028.

[90] M. Aguilar et al. "First Result from the Alpha Magnetic Spectrometer on the International Space Station: Precision Measurement of the Positron Fraction in Primary Cosmic Rays of 0.5-350 GeV." In: *Phys. Rev. Lett.* 110 (2013), p. 141102. DOI: 10.1103/PhysRevLett.110.141102.

[91] C. Consolandi. "Primary Cosmic Ray Proton Flux Measured by AMS-02." In: *Proceedings, 33rd International Cosmic Ray Conference (ICRC2013): Rio de Janeiro, Brazil, July 2-9, 2013*. [,1265(2014)]. 2014, p. 1265. arXiv: 1402.0467 [astro-ph.HE].

[92] L. Baldini. "Space-Based Cosmic-Ray and Gamma-Ray Detectors: a Review." In: (2014). arXiv: 1407.7631 [astro-ph.IM].

[93] K. Bernloehr et al. "The optical system of the HESS imaging atmospheric Cherenkov telescopes, Part 1: Layout and components of the system." In: *Astropart. Phys.* 20 (2003), pp. 111–128. DOI: 10.1016/S0927-6505(03)00171-3. arXiv: -0308246 [astro-ph].

[94] J. A. Barrio. "The MAGIC Telescope - Design Study for the Construction of a 17 m Cherenkov Telescope for Gamma Astronomy above 10 GeV." In: (1998).

[95] H. Tokuno et al. "New air fluorescence detectors employed in the Telescope Array experiment." In: *Nuclear Instruments and Methods in Physics Research Section A: Accelerators, Spectrometers, Detectors and Associated Equipment* 676 (2012), pp. 54 –65. ISSN: 0168-9002. DOI: 10.1016/j.nima.2012.02.044.

[96] Schröder, F. G. "Radio detection of high-energy cosmic rays with the Auger Engineering Radio Array." In: *Proceedings, 13th Pisa Meeting on Advanced Detectors : Frontier Detectors for Frontier Physics (FDFP 2015): La Biodola, Isola d'Elba, Italy, May 24-30, 2015*. Vol. A824. 2016, pp. 648–651. DOI: 10.1016/j.nima.2015.08.047. arXiv: 1601.00462 [astro-ph.IM].

[97] H. Falcke et al. "Detection and imaging of atmospheric radio flashes from cosmic ray air showers." In: *Nature* 435 (2005), pp. 313–316. DOI: 10.1038/nature03614. arXiv: 0505383 [astro-ph].

[98] P. H. Barrett, L. M. Bollinger, G. Cocconi, Y. Eisenberg, and K. Greisen. "Interpretation of Cosmic-Ray Measurements Far Underground." In: *Rev. Mod. Phys.* 24 (3 1952), pp. 133–178. DOI: 10.1103/RevModPhys.24.133.

[99] D. E. Groom, N. V. Mokhov, and S. I. Striganov. "Muon stopping power and range tables 10-MeV to 100-TeV." In: *Atom. Data Nucl. Data Tabl.* 78 (2001), pp. 183–356. DOI: 10.1006/adnd.2001.0861.

[100] H. Bethe. "Zur Theorie des Durchgangs schneller Korpuskularstrahlen durch Materie." In: *Annalen Phys.* 5 (1930). [Annalen Phys.397,325(1930)], pp. 325–400. DOI: 10.1002/andp.19303970303.

[101] D. E. Groom and S. R. Klein. "Passage of particles through matter." In: *The European Physical Journal C - Particles and Fields* 15.1 (2000), pp. 163–173. DOI: 10.1007/BF02683419.

[102] H. Bethe and W. Heitler. "On the Stopping of Fast Particles and on the Creation of Positive Electrons." In: *Proceedings of the Royal Society of London A: Mathematical, Physical and Engineering Sciences* 146.856 (1934), pp. 83–112. DOI: 10.1098/rspa.1934.0140.

[103] A. A. Petrukhin and V. V. Shestakov. "The influence of the nuclear and atomic form factors on the muon bremsstrahlung cross section." In: *Canadian Journal of Physics* 46.10 (1968), S377–S380. DOI: 10.1139/p68-251.

[104] Y. .M. Andreev, L.B. Bezrukov, and E.V. Bugaev. "Excitation of a target in muon bremsstrahlung." In: *Physics of Atomic Nuclei* 57.12 (1994).

[105] S. R. Kelner, R. P. Kokoulin, and A. A. Petrukhin. "Bremsstrahlung from muons scattered by atomic electrons." In: *Physics of Atomic Nuclei* 60.4 (1997), pp. 576–583. DOI: 101134/1854854.

[106] S. R. Kelner, R. P. Kokoulin, and A. A. Petrukhin. "Cross Section for High Energy Muon Bremsstrahlung." In: *Preprint of Moscow Engineering Physics Inst.* (1995).

[107] A. Van Ginneken. "Energy Loss and Angular Characteristics of High-Energy Electromagnetic Processes." In: *Nucl. Instrum. Meth.* A251 (1986), p. 21. DOI: 10.1016/0168-9002(86)91146-0.

[108] J. H. Koehne, K. Frantzen, M. Schmitz, T. Fuchs, W. Rhode, D. Chirkin, and J. Becker Tjus. "PROPOSAL: A tool for propagation of charged leptons." In: *Comput. Phys. Commun.* 184 (2013), pp. 2070–2090. DOI: 10.1016/j.cpc.2013.04.001.

[109] S. R. Kelner and Y. D. Kotov. "Muon energy loss to pair production." In: *Soviet Journal of Nuclear Physics* 7 (1968), p. 237.

[110] R. P. Kokoulin and A. A. Petrukhin. "Analysis of the cross-section of direct pair production by fast muons." In: *Proceedings of the 11th International Conference on Cosmic Rays, held in Budapest, 25 August - 4 September 1969*. 1969.

[111] L.B. Bezrukov and E.V. Bugaev. "Nucleon shadowing effects in photonuclear interactions." In: *Sov. J. Nucl. Phys. (Engl. Transl.); (United States)* 33:5 (1981).

[112] E. V. Bugaev and Y. V. Shlepin. "Photonuclear interactions of super-high energy muons and tau-leptons." In: *Nuclear Physics B - Proceedings Supplements* 122 (2003), pp. 341 –344. DOI: 10.1016/S0920-5632(03)80414-0.

[113] E. Rutherford. "The Scattering of α and β Particles by Matter and the Structure of the Atom." In: *Philosophical Magazine* 21.6 (1911), pp. 669–688.

[114] G. Moliere. "Theory of the scattering of fast charged particles. 2. Repeated and multiple scattering." In: *Z. Naturforsch.* A3 (1948), pp. 78–97.

[115] H. A. Bethe. "Moliere's theory of multiple scattering." In: *Phys. Rev.* 89 (1953), pp. 1256–1266. DOI: 10.1103/PhysRev.89.1256.

[116] V. L. Highland. "Some practical remarks on multiple scattering." In: *Nuclear Instruments and Methods* 129.2 (1975), pp. 497 –499. DOI: http://dx.doi.org/10.1016/0029-554X(75)90743-0.

[117] Y.-S. Tsai. "Pair production and bremsstrahlung of charged leptons." In: *Rev. Mod. Phys.* 46 (4 1974), pp. 815–851. DOI: 10.1103/RevModPhys.46.815.

[118] A.V. Butkevich, R.P. Kokoulin, G.V. Matushko, and S.P. Mikheyev. "Comments on multiple scattering of high-energy muons in thick layers." In: *Nuclear Instruments and Methods in Physics Research Section A: Accelerators, Spectrometers, Detectors and Associated Equipment* 488.1–2 (2002), pp. 282 –294. DOI: http://dx.doi.org/10.1016/S0168-9002(02)00478-3.

[119] P. A. Cherenkov. "Visible emission of clean liquids by action of gamma radiation." In: *Doklady Akademii Nauk SSSR* 2 (1934), pp. 451+. URL: http://ufn.ru/en/articles/2007/4/g/.

[120] I. M. Frank and I. E. Tamm. "Coherent radiation of a fast electron in a medium." In: *Dokl. Akad. Nauk SSSR* 14 (1937), pp. 107–112.

[121] Jelley J. V. "Cherenkov Radiation and its Applications." In: (1958).

[122] C. Huygens. "Traité de la Lumière." In: *Leyden by Van der Aa (published 1960)* (1678), pp. 107–112.

[123] A. Fresnel. "Mémoire sur la diffraction de la lumière." In: *Ann. Chim. et Phys.* 1.1 (1816), pp. 239–281.

[124] S. G. Warren. "Optical constants of ice from the ultraviolet to the microwave." In: *Appl. Opt.* 23.8 (1984), pp. 1206–1225. DOI: 10.1364/AO.23.001206.

[125] T. Abu-Zayyad et al. "The surface detector array of the Telescope Array experiment." In: *Nucl. Instrum. Meth.* A689 (2013), pp. 87–97. DOI: 10.1016/j.nima.2012.05.079. arXiv: 1201.4964 [astro-ph.IM].

[126] W. D. Apel et al. "The KASCADE-Grande experiment." In: *Nucl. Instrum. Meth.* A620 (2010), pp. 202–216. DOI: 10.1016/j.nima.2010.03.147.

[127] T. Antoni et al. "KASCADE measurements of energy spectra for elemental groups of cosmic rays: Results and open problems." In: *Astropart. Phys.* 24 (2005), pp. 1–25. DOI: 10.1016/j.astropartphys.2005.04.001. arXiv: 0505413 [astro-ph].

[128] W. D. Apel et al. "The spectrum of high-energy cosmic rays measured with KASCADE-Grande." In: (2012). arXiv: 1206.3834 [astro-ph.HE].

[129] "The Pierre Auger Cosmic Ray Observatory." In: *Nuclear Instruments and Methods in Physics Research Section A: Accelerators, Spectrometers, Detectors and Associated Equipment* 798 (2015), pp. 172 –213. ISSN: 0168-9002. DOI: 10.1016/j.nima.2015.06.058.

[130] K. Greisen. "Cosmic ray showers." In: *Ann. Rev. Nucl. Part. Sci.* 10 (1960), pp. 63–108. DOI: 10.1146/annurev.ns.10.120160.000431.

[131] S. P. Swordy et al. "The Composition of cosmic rays at the knee." In: *Astropart. Phys.* 18 (2002), pp. 129–150. DOI: 10.1016/S0927-6505(02)00108-1. arXiv: 0202159 [astro-ph].

[132] R. Abbasi et al. "IceTop: The surface component of IceCube." In: *Nucl. Instrum. Meth.* A700 (2013), pp. 188–220. DOI: 10.1016/j.nima.2012.10.067. arXiv: 1207.6326 [astro-ph.IM].

[133] M. G. Aartsen et al. "The IceCube Neutrino Observatory - Contributions to ICRC 2015 Part III: Cosmic Rays." In: (2015). arXiv: 1510.05225 [astro-ph.HE].

[134] H. Hanada et al. "A highly sensitive optical detector for use in deep underwater." In: *Nucl. Instrum. Meth.* A408 (1998), pp. 425–437. DOI: 10.1016/S0168-9002(98)00196-X.

[135] E. Andres et al. "The AMANDA neutrino telescope: Principle of operation and first results." In: *Astropart. Phys.* 13 (2000), pp. 1–20. DOI: 10.1016/S0927-6505(99)00092-4. arXiv: 9906203 [astro-ph].

[136] E. Andres et al. "Observation of high-energy neutrinos using Cherenkov detectors embedded deep in Antarctic ice." In: *Nature* 410 (2001), pp. 441–443. DOI: 10.1038/35068509.

[137] E. Aslanides et al. "A deep sea telescope for high-energy neutrinos." In: (1999). arXiv: 9907432 [astro-ph].

[138] M. Ageron et al. "ANTARES: The first undersea neutrino telescope." In: *Nuclear Instruments and Methods in Physics Research Section A: Accelerators, Spectrometers, Detectors and Associated Equipment* 656.1 (2011), pp. 11 –38. ISSN: 0168-9002. DOI: 10.1016/j.nima.2011.06.103.

[139] S. Adrian-Martinez et al. "The prototype detection unit of the KM3NeT detector." In: *Eur. Phys. J.* C76.2 (2016), p. 54. DOI: 10.1140/epjc/s10052-015-3868-9. arXiv: 1510.01561 [astro-ph.IM].

[140] I.A Belolaptikov et al. "The Baikal underwater neutrino telescope: Design, performance, and first results." In: *Astroparticle Physics* 7.3 (1997), pp. 263 –282. ISSN: 0927-6505. DOI: 10.1016/S0927-6505(97)00022-4.

[141] M. G. Aartsen et al. "Measurement of the Atmospheric ν_e Spectrum with IceCube." In: *Phys. Rev.* D91 (2015), p. 122004. DOI: 10.1103/PhysRevD.91.122004. arXiv: 1504.03753 [astro-ph.HE].

[142] M. G. Aartsen et al. "Atmospheric and astrophysical neutrinos above 1 TeV interacting in IceCube." In: *Phys. Rev.* D91.2 (2015), p. 022001. DOI: 10.1103/PhysRevD.91.022001. arXiv: 1410.1749 [astro-ph.HE].

[143] M. G. Aartsen et al. "Neutrino oscillation studies with IceCube-DeepCore." In: *Nucl. Phys.* B908 (2016), pp. 161–177. DOI: 10.1016/j.nuclphysb.2016.03.028.

[144] M. G. Aartsen et al. "Searches for Sterile Neutrinos with the IceCube Detector." In: *Phys. Rev. Lett.* 117.7 (2016), p. 071801. DOI: 10.1103/PhysRevLett.117.071801. arXiv: 1605.01990 [hep-ex].

[145] M. G. Aartsen et al. "Search for annihilating dark matter in the Sun with 3 years of IceCube data." In: (2016). arXiv: 1612.05949 [astro-ph.HE].

[146] M. G. Aartsen et al. "First search for dark matter annihilations in the Earth with the IceCube Detector." In: (2016). arXiv: 1609.01492 [astro-ph.HE].

[147] M. G. Aartsen et al. "All-flavour Search for Neutrinos from Dark Matter Annihilations in the Milky Way with IceCube/DeepCore." In: *Eur. Phys. J.* C76.10 (2016), p. 531. DOI: 10.1140/epjc/s10052-016-4375-3. arXiv: 1606.00209 [astro-ph.HE].

[148] M. G. Aartsen et al. "Searches for Relativistic Magnetic Monopoles in IceCube." In: *Eur. Phys. J.* C76.3 (2016), p. 133. DOI: 10.1140/epjc/s10052-016-3953-8. arXiv: 1511.01350 [astro-ph.HE].

[149] M. G. Aartsen et al. "Search for non-relativistic Magnetic Monopoles with IceCube." In: *Eur. Phys. J.* C74.7 (2014), p. 2938. DOI: 10.1140/epjc/s10052-014-2938-8. arXiv: 1402.3460 [astro-ph.CO].

[150] M. G. Aartsen et al. "The IceCube Neutrino Observatory Part IV: Searches for Dark Matter and Exotic Particles." In: (2013), pp. 25 –32. arXiv: 1309.7007 [astro-ph.HE].

[151] S. Kopper. "Search for exotic double tracks with the IceCube Neutrino Telescope." PhD thesis. University of Wuppertal, 2014.

[152] M. G. Aartsen et al. "Anisotropy in Cosmic-ray Arrival Directions in the Southern Hemisphere Based on six Years of Data From the IceCube Detector." In: *Astrophys. J.* 826.2 (2016), p. 220. DOI: 10.3847/0004-637X/826/2/220. arXiv: 1603.01227 [astro-ph.HE].

[153] F. Halzen and S. R. Klein. "IceCube: An Instrument for Neutrino Astronomy." In: *Rev. Sci. Instrum.* 81 (2010), p. 081101. DOI: 10.1063/1.3480478. arXiv: 1007.1247 [astro-ph.HE].

[154] R. Abbasi et al. "The Design and Performance of IceCube DeepCore." In: *Astropart. Phys.* 35 (2012), pp. 615–624. DOI: 10.1016/j.astropartphys.2012.01.004. arXiv: 1109.6096 [astro-ph.IM].

[155] M. Ackermann et al. "Optical properties of deep glacial ice at the South Pole." In: *J. Geophys. Res. Atmos.* 111.D13 (2006), p. D13203. DOI: 10.1029/2005JD006687.

[156] M. G. Aartsen et al. "Measurement of South Pole ice transparency with the IceCube LED calibration system." In: *Nucl. Instrum. Meth.* A711 (2013), pp. 73–89. DOI: 10.1016/j.nima.2013.01.054. arXiv: 1301.5361 [astro-ph.IM].

[157] N. E. Bramall, R. C. Bay, K. Woschnagg, R. A. Rohde, and P. B. Price. "A deep high-resolution optical log of dust, ash, and stratigraphy in South Pole glacial ice." In: *Geophysical Research Letters* 32.21 (2005). L21815. DOI: 10.1029/2005GL024236.

[158] P. B. Price, K. Woschnagg, and D. Chirkin. "Age vs depth of glacial ice at South Pole." In: *Geophysical Research Letters* 27.14 (2000), pp. 2129–2132. DOI: 10.1029/2000GL011351.

[159] R. Abbasi et al. "Calibration and Characterization of the IceCube Photomultiplier Tube." In: *Nucl. Instrum. Meth.* A618 (2010), pp. 139–152. DOI: 10.1016/j.nima.2010.03.102. arXiv: 1002.2442 [astro-ph.IM].

[160] R. Abbasi et al. "The IceCube Data Acquisition System: Signal Capture, Digitization, and Timestamping." In: *Nucl. Instrum. Meth.* A601 (2009), pp. 294–316. DOI: 10.1016/j.nima.2009.01.001. arXiv: 0810.4930 [physics.ins-det].

[161] A. Achterberg et al. "First Year Performance of The IceCube Neutrino Telescope." In: *Astropart. Phys.* 26 (2006), pp. 155–173. DOI: 10.1016/j.astropartphys.2006.06.007. arXiv: 0604450 [astro-ph].

[162] P. B. Coates. "Photomultiplier collection efficiencies and nonpoissonian pulse height distributions." In: *Journal of Physics D: Applied Physics* 6.2 (1973), p. 153. URL: http://stacks.iop.org/0022-3727/6/i=2/a=303.

[163] S. Kleinfelder. "Gigahertz waveform sampling and digitization circuit design and implementation." In: *Nuclear Science, IEEE Transactions on* 50 (2003), pp. 955–962.

[164] R. Stokstad. "Design and performance of the IceCube electronics." In: *Proceedings, eleventh Workshop on Electronics for LHC and Future Experiments, Heidelberg, Germany, 12-16 September 2005*. 2005, p. 4. URL: http://lhc-workshop-2005.web.cern.ch/lhc%2Dworkshop%2D2005/PlenarySessions/4-Stokstad.pdf.

[165] "The IceCube Collaboration: Contributions to the 30th International Cosmic Ray Conference (ICRC 2007)." In: *Proceedings, 30th International Cosmic Ray Conference (ICRC 2007): Merida, Yucatan, Mexico, July 3-11, 2007*. 2007. arXiv: 0711.0353 [astro-ph].

[166] S. R. Klein. "IceCube: A Cubic Kilometer Radiation Detector." In: *IEEE Transactions on Nuclear Science* 56.3 (2009), pp. 1141–1147. DOI: 10.1109/TNS.2009.2015300.

[167] W. H. Press, S. A. Teukolsky, W. V. Vetterling, and B. P. Flannery. *Numerical Recipies in C – The Art of Scientific Computing*. Cambridge Univ. Press, 1997.

[168] E.-J. Ahn, R. Engel, T. K. Gaisser, P. Lipari, and T. Stanev. "Cosmic ray interaction event generator SIBYLL 2.1." In: *Phys. Rev.* D80 (2009), p. 094003. DOI: 10.1103/PhysRevD.80.094003. arXiv: 0906.4113 [hep-ph].

[169] H. C. Fesefeldt. "Simulation of hadronic showers, physics and applications." In: *RWTH Aachen Technical Report PITHA 85-02* (1985).

[170] M. Gyulassy and X.-N. Wang. "HIJING 1.0: A Monte Carlo program for parton and particle production in high-energy hadronic and nuclear collisions." In: *Comput. Phys. Commun.* 83 (1994), p. 307. DOI: 10.1016/0010-4655(94)90057-4. arXiv: 9502021 [nucl-th].

[171] G. Calucci and D. Treleani. "Minijets: Cross section and energy distribution in very-high-energy nuclear collisions." In: *Phys. Rev. D* 41 (11 1990), pp. 3367–3380. DOI: 10.1103/PhysRevD.41.3367.

[172] Andersson, B. and Gustafson, G. and Ingelman, G. and Sjöstrand, T. "Parton fragmentation and string dynamics." In: *Physics Reports* 97.2 (1983), pp. 31 –145. ISSN: 0370-1573. DOI: 10.1016/0370-1573(83)90080-7.

[173] H. U. Bengtsson and G. Ingelman. "The Lund Monte Carlo for High p_T Physics." In: *Comput. Phys. Commun.* 34 (1985), p. 251. DOI: 10.1016/0010-4655(85)90003-7.

[174] R. J. Glauber and G. Matthiae. "High-energy scattering of protons by nuclei." In: *Nucl. Phys.* B21 (1970), pp. 135–157. DOI: 10.1016/0550-3213(70)90511-0.

[175] J. Engel, T. K. Gaisser, T. Stanev, and Paolo Lipari. "Nucleus-nucleus collisions and interpretation of cosmic ray cascades." In: *Phys. Rev.* D46 (1992), pp. 5013–5025. DOI: 10.1103/PhysRevD.46.5013.

[176] N. N. Kalmykov and S. S. Ostapchenko. "The Nucleus-nucleus interaction, nuclear fragmentation, and fluctuations of extensive air showers." In: *Phys. Atom. Nucl.* 56 (1993). [Yad. Fiz.56N3,105(1993)], pp. 346–353.

[177] N. N. Kalmykov, S. S. Ostapchenko, and A. I. Pavlov. "EAS and a quark - gluon string model with jets." In: *Bull. Russ. Acad. Sci. Phys.* 58 (1994). [Izv. Ross. Akad. Nauk Ser. Fiz.58N12,21(1994)], pp. 1966–1969.

[178] A. B. Kaidalov and K. A. Ter-Martirosian. "Multiple Production of Hadrons at High-Energies in the Model of Quark-Gluon Strings." In: *Sov. J. Nucl. Phys.* 39 (1984). [Yad. Fiz.39,1545(1984)], p. 979.

[179] V. N. Gribov. "A Reggeon Diagram Technique." In: *Sov. Phys. JETP* 26 (1968). [Zh. Eksp. Teor. Fiz.53,654(1967)], pp. 414–422.

[180] G. Veneziano. "Regge Intercepts and Unitarity in Planar Dual Models." In: *Nucl. Phys.* B74 (1974), pp. 365–377. DOI: 10.1016/0550-3213(74)90203-X.

[181] V. A. Abramovsky, V. N. Gribov, and O. V. Kancheli. "Character of Inclusive Spectra and Fluctuations Produced in Inelastic Processes by Multi - Pomeron Exchange." In: *Yad. Fiz.* 18 (1973). [Sov. J. Nucl. Phys.18,308(1974)], pp. 595–616.

[182] S. Donnachie, G. Dosch, P. Landshoff, and O. Nachtmann. *Pomeron Physics and QCD*. Cambridge Monographs on Particle Physics, Nuclear Physics and Cosmology. Cambridge Univ. Press, 2002.

[183] S. S. Ostapchenko. Priv. Comm. June 10, 2015.

[184] T. Pierog and K. Werner. "EPOS Model and Ultra High Energy Cosmic Rays." In: *Nucl. Phys. Proc. Suppl.* 196 (2009), pp. 102–105. DOI: 10.1016/j.nuclphysbps.2009.09.017. arXiv: 0905.1198 [hep-ph].

[185] S. G. Matinyan and W. D. Walker. "Multiplicity distribution and mechanisms of the high-energy hadron collisions." In: *Phys. Rev.* D59 (1999), p. 034022. DOI: 10.1103/PhysRevD.59.034022. arXiv: 9801219 [hep-ph].

[186] P. Z. Skands. "Tuning Monte Carlo Generators: The Perugia Tunes." In: *Phys. Rev.* D82 (2010), p. 074018. DOI: 10.1103/PhysRevD.82.074018. arXiv: 1005.3457 [hep-ph].

[187] T. Sjostrand, S. Mrenna, and P. Z. Skands. "PYTHIA 6.4 Physics and Manual." In: *JHEP* 05 (2006), p. 026. DOI: 10.1088/1126-6708/2006/05/026. arXiv: 0603175 [hep-ph].

[188] A. Capella, U. Sukhatme, C.-I. Tan, and J. Tran Thanh Van. "Dual parton model." In: *Physics Reports* 236.4 (1994), pp. 225 –329. ISSN: 0370-1573. DOI: 10.1016/0370-1573(94)90064-7.

[189] S. Roesler, R. Engel, and J. Ranft. "The Monte Carlo event generator DPMJET-III." In: *Advanced Monte Carlo for radiation physics, particle transport simulation and applications. Proceedings, Conference, MC2000, Lisbon, Portugal, October 23-26, 2000*. 2000, pp. 1033–1038. DOI: 10.1007/978-3-642-18211-2_166. arXiv: 0012252 [hep-ph].

[190] J. Ranft. "DPMJET version II.5: Sampling of hadron hadron, hadron - nucleus and nucleus-nucleus interactions at accelerator and cosmic ray energies according to the two component dual parton model: Code manual." In: (1999). arXiv: 9911232 [hep-ph].

[191] J. Ranft. "Hadron Production in Hadron - Nucleus and Nucleus-nucleus Collisions in the Dual Monte Carlo Multichain Fragmentation Model." In: *Phys. Rev.* D37 (1988), p. 1842. DOI: 10.1103/PhysRevD.37.1842.

[192] M. Honda, T. Kajita, K. Kasahara, and S. Midorikawa. "New calculation of the atmospheric neutrino flux in a three-dimensional scheme." In: *Phys. Rev. D* 70 (4 2004), p. 043008. DOI: 10.1103/PhysRevD.70.043008.

[193] K. Pearson. *Proceedings of the Royal Society of London*. Bd. 58. Taylor & Francis, 1895, pp. 240–242. URL: https://books.google.de/books?id=60aL0zlT-90C.

[194] SciPy.org. *SciPy Documentation: scipy.interpolate.UnivariateSpline*. 2017. URL: http://docs.scipy.org/doc/scipy/reference/generated/scipy.interpolate.UnivariateSpline.html (visited on 06/03/2016).

[195] T. Sjostrand, S. Mrenna, and P. Z. Skands. "A Brief Introduction to PYTHIA 8.1." In: *Comput. Phys. Commun.* 178 (2008), pp. 852–867. DOI: 10.1016/j.cpc.2008.01.036. arXiv: 0710.3820 [hep-ph].

[196] P. Lipari. "Lepton spectra in the earth's atmosphere." In: *Astropart. Phys.* 1 (1993), pp. 195–227. DOI: 10.1016/0927-6505(93)90022-6.

[197] G. R. Grimmett and D. R. Stirzaker. *Probability and Random Processes*. Oxford: Clarendon Press, 1992.

[198] S. D. Poisson. *Probabilité des jugements en matière criminelle et en matiière civile, précédées des règles générales du calcul des probabilitiés*. Paris, France: Paris, Bachelier, 1837, p. 206. URL: http://www.archive.org/details/recherchessurlap00pois.

[199] F. A. Haight. *Handbook of the Poisson distribution*. Publications in operations research. New York, London: J. Wiley, 1967. URL: http://opac.inria.fr/record=b1080435.

[200] T. DeYoung. "IceTray: A software framework for IceCube." In: *Computing in high energy physics and nuclear physics. Proceedings, Conference, CHEP'04, Interlaken, Switzerland, September 27-October 1, 2004*. 2005, pp. 463–466. URL: http://doc.cern.ch/yellowrep/2005/2005-002/p463.pdf.

[201] A. Gazizov and M. P. Kowalski. "ANIS: High energy neutrino generator for neutrino telescopes." In: *Comput. Phys. Commun.* 172 (2005), pp. 203–213. DOI: 10.1016/j.cpc.2005.03.113. arXiv: 0406439 [astro-ph].

[202] H. L. Lai, J. Huston, S. Kuhlmann, J. Morfin, Fredrick I. Olness, J. F. Owens, J. Pumplin, and W. K. Tung. "Global QCD analysis of parton structure of the nucleon: CTEQ5 parton distributions." In: *Eur. Phys. J.* C12 (2000), pp. 375–392. DOI: 10.1007/s100529900196. arXiv: 9903282 [hep-ph].

[203] A. M. Dziewonski and D. L. Anderson. "Preliminary reference Earth model." In: *Physics of the Earth and Planetary Interiors* 25.4 (1981), pp. 297–356. DOI: 10.1016/0031-9201(81)90046-7.

[204] M. G. Aartsen et al. "Measurement of South Pole ice transparency with the IceCube LED calibration system." In: *Nucl. Instrum. Meth.* A711 (2013), pp. 73–89. DOI: 10.1016/j.nima.2013.01.054. arXiv: 1301.5361 [astro-ph.IM].

[205] J. Ahrens et al. "Muon track reconstruction and data selection techniques in AMANDA." In: *Nucl. Instrum. Meth.* A524 (2004), pp. 169–194. DOI: 10.1016/j.nima.2004.01.065. arXiv: 0407044 [astro-ph].

[206] M. G. Aartsen et al. "Improvement in Fast Particle Track Reconstruction with Robust Statistics." In: *Nucl. Instrum. Meth.* A736 (2014), pp. 143–149. DOI: 10.1016/j.nima.2013.10.074. arXiv: 1308.5501 [astro-ph.IM].

[207] S. Boyd and L. Vandenberghe. *Convex Optimization*. Cambridge Univ. Press, 2009, pp. 298–300.

[208] T. Bayes. "An Essay towards solving a Problem in the Doctrine of Chances." In: *Philos. Trans.* 53 (1763), pp. 370–418. DOI: 110.1098/rstl.1763.0053.

[209] G. C. Hill. "Bayesian event reconstruction and background rejection in neutrino detectors." In: vol. 3. 2001, p. 1279. arXiv: 0106081 [astro-ph].

[210] D. MacKay. *Information Theory, Inference and Learning Algorithms*. Cambridge: Cambridge Univ. Press, 2003, pp. 284–292.

[211] J. Neyman. "Outline of a Theory of Statistical Estimation Based on the Classical Theory of Probability." In: *Philosophical Transactions of the Royal Society of London A: Mathematical, Physical and Engineering Sciences* 236.767 (1937), pp. 333–380. ISSN: 0080-4614. DOI: 10.1098/rsta.1937.0005. eprint: http://rsta.royalsocietypublishing.org/content/236/767/333.full.pdf.

[212] G. Casella and L. B. Berger. *Statistical Inference*. Cambridge Monographs on Particle Physics, Nuclear Physics and Cosmology. Duxbury Press, 2001.

[213] R. Abbasi et al. "An improved method for measuring muon energy using the truncated mean of dE/dx." In: *Nucl. Instrum. Meth.* A703 (2013), pp. 190–198. DOI: 10.1016/j.nima.2012.11.081. arXiv: 1208.3430 [physics.data-an].

[214] D. A. Chirkin. "Cosmic Ray Energy Spectrum Measurement with the Antarctic Muon and Neutrino Detector Array (AMANDA)." PhD thesis. University of California at Berkeley, 2003.

[215] A.. Kolmogorov. "Sulla determinazione empirica di una legge di distribuzione." In: *G. Ist Ital. Attuari* 4 (1933), pp. 83–91.

[216] N. Smirnov. "Table for estimating the goodness of fit of empirical distributions." In: *Ann. Math. Stat.i* 19 (1948), pp. 279–281.

[217] R. Abbasi et al. "Cosmic Ray Composition and Energy Spectrum from 1-30 PeV Using the 40-String Configuration of IceTop and IceCube." In: *Astropart. Phys.* 42 (2013), pp. 15–32. DOI: 10.1016/j.astropartphys.2012.11.003. arXiv: 1207.3455 [astro-ph.HE].

[218] T. Feusels and K. Rawlins. "Cosmic Ray Composition and Energy Spectrum between 2.5 PeV and 1 EeV with IceTop and IceCube." In: *Proceedings, 33rd International Cosmic Ray Conference (ICRC2013): Rio de Janeiro, Brazil, July 2-9, 2013*. 2013, p. 0861. URL: http://www.cbpf.br/%7Eicrc2013/papers/icrc2013-0861.pdf.

[219] A. Bouchta. "Seasonal variation of the muon flux seen by AMANDA." In: *International Cosmic Ray Conference* 2 (1999), p. 108.

[220] S. Tilav et al. "Atmospheric Variations as observed by IceCube." In: *International Cosmic Ray Conference* (2009). arXiv: 1001.0776 [astro-ph].

[221] G. Bellini et al. "Cosmic-muon flux and annual modulation in Borexino at 3800 m water-equivalent depth." In: *JCAP* 1205 (2012), p. 015. DOI: 10.1088/1475-7516/2012/05/015. arXiv: 1202.6403 [hep-ex].

[222] M. Ambrosio et al. "Seasonal variations in the underground muon intensity as seen by MACRO." In: *Astropart. Phys.* 7 (1997), pp. 109–124. DOI: 10.1016/S0927-6505(97)00011-X.

[223] AIRS Project (NASA Goddard Institute for Space Studies). *Infrared Infrared Sounder (AIRS) Data Center*. 2017. URL: https://disc.gsfc.nasa.gov/AIRS/ (visited on 03/10/2017).

[224] M. G. Aartsen et al. "The IceCube Neutrino Observatory: instrumentation and online systems." In: *Journal of Instrumentation* 12.03 (2017), P03012. URL: http://stacks.iop.org/1748-0221/12/i=03/a=P03012.

[225] M. E. Peskin. "Beyond the standard model." In: *High-energy physics. Proceedings, European School, Carry-le-Rouet, France, September 1-14, 1996*. 1997. arXiv: 9705479 [hep-ph].

[226] H. W. Baer and X. Tata. *Weak scale supersymmetry: from superfields to scattering events*. Cambridge: Cambridge Univ. Press, 2006. URL: https://cds.cern.ch/record/988941.

[227] S. P. Martin. "A Supersymmetry primer." In: *Adv. Ser. Direct. High Energy Phys.* 18.1 (1998). DOI: 10.1142/9789812839657_0001, 10.1142/9789814307505_0001. arXiv: 9709356 [hep-ph].

[228] I. Albuquerque, G. Burdman, and Z. Chacko. "Neutrino telescopes as a direct probe of supersymmetry breaking." In: *Phys. Rev. Lett.* 92 (2004), p. 221802. DOI: 10.1103/PhysRevLett.92.221802. arXiv: 0312197 [hep-ph].

[229] M. Ahlers, J. Kersten, and A. Ringwald. "Long-lived staus at neutrino telescopes." In: *JCAP* 0607 (2006), p. 005. DOI: 10.1088/1475-7516/2006/07/005. arXiv: 0604188 [hep-ph].

[230] I. F. M. Albuquerque, G. Burdman, C. A. Krenke, and B. Nosratpour. "Direct Detection of Kaluza-Klein Particles in Neutrino Telescopes." In: *Phys. Rev.* D78 (2008), p. 015010. DOI: 10.1103/PhysRevD.78.015010. arXiv: 0803.3479 [hep-ph].

[231] I. J. R. Aitchison. "Supersymmetry and the MSSM: An Elementary introduction." In: (2005). arXiv: 0505105 [hep-ph].

[232] C. F. Berger, J. S. Gainer, J. A. L. Hewett, and T. G. Rizzo. "Supersymmetry Without Prejudice." In: *JHEP* 02 (2009), p. 023. DOI: 10.1088/1126-6708/2009/02/023. arXiv: 0812.0980 [hep-ph].

[233] H. P. Nilles. "Dynamically Broken Supergravity and the Hierarchy Problem." In: *Phys. Lett.* B115 (1982), p. 193. DOI: 10.1016/0370-2693(82)90642-6.

[234] A. H. Chamseddine, R. L. Arnowitt, and P. Nath. "Locally Supersymmetric Grand Unification." In: *Phys. Rev. Lett.* 49 (1982), p. 970. DOI: 10.1103/PhysRevLett.49.970.

[235] H. P. Nilles. "Supergravity Generates Hierarchies." In: *Nucl. Phys.* B217 (1983), pp. 366–380. DOI: 10.1016/0550-3213(83)90152-9.

[236] B. C. Allanach et al. "The Snowmass points and slopes: Benchmarks for SUSY searches." In: *Eur. Phys. J.* C25 (2002), pp. 113–123. DOI: 10.1007/s10052-002-0949-3. arXiv: 0202233 [hep-ph].

[237] G. F. Giudice and R. Rattazzi. "Theories with gauge mediated supersymmetry breaking." In: *Phys. Rept.* 322 (1999), pp. 419–499. DOI: 10.1016/S0370-1573(99)00042-3. arXiv: 9801271 [hep-ph].

[238] L. Randall and R. Sundrum. "Out of this world supersymmetry breaking." In: *Nucl. Phys.* B557 (1999), pp. 79–118. DOI: 10.1016/S0550-3213(99)00359-4. arXiv: 9810155 [hep-th].

[239] G. F. Giudice, M. A. Luty, H.i Murayama, and R. Rattazzi. "Gaugino mass without singlets." In: *JHEP* 12 (1998), p. 027. DOI: 10.1088/1126-6708/1998/12/027. arXiv: 9810442 [hep-ph].

[240] S. Dawson, E. Eichten, and C. Quigg. "Search for Supersymmetric Particles in Hadron - Hadron Collisions." In: *Phys. Rev.* D31 (1985), p. 1581. DOI: 10.1103/PhysRevD.31.1581.

[241] W. Porod. "SPheno, a program for calculating supersymmetric spectra, SUSY particle decays and SUSY particle production at e+ e- colliders." In: *Comput. Phys. Commun.* 153 (2003), pp. 275–315. DOI: 10.1016/S0010-4655(03)00222-4. arXiv: 0301101 [hep-ph].

[242] S. Ando, J. F. Beacom, S. Profumo, and D. Rainwater. "Probing new physics with long-lived charged particles produced by atmospheric and astrophysical neutrinos." In: *JCAP* 0804 (2008), p. 029. DOI: 10.1088/1475-7516/2008/04/029. arXiv: 0711.2908 [hep-ph].

[243] G. Aad et al. "Summary of the searches for squarks and gluinos using $\sqrt{s} = 8$ TeV pp collisions with the ATLAS experiment at the LHC." In: *JHEP* 10 (2015), p. 054. DOI: 10.1007/JHEP10(2015)054. arXiv: 1507.05525 [hep-ex].

[244] G. Aad et al. "Summary of the ATLAS experiment sensitivity to supersymmetry after LHC Run 1 nterpreted in the phenomenological MSSM." In: *JHEP* 10 (2015), p. 134. DOI: 10.1007/JHEP10(2015)134. arXiv: 1508.06608 [hep-ex].

[245] Serguei Chatrchyan et al. "Interpretation of Searches for Supersymmetry with simplified Models." In: *Phys. Rev.* D88.5 (2013), p. 052017. DOI: 10.1103/PhysRevD.88.052017. arXiv: 1301.2175 [hep-ex].

[246] V. Khachatryan et al. "Phenomenological MSSM interpretation of CMS searches in pp collisions at sqrt(s) = 7 and 8 TeV." In: *JHEP* 10 (2016), p. 129. DOI: 10.1007/JHEP10(2016)129. arXiv: 1606.03577 [hep-ex].

[247] J.R. Hansen, M. Ruedy, M Sato, and K Lo. "Global surface temperature change." In: *Rev. Geophys.* 48 (2016), RG4004. DOI: 10.1029/2010RG0003453.

[248] GISTEMP Team (NASA Goddard Institute for Space Studies). *GISS Surface Temperature Analysis (GISTEMP)*. 2017. URL: http://data.giss.nasa.gov/gistemp/ (visited on 03/10/2017).

LIST OF FIGURES

LIST OF TABLES

INDEX

T

COLOPHON

This document was typeset based on the typographical look-and-feel `classicthesis` developed by A. Miede.

`http://bitbucket.org/amiede/classicthesis/`